This electronic thesis or dissertation has been downloaded from Explore Bristol Research, http://research-information.bristol.ac.uk

Author:
Asplet, Joseph

Title:
New techniques for the robust detection and quantification of seismic anisotropy in the lowermost mantle

General rights
Access to the thesis is subject to the Creative Commons Attribution - NonCommercial-No Derivatives 4.0 International Public License. A copy of this may be found at https://creativecommons.org/licenses/by-nc-nd/4.0/legalcode This license sets out your rights and the restrictions that apply to your access to the thesis so it is important you read this before proceeding.

Take down policy
Some pages of this thesis may have been removed for copyright restrictions prior to having it been deposited in Explore Bristol Research. However, if you have discovered material within the thesis that you consider to be unlawful e.g. breaches of copyright (either yours or that of a third party) or any other law, including but not limited to those relating to patent, trademark, confidentiality, data protection, obscenity, defamation, libel, then please contact collections-metadata@bristol.ac.uk and include the following information in your message:

- Your contact details
- Bibliographic details for the item, including a URL
- An outline nature of the complaint

Your claim will be investigated and, where appropriate, the item in question will be removed from public view as soon as possible.

New techniques for the robust detection and quantification of seismic anisotropy in the lowermost mantle

By

JOSEPH P. R. ASPLET

School of Earth Sciences
UNIVERSITY OF BRISTOL

A dissertation submitted to the University of Bristol in accordance with the requirements of the degree of DOCTOR OF PHILOSOPHY in the Faculty of Sciences.

AUGUST 2021

Word count: 30547

ABSTRACT

The lowermost mantle — D$''$ — is a crucial thermochemical boundary layer within the Earth, exerting control over dynamic processes in both the overlying mantle and the core below. Constraining seismic anisotropy (the variation of seismic velocity with direction) within this layer could give us key insights into its dynamics and composition. In this thesis I collect a new broadband dataset of SKS-SKKS shear-wave splitting, where ca. 17 % of global observations are discrepant representing a significant increase compared to previous analysis. Using this dataset I develop new techniques to study discrepant SKS-SKKS shear-wave splitting and to invert of shear-wave waveforms for the orientation and strength of seismic anisotropy. I apply both these new techniques to study seismic anisotropy in D$''$ beneath the Eastern Pacific. Analysis of SKS-SKKS shear-wave splitting discrepancies highlight a significant region of azimuthal anisotropy in D$''$ which is most plausibly explained by the lattice preferred orientation of post-perovskite. I then test these qualitative interpretations, which are typical of SKS-SKKS shear-wave splitting studies, by jointly inverting ScS, SKS and SKKS waveforms for seismic anisotropy in a fast shear-wave velocity anomaly beneath the Eastern Pacific. I evaluate four candidate mechanisms for seismic anisotropy in D$''$: elliptical transverse isotropy (TI; representing for example anisotropy due to melt or layering), bridgmanite, and post-perovskite (for fabrics dominated by either [100](001) or [100](010) slip). Elliptical TI and both post-perovskite fabrics reasonably explain the input data, with predictions of horizontal flow for elliptical TI and post-perovskite [100](001) agreeing with recent mantle flow models. The techniques I have developed give seismologists powerful new tools to constrain lowermost mantle anisotropy.

DEDICATION AND ACKNOWLEDGEMENTS

I will be eternally grateful to my supervisor James Wookey for all the support he has given me throughout my PhD. My deepest thanks also go to my second supervisor, Mike Kendall, for the wisdom he has shared and for always pushing me to look at the bigger picture. I look forward to continue working with you both over the coming years.

Thank you to Jack Walpole for all the help you gave me when I was starting out on this journey.

Thank you to my examiners, Oliver Lord and Sanne Cottaar. The engaging and insightful discussion that we had in my viva (and the subsequent suggestions) have helped to improve the quality of this final version of my thesis.

Thank you to Nick Teanby and Tim Elliot, for enduring the APM process with me. Your advice and guidance helped me stay focused on what was important in my project.

Thank you to the NERC GW4+ Doctoral Training Partnership and to Emiliana Palk and Sara Tonge. The support of the DTP and the additional training that they provided were invaluable to my studies. I am also incredibly grateful to the support I have received from the Government of Jersey, in the form of a postgraduate grant.

Thank you to Andrew Walker and Nicolas Flament for providing the mantle flow models used in this work.

To everyone in the Geophysics group, those who I've shared an office (G.9, G.10a, G.10b and, finally, G.42) with as I have slowly migrated round the Wills Memorial Memorial and everyone throughout the department — thank you for making my time in Bristol so amazing! Particular thanks goes to my flatmates, Adam Klinger and Robbie Churchill, and to the regular attendees of the virtual Geophysics Coffee breaks, Hannah Susorny, Melody Slyvestre, David Schlaphort, Alan Baird, Anthony Butcher and Anna Horleston, for helping me to stay sane over the last year whilst I toiled writing my thesis from home.

Special thanks go to my self-appointed “PhD parents” Tom Kettlety and Anna Williams. Your friendship and support have meant a lot over the last few years.

Finally, thank you to my family. Without your support for so many years none of this would have been possible. All the little deliveries of Jersey Royals, choccies and cider have really helped me power through these last few months. I am now able to definitively answer some of your favourite “ask Joseph’s”:

- Yes — I *have* finished my thesis.
- Yes — I am *finally* going to get a “real job”.
- No — the mantle *still* isn’t made of cheese.

AUTHOR'S DECLARATION

I declare that the work in this dissertation was carried out in accordance with the requirements of the University's Regulations and Code of Practice for Research Degree Programmes and that it has not been submitted for any other academic award. Except where indicated by specific reference in the text, the work is the candidate's own work. Work done in collaboration with, or with the assistance of, others, is indicated as such. Any views expressed in the dissertation are those of the author.

SIGNED: ....JOSEPH ASPLET............................ DATE: ....31/07/2021..................

TABLE OF CONTENTS

LIST OF TABLES

LIST OF FIGURES

FIGURE **Page**

CHAPTER 1

INTRODUCTION

The Earth's core-mantle boundary constitutes one of the most crucial thermochemical boundaries within our planet. Early in Earth history dense iron-rich alloys and lighter magnesium-rich silicates segregated into the core and mantle. The exchange of energy and matter between the core and mantle drive a myriad of geodynamic processes within the Earth. The power of the Earth's geodynamo, created by convection of the liquid iron outer core, is controlled by the heat flow into the lowermost mantle and convective power generated at the inner core boundary. In turn this heat flow into the mantle, estimated to be in excess of 10 TW (Hernlund and McNamara, 2015), drives mantle dynamics which are ultimately expressed as tectonic processes at the Earth's surface.

The stark change in physical properties — such as density, viscosity, temperature and thermal conductivity — at the core-mantle boundary is perhaps matched only by Earth's surface. There is a pronounced density contrast, where at current pressure and temperature conditions (136 GPa and 4000 K) the core has a density of 9900 $\mathrm{kg\,m^{-3}}$ while the overlying mantle has a density of ca. 5500 $\mathrm{kg\,m^{-3}}$ (Dziewonski and Anderson, 1981). There is also a substantial viscosity contrast between the highly viscous, ca. $10^{20} - 10^{21}$ Pa s (Mitrovica and Forte, 2004), solid silicate mantle and the fluid iron outer core, ca. 10^{-2} Pa s (De Wijs et al., 1998). This contrast means that mantle controls heat exchange across the core-mantle boundary, insulating the core and preserving a molten iron core until the present day.

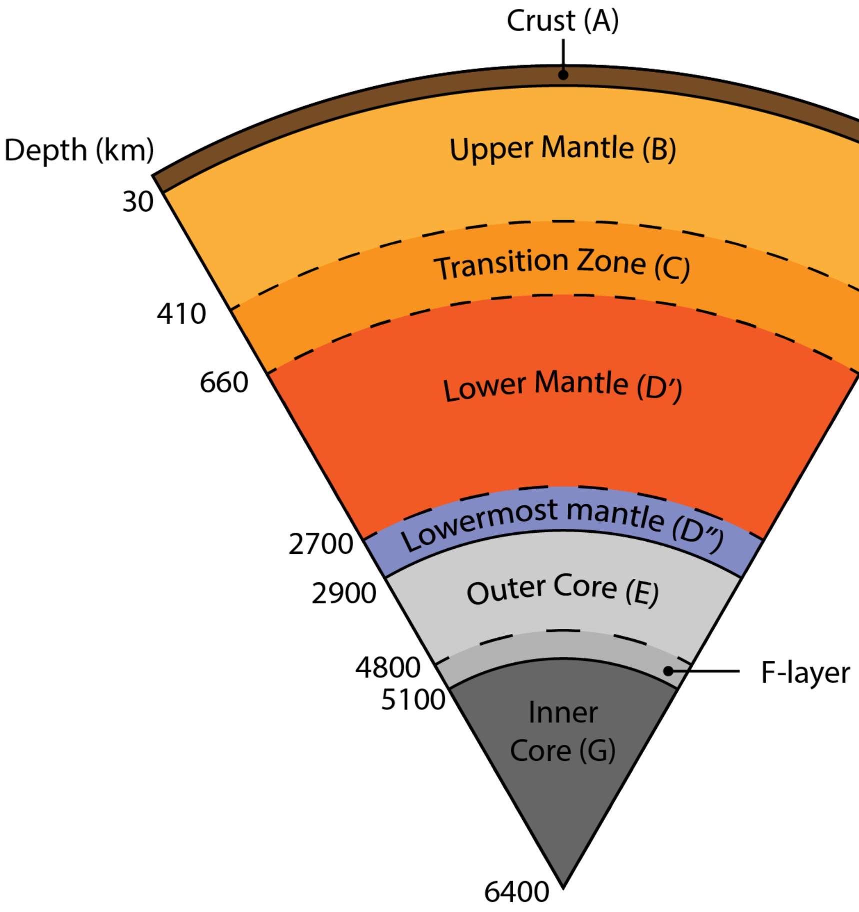

Figure 1.1: A schematic cartoon showing the layers of the Earth, as defined by Bullen (1949). The depth scale is intended to be indicative only and is not drawn to scale.

1.1 Earth Structure

The Earth can be subdivided into distinct layers following the compressibility-pressure hypothesis of Bullen (1949) who labelled these layers A to G, where A is the crust and G the inner core (Fig. 1.1). A subsequent revision to this model subdivided the D layer (the lower mantle) into the D′ and D″ layers (Bullen, 1949), giving us the nomenclature that has persisted until the present day. Before discussing the composition and dynamics of the lower mantle, I will give a brief overview of the other layers.

The Earth's crust (the A layer) is another significant boundary layer in our planet, along with the core-mantle boundary. It is also the thinnest of the Earth's layers, with oceanic crust having a mean thickness of 7.9km[1], with the mean thickness of continental crust ranging from ca. 36 - 41km with some variance in thickness with the age (Szwillus et al., 2019). Due to this, this crust is generally disregarded when studying mantle processes, especially the lowermost mantle. One notably exception is in geodynamics, where tectonic plate motion reconstructions and crustal dynamic topography are used to constrain mantle circulation models (e.g., Flament, 2019).

The upper mantle, or the B layer, is bounded by the Mohorovicic and 410km discontinuities (Fig. 1.1). Upper mantle dynamics can be inferred from the motion of the overlying tectonic plates (e.g., Long and Becker, 2010; Faccenna et al., 2014) and from high resolution seismic images of subducted slabs (e.g., Rodríguez et al., 2021) and upwelling mantle plumes (e.g., French and Romanowicz, 2014). The composition of the upper mantle can also be sampled directly by studying mid-ocean ridge basalts and xenoliths (e.g., Helffrich and Wood, 2001), which reveal an upper mantle that has a pyrolitic bulk composition, a chemical mixture that is 1 part basalt and 3 parts dunite (Ringwood and Major, 1966), and is comprised primarily of olivine (Fig. 1.2).

The mantle transition zone, or the C layer, is bounded by the 410 km and 660 km discontinuities (Fig.1.1), and is characterised by a number of significant pressure driven phase transitions (Fig. 1.2). Both the 410km and 660km discontinuities are globally persistent and seismically sharp (e.g., Shearer and Masters, 1992; Flanagan and Shearer, 1999). The 660km discontinuity has a pronounced effect on mantle dynamics, with seismic tomography showing subducting slabs being deflected horizontally and stagnating along the discontinuity (e.g., Fukao et al., 1992, 2009; Fukao and Obayashi, 2013; Li et al., 2013; King et al., 2015).

The mantle transition zone is dominated by the high-pressure polymorphs of olivine, wadsleyite and ringwoodite, along with majorite (Fig. 1.2; Ringwood and Major, 1970). It is believed that the mantle transition zone is hydrous, with both wadsleyite and ringwoodite hosting ca. 1 % of their weight as water (e.g., Sun et al., 2018b; Fei and Katsura, 2020). Samples of ringwoodite inclusions in diamonds have been found to contain ca. 1 wt% water (Pearson et al., 2014), although these results only reflect the conditions of one sample region. Locally hydrous regions of the transition zone have also been invoked to explain intra-plate volcanism (Yang and Faccenda, 2020). Whether the mantle transition zone is globally hydrous or not is unclear. Modelling of

---

[1] and of course is non-existent at the centre of mid-ocean ridges

transition zone viscosity profiles argues for a globally saturated layer (Fei et al., 2017), whilst there is limited seismic evidence for a hydrous transition zone (Houser, 2016).

The outer core, or E layer (Fig. 1.1), is composed of a liquid iron alloy (Birch, 1952). This liquid iron layer has vigorous convection, with the horizontal temperature fluctuations expected to be of the order of 10^{-3} K (Jones, 2011). This vigorous convection creates the Earth's geodynamo, which generates the Earth's magnetic field. The geodynamo has proved difficult to model, with numerical simulations unable to model convection at realistic outer core conditions (e.g., Schaeffer et al., 2016).

Despite the vigorous convection, there is evidence for stratified layers in the outer core. In the uppermost outer core there is seismic evidence that suggests anomalously slow, ca. 300 km thick stratified layer (e.g., Helffrich and Kaneshima, 2010; Irving et al., 2018). The global extent of this layer is disputed however, with some authors interpreting it as regional stratification due to variations in heat flux across the core-mantle boundary (Mound et al., 2019).

A second, 150 - 300km thick, seismically distinct layer exists at the base of the outer core (e.g., Souriau and Poupinet, 1991; Song and Helmberger, 1992; Adam and Romanowicz, 2015). Known only by Bullen (1949)'s nomenclature (Fig. 1.1), the existence of the F-layer poses important questions for the dynamics of the core such as: How did the layer develop in a vigorously convecting core? How do light elements, which help drive core convection, pass into the overlying outer core whilst preserving a stable layer? Whilst this area of research is undoubtedly exciting, it falls outside of the scope of this thesis.

The inner core, or the G-layer, is the final layer at the centre of the Earth, although there is growing evidence for yet further subdivision adding an innermost inner core (Stephenson et al., 2021). Following its discovery by Lehmann (1936), who observed differences in elastic properties of core-transiting P waves, the leading hypothesis for the composition of the inner core has been that it is solid iron (Birch, 1940; Bullen, 1946). This hypothesis was later confirmed by measurements of eigenfrequencies of inner-core sensitive normal mode oscillations (Dziewonski and Gilbert, 1971).

It is now well established that the growth of the inner core, through the freezing of the molten iron outer core (Jacobs, 1953), is driving convection in the outer core (Lister and Buffett, 1995) and therefore, indirectly, drives geodynamic processes throughout the planet. The age of the inner core is uncertain, with estimates ranging from $0.5 - 2.5$ Ga (Bono et al., 2019). It is believed that initially the Earth's core was wholly molten, with the inner core forming once secular cooling had reduced temperatures at the centre of the Earth to a point where solid metals are thermodynamically stable (Nimmo, 2015). Accurately estimating the age of the inner core requires geomagnetic observations and constraints on present-day energy and entropy budgets of the core, with the greatest source of uncertainty being uncertainty in present-day heat flow (ca. 12 ± 5TW) across the core-mantle boundary (Nimmo, 2015). Therefore by improving our understanding of the core-mantle boundary region, we can add constraints to modelling of the geodynamo and to the evolution of the Earth's core.

The lowermost mantle (or D'' layer) forms a substantial thermochemical boundary layer above the core-mantle boundary, which is estimated to range in thickness from 150 km to 350 km with a mean thickness of 260 km (Kendall and Shearer, 1994; Wysession et al., 1998). Our understanding of this region has greatly improved in recent years with a picture emerging of D'' as a layer with strong lateral heterogeneity. Recent efforts to map heterogeneities across the core-mantle boundary using SPdKS waveforms finding that at least 20% may contain resolvable heterogeneities (Thorne et al., 2021). It is likely that the strong heterogenous nature of D'' plays an important role in mantle and core dynamics. Despite recent advances, D'' remains a somewhat enigmatic region and advancing our knowledge requires multidisciplinary effort. Imaging flow in D'' has been a longstanding aim of lowermost mantle research, requiring advances in seismic observations and mineral physics frameworks needed to interpret flow (e.g., Creasy et al., 2020; Nowacki and Cottaar, 2021). Constraining the dynamics of D'' is crucial to developing a deeper understanding of the Earth's dynamic mantle. Here I will briefly review our current understanding of the structure and composition of D'' before reflecting on what can be done to constrain D'' dynamics.

1.2 Composition of the lower mantle

The lower mantle (i.e., the mantle below the 660km discontinuity) comprises ca. 56 % of the Earth's volume, yet the bulk composition remains relatively poorly constrained. For a long time it was assumed that mantle composition was broadly pyrolitic as the major phase transitions of the pyrolite model (a chemical mixture that is 1 part basalt and 3 parts dunite Ringwood and Major, 1966) align with known layering in the mantle at the 410 km and 660 km discontinuities (Fig. 1.2).

Using pyrolite as a model model gives the approximate composition of the lower mantle as 80% $MgSiO_3$ (bridgmanite or post-perovskite), 15% (Mg, Fe)O (ferropericlase) and 5% Ca-perovskite (Hirose et al., 2017).

Whilst pyrolite provides a good model for the upper mantle, there have been arguments for a compositionally distinct lower mantle. Modelling of seismic profiles (Cammarano et al., 2005) has shown that a dry pyrolitic composition could not fit lower mantle velocity depth gradients. An alternate model that has been postulated is for a "perovskitic" lower mantle with enrichment in $MgSiO_3$ of up to 93%, based on measurements of $MgSiO_3$ (bridgmanite) and (Mg,Fe)O (ferropericlase) at realistic lower mantle conditions of 2700 K and 91 GPa (Murakami et al., 2012). This model has proved contentious however, with criticisms of the methodology used. Repeated analysis of the data using improved Voight-Ruess-Hill averaging schemes (Cottaar et al., 2014a) and improved *ab initio* simulations of the seismic velocities of $MgSiO_3$ bridgmanite (Zhang et al., 2013; Wang et al., 2015; Zhang et al., 2016) refute the "perovskitic" model and show pyrolite is still that modle that best fits observed lower mantle seismic velocities and densities, represented by PREM (at least outside of D'' Zhang et al., 2016). Furthermore, the Murakami et al. (2012) model requires there to be little mass exchange between the upper and lower mantle. There is, however, reasonable evidence for mixing of the upper and lower mantle as we can image subducting slabs pierce the 660km discontinuity and descend towards the core-mantle boundary (e.g., Van der Hilst et al., 1997) and some upwelling mantle plumes can be traced from near the core-mantle boundary into the upper mantle (e.g., French and Romanowicz, 2015).

If we consider the Earth's bulk composition, there is further support for a silica enriched lower mantle. The Earth is widely regarded to have a refractory element abundance similar to solar abundance or C1 chondrites (e.g., Anders, 1977; Ringwood, 1977; Wänke, 1981) with a Mg/Si ratio close to 1.0, whilst the pyrolitic upper mantle has a Mg/Si ratio of 1.27 (e.g., Ringwood, 1991). Reconciling the Earth's Si budget requires enrichment in the deep interior. It has been suggested that this is accommodated by Si being the primary light element, up to 5 wt%, in the core (Allègre et al., 1995), although the seismic evidence does not support such significant wt% Si (Badro et al., 2014). This leaves bridgmanite enrichment in the lower mantle as the most plausible Si reservoir, with a bridgmanite enriched layer potentially being due to fractional crystallisation of a basal magma ocean (e.g., Xie et al., 2020). There is good geochemical evidence to support a differentiation event with Nd-W-Hf isotopic data from ocean island basalt samples from Réunion

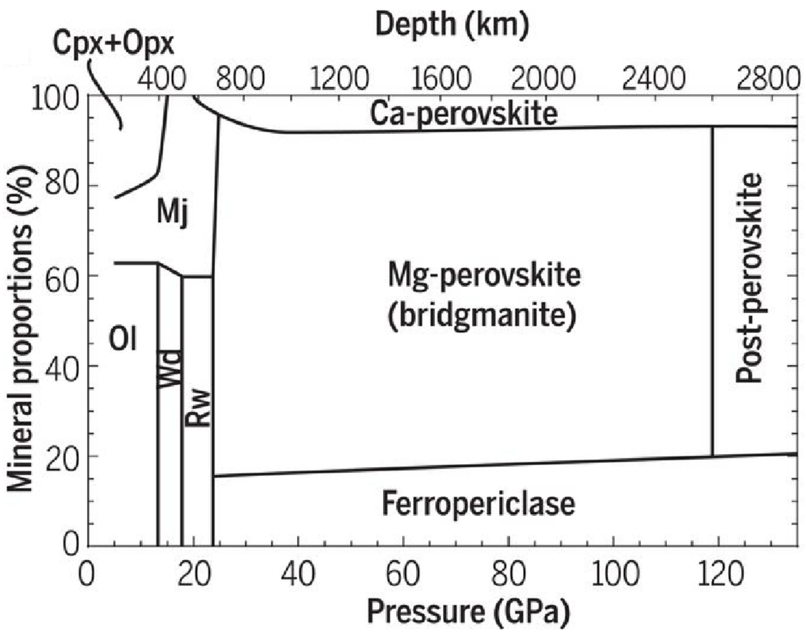

Figure 1.2: Mineral proportions in a pyrolitic mantle composition. Abbreviated minerals are olivine (Ol), wadsleyite (Wd), ringwoodite (Rw), clinopyroxene (Cpx), orthopyroxene (Opx) and majorite (or garnet, Mj). Figure from Hirose et al. (2017).

(e.g., Peters et al., 2018, 2021) and Samoa (e.g., Horan et al., 2018) recording remnants from Hadean silicate differentiation events in the modern lowermost mantle.

1.2.1 Post-perovskite transition

Regardless of the exact composition of the lower mantle, $MgSiO_3$ bridgmanite is by far the dominant mineral phase with estimates ranging from 69 - 93 wt % (Hirose et al., 2015). At expected lowermost mantle pressure and temperature conditions (> 120 GPa and 2500 K) bridgmanite undergoes a phase transformation from a perovskite to a post-perovskite crystal structure (Fig. 1.3; Murakami et al., 2004; Oganov and Ono, 2004; Tateno et al., 2009). The existence of such a phase transition, with a positive Claperyon slope of $6\,\mathrm{MPa\,K^{-1}}$, in the lowermost mantle had long been speculated to explain the D'' discontinuity (Sidorin et al., 1999). The discovery of post-perovskite, confirming the predictions, has revolutionised our understanding of the lowermost mantle.

The physical properties of post-perovskite can be determined experimentally and from *ab initio* calculations, (e.g., Oganov and Ono, 2004). From a seismologists perspective the elastic properties are the most intriguing as they inform whether post-perovskite can explain our observations of D'', namely the D'' discontinuity, the anti-correlation of shear and bulk velocities, and seismic anisotropy. There have been numerous *ab initio* estimates of post-perovskite bulk and shear moduli, with the consensus being that the bulk modulus is similar to bridgmanite for pressures > 80 GPa whilst the shear modulus is larger for post-perovskite, with larger pressure and temperature gradients at lowermost mantle conditions (see review by Hirose et al., 2015). Given that post-perovskite is ca. 1.5 % denser than bridgmanite this results in a 4% increase is shear-wave velocity (V_S), a negligible increase in compressional wave velocity (V_P) and a strong reduction in bulk sound velocity (Wookey et al., 2005b).

The stability of post-perovskite in the lowermost mantle is an important outstanding question and the exact nature of the post-perovskite transition in D$''$ conditions is unknown. Experiments estimate the Claperyon slope to be in the range of $5\,\mathrm{MPa\,K^{-1}}$ - $14\,\mathrm{MPa\,K^{-1}}$, with results being highly dependent on the pressure scale used (Hirose et al., 2015). Composition, most notably the addition of Al and Fe, also affects the phase transition. The presence of Al has been shown to improve the stability of bridgmanite with pressure (e.g., Tateno et al., 2005). The effect of Fe is still a subject of debate with some experimental and theoretical studies showing that Fe lowers the pressures needed to form post-perovskite (Mao et al., 2004; Dorfman et al., 2012) and others that Fe stabilises bridgmanite relative to post-perovskite (e.g., Murakami et al., 2005; Tateno et al., 2007).

Consequently any lateral variation in temperature or composition in D$''$ affects the stability of post-perovskite. The steep Claperyon slope of the phase transition means that lateral temperature variations can have a significant effect on the height of the phase transition, which matches with observations of the D$''$ discontinuity (e.g., Kendall and Shearer, 1994). It has also been suggested that behaviour of the geotherm near the core-mantle boundary causes post-perovskite to transform back to bridgmanite, forming lenses of post-perovskite in D$''$ (Hernlund et al., 2005). Within warmer regions of D$''$ post-perovskite may not be stable at all.

The composition of D$''$ can also have a pronounced effect on size of the bridgemanite to post-pervoskite transition, or post-perovskite boundary. Diamond anvil cell experiments suggest that a pyrolitic D$''$ would have a gradual transition, where both bridgmanite and post-perovskite are present. Experimental results suggest this transition zone could be $400-600 \pm 100$ km thick for a pyrolitic mantle composition, rendering it seismically undetectable (Catalli et al., 2009; Grocholski et al., 2012). Regions of D$''$ enriched in material from the lithosphere, such as mid-ocean ridge basalt or harzburgite, produce a much narrower transition (Grocholski

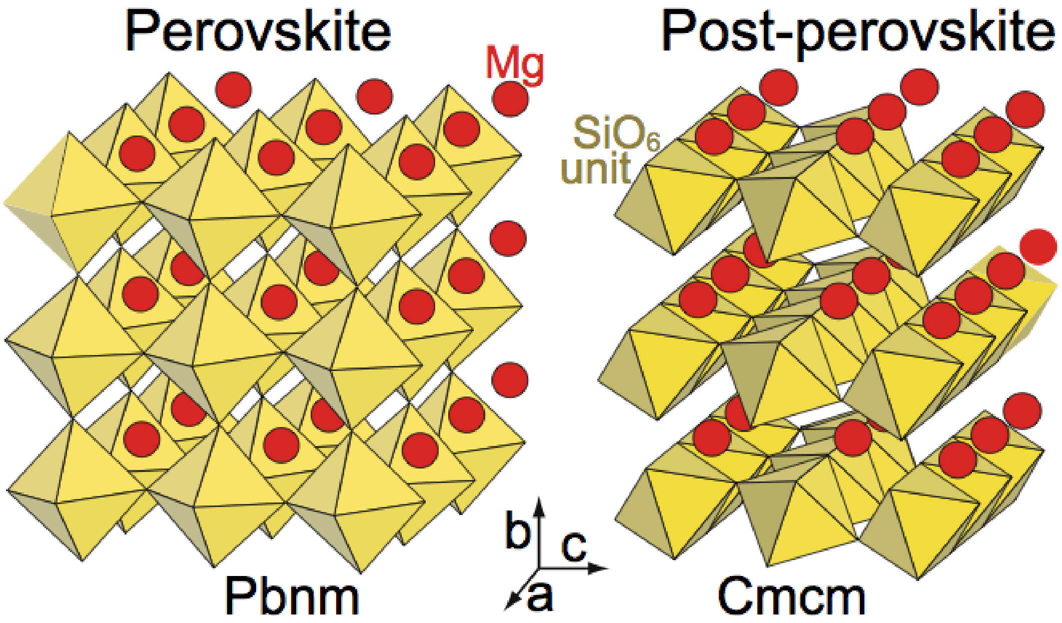

Figure 1.3: Crystal structure of $MgSiO_3$ perovskite (now named bridgmanite) and post-perovskite. Figure from Trønnes (2010).

et al., 2012). These results suggest that the bridgmanite to post-perovskite transition will only produce an observable D′′ discontinuity near colder subducted slab material (e.g., Sun et al., 2018a). Therefore, if we can improve our understanding of the post-perovskite transition and achieve observational constraints on post-perovskite in D′′ we can constrain the composition and temperature of the lowermost mantle.

1.2.2 Melt in the lowermost mantle

Large scale melting of the mantle, also known as the basal magma ocean (BMO), is a popular theory for early Earth evolution (Labrosse et al., 2007). The existence of any melt in the present-day lowermost mantle is unclear. If there is any melt, or partial melt, present in the lowermost mantle is it likely to be a remnant of the BMO, extruded core material or subducted material that has melted in lowermost mantle conditions. In all three cases, the expected melts should be Fe-rich. In the case of a BMO, fractional crystallisation causes Fe concentration to increase towards the core-mantle boundary (Labrosse et al., 2007). If material is escaping from the core it is necessarily going to be Fe-rich compared to the background mantle (e.g., Otsuka and Karato, 2012). For subducted mantle material, melting experiments of mid-ocean ridge basalts (MORBs) using a laser-heated diamond anvil cell (Andrault et al., 2014) shows that MORBs should undergo partial melting if the temperature of D$''$ is between 3800 K and 4150 K due to the large temperature gap between the MORB solidus and liquidus. More recent eutectic melt experiments of bridgmanite and stishovite mixtures[2] find the euctic melting curve to be ca. 300 K higher (Baron et al., 2017). This melt curve intersects the mantle adiabat just above the core-mantle boundary, implying that any partial melting of subducted slab material is constrained to just above the core-mantle boundary.

Similar melting experiments of peridotite (Tateno et al., 2014) formed significant (46 - 77 wt%) partial melt that became more Fe-enriched at pressure was increased. These Fe-rich melts are expected to be denser than other lowermost mantle minerals (e.g., Nomura et al., 2011) and therefore we might expect them to accumulate at the core-mantle boundary. However, it is currently unclear if these melts would be dynamically stable and resist entrainment into the rest of the lower mantle. The presence of Fe-rich melts is commonly invoked to explain ultra low velocity zones (e.g., Rost et al., 2005; Yuan and Romanowicz, 2017), However, recent coupled geodynamic and thermodynamic modelling by Dannberg et al. (2021) suggests that it is challenging to form molten or partially molten layers of present day lower mantle material that persist near the core-mantle boundary. It is also worth noting that there is currently little direct observational evidence for lowermost mantle melt. This makes it unclear if there is melt present in the lowermost mantle or not, which clearly has significant implications for our understanding for the region and its dynamics.

1.3 Structure in the lower mantle

Our understanding of lowermost mantle structure primarily relies on seismic observations. The idea of an anomalous region at the base of the mantle can be traced back to the beginnings of modern seismology, with observations of an anomaly in seismic velocity gradients above the core dating back to at least 1914 (e.g., Gutenberg, 1914). Repeated observations of low velocity gradients (e.g., Witte, 1932; Jeffreys, 1939, etc.,) led to Bullen (1949) subdividing the lower mantle D layer at 2700 km into the D$'$ (above 2700 km depth) and D$''$ (from 2700 km to the core-mantle boundary). Early velocity profiles disagreed on the existence and nature of anomalous velocity gradients in D$''$ and all models assumed a smooth velocity profile down to the core-mantle boundary (see review by Cleary, 1974).

---

[2] an analogue for natural basalt in lower mantle conditions

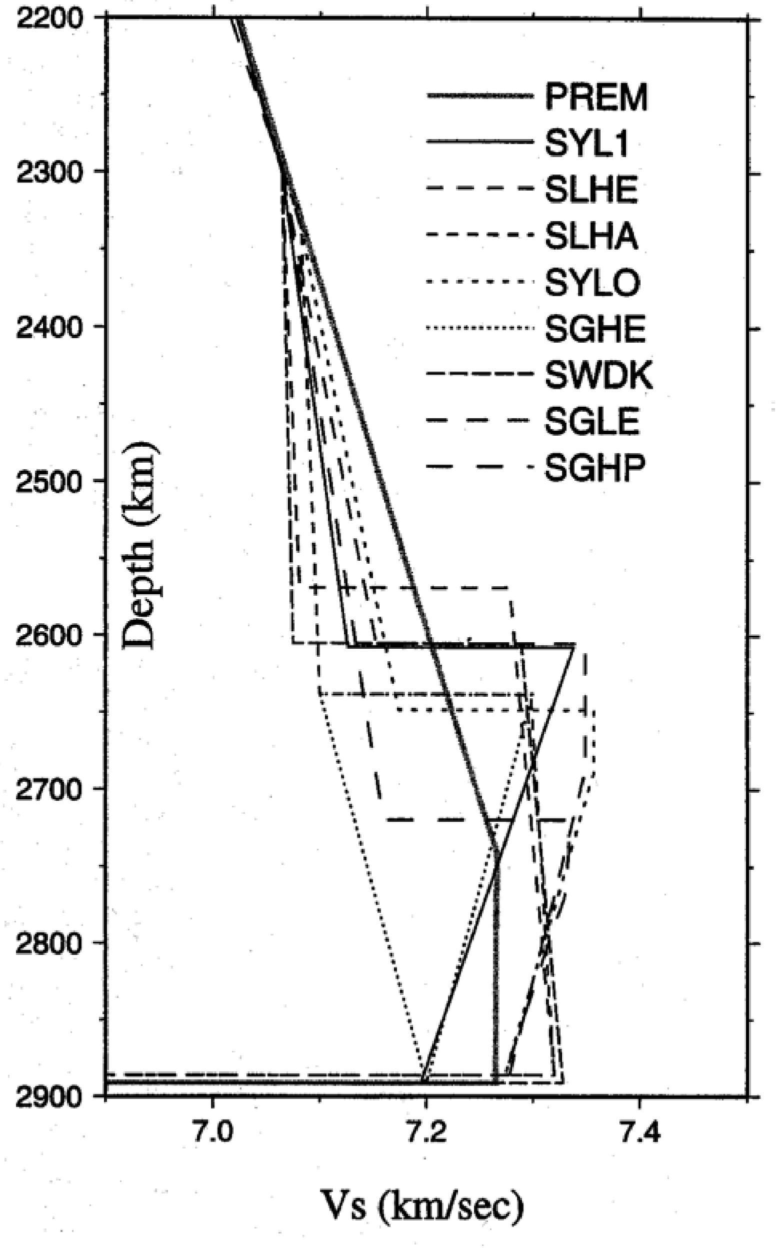

Figure 1.4: A comparison of 8 shear-wave velocity profiles that include the D″ discontinuity and the PREM 1-D velocity model (Dziewonski and Anderson, 1981). Note how all 8 profiles show a similar discontinuous increase of 2.5-3.0% in shear-wave velocity, yet there is no consensus on the depth of the D″ discontinuity or the mean vertical velocity. The models shown are SLHA and SLHE (Lay and Helmberger, 1983), SYL1 (Young and Lay, 1987), SGHE (Garnero et al., 1988), SYLO (Young and Lay, 1990), SWDK (Weber and Davis, 1990), SGLE (Gaherty and Lay, 1992) and SGHP (Garnero et al., 1993). Figure from Wysession et al. (1992).

1.3.1 The D$''$ discontinuity

The discovery of the D$''$ discontinuity, a sharp 2.75 % increase in shear-wave velocity (Lay and Helmberger, 1983) provided the first evidence for significant D$''$ heterogeneity. Further observations of the discontinuity using the newly dubbed SdS phase, an ScS precursor phase that reflects at the D$''$ discontinuity, found that unlike the upper mantle discontinuities at 410 km and 660 km the D$''$ discontinuity was inconsistent in the depths at which it was observed and there were numerous non-observations of the discontinuity (Fig 1.4; Wysession et al., 1992). Global mapping of the discontinuity shows consistent evidence for lateral heterogeneity, with the height of the D$''$ discontinuity above the core-mantle boundary ranging between 150 km and 350 km, with a mean thickness of 250 km (Kendall and Shearer, 1994; Wysession et al., 1998). In some regions, a second discontinuity with a sharp decrease in shear-wave velocity was observed, with the pairs of discontinuities tracing out lens like structures (Thomas et al., 2004; Van der Hilst et al., 2007). In others, such as beneath Alaska, the D$''$ discontinuity is very thin or even non-existent (Sun et al., 2016).

The D$''$ discontinuity is commonly explained by the phase transition from bridgmanite to post-perovskite (e.g., Murakami et al., 2004). However recent modelling of seismic reflection polarities suggests that thermo-chemical anomalies due to subducting slabs or primitive mantle material or the brigmanite to post-perovskite phase transition could reasonable explain observed reflection polarities (Cobden and Thomas, 2013). Multiple mechanisms could go some way to explaining the strong lateral heterogeneity that we see in the lowermost mantle.

1.3.2 LLSVPs

Seismic tomography has provided the clearest observation of large scale structures in D$''$. For the past 20 years it has become increasingly clear that the lowermost mantle is dominated by two continental sized low shear-wave velocity anomalies (Fig. 1.5; e.g., Megnin and Romanowicz, 2000; Simmons et al., 2009; Dziewonski et al., 2010; Ritsema et al., 2011; French and Romanowicz, 2014, etc.). These anomalies, referred to as the large low shear-wave velocity provinces (or LLSVPs), are believed to play an integral role in mantle dynamics with there being good tomographic evidence for some mantle plume structures being rooted at LLSVP margins (e.g., French and Romanowicz, 2014). Furthermore, joint inversions for compressional (V_p) and shear-wave (V_s) velocities repeatedly observe non- or anti-correlation between shear-wave velocity and bulk sound

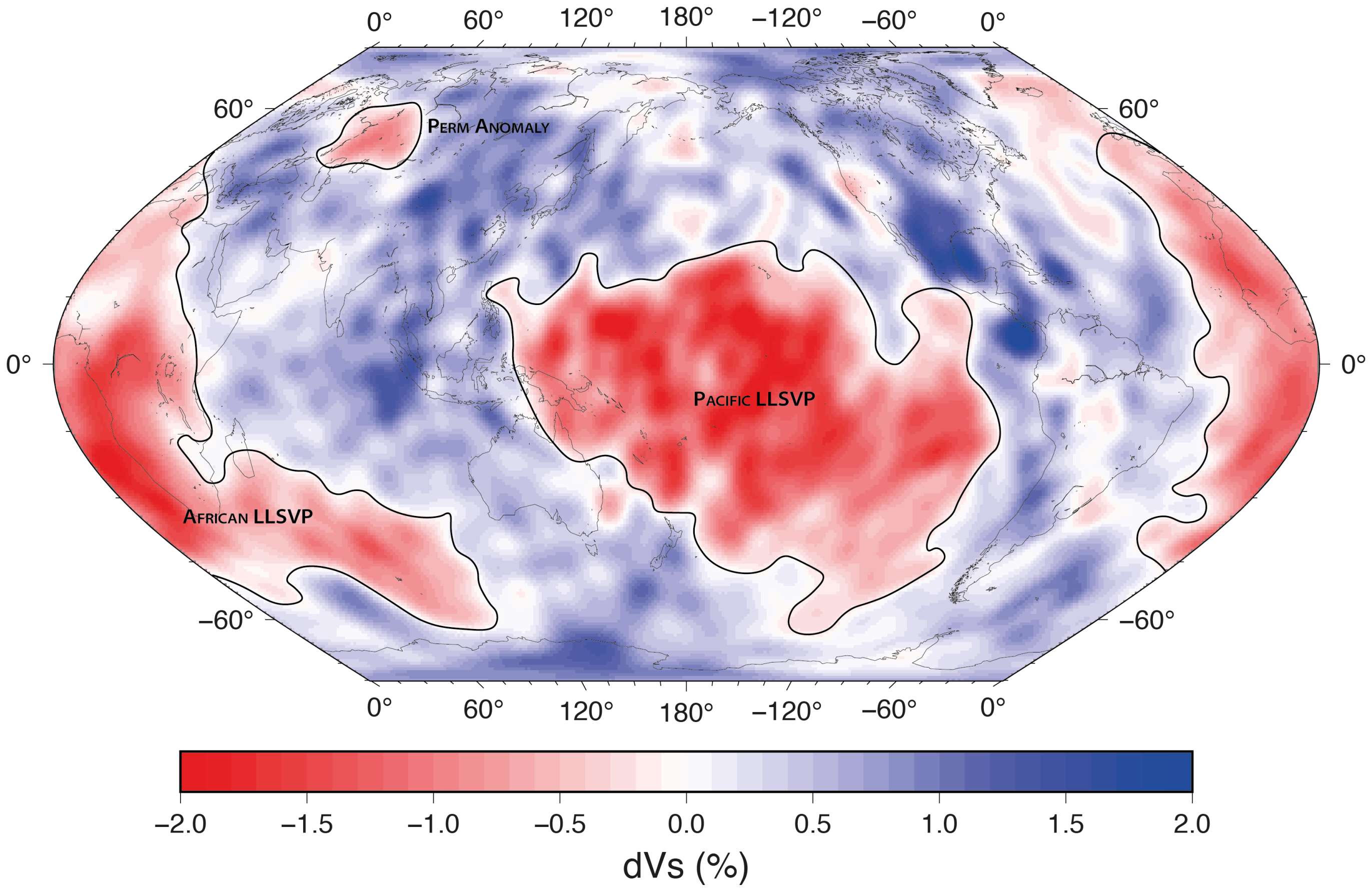

Figure 1.5: Map of the lowermost mantle as seen by seismic tomography. The model shown is the shear-wave tomography model S40RTS (Ritsema et al., 2011). The approximate margins of the large low shear-wave velocity provinces (LLSVPs) are indicated by the solid lines.

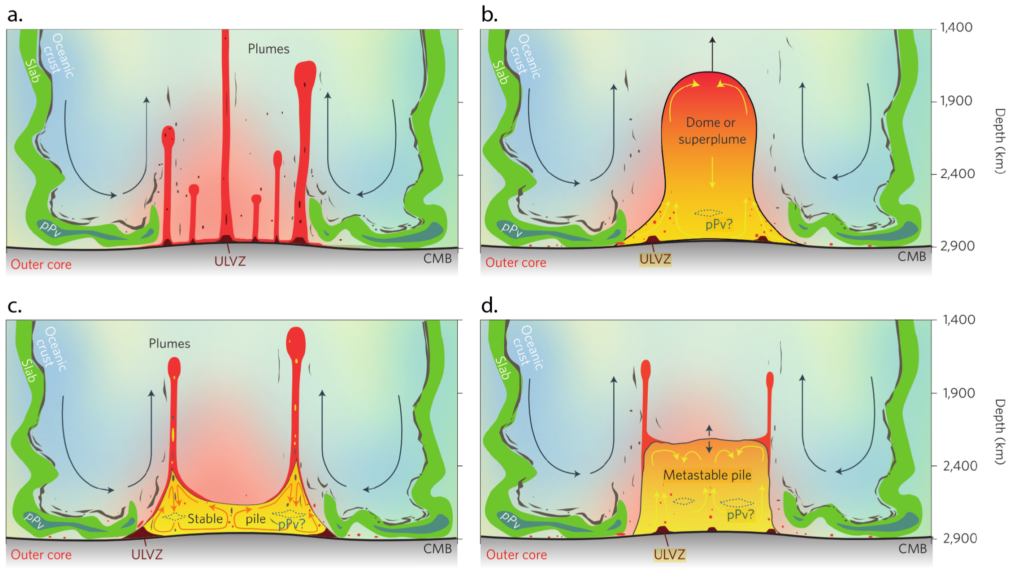

Figure 1.6: Cartoons detailing different end-member models for LLSVPs as (a) plume bundles; (b) thermal or thermochemical domes or superplumes; (c) stable thermochemical piles; (d) metastable piles. In each idealised case subducted material, which may include post-perovskite, surrounds the LLSVP. Figure from Garnero et al. (2016).

velocity, particularly where the LLSVPs are located (e.g., Su and Dziewonski, 1997; Koelemeijer et al., 2016). This strongly suggests compositional heterogeneity in the lowermost mantle, which might be explained by a lateral phase transition such as bridgmanite to post-perovskite or distinct chemical heterogeneity (Hernlund and Houser, 2008). However, others have suggested that chemical heterogeneity is not compatible with the tomography (e.g., Davies et al., 2012a).

Tomographic models, despite improvements in resolution, give inherently blurry images of the lowermost mantle. This makes them unable to delineate the exact boundaries of LLSVPs. Cluster analysis between tomographic models (Lekic et al., 2012) gives some insight, but assumes that different tomographic models use independent datasets which is often not the case with models using overlapping datasets. At best, cluster analysis defines the regions where tomographic model agree LLSVPs exist and therefore where we might expect the margins to be. Through careful analysis of travel time residuals and multipathing observations it is apparent that LLSVP margins are seismically sharp, with steep lateral velocity gradients ranging from 3% dVs per 50 km to 2% dVs per 300 km (e.g., Ritsema et al., 1998; Ni et al., 2002; Frost and Rost, 2014; Ward et al., 2020). These LLSVP margins have also been observed to contain small wavelength heterogeneous scatterers (Frost et al., 2013) and are the only part of the LLSVPs to exhibit significant seismic anisotropy (e.g., Wang and Wen, 2007).

Despite the wealth of intriguing seismic observations the exact nature of LLSVPs is currently unknown. We arguably have a better understanding of the faster than average regions of D$''$, which can be associated with subducted slab material (e.g., Kellogg et al., 1999; Jellinek et al., 2003; Torsvik et al., 2014). Geodynamics currently gives us several plausible models for LLSVP formation and how they relate to the rest of the mantle, with different models having important implications for the dynamics, chemical composition and formation of the lower mantle (see reviews by Garnero et al., 2016; McNamara, 2019). These competing models all seek to answer the fundamental question: Are LLSVPs purely thermal anomalies upwelling in an isochemical lower mantle, perhaps associated with a phase transition, or are they chemically distinct bodies accumulating along the core-mantle boundary?

Purely thermal models broadly divide into two views. At one end is the view that LLSVPs are bundles of thin mantle plumes (Fig. 1.6a) that are blurred together in tomographic models by a combination of imperfect data coverage and the damping and smoothing used in the tomographic inversions (e.g., Schubert et al., 2004; Bull et al., 2009). An alternate, simplistic, hypothesis is that LLSVPs are singular large upwelling domes or superplumes (Fig 1.6b). This hypothesis, along with its thermochemical variants, seems unlikely to be geodynamically stable over geological timescale and are generally disregarded (McNamara, 2019). The morphology of LLSVPs, as resolved by detailed cluster analysis of 5 tomographic models, favours an intermediate view where the African and Pacific LLSVPs appear to consist of 3-4 smaller ‘regional’ anomalies (Cottaar and Lekic, 2016). Although it is worth noting that this cluster analysis does assume the tomographic models are independent, which is not necessarily the case.

The prevailing view is that LLSVPs are stable piles of chemically distinct material (Fig. 1.6c). To remain at the core-mantle boundary these piles must be negatively buoyant compared to the surrounding mantle. Geodynamic modelling of thermochemical piles show the intrinsic density increase must be small (up to a few per cent), with large intrinsic density contrasts resulting in a uniform global layer of denser material (see review by McNamara, 2019). If the bulk modulus of the piles is different to the surrounding mantle, then a depth-dependent density contrast could form. This could lead to slowly overturning “metastable” piles where deeper pile material is more buoyant than the overlying material (Fig. 1.6d; Garnero et al., 2016).

Thermochemical anomalies in the lowermost mantle offer a reasonable explanation for the sharp lateral velocity gradients at LLSVP margins and for anti-correlation between shear-wave and bulk sound velocity. How such thermochemical anomalies could be formed in the lower mantle is still an outstanding question. Models of LLSVP formation fundamentally differ in how they view early Earth evolution. The contrasting views are that LLSVPs either represent primordial material from a mantle differentiation event in early Earth history or they have grown through geological time from the accretion of denser subducted material (e.g., Hofmann and White, 1982; Christensen and Hofmann, 1994). A challenge for the "growing LLSVPs" model is that it is difficult to accumulate present-day ca. 6 km thick oceanic crust due to viscous forces acting to stir the material into the background mantle (Li and McNamara, 2013; Li et al., 2014). However if there is rheological weakening due to the bridgmanite to post-perovskite phase transition (Nakagawa and Tackley, 2011) or if ancient oceanic crust was significantly thicker (Li and McNamara, 2013) then it is possible to generate LLSVP sized accumulations of material, although such models are notably "messier" and lack the clearly defined boundaries that can be achieved by primordial models (McNamara, 2019).

For primordial LLSVPs the challenge is one of survival. Current estimates expect that dense chemical heterogeneities could resist entrainment into the bulk mantle for over 4 billion years (Tackley, 2012). If LLSVPs are remnants of primordial mantle material then they could constitute the "hidden reservoir" invoked in geochemistry to reconcile the depleted upper mantle with the expected chondritic composition of the Earth (Hofmann, 1997), especially if LLSVPs formed from the crystallisation of a basal magma ocean (Labrosse et al., 2007). This conceptual model of LLSVPs as geochemical reservoirs also explains discrepancies between trace element compositions of ocean island basalt (OIB) and mid-ocean ridge basalt (MORB) (e.g., Tackley, 2000). The broad geodynamic view of this model is one where mid-ocean ridges sample the well-mixed homogeneous mantle, whilst mantle plumes tap into the geochemically distinct LLSVPs producing basalts with different trace element compositions at different hotspots. It must be noted that these interpretations are conjectural and whilst it provides a clean geodynamic and geochemical narrative, there is insufficient supporting observational evidence as of yet (McNamara, 2019). A further complication is that current seismic observations do not conclusively prove that LLSVPs are thermochemical anomalies. Indeed modelling has shown that thermal heterogeneity is perfectly capable of reconciling our seismic observations of LLSVPs (Davies et al., 2012b). Further seismic observations, including potential constraints on the present day composition and dynamics of the lowermost mantle, are needed to improve our understanding of LLSVPs.

1.3.3 ULVZs

There are further, smaller wavelength, heterogeneities within D$''$. Ultra low velocity zones, thin ca. 10 km — 40 km thick regions with P- and S-wave velocity reductions of 10% and 30% respectively, have been detected as small patches along the core-mantle boundary (e.g., Vanacore and Niu, 2011; Cottaar and Romanowicz, 2012; Thorne et al., 2013; Yuan and Romanowicz, 2017; Kim et al., 2020). There is further evidence for yet more ULVZs that have not been mapped in detail from recent modelling of the most parsimonious distribution of heterogeneities that explain anomalous SPdKS waveforms (Thorne et al., 2021). Typically these features extend laterally on the order of 100 km, with notable “mega ULVZs" detected beneath Hawaii (Cottaar and Romanowicz, 2012), Samoa (Thorne et al., 2013), Iceland (Yuan and Romanowicz, 2017), the Galapagos (Vanacore and Niu, 2011; Cottaar and Li, 2019) and the Marquesas (Kim et al., 2020).

We do not yet know what ULVZs represent. The first detailed mapping of the Hawaiian ULVZ, which is the most widely studied, suggests that is in fact not a signal distinct feature (Jenkins et al., 2021). As much of the core-mantle boundary region has not been imaged in detail, our current observations of ULVZs concentrating at LLSVP margins could be pure coincidence. Hypotheses for ULVZ formation tend to invoke either melts or some form of compositional heteorgeneity, typically enrichment in iron as this explains the expected 0-20% density increase (Garnero et al., 1998; Rost et al., 2005) required to explain the substantial velocity reductions (McNamara, 2019). Some ULVZ hypotheses include: a global melt layer of varying topograpy (e.g., Rost et al., 2005; Yuan and Romanowicz, 2017), Fe-enriched slab derived melts (Liu et al., 2016), partially molten subducted oceanic crust (Andrault et al., 2014; Pradhan et al., 2015), subducted banded-iron formations (Dobson and Brodholt, 2005), Fe-rich remnants of the basal magma ocean (Labrosse et al., 2007) and material extruded from the core (Buffett et al., 2000; Otsuka and Karato, 2012). However, recent geodynamic and thermodynamic modelling of lowermost mantle melt suggests that it is difficult to form pockets of melt in D$''$ from present-day mantle material that do not sink to form a single molten layer at the base of the mantle and that also resist being stirred into the overlying material (Dannberg et al., 2021). These results suggest that chemical heterogeneity in D$''$, which can match seismic observations of ULVZs, may be more plausible than previously posited models (Dannberg et al., 2021).

1.3.4 Bridgmanite enriched ancient mantle structures

Bridgmanite enrichment might have profound effects on the viscosity, and therefore the dynamics, of the lower mantle. The viscosity of bridgmanite is estimated to be approximately 1000 times greater than ferropericlase, the other main constituent phase of the lower mantle (Yamazaki and Karato, 2001). Consequently the abundance (or paucity) of ferropericlase has strong effect on the viscosity of lower mantle rocks, with bridgmanite enriched lower mantle material being significantly more viscous than pyrolite (Ballmer et al., 2017).

Geodynamic modelling of a bridgmanite enriched layer in the lower mantle has revealed that the contrasts in compositional rheology could result in bridgmanite enriched structures controlling lower mantle convection patterns (Ballmer et al., 2017). If the viscosity contrast is sufficiently large then the enriched material accumulates into large domains of stronger material, dubbed bridgmanite enriched ancient mantle structures (BEAMS), at depths of 1000 - 2200 km that are surrounded by conduits of weaker pyrolitic material (Fig. 1.7). BEAMS have been shown to be stable for in excess of 4.6 billion years and have been suggested to have a stabilising effect on mantle convection patterns and could explain why some subducting slabs stagnate and mantle plumes are deflected at ca. 1000 km depth (e.g., Fukao and Obayashi, 2013; French and Romanowicz, 2015). In the lowermost mantle BEAMS would stabilize the location of convergent flow. This would allow denser material to accumulate into piles, forming the LLSVPs. It is worth noting that whilst the BEAMS hypothesis is an exciting one, currently there are limited geophysical observations that support (or refute) their existence in the lower mantle. Geoid inversions do suggest a sharp jump in viscosity at depths around 1000 km (Rudolph et al., 2015), but these results do not required BEAMS as an explanation. Given that BEAMS are expected to be stable features we can predict mantle circulation patterns around them. For example BEAMS would predict predominantly horizontal flow in the lowermost mantle, with small concentrated upwelling and downwelling conduits. Therefore if we can constrain the dynamics of the lowermost mantle, we will be able to further test this hypothesis.

1.4 Seismic anisotropy as a constraint on D$''$ dynamics

The dynamics of the lowermost mantle are not well understood. Globally mapping lowermost mantle flow remains a truly ambitious objective at the present. If we are even able to constrain

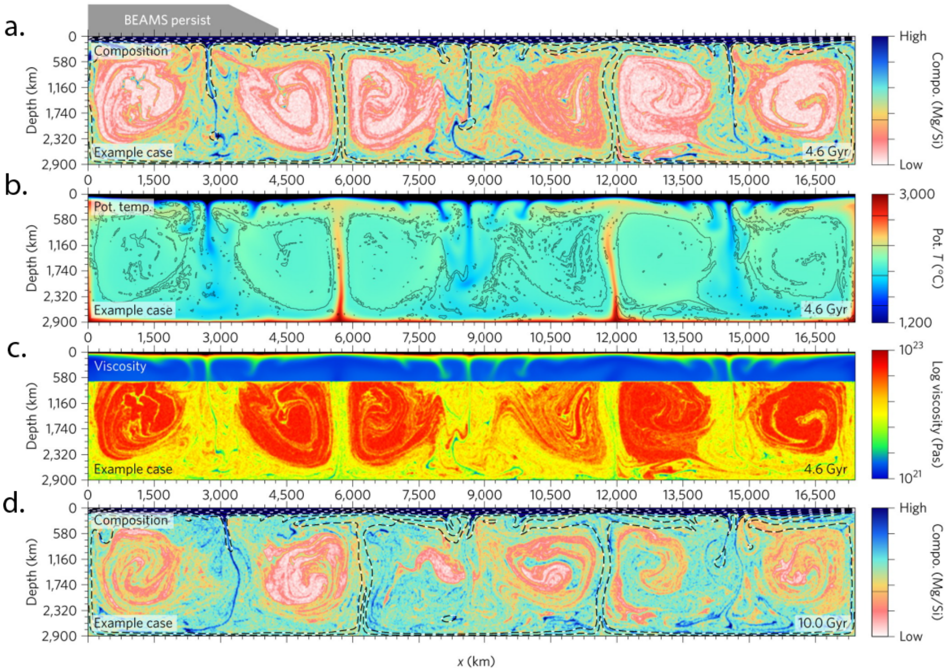

Figure 1.7: Results from geodynamic calculations demonstrating how compositional rheology of bridgmanite enriched structures in the lower mantle (at depths of 1000 - 2200 km) can stabilise mantle convection patterns. Models are coloured by (a,d) mantle composition (Mg/Si ratio), (b) potential temperature and (c) viscosity. Note that panel (d) shows that these structures can resist entrainment into the background mantle for at least 10 billion years. Figure from Ballmer et al. (2017).

the dynamics of key regions of D″, such as LLSVP margins, we could illuminate their true nature. We are able to create geodynamic models of global mantle flow, including the lowermost mantle (Fig 1.8). This can be done by jointly inverting global seismic tomography, dynamic surface and core-mantle boundary topography, global free air gravity anomalies, present day tectonic plate motions and a mantle viscosity profile (Fig 1.8a; e.g., Simmons et al., 2009; Forte et al., 2015).

An alternative approach is to use tectonic plate motion reconstructions, along with subducted slab and LLSVP locations to constrain geodynamic inversions (Fig. 1.8b Flament, 2019). The plate motion reconstructions cover the past 200 - 250 Myr and are currently one of our best sources of insight into mantle dynamics as they record the surface expression of mantle convection. However, there is currently very limited consensus between mantle flow models, particularly for the lowermost mantle (Fig. 1.8). It is also worth noting that these models offer only predictions of lowermost mantle flow, without clear observations we have no means with which we can test competing mantle flow models.

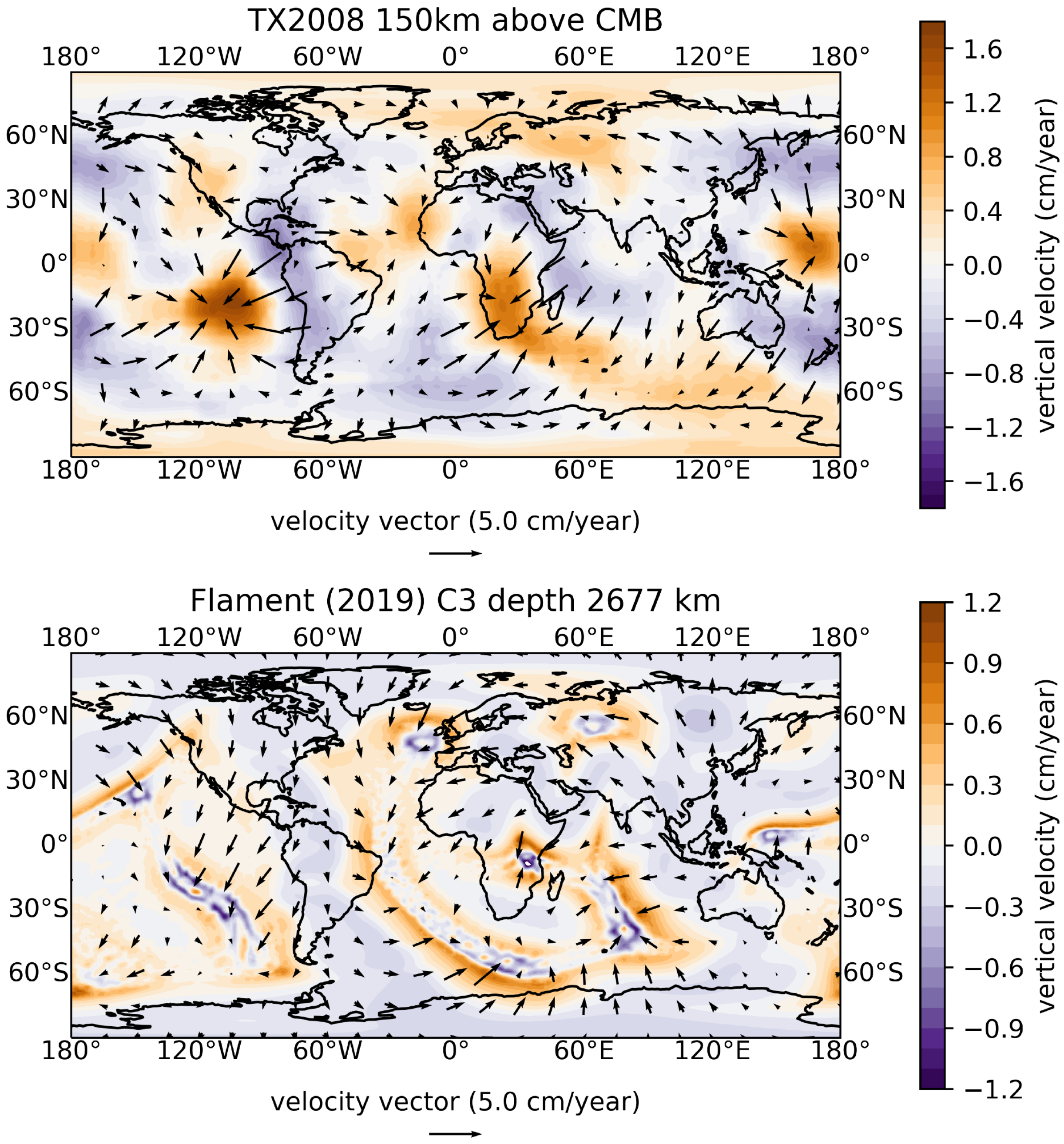

Figure 1.8: Comparison of two models for lowermost mantle flow. Panels show the mantle flow velocity in the vertical (colors) and horizontal (arrows) directions predicted by (top) Simmons et al. (2009) at a depth of 2685 km and (bottom) Flament (2019) at a depth of 2677 km.

Observing seismic anisotropy offers us a potent tool with which we can constrain models of lowermost mantle dynamics. Seismic anisotropy, the directional variation in seismic velocities, is well known to be a good indicator of a rocks dynamic history and develops in response to plastic flow in the mantle (e.g., Tommasi et al., 2000; Mainprice, 2015). Over the past couple of decades seismic anisotropy has been routinely used to study the dynamics of the upper mantle (e.g., Silver, 1996; Savage, 1999; Long and Becker, 2010; Becker and Lebedev, 2021) and there has long been anticipation that seismic anisotropy will revolutionise our understanding of lowermost mantle dynamics (e.g., Wookey and Kendall, 2007). Whilst great progress has been made in recent years towards constraining seismic anisotropy in the lowermost mantle, there is still much work to be done. Numerous seismic observations have highlighted intriguing regions of seismic anisotropy (e.g., Wookey et al., 2005a; Long, 2009; Nowacki et al., 2010; Ford et al., 2015; Pisconti et al., 2019; Wolf et al., 2019), but we still lack robust frameworks to interpret seismic anisotropy in terms of lowermost mantle flow.

1.4.1 Seismic Anisotropy

In the Earth's mantle there are two overarching types of dominant mechanism that generate seismic anisotropy: intrinsic and extrinsic mechanisms. Intrinsic mechanisms are independent of the seismic wavelength used to observe them and are produced by the alignment of inherently anisotropic minerals within the rock. Deformation in the mantle is predominately plastic, due to the high temperatures and low strain rates, and is accommodated within crystalline rock through diffusion or dislocation creep (e.g., Karato, 1998a; Cordier et al., 2004; Karato et al., 2008). These creep mechanisms produce a lattice preferred orientation for crystals (e.g., Tommasi et al., 2000), which is referred to as lattice or crystal preferred orientation (LPO or CPO). Extrinsic mechanisms are characterised by heterogenieties with one set of elastic properties embedded within another medium with a second set of elastic properties. If the heterogenieties are smaller than the sampling seismic wavelength preferential alignment of the heterogenieties due to, for example, deformation will result in a medium with effective seismic anisotropy. This is commonly referred to as shape preferred orientation (SPO). Examples of SPO in the crust and upper mantle include fluid filled cracks (e.g., Hudson, 1980) or periodic variations of thin layers with different seismic velocities related to, for example, depositional processes (Backus, 1962). Early studies of D$''$ favoured SPO as a mechanism with various shapes of melt filled inclusions proposed (e.g., Kendall and Silver, 1998). However, following the discovery of the post-perovskite phase by Murakami et al. (2004) the lattice-preferred orientation of post-perovskite has become the favoured mechanism (e.g., Creasy et al., 2019). Of course, it is entirely plausible that there are multiple mechanisms at play throughout D$''$.

The seismic anisotropy of an elastic medium is described by the symmetry of its elastic tensor, c_{ijkl}. The elastic tensor links the applied stress, τ_{ij} and resulting strain, ϵ_{kl}, in an elastic medium through a generalised version of Hooke's law (Shearer, 2019),

$$\tau_{ij} = c_{ijkl}\epsilon_{kl}, \tag{1.1}$$

where the strain tensor is defined as

$$\epsilon_{kl} = \frac{1}{2}\left(\frac{\partial u_k}{\partial x_l} + \frac{\partial u_l}{\partial x_k}\right) \tag{1.2}$$

where u_n is displacement and x_n the corresponding Cartesian direction.

At this point it is worth noting that we are assuming that we can treat material in the Earth's mantle as linearly elastic solids. Strictly speaking linear stress-strain theory should be invalid in the Earth's deep interior as the hydrostatic stress and the resulting strains, representing the compression of rock under the extreme pressures of the deep mantle, are too large (Shearer, 2019). To navigate this issue we instead apply equation 1.1 to perturbations in stress, or incremental stress, where there is no strain in the initial state (Shearer, 2019).

The elastic tensor is 4th rank tensor, with a maximum of 81 free parameters. From inherent symmetries in the stress and strain tensors ($\tau_{ij} = \tau_{ji}$, $\epsilon_{kl} = \epsilon_{lk}$), we can reduce the number of independent elastic constants to 36. This can be further reduced using thermodynamic constraints, derived by combining the first and second laws of thermodynamics expressed in terms of stress-strain variables for an elastic body (e.g., Mainprice, 2015). The first law of thermodynamics states that the change in internal energy $\frac{dU}{dt}$ is due to work, δW and heat δQ provided from the outside. This can be expressed as:

$$\frac{dU}{dt} = \delta W + \delta Q. \tag{1.3}$$

For a reversible process, such as elastic behaviour[3], we can write the second law of thermodynamic as:

$$\delta Q = T_0 \frac{dS}{dt}, \tag{1.4}$$

---

[3] where all outside work supplied is stored as recoverable energy and therefore the internal heat source, or dissipation $\frac{dD}{dt} = 0$.

where T_0 is the absolute temperature of the system and assumed to be constant and S is the internal entropy. By combining these two laws of thermodynamics and substituting the expression of the work rate for a 3-D elastic solid:

$$\delta W = \sigma_{ij}\dot{\epsilon}_{ij}, \tag{1.5}$$

we get, as in Mainprice (2015)

$$\dot{U} = \sigma_{ij}\dot{\epsilon}_{ij} + T_0\dot{S}. \tag{1.6}$$

From this equation we can define the stress tensor for a constant entropy as

$$\sigma_{ij} = \left(\frac{\delta U}{\delta \epsilon_{ij}}\right)_S = c_{ijkl}\epsilon_{ij} \tag{1.7}$$

hence

$$c_{ijkl} = \frac{\delta \sigma_{ij}}{\delta \epsilon_{kl}} = \frac{\delta}{\delta \epsilon_{kl}}\left(\frac{\delta U}{\delta \epsilon_{ij}}\right)_S \tag{1.8}$$

and

$$c_{klij} = \frac{\delta \sigma_{kl}}{\delta \epsilon_{ij}} = \frac{\delta}{\delta \epsilon_{ij}}\left(\frac{\delta U}{\delta \epsilon_{kl}}\right)_S. \tag{1.9}$$

From 1.8 and 1.9 it is clear that $c_{ijkl} = c_{klij}$. This third symmetry allows us to fully describe an anisotropic medium with 21 elastic constants (e.g., Mainprice, 2015). We can exploit these symmetries to reduce c_{ijkl} to a more compact symmetrical 6×6 matrix, $C_{\alpha\beta}$ using Voight notation. The relation between the Voight (mn) and elastic tensor ($ijkl$) indices is best expressed by

$$m = \delta_{ij}i + (1-\delta_{ij})(9-i-j) \text{ and } n = \delta_{kl}k + (1-\delta_{kl})(9-k-1) \tag{1.10}$$

where δ_{ij} is the Kronecker delta, so $\delta_{ij} = 1$ if $i = j$ and $\delta_{kl} = 0$ if $i \neq j$ (Mainprice, 2015).

$$c_{ijkl} \rightarrow C_{\alpha\beta} = \begin{bmatrix} C_{11} & C_{12} & C_{13} & C_{14} & C_{15} & C_{16} \\ & C_{22} & C_{23} & C_{24} & C_{25} & C_{26} \\ & & C_{33} & C_{34} & C_{35} & C_{36} \\ & & & C_{44} & C_{45} & C_{46} \\ & & & & C_{55} & C_{56} \\ & & & & & C_{66} \end{bmatrix}. \tag{1.11}$$

We are typically not concerned with this most general form of anisotropy, as it proves to be both difficult to solve for and unnecessary to constrain seismic anisotropy within the Earth.

Instead we consider media with higher symmetry that either reflect an anisotropic mechanism, such as single crystal symmetry, or simplify the anisotropic problem. The simplest case is an isotropic medium where the elasticity can be described by the Lamé parameters, λ and μ. The simplest anisotropic case is cubic symmetry, which has 3 independent elastic constants (C_{11},C_{12},C_{44}). The most commonly treated forms of anisotropy, and the forms that I consider in chapter 4, are hexagonal and orthorhombic symmetry. Hexagonal symmetry, also referred to as transverse isotropy, is characterised by a singular symmetry axis around which velocity is constant (i.e., velocity only varies as a function of the angle subtended to the symmetry axis) and has 5 independent elastic constants (C_{11},C_{13},C_{33},C_{44},C_{66}). Transverse isotropy, particularly the end member models with a vertical (VTI) or horizontal (HTI) symmetry axis, is a common approximation that can represent various styles of SPO such as sedimentary layering, fluid filled cracks or aligned inclusions. Orthorhombic symmetry is more complex, requiring 9 independent elastic constants (C_{11},C_{12},C_{13},C_{22},C_{23},C_{33},C_{44},C_{55},C_{66}) and is usually associated with LPO anisotropy as well known anisotropic minerals such as olivine, bridgmanite and post-perovskite have an orthorhombic crystal system.

1.4.2 Observing seismic anisotropy

There are two principal approaches that can be taken to observe D$''$ seismic anisotropy: global anisotropic tomography and waveform based studies of shear-wave splitting. The approaches differ in scope and also in how they seek to deal with one of the fundamental challenges in observing D$''$ seismic anisotropy, accounting for the strong anisotropy in the crust and upper mantle.

Global anisotropic tomography

Global anisotropic tomography is an incredibly attractive solution to this problem as modelling anisotropy in the entire mantle allows for the inclusion of a wide range of seismic data types which have greater sensitivity to anisotropy in different mantle depths, such as body waves, normal modes and surface waves (e.g., Moulik and Ekstrom, 2014; French and Romanowicz, 2014). This approach is highly successful for constraining azimuthal seismic anisotropy in the upper mantle, particularly through the use of surface waves (e.g., Schaeffer et al., 2016), however for the lowermost mantle limited azimuthal coverage[4] limits anisotropic tomography efforts to VTI models (see review by Romanowicz and Wenk, 2017). Furthermore, most tomographic studies are limited to solving for the velocities of the vertical and horizontal shear-waves (V_{SV} and V_{SH}) or isotropic velocity and the radial anisotropic parameter ξ , where $\xi = (\frac{V_{SH}}{V_{SV}})^2$, (e.g., Panning and Romanowicz, 2006; Panning et al., 2010; Moulik and Ekstrom, 2014; French and Romanowicz, 2014, etc.,) and derive the remaining elastic constants using upper mantle scaling relationships which may not be suitable for the lower mantle (Romanowicz and Wenk, 2017).

Whilst global whole mantle models are undoubtedly desirable, the limitations are significant. Current radial anisotropy models of D″ have only limited agreement, with common features being regions of $V_{SH} > V_{SV}$ surrounding LLSVPs and $V_{SH} < V_{SV}$ inside the LLSVPs (Fig. 1.9). Even where the models broadly agree there is limited consensus on the wavelength or amplitude of features. This largely arises from differences in datasets, authors preferences for model parameterisation and in theoretical assumptions made during the inversions (Romanowicz and Wenk, 2017). These methods are also limited by potential trade-offs between isotropic and anisotropic structure (e.g., Ferreira et al., 2010). At this stage global models leave a lot to be desired, particularly with increasing evidence from local shear-wave splitting studies that large swaths of the lowermost mantle cannot be explained with simple VTI anisotropy. Without the large scale deployments of ocean bottom seismometers, it is unlikely we will ever be able to achieve sufficient coverage to perform detailed global tomography for radial, let alone azimuthal, anisotropy in the lowermost mantle. In the future the incorporation of techniques for the inversion of shear-wave splitting for seismic anisotropy, such as the probabilistic framework laid out by Wookey (2012) and further explored here (Chapter 4), may enhance global inversions but these techniques are still very much in their infancy.

Shear-wave splitting

Shear-wave splitting, or seismic birefringence, is a phenomena that occurs when a shear-wave propagates through an anisotropic medium. This makes observations of shear-wave splitting a vital tool for studying seismic anisotropy of the lowermost mantle as if we observe shear-wave splitting in D″, this can only be explained by seismic anisotropy.

The propagation of waves from teleseismic earthquakes through an elastic medium can be

---

[4] the bane of all seismologists who study the lowermost mantle

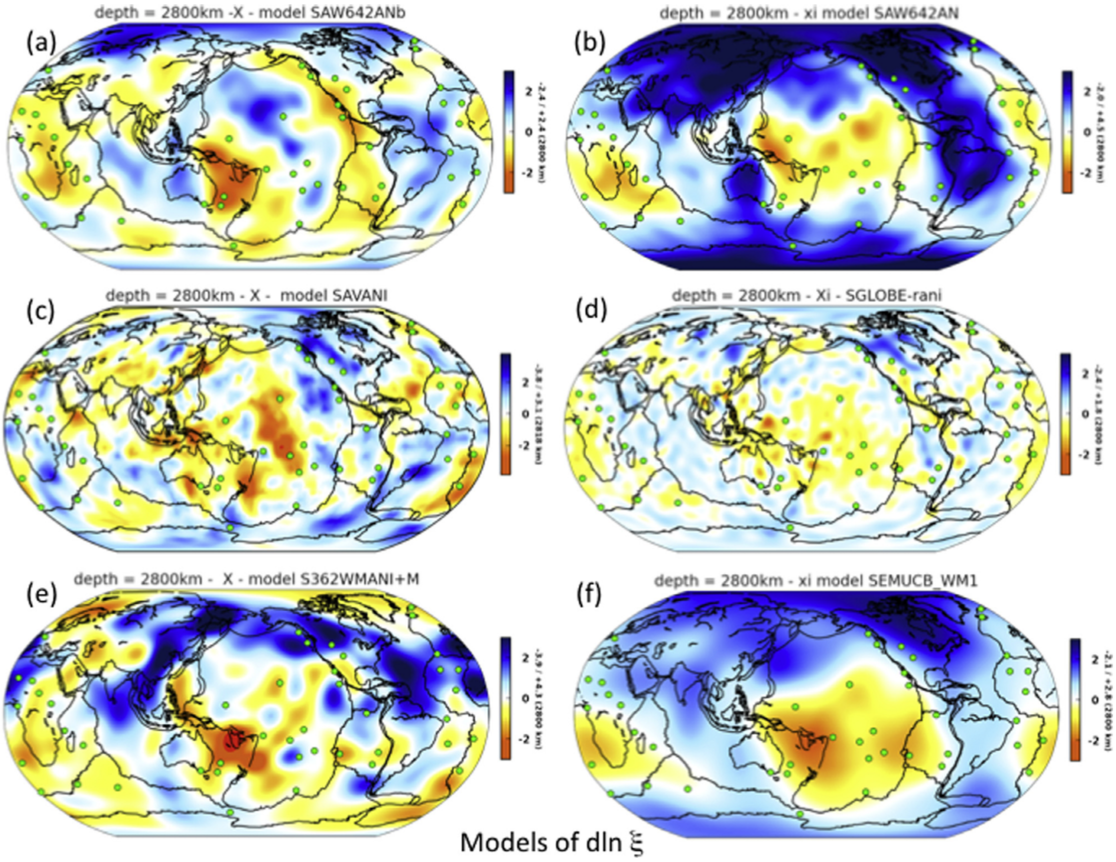

Figure 1.9: A comparison of 6 recent models of radial anisotropy ($\xi = \frac{V_{SH}}{V_{SV}}^2$) in D″. Models are plotted in terms of dlnξ referred to isotropy. Common features in the models are $V_{SH} > V_{SV}$ (blue) that surrounds the Pacific and regions of $V_{SV} > V_{SH}$ (red/orange) that roughly correspond to the locations of the LLSVPS (see figure 1). Models shown are: (a) SAW642ANb (Panning et al., 2010), (b) SAW642AN (Panning and Romanowicz, 2006), (c) SAVANI (Auer et al., 2014), (d) SGLOBE-rani (Chang et al., 2015), (e) S362WANI + M (Moulik and Ekstrom, 2014) and (f) SEMUCB_WM1 (French and Romanowicz, 2014). This figure is taken from Romanowicz and Wenk (2017).

described by the homogeneous equation of motion,

$$\rho \frac{\partial^2 u_i}{\partial t^2} = \partial_j \tau_{ij}, \tag{1.12}$$

where ρ is density and u_i is displacement. Recalling 1.1, 1.2 and that $\epsilon_{kl} = \epsilon_{lk}$ we can rewrite the equation of motion as:

$$\rho \frac{\partial^2 u_i}{\partial t^2} = c_{ijkl} \partial_j \partial_l u_k, \tag{1.13}$$

assuming that c_{ijkl} is constant through the medium (Shearer, 2019). Steady-state plane waves can propagate with a constant slowness, **s**, with displacement:

$$\mathbf{u} = \mathbf{U} e^{-i\omega(t - \mathbf{s} \cdot \mathbf{x})}, \tag{1.14}$$

where **U** is a constant polarisation vector, which gives the direction of particle motion. By substituting this general plane-wave solution we obtain the Christoffel equation[5]:

$$(c_{ijkl} s_j s_l - \rho \delta_{ik}) U_k = 0. \tag{1.15}$$

Where s_i, s_j are components of the slowness vector, U_k is the polarisation direction and δ_{kl} is the Kroneker delta. For plane-wave propagation in isotropic media this gives us 3 solutions for a given slowness direction, corresponding to P-waves and two types of shear-wave (SH and SV) which propagate with spherical wavefronts. In anisotropic media there is no simple analytical solution to the Christoffel equation (Mainprice, 2015; Shearer, 2019). In general three distinct body waves will remain, with 1 compressional-wave and 2 shear-waves. Strictly speaking these wave should be referred to as quasi-P (qP) and quasi-S (qS) waves[6] as the wavefronts are folded and can exhibit cusps (Musgrave, 1970) and therefore the wavefront normal and propagation direction are not coincident, with the waves exhibiting different phase and group velocity directions for the majority of propagation directions (Shearer, 2019). The two, approximately orthogonally polarised, qS waves are of interest here as they become decoupled in an anisotropic medium as they propagate at different velocities. This splitting between the two qS waves[7] persists outside of the anisotropic medium and the time delay between the two can be observed. If the time delay is less than the dominant period of the waves then this will be recorded as an S-wave with elliptical particle motion.

---

[5] This equation can (and indeed is) written in various forms by different authors, often with c_{ijkl} normalised by density (e.g., Shearer, 2019). For clarity, as it is the elastic tensor c_{ijkl} we are interested in, I have elected to follow Mainprice (2015) and not perform this final re-arrangement.

[6] In practice this prefix is often dropped for convenience and I shall follow this convention outside of this section.

[7] Hence the term *shear-wave splitting*

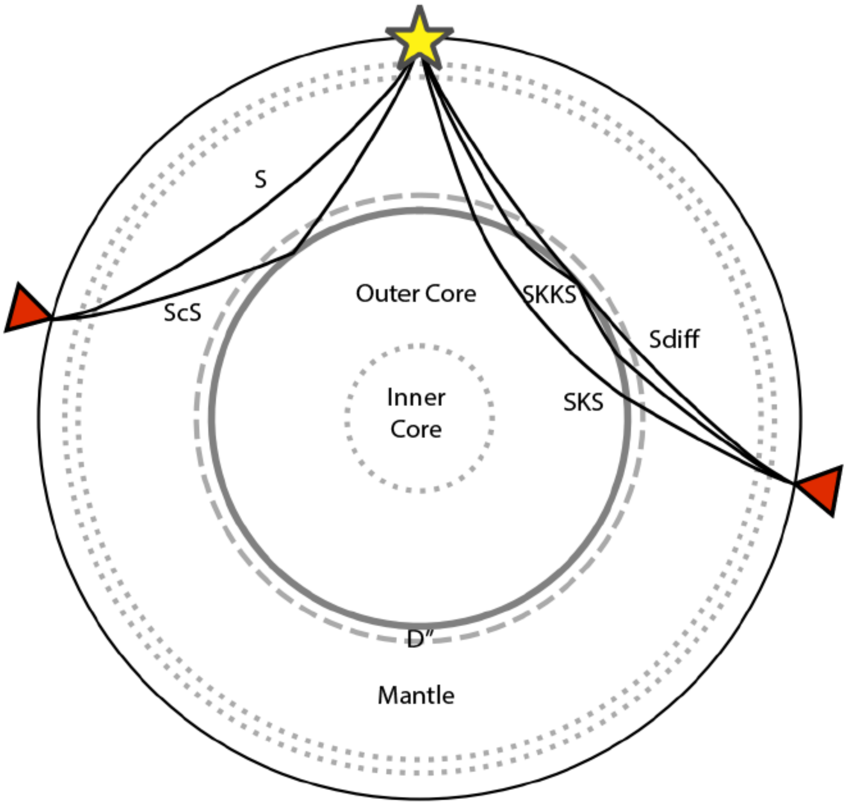

Figure 1.10: Raypaths of the principle shear-wave phases that have been used to study seismic anisotropy of D″. Earthquake location is shown by the star and receiver stations by the triangles.

Early studies observed shear-wave splitting in ScS and Sdiff phases, which propagate sub-horizontally in D″ (Fig. 1.10), attributing this to seismic anisotropy in D″ (e.g., Lay and Helmberger, 1983; Lay and Young, 1991; Vinnik et al., 1995; Kendall and Silver, 1996). As this early work consisted of comparing the delay times of the SH and SV components results were interpreted in a framework of radial anisotropy (i.e., VTI anisotropy where $V_{SH} > V_{SV}$ or vice-versa). Today shear-wave splitting analysis of (predominantly of S, ScS, Sdiff, SKS and SKKS phases) is used to study seismic anisotropy in D″. Shear-wave splitting is either measured in terms of the splitting parameters, ϕ and δt, which correspond to the polarisation direction of the fast shear-wave and the delay time between the fast and slow shear-waves (Silver and Chan, 1991; Walsh et al., 2013) or in terms of splitting intensity, a scalar measure devised by Chevrot (2000). I shall reflect further on the merits of the different methods with which we can measure shear-wave splitting and how we can combine them in the study of D″ in Chapters 2 and 3.

There are two principal challenges faced by any shear-wave splitting study of the lowermost mantle: accounting for potential contamination by upper mantle anisotropy and obtaining sufficient azimuthal coverage to constrain potential mechanisms for seismic anisotropy. Upper mantle anisotropy can be accounted for in several ways in the design of a study, depending on the choice of phase. For ScS and Sdiff it is highly desirable to use deep (> 500 km) earthquakes to minimise source-side contamination, with the downside being that this considerably reduces the regions that can be studied. This is not necessary for the core-transiting phases, such as SKS and SKKS, as they are radially polarised by the P-to-S conversion exiting the core (Hall et al., 2004). The core-transiting phases effectively emerge as fresh shear-waves with no record of any shear-wave splitting that the phases may have encountered prior to transiting the core. Azimuthal coverage in the lowermost mantle is always going to be a limiting factor as good source earthquakes, ideally where $5.5 < M_w < 7.0$, are far from uniformly distributed around the Earth. One potential method to improve coverage is to use multiple shear-wave phases, although regions where this can be achieved is currently limited.

In practice using reference phases is the best approach to correct for contamination from upper mantle anisotropy. At the epicentral distance range of 65° — 85° direct S arrivals can be used to correct ScS as they have similar raypaths in the upper mantle with S sampling the, what is assumed to be, isotropic bulk lower mantle and ScS sampling D″. Any differential shear-wave splitting between S and ScS can then be attributed to anisotropy in D″ (e.g., Wookey et al., 2005a; Thomas et al., 2007; Nowacki et al., 2010). At larger epicentral distances ($\Delta > 85°$) S and ScS arrivals begin to merge and SKS becomes visible and can be used as a reference phase for ScS and Sdiff (which is only visible at distances >100°), although deriving these corrections requires some care (Wookey and Kendall, 2007).

Alternatively SKS and SKKS phases can be used at epicentral distances of 100° — 140°. As the raypaths of SKS and SKKS only diverge in D″ (Fig. 1.10) any discrepancy in the observed shear-wave splitting can be reasonably assumed to be due to a change in anisotropy in D″ as this it the only region of the mantle where the raypaths of SKS and SKKS deviate significantly (Fig.1.10). This is an important distinction from S-ScS that is worth noting.

As SKS and SKKS phases are radially polarised when they exit the core (Hall et al., 2004)

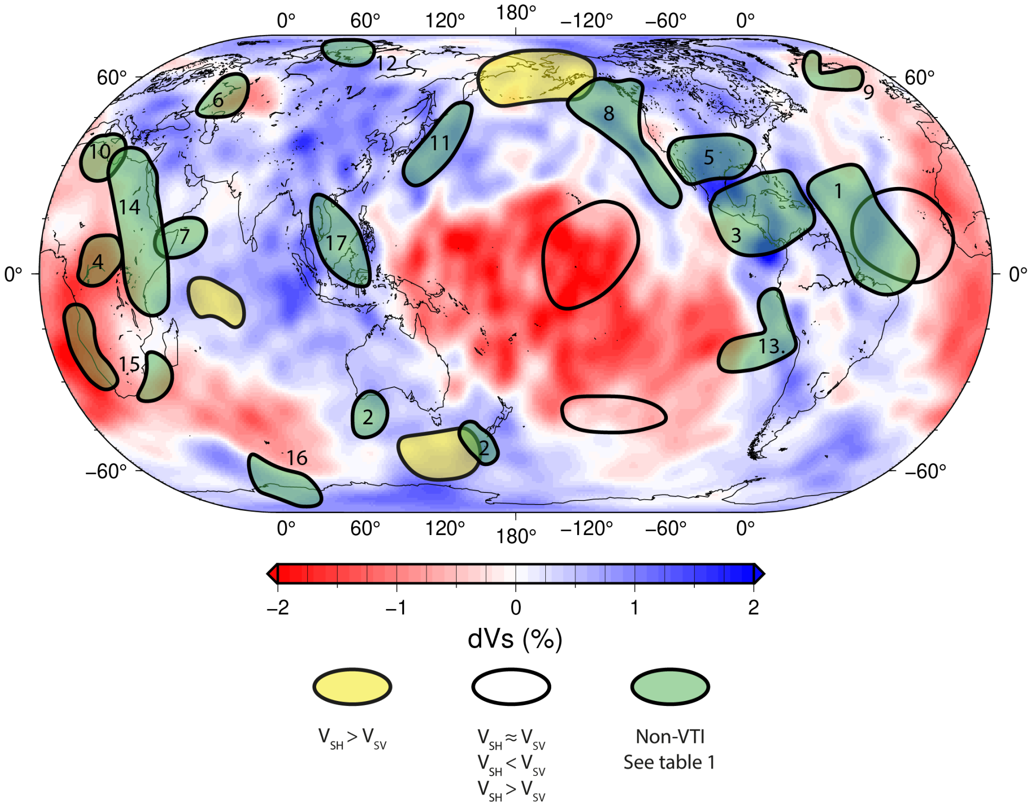

Figure 1.11: A summary of previous observations of seismic anisotropy in the lowermost mantle, updated and adapted from Nowacki et al. (2011). Observations are annotated over the S40RTS tomography model (Ritsema et al., 2011). Numbers refer to table 1.1.

this means they are not sensitive to VTI anisotropy in D″. This combined with their shorter path lengths in D″ when compared to ScS, as the phases propagate sub-vertically whilst ScS propagates sub-horizontally, we should see little or no shear-wave splitting discrepancies between these two phases if seismic anisotropy in D″ is predominantly VTI. Early work did indeed observe few (ca. 5%) discrepancies in SKS and SKKS phases on the same seismogram (Niu and Perez, 2004). Restivo and Helffrich (2006) argued that the few shear-wave splitting discrepanices that were observed were better explained by polarisation anomalies due to core-mantle boundary topography than azimuthal anisotropy that only exists in a few limited regions of D″, although they noted that both explanations were unsatisfactory.

Advances in instrumentation have proved crucial to studies of SKS and SKKS discrepant splitting. The deployment of dense networks of broadband seismometers allows us to collect sufficient data to perform detailed regional studies, with the switch to broadband seismology increasing our sensitivity to weak splitting that would have previously been identified as “null” (i.e., no detected shear-wave splitting e.g., Walpole et al., 2014). This has led to a substantial growth in SKS-SKKS shear-wave splitting studies in recent years (e.g., Long, 2009; Lynner and Long, 2014; Ford et al., 2015; Creasy et al., 2017; Deng et al., 2017; Grund and Ritter, 2018; Reiss et al., 2019; Lutz et al., 2020; Asplet et al., 2020, etc.,). Discrepant SKS-SKKS shear-wave splitting has now been observed in numerous regions in D$''$ (Fig. 1.11). Whilst discrepant SKS-SKKS shear-wave splitting is still far from ubiquitous in D$''$ it is now clear that the discrepancies are arising due to azimuthal seismic anisotropy in the lowermost mantle. This forces us to move away from simple models of VTI seismic anisotropy towards modelling either tilted transverse isotropic (TTI) models of anisotropy, which still may be a simplification, or more directly considering the orientation of elastic tensors for different models of seismic anisotropy in D$''$ (Fig. 1.11). The increasing prevalence of discrepant SKS-SKKS shear-wave splitting also raises an interesting question of how SKS phases, which are widely used to study seismic anisotropy in the upper mantle (e.g., Long et al., 2010; Walpole et al., 2014; Schlaphorst et al., 2017; Eakin et al., 2019), should be treated in the future. Perhaps future upper mantle studies will have to start correcting for contamination from seismic anisotropy due to D$''$?

One overarching criticism that can be made of the vast majority of shear-wave splitting studies of D$''$ is that their interpretations are broadly qualitative. Whilst this does not diminish the significant work that has been done to find evidence for seismic anisotropy in D$''$, if the results can be "plausibly explained"[8] by a broad range of candidate mechanisms then it is difficult to see how these result can be used to answer the broader questions surrounding the composition and dynamics of the D$''$ region. Forward modelling of candidate elastic tensors (e.g., Ford et al., 2015; Creasy et al., 2017), where orientation of an elastic tensor that best reproduces the observed shear-wave splitting parameters is sought, offers one potential resolution to this challenge. Although these methods have thus far been unable to conclusively prefer a unique mechanism for D$''$ seismic anisotropy. To adequately constrain candidate mechanisms having good azimuthal coverage is crucial and it has been shown that data from multiple unique azimuths is required (Wookey and Kendall, 2008; Creasy et al., 2019). Advances have also been made in incorporating reflection polarities, using the D$''$ reflacted phases SdS and PdP, to constrain seismic anisotropy (Pisconti et al., 2019). If we are able to jointly consider ScS, SKS and SKKS shear-wave splitting then we may be able to better constrain D$''$ seismic anisotropy.

---

[8] a modern day phrase that has undergone the high-pressure transition when applied to the Deep Earth (see Birch, 1952)

Region	Study	Phases Used	Suggested style of anisotropy	Notes
1. Atlantic Ocean	Pisconti et al. (2019)	ScS, SdS	TTI	
2. Australasia	Creasy et al. (2017)	ScS, SKS, SKKS	LPO of bridgmanite (br), ferropericlase (fp) or post-perovskite (ppv)	
	Creasy et al. (2020)	ScS, SKS, SKKS	LPO of ppv or fp	Revisiting Creasy et al. (2017)
3. Caribbean	Garnero et al. (2004)	S, ScS, Sdiff	TTI	
	Maupin et al. (2005)	S, ScS, Sdiff	TTI	
	Rokosky et al. (2006)	ScS	TTI	
	Nowacki et al. (2010)	ScS	TTI	
	Creasy et al. (2020)	ScS	LPO of ppv	Revisiting Nowacki et al. (2010)
4. Central Africa	Reiss et al. (2019)	SKS, SKKS	SPO of melt tubules or discs	Observations geopgraphically coincident with Afar ULVZ
5. Central US	Nowacki et al. (2010)	ScS	TTI	
	Lutz et al. (2020)	SKS, SKKS	Azimuthal	

6. Central Russia	Long and Lynner (2015)	SKS, SKKS	Azimuthal	Perm Anomaly
7. East Africa	Ford et al. (2015)	SKS, SKKS	LPO of ppv	4 different plausible orientations of ppve
	Reiss et al. (2019)	SKS, SKKS	LPO of ppv	Only considered ppv
	Creasy et al. (2020)	SKS-SKKS	LPO of ppv or fp	Revisiting Ford et al. (2015)
8. Eastern Pacific	Long (2009)	SKS-SKKS	Azimuthal	
	Asplet et al. (2020)	SKS-SKKS	Azimuthal	See Chapter 3
9. Iceland	Grund and Ritter (2018)	SKS-SKKS	Azimuthal	
	Wolf et al. (2019)	ScS, SKS, SKKS	SPO of melt tubules or LPO of br or fp	
10. North Africa	Reiss et al. (2019)	SKS, SKKS	LPO of ppv	Only considered ppv
11. Northwestern Pacific	Wookey et al. (2005a)	ScS	TTI	
12. Siberia	Wookey and Kendall (2008)	ScS	SPO or LPO	
	Creasy et al. (2020)	ScS	LPO of ppv or fp	Revisiting Wookey and Kendall (2008)

13. South America	Deng et al. (2017)	SKS, SKKS	Azimuthal
14. Southeastern Africa	Lynner and Long (2014)	SKS-SKKS	Azimuthal
15. Southern Africa	Wang and Wen (2007)	SKS-SKKS	TTI
16. Southern Ocean	Cottaar and Romanowicz (2013)	Sdiff	Azimuthal
17. South east Asia	Thomas et al. (2007)	ScS	TTI

Table 1.1: Summary table of recent studies of seismic anisotropy in the lowermost mantle. Studies prior to ca. 2011 that interpret a VTI style anisotropy are not included (see Nowacki et al., 2011; Romanowicz and Wenk, 2017, for thorough reviews). Such work, whilst important in establishing the presence of seismic anisotropy in D$''$, is not easily comparable to modern work. Where a study interprets a mechanism for seismic anisotropy, such as lattice-preferred orientation (LPO), through modelling of results, it is reported as such. Studies that interpret an anisotropic mechanism without robust modelling (e.g., Long, 2009) are reported as either azimuthal (in some work this is referred to as ‘complex’ anisotropy, where the results clearly cannot be explained by simple VTI) or TTI where the authors only interpret result in terms of a TTI geometry (e.g, Nowacki et al., 2010).

1.4.3 Candidate mechanisms

If we are to relate observations of seismic anisotropy to the composition and dynamics of D″, we need a good understanding of potential mechanisms for that seismic anisotropy. For example in studies of seismic anisotropy in the upper mantle it is well understood that the lattice-preferred orientation of olivine can be used as a framework to relate observations to upper mantle flow (e.g., Silver, 1996; Long and Becker, 2010; Becker and Lebedev, 2021). In the lowermost mantle we do not yet have such a framework and there are several plausible candidate mechanisms for seismic anisotropy due to lattice-preferred orientation and shape-preferred orientation. Here I shall briefly overview the main candidate mechanisms.

Post-perovskite

The lattice-preferred orientation of $MgSiO_3$ post-perovskite is currently the most popular mechanism for D″ seismic anisotropy. The elastic coefficients of post-perovskite differ significantly from bridgmanite (e.g., Tsuchiya et al., 2005; Wentzcovitch et al., 2006), with post-perovskite exhibiting strong single-crystal seismic anisotropy for both P (ca. 15%) and S (ca. 25%) waves, making it a good candidate to explain seismic anisotropy in the lowermost mantle (Fig. 1.12a; Wookey et al., 2005b; Stackhouse et al., 2005; Wentzcovitch et al., 2006). These elastic properties, along with the post-perovskite phase transition only occurring at lowermost mantle conditions make it a natural candidate mechanism that is often interpreted in shear-wave splitting studies (e.g., Long, 2009; Nowacki et al., 2010).

One important outstanding question is what slip system dominates in post-perovskite. Several slip systems have been proposed, with [100](001) preferred when fitting seismic data (e.g., Wookey et al., 2005b; Stackhouse et al., 2005; Miyagi et al., 2008; Cottaar et al., 2014b; Zhang et al., 2016), although some recent forward modelling of ScS shear-wave splitting has favoured the [100](010) slip system (Nowacki et al., 2013). The [100](010) slip system is also generally preferred by laboratory deformation experiments and microstructural analysis (e.g., Oganov and Ono, 2004; Yamazaki et al., 2006). More recent deformation experiments prefer (001) textures, with slip along [100](001) (Wu et al., 2017).

A challenge in studying the deformation of post-perovskite is the extreme pressure and temperature conditions needed by experiments to synthesise a sample of this mineral phase. Achieving these conditions requires the use of laser heated diamond anvil cells and tiny, ca. 25 µm

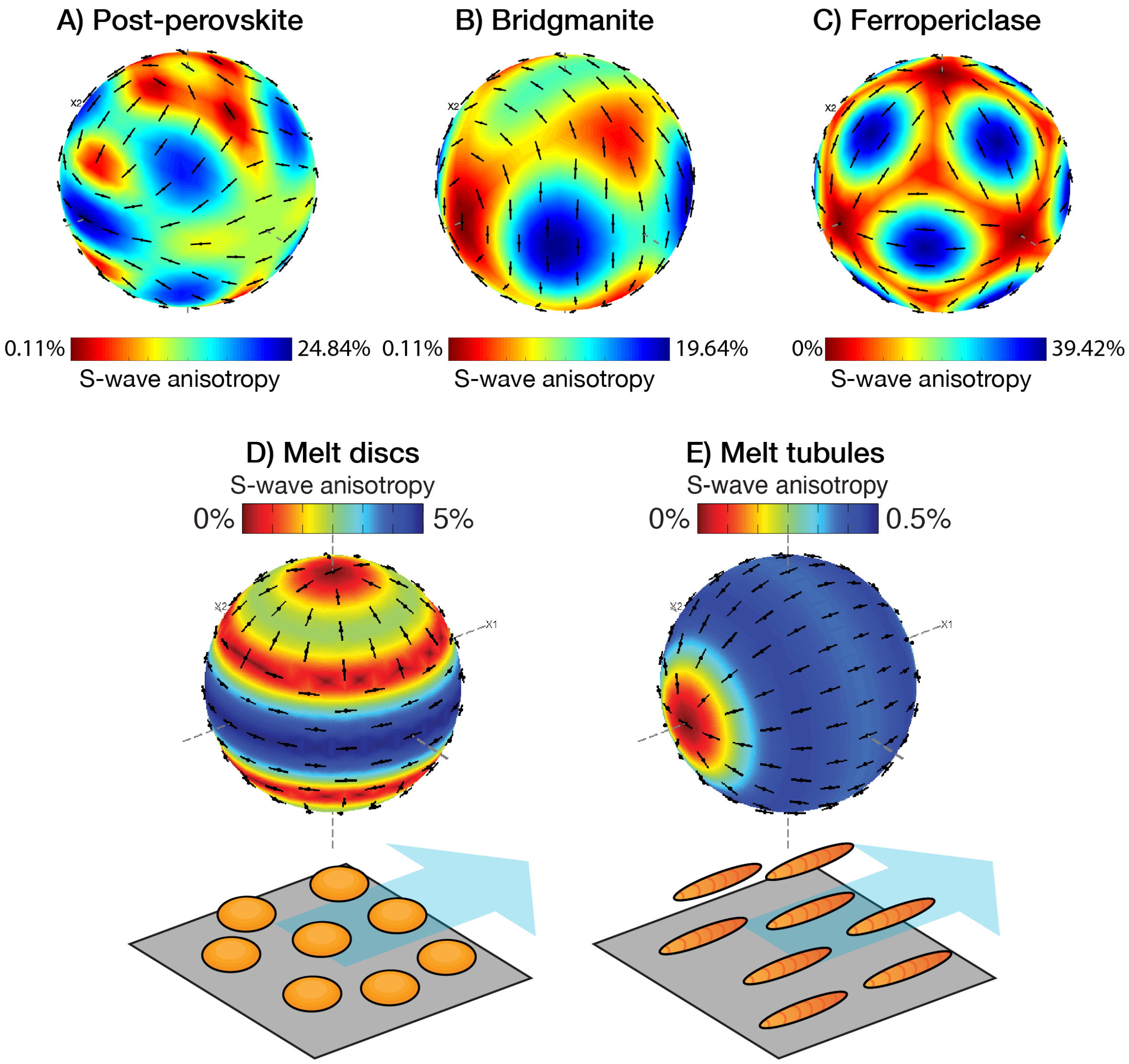

Figure 1.12: Spherical representations of the elastic properties of the three main mineral phases thought to be in D″ and the two end-members for spheroidal shape-preferred orientation (SPO) of melt inclusions (Kendall and Silver, 1998). For post-perovskite (a), bridgmanite (b) the elastic properties are taken from *ab initio* calculation calculations by Wookey et al. (2005b) at conditions of 2800 K and 126 GPa. For ferropericlase (c) the elastic properties are from *ab initio* calculation by (Karki et al., 2000) for pure periclase (i.e., MgO) at conditions of 3000 K and 125 GPa. At D″ conditions the Fe-Mg substitution results in similar, if not stronger, anisotropy with the same cubic symmetry Marquardt et al. (2009). For SPO the tensors for this spherical discs (d) and elongated melt tubules (e) are estimated using the effective medium theory (Tandon and Weng, 1984).

thick, samples (e.g., Murakami et al., 2004). This makes it difficult for experiments to produce a deformation texture in the samples and distinguish it from the separate ‘phase transformation texture’ that forms where the phase boundary is crossed (Walte et al., 2009). These diamond anvil cell experiments are also limited to experiments of deformation due to uniaxial pure shear.

Analogue minerals, which are stable at ambient or lower pressure and temperature conditions, can be used to more fully study the deformation of post-perovskite. Despite sharing a crystal structure these analogues do not necessarily share a slip system or produce the same deformation texture as post-perovskite, or other analogue materials. For example the consensus for the analogue $CaIrO_3$, which is stable at ambient conditions, is that slip along [100](010) is dominant over a wide temperature range (e.g., Miyagi et al., 2008; Walte et al., 2009), whilst $MnGeO_3$ and $MgGeO_3$ show slip along [100](001) dominating (Hirose et al., 2010; Miyagi et al., 2011).

Another avenue for studying post-perovskite deformation is through *ab initio* simulations, which can simulate deformation of post-perovskite crystal lattices at realistic pressures, temperatures and strain rates (e.g., Goryaeva et al., 2016). Recent atomistic calculations find that slip along the (010) plane, in either the [100] or [001] direction, has the lowest lattice friction and therefore are the most likely (Goryaeva et al., 2015, 2016, 2017). Attempts to couple these *ab initio* solutions and polycrystal plasticity simulations to model the evolution of LPO textures in D′′ have so far found mixed result. Models using 70% post-pervoskite and 30% periclase find that post-perovskite LPO rapdily rotates to align the dominant [100](010) slip system and the simple shear direction (Tommasi et al., 2018).

Thus far it has proved difficult to clearly identify which slip system dominates in D′′ from seismic observations. Recent geodynamic modelling, advancing on the work of Cottaar et al. (2014b), uses a pyrolitic composition (17 % MgO, 9 % $CaSiO_3$ and 74 % $MgSiO_3$) finds that post-perovskite with dominant slip on either (010) or (001) can explain seismic observation, with the (001) texture being inherited from the brigmanite to post-perovskite phase transition (Chandler et al., 2021). We must also be conscious that whilst seismologists favour post-perovskite as an interpretation for D′′ seismic anisotropy (e.g.. Wookey et al., 2005b; Long, 2009; Nowacki et al., 2010; Lutz et al., 2020, etc.,) the mineral physics is less clear. Experimental results constraints predict a 400-600 km thick bridgmanite to post-perovskite phase transition in pyrolitic samples, which is the expected bulk composition of the lowermost mantle (Catalli et al., 2009; Grocholski et al., 2012). These mineral physics studies predict that such broad transitions would not be seismically resolvable, with only regions of D″ containing slab material capable of producing a D″ discontinuity (Grocholski et al., 2012; Sun et al., 2018a). However we still would expect there to be observable seismic anisotropy in a broad transition zone. Post-perovskite is a significantly weaker than bridgmanite, up to 50 times weaker in the low-pressure analog $CaIrO_3$ (Hunt et al., 2009). When post-perovskite comprises a critical fraction of transition zone it will undergo rapid weakening and generate a strong LPO (Ammann et al., 2010). It is worth noting, however, that the work of Ammann et al. (2010) only considers bridgmanite and post-perovskite, neglecting other minor phases such as ferropericlase and Ca-perovskite. There has since been modelling of anisotropy in post-perovskite and ferropericlase mixtures (Tommasi et al., 2018), but thus far work has been restricted to assemblages of 2 phases. Until we have a clearer understanding of what post-perovskite texture are the most likely in a multi-phase lowermost mantle it will prove difficult to relate observations of seismic anisotropy to D″ dynamics.

Bridgmanite

Bridgmanite also exhibits strong orthorhobmic single crystal seismic anisotropy (Fig. 1.12b), albeit weaker than post-perovskite (Wookey et al., 2005b). If post-perovskite is not stable throughout D″, given the positive Calpeyron slope of the phase transition (Hirose et al., 2017), then bridgmanite would appear to be the logical alternative mechanism. Our understanding of bridgmanite is better than post-perovskite and there is reasonable consensus that [001](100) is the dominant slip system (Tsujino et al., 2016; Couper et al., 2020). Invoking bridgmanite does raise one important question for the lower mantle: if bridgmanite generates anisotropy in D″ then why is the lower mantle viewed as being broadly isotropic (e.g., Meade et al., 1995)? There is growing evidence for anisotropy in the uppermost lower mantle (between 660km and ca. 1200km), particularly beneath subduction zones (e.g., Montagner and Kennett, 1996; Wookey et al., 2002; Walpole et al., 2017a; Ferreira et al., 2019). There have also been suggestions of weak seismic anisotropy 1000 km above the core-mantle boundary from normal modes (de Wit and Trampert, 2015), but there is still consensus, for now, that the bulk lower mantle is, outside of D″, predominantly isotropic (Romanowicz and Wenk, 2017). A further complication is the suggestion from dislocation dynamics simulations that bridgmanite deforms by pure climb creep in lower mantle conditions, a mechanism that does not produce lattice-preferred orientation anisotropy (Boioli et al., 2017).

Ferropericlase

Ferropericlase is the second most abundant mineral in the lower mantle after $MgSiO_3$ (either as bridgmanite or post-perovskite), consisting of ca. 15% of the lower mantle (Hirose et al., 2017), and is also strongly anisotropic with a cubic symmetry (e.g., Karki et al., 1999). Generally disregarded in favour of post-perovskite, ferropericlase does in fact show stronger single crystal anisotropy (Fig. 1.12c), although this strongly depends on the iron content (Marquardt et al., 2009). As ferropericlase is present throughout the lower mantle, invoking it as an explanation for D″ anisotropy again raises the question of the bulk isotropy of the lower mantle. This can be somewhat explained by experiments that show the seismic anisotropy of ferropericlase increases with depth, aided by the iron-spin crossover in the lower mantle (Marquardt et al., 2009), and that the slip system changes to $\{100\} < 011 >$ in the mid-lower mantle potentially causing a new LPO fabric to develop (Immoor et al., 2018). The cubic symmetry can make ferropericlase difficult to use to constrain dynamics, as there is nearly always some orientation that can be found that plausibly explains seismic observations (e.g., Creasy et al., 2020).

Aligned heteogeneities

The alignment of heterogeneities smaller than the seismic wavelength, or shape-preferred orientation (SPO), is another mechanism that has slightly fallen out of favour following the discovery of post-perovskite. In lowermost mantle conditions, this may be due to layering of different materials, such as thin lenses of post-perovskite, or alignment of melt pockets. The most commonly invoked style of SPO is melt inclusions (e.g., Kendall and Silver, 1996, 1998), which are assumed to be spheroidal (Fig. 1.12d,e) allowing the seismic anisotropy to be modelled using effective medium theory (e.g., Tandon and Weng, 1984). Modelling of melt SPO has shown if melt forms thin disc-shaped inclusions, which are effectively the same as a medium with periodic thin layering (Backus, 1962), then seismic observations can be well explained by very low volume fractions (≤ 0.0001) with the discs exhibiting a hexagonal symmetry (Kendall and Silver, 1998). There is one significant outstanding question for SPO anisotropy in D″: is melt present in the lowermost mantle? It is currently unclear if melt is present, although the presence of melt is often inferred to explain ULVZs (e.g., Rost et al., 2005; Labrosse et al., 2007; Andrault et al., 2014; Pradhan et al., 2015; Liu et al., 2016; Yuan and Romanowicz, 2017) and therefore we might expect to observe significant seismic anisotropy from ULVZs. Although, the thickness (ca. 10 km - 40 km) makes it problematic to probe ULVZ anisotropy. Ultimately, until we have definitive evidence for the existence of melt in D$''$, the interpretation of SPO anisotropy is slightly speculative.

1.5 Thesis overview

It is an exciting time to be studying the lowermost mantle. Through advances in mineral physics and geodynamics we have a greater understanding of the potential composition and dynamics present, but a lack of strong observational constraints. In seismology we have access to ever larger teleseismic datasets, which has allowed us probe the D$''$ region in increasing detail. However, there is still a limited framework to ensure some of our observations are robust and to quantitatively relate shear-wave splitting observations to mechanisms of seismic anisotropy in D$''$. The aim of this Thesis is to address some of these limitations by developing new methods to allow for more robust analysis of shear-wave splitting and seismic anisotropy. Using broadband datasets of SKS, SKKS and ScS shear-wave splitting I will demonstrate the efficacy of these new techniques and use them to probe seismic anisotropy in D$''$ beneath the Eastern Pacific.

In Chapter 2 I will outline the collection of the datasets used for the work in this thesis. I collect a new broadband dataset of SKS and SKKS shear-wave splitting derived from an existing SKS shear-wave splitting catalogue. Additionally I collect and re-process ScS shear-wave splitting data used by Walpole et al. (2017b). I perform some preliminary analysis using my global SKS-SKKS shear-wave splitting dataset. This analysis helps to inform the design of the work undertaken in subsequent chapters. Using the combined SKS, SKKS and ScS datasets I perform some additional analysis exploring methods for measuring splitting intensity.

In Chapter 3 I develop a new technique for the robust identification and classification of discrepant shear-wave splitting. I then use this method to study discrepant SKS-SKKS shear-wave splitting in the Eastern Pacific region. The contents of this chapter is published as Asplet et al. (2020).

In Chapter 4 I revisit and revise a method for the direct inversion of shear-wave waveform data first outlined by Wookey (2012). I have made improvements to this method by switching to using a Metropolis-Hasting Markov Chain Monte Carlo sampler, developing a framework for using model misfit to quantitatively compare different candidate mechanisms and by making various improvements to the codebase. Using the improvements made, I jointly invert ScS, SKS and SKKS shear-wave waveform data for the orientation and strength of different plausible elastic tensors to test the interpretations made in Chapter 3 for the Eastern Pacific region. The contents of this Chapter has been submitted as Asplet et al., (submitted).

Finally, in Chapter 5 I will summarise the key results of my work and the current state-of-the-art work in this field. The future of studying D$''$ seismic anisotropy is an exciting one and I will offer my view of potential future directions for research.

CHAPTER 2

CONSTRUCTING A BROADBAND DATASET OF SHEAR-WAVE SPLITTING: PRELIMINARY VIEWS OF GLOBAL LOWERMOST MANTLE SEISMIC ANISOTROPY

Part of sections 2.2 and 2.4 of this chapter are published as part of Asplet et al. (2020). This work was done in collaboration with my supervisors James Wookey and Michael Kendall.

2.1 Introduction

If we are to probe seismic anisotropy in D$''$, first we must collect sufficient data. As part of this thesis I have collected a global dataset of SKS and SKKS shear-wave splitting, derived from a global long-period SKS dataset collected by Walpole et al. (2014). The dataset of SKS-SKKS event station pairs that I collect here is integral to the work have done throughout my thesis. In this chapter I will outline my approach for measuring SKS and SKKS shear-wave splitting using broadband data. Additionally I will give an overview of the collection and reprocessing of the ScS dataset (taken from Walpole et al., 2017b) which is used in Chapter 4. Using this data I will describe some common techniques for measuring shear-wave splitting and perform some preliminary analysis of the global SKS-SKKS dataset. Following this preliminary analysis I will outline how the coverage afforded by the data affects the design of the research that I undertake in Chapters 3 and 4.

2.2 Measuring shear-wave splitting

There are a variety of methods for measuring shear-wave splitting. The traditionally more popular methods characterise shear-wave splitting in terms of the splitting parameters ϕ (the polarisation direction of the fast shear-wave) and δt (the time delay between the fast and slow shear-waves). Early techniques for measuring shear-wave splitting relied on visual interpretations of particle motion plots and the manual identification of orientation of seismograms where the fast and slow shear-waves were most clearly separated (Crampin, 1985; Crampin and Gao, 2006). These visual methods are laborious, particularly with the large datasets available to modern seismologists, and can be heavily subjective. Today automated approaches dominate when it comes to studying teleseismic shear-wave splitting (e.g., Long, 2009; Nowacki et al., 2010; Deng et al., 2017; Creasy et al., 2017; Lutz et al., 2020, etc.,). However automation alone does not guarantee that measurements are accurate, and the objectivity of automated measurements can be “suspect” (Crampin and Gao, 2006), and typically even if measurement routines are automated manual oversight is needed to ensure data quality.

Cross-correlation of the horizontal components is the simplest automation approach, where the components are rotated to search for the orientation which maximises the cross-correlation between the orthogonal components[1], at which point the delay time between the phases can be estimated (e.g., Fukao, 1984; Bowman and Ando, 1987). There are some limitations with this cross-correlation approach as it relies on the assumption that fast and slow shear-wave are similar and that they are orthogonal. The fast and slow shear-waves are only truly orthogonal if the waves are propagating at the phase velocity, in anisotropic media generally the waves are propagating at the group velocity (Crampin and Gao, 2006). For small earthquakes used in crustal shear-wave splitting studies, where higher frequencies are used, the fast and low shear-waves are not necessarily similar due to factors such as differences in attenuation (Hudson, 1980), this is not an issue for shear-wave splitting studies of the mantle as the fast and slow shear-wave generally have similar waveforms at the lower frequencies used (ca. 0.1 - 0.5 Hz ; Crampin and Gao, 2006).

There are a range of methods that use the linearity of the corrected particle motion to measure shear-wave splitting[2]. This can be done by minimising the energy on the transverse component

---

[1] as opposed for visually assessing the rotation where the components look the same

[2] even cross-correlation methods are effectively doing this, as noted by Silver and Chan (1991)

(Silver and Chan, 1988), minimising the second eigenvalue, λ_2, of the trace covariance matrix (Silver and Chan, 1991; Walsh et al., 2013) or maximising the particle motion aspect ratio (λ_1/λ_2) (Shih et al., 1989). The eigenvalue minimisation method (EV) is generally considered to be the most robust[3] and is a generalised version of transverse minimisation (Silver and Chan, 1988), where both methods are equivalent in the special case where the polarisation direction is known. In theory this special case can be applied to SKS and SKKS phases where, as the phases are radially polarised, it can be assumed that the source polarisation is equal to backazimuth. I measure shear-wave splitting using the eigenvalue method as implemented in the analysis code SHEBA (Teanby et al., 2004; Wuestefeld et al., 2010).

In the absence of noise a shear-wave that has not undergone any shear-wave splitting (generally referred to as a "null" measurement) will have a rank 1 trace covariance matrix, i.e., all shear-wave energy is in the component whose orientation is defined by the source moment tensor, which in the case of SKS and SKKS phases is the radial component (Silver and Chan, 1991; Walsh et al., 2013). The shear-wave splitting experienced by a given waveform can be concisely expressed in terms of the splitting operator $\mathbf{\Gamma}(\phi, \delta t)$ which can be expressed as:

$$\mathbf{\Gamma} = e^{-i\omega\delta\hat{\mathbf{f}}\hat{\mathbf{f}}^T} + e^{-i\omega\delta\hat{\mathbf{s}}\hat{\mathbf{s}}^T}, \tag{2.1}$$

where ω is frequency, $\hat{\mathbf{f}}$ is the fast polarisation direction and $\hat{\mathbf{s}}$ is the slow direction (Walsh et al., 2013). It should be noted that the fast polarisation $\hat{\mathbf{f}}$ should not be confused with the splitting parameter ϕ, commonly referred to as *fast polarisation*, which is defined in the ray reference frame as the angle between $\hat{\mathbf{f}}$ and the initial polarisation direction of the un-split waveform $\hat{\mathbf{p}}$. Throughout this thesis I measure shear-wave splitting in the geographic reference frame, where ϕ is defined as the angle between $\hat{\mathbf{f}}$ and North. The splitting operator $\mathbf{\Gamma}$ is both symmetric and unitary, so $\mathbf{\Gamma}^{-1} = \mathbf{\Gamma}^{*}$ (Silver and Chan, 1991; Walsh et al., 2013). Using this relation we can generate inverse splitting operator for any combination of splitting parameters, allowing us to invert for the set of $(\phi, \delta t)$ that best minimise the second eigenvalue of the trace covariance matrix (and third if we include the vertical component as in Walsh et al., 2013). Uncertainties in the measured splitting parameters are estimated from the 95% confidence region

$$\lambda_2^{0.95}(\phi, \delta t) = \lambda_{2_{min}}\{1 + [k/(v-k)]F^{0.05}_{k,v-k}\}, \tag{2.2}$$

---

[3] or at least, it has proven to be the most popular

where $k = 2$, the number of estimated splitting parameters, v is the estimated degrees of freedom of the data and $F_{k,v-k}$ is an F-distribution (Silver and Chan, 1991; Walsh et al., 2013). Uncertainties can also be estimated using a bootstrapping method (Sandvol and Hearn, 1994), although this adds significant computational burden and produces uncertainty estimates which are generally similar to the Silver and Chan (1991) method.

The quality of shear-wave splitting measurements can be assessed using the quality factor Q (Wuestefeld et al., 2010). By taking advantage of the difference in behaviour of the cross-correlation (XC) and eigenvalue minimisation (EV) methods when measuring nulls, where cross-correlation systematically fails returning a maximum correlation for a rotation of 45 ° (Wüstefeld and Bokelmann, 2007), it is possible to automatically detect null measurements and measure overall measurement quality. Shear-wave splitting is measured using both XC and EV, with the measurements compared by calculating the ratio of delay time measurements:

$$\Delta = \frac{\delta t_{XC}}{\delta t_{EV}} \tag{2.3}$$

and the difference in fast directions, normalised by 45°:

$$\Omega = \frac{\phi_{EV} - \phi_{EX}}{45}. \tag{2.4}$$

For a perfect split measurement both EV and XC should return the same splitting parameters (i.e., $\Delta = 1$, $\Omega = 0$), whilst for a perfect null measurements $\delta t_{XC} = 0$ and the estimates for fast polaristion will differ by 45° (i.e., $\Delta = 0$, $\Omega = 1$). To assess the quality of a splitting measurement we can calculate the distance to each of these ideal cases:

$$d_{\text{null}} = \sqrt{\Delta^2 + (\Omega - 1)^2}\sqrt{2}, \tag{2.5}$$

$$d_{\text{good}} = \sqrt{(\Delta - 1)^2 + \Omega^2}\sqrt{2} \tag{2.6}$$

these distances can then be related to calculate the quality factor

$$Q = \begin{cases} -(1 - d_{null}), \text{for } d_{null} \leq d_{good} \\ (1 - d_{good}), \text{for } d_{null} \geq d_{good} \end{cases}. \tag{2.7}$$

Where Q ranges from -1 for a clear null measurement, through 0 (a poor or indeterminate measurement) to +1 for a clear split measurement.

Another useful measure of data quality is the signal-to-noise ratio (SNR). If SNR is low, then shear-wave splitting measurements tend to be poorly constrained. The SNR for shear-wave splitting measurements throughout this thesis is estimated following the method of Restivo and Helffrich (1999), as implemented in SHEBA. The signal level is assumed to be the maximum amplitude on the corrected radial component and the noise level is represented by the 2σ value for the corrected transverse component (Restivo and Helffrich, 1999).

An alternative approach is to measure shear-wave splitting in terms of splitting intensity (Chevrot, 2000). Initially developed as a tool for multi-channel analysis of shear-wave splitting, where multiple SKS and SKKS phases sampling a range of backazimuths are combined to yield better estimates of the splitting parameters, measurements of splitting intensity for individual phases are now used to study seismic anisotropy in D'' (e.g., Deng et al., 2017; Grund and Ritter, 2018; Reiss et al., 2019). This method utilises the variation of energy on the uncorrected transverse component with incoming polarisation direction (or backazimuth for SKS and SKKS phases). Transverse component energy, termed the splitting intensity (SI), is measured relative to the time derivative of the radial component.

Splitting intensity can only be reasonably used if the lag time δt is much less than the dominant period of the waveform and this is assumed to be the case of teleseismic shear-wave splitting. In this case, assuming a simple homogeneous layer of anisotropy, the radial and transverse seismogram components can be expressed as

$$r(t) = w\left(t + \frac{\delta t}{2}\right)\cos^2\phi + w(t - \frac{\delta t}{2}\sin^2\phi \tag{2.8}$$

$$t(t) = -\frac{1}{2}\left[w\left(t + \frac{\delta t}{2}\right) - \left(t - \frac{\delta t}{2}\right)\right]\sin 2\beta \tag{2.9}$$

$$r(t) \approx w(t) \tag{2.10}$$

$$t(t) \approx -\frac{1}{2}\delta t \sin(2\beta) u'(t) \tag{2.11}$$

where $w(t)$ is the source wavelet and β is the angle between the fast polarisation and source polarisation directions (Silver and Chan, 1988; Chevrot, 2000). Notice here that in this approximation the transverse component $t(t)$ can be written in terms of the radial component $r(t)$. This relationship can be generalised for a set of m transverse components containing n datapoints where the $m \times n$ matrix $\mathbf{T}$ can be expressed as the tensor (or outer) product between the splitting vector $\mathbf{s}$, which contains the splitting intensity relating each transverse and radial component, and $\dot{\mathbf{r}}$ the time derivative of the radial component:

$$\mathbf{T} = a\mathbf{s} \otimes \dot{\mathbf{r}} = a\mathbf{s}\dot{\mathbf{r}}^T, \tag{2.12}$$

where $a = -0.5$ is a constant (Chevrot, 2000). This equation can be re-arranged to solve for the splitting vector $\mathbf{s}$ by singular value decomposition of $\mathbf{T}$ or by expressing $\mathbf{s}$ in terms of $\mathbf{T}$ and $\dot{\mathbf{r}}$. Where the equation

$$\mathbf{s} = -2\frac{\mathbf{T}\dot{\mathbf{r}}}{\dot{\mathbf{r}}^{\mathbf{T}}\dot{\mathbf{r}}}, \tag{2.13}$$

is referred to as the projection of the transverse component data onto $\dot{\mathbf{r}}$ and $\dot{\mathbf{r}}^{\mathbf{t}}\dot{\mathbf{r}} = ||\dot{\mathbf{r}}^{\mathbf{2}}||$ or the squared norm of $\dot{\mathbf{r}}$ (Chevrot, 2000). It is unclear from Chevrot (2000) whether this is a geometric projection as naturally we would expect the projection of two orthogonal vectors to be equal to zero. To me it appears this may be a case of imprecise language, which the term projection refers to the fact that splitting intensity is estimated by multiplying the two components, as opposed to the singular value decomposition method. In reality, almost all authors use equation 2.13 for splitting intensity (e.g., Li et al., 2014; Deng et al., 2017; Grund and Ritter, 2018; Asplet et al., 2020, etc.,) and use the phrasing of Chevrot (2000) to describe the method. In multi-channel analysis the measured splitting can be used to retrieve the best fitting splitting parameters $(\phi, \delta t)$ by fitting a sine curve using:

$$\mathbf{s}(\theta) = \delta t \sin 2(\theta - \phi), \tag{2.14}$$

where θ is the incoming polarisation direction (Chevrot, 2000). This sinusoidal relationship, which assumes a vertically incident plane wave, is a straight forward relation that defines a uniform layer of anisotropy beneath the station where the amount of shear-wave splitting varies with backazimuth only and has been widely used, particularly in early shear-wave splitting studies (e.g., Silver and Chan, 1988; Savage, 1999). Sampling a large range of backazimuths makes the multi-channel analysis of shear-waves highly effective for estimating the shear-wave splitting parameters in noisy environments. However it is worth remembering that equation 2.14 is only an approximate relationship, when full waveform effects are considered contamination from other phases and other frequency effects can cause measurement discrepancies (Lin et al., 2014).

A current quirk of splitting intensity literature is a disagreement in the exact formulation of 2.14, with some authors adding a factor of $\frac{1}{2}$ (e.g., Deng et al., 2017; Lutz et al., 2020). This has been attributed in some cases to Lin et al. (2014) (e.g., Deng et al., 2017), although this does not appear to be the case to me. Substituting the equations 2.10, 2.11 for $r(t)$ and $t(t)$ respectively into equation 2.13 it is quite clear that the approximate sinusoidal relationship for splitting intensity is as set out in equation 2.14. Whilst this is a minor discrepancy and it does not have any significant effect on splitting intensity results, as there is consistency in the formulation of the projection equation (2.13) which is used to measure splitting, the lack of a clear consensus is troubling. It is currently somewhat of a non-issue, as splitting intensity studies of the lowermost mantle tend to only focus on splitting intensity and if they do use splitting parameters they have measured them independently (e.g., Wolf et al., 2019; Lutz et al., 2020). However potentially we are left with a situation where some splitting intensity studies imply double the delay time (δt) of others, which is a significant discrepancy.

The primary advantage of using splitting intensity is that it is commutative (Silver and Long, 2011), unlike splitting operators $\Gamma(\phi, \delta t)$ which are well known to be non-commutative (e.g., Silver and Savage, 1994). This makes splitting intensity an exciting tool with which we can study D$''$ as any significant difference in the measured splitting intensity for different phases sampling D$''$ can be reasonably attributed to a change in D$''$ seismic anisotropy (e.g., Deng et al., 2017). As splitting intensity commutes it can in theory be treated analogously to travel times and used to perform splitting intensity tomography (Silver and Long, 2011). The disadvantage of splitting intensity is that commutativity comes at the expense of the loss of information, namely that splitting intensity measurements can 'lose' homogenous anisotropic layers at depth (Chevrot and Monteiller, 2009). For example, in the classic problem of two homogeneous layers of anisotropy (e.g., Silver and Savage, 1994) measurements of splitting intensity cannot distinguish the order of the layers, or between two layers and a single anisotropic layer.

There now exist a wide variety of programs, written in a variety of languages, which implement the various methods to measure shear-wave splitting. I choose to use the shear-wave splitting analysis code SHEBA (Wuestefeld et al., 2010), which incorporates the cluster analysis codes of Teanby et al. (2004) that identify optimum analysis windows. This cluster analysis gives more reliable measurements as otherwise the choice of analysis window can affect the accuracy and reliability of measurements (Crampin and Gao, 2006). I perform a grid search for both splitting parameters over a range of $0\,\mathrm{s} \le \delta t \le 4\,\mathrm{s}$ and $-90° \le \phi \le 90°$. SHEBA utilises eigenvalue minimisation to measure $(\phi, \delta t)$ and also measures splitting intensity by projection as in equation 2.13.

Another factor to consider is what filtering strategy to employ. It is common to use an upper corner frequency of 0.1 or 0.125 Hz, with some studies selecting one of these corners for each waveform to minimise noise (e.g., Deng et al., 2017; Lutz et al., 2020). There is a lot of merit in this approach, particularly with noisier data where the signal-to-noise ratio can have a significant effect on measurements (e.g., Restivo and Helffrich, 2006). However, the frequency content of the data controls what delay times can be resolved. Increasing the upper corner from 0.1 Hz to 0.5 Hz when using broadband data, has shown that previous null measurements do in fact show weak shear-wave spitting (Walpole et al., 2014). This is one of the main motivating factors for why I am collecting broadband datasets as to detect signals from D$''$ we want to ensure we can detect these weakly split results, which may well be indicative of D$''$ seismic anisotropy. This does, however, come at the expense of allowing increased high frequency noise into our data. Throughout my thesis I choose to employ a uniform two-pass two-pole butterworth bandpass filter, with corner frequencies of 0.01 Hz and 0.5 Hz.

2.3 Data collection

2.3.1 Global event-station pairs of SKS and SKKS

The initial dataset consists of ca. 50,000 long-period measurements of SKS shear-wave splitting made by Walpole et al. (2014). This dataset covers earthquakes where $4.0 \le M_W \le 7.3$ for the years 1976 to 2010. I select a subset of these SKS measurements, where $Q \ge 0.7$ for split events or $Q \le -0.7$ for nulls; this selects a subset of 1525 clearly split SKS phases and 15276 nulls. Additionally I incorporate 169 events recorded at South American stations, which have been previously found to show clear discrepant SKS-SKKS shear-wave splitting (Deng et al., 2017), to expand our coverage and potentially provide a point of comparison. This gives an initial dataset of 16970 events, which I use to query the IRIS data management centre for broadband seismograms. I only query events where $5.5 \le M_w \le 7.5$. This results in a set of 14510 events being passed

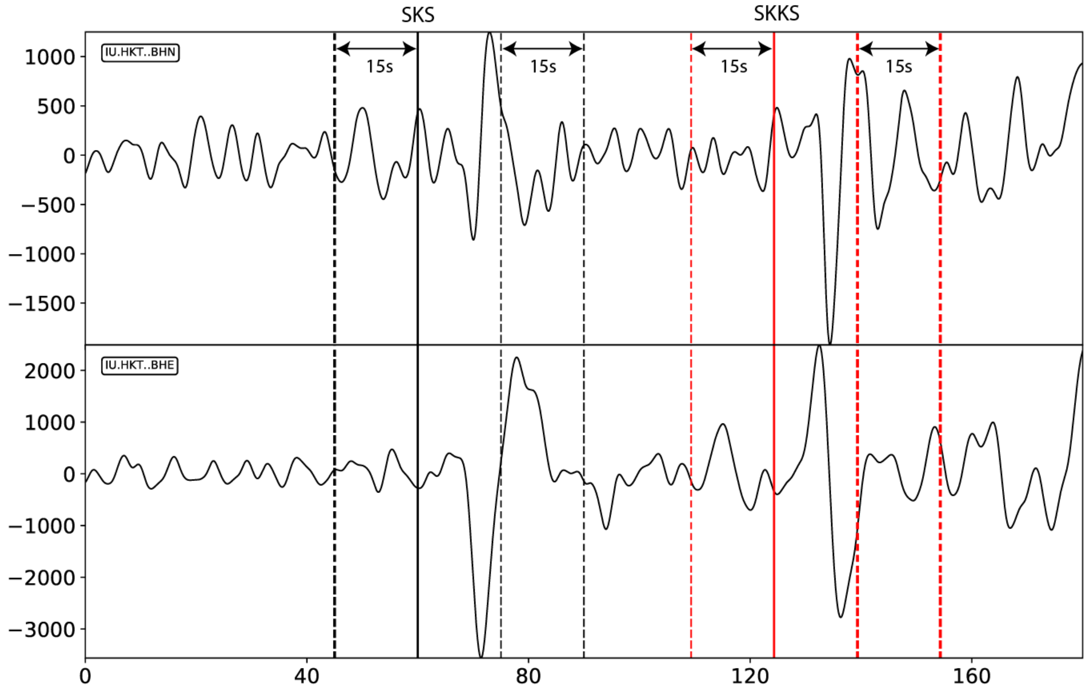

Figure 2.1: Window ranges used for the shear-wave splitting analysis. The solid lines indicate the travel time predictions made using the TauP toolkit (Crotwell et al., 1999) and the IASP91 1-D velocity model (Kennett and Engdahl, 1991). Dotted lines indicate the range the cluster analysis code is provided to search for the optimal window start/end point. The top panel shows the broadband East component (BHE) and the bottom panel shows the broadband North component (BHN).

into my SKS/SKKS shear-wave splitting workflow. The loss of data can be attributed to a lack of broadband data for older events which were recorded before broadband seismometers were widely available and to the exclusion of the smaller magnitude events included in the Walpole et al. (2014) dataset.

Using this dataset I then search for records where clear SKS and SKKS phases can be detected. Seismograms with an epicentral distance, $\Delta \leq 105°$ are rejected in order to ensure sufficient separation between the two phases. Having clear SKS and SKKS arrivals allows both phases to be initially picked automatically based on the expected arrival time calculated using TauP (Crotwell et al., 1999) and the IASP91 1-D global velocity model (Kennett and Engdahl, 1991). I choose to do this as for shear-wave splitting analysis defining a reasonable analysis window is more important that getting a 100% accurate phase pick and this initially automated approach

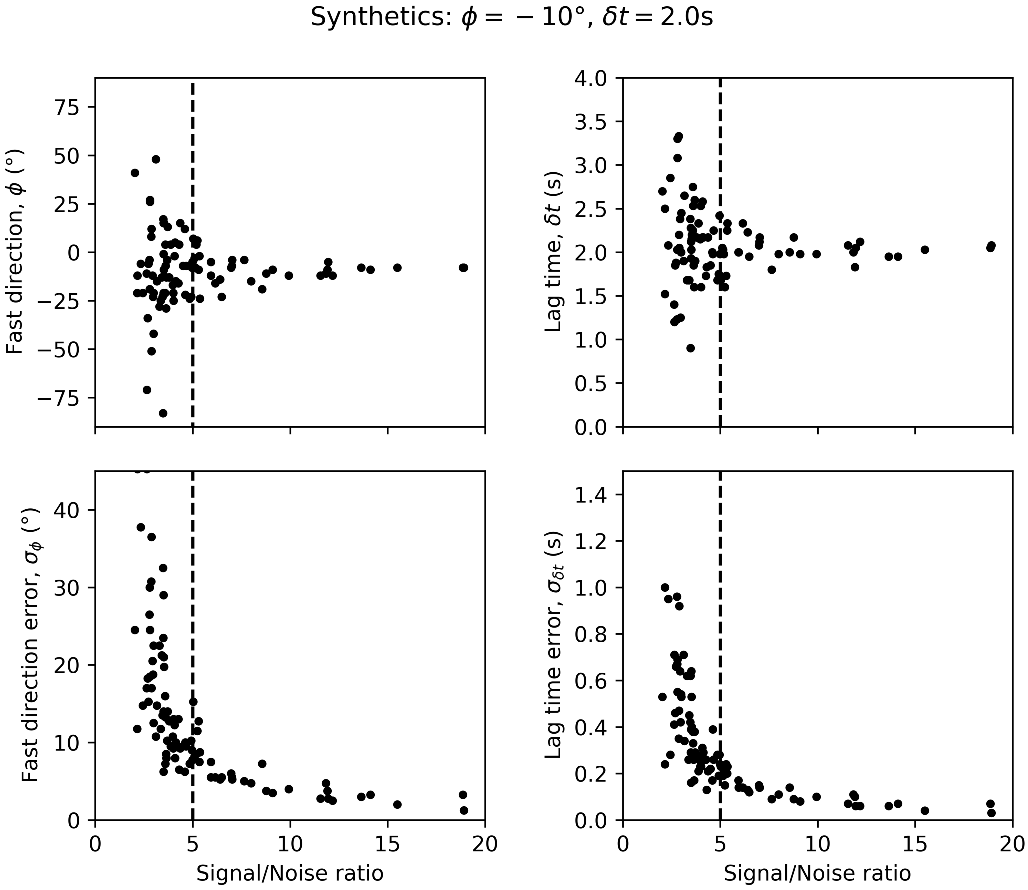

Figure 2.2: Relationship between measured splitting parameters and signal-to-noise ratio, explored using synthetic shear-waves. In this example the synthetics are generated with a source polarisation of 30°, a fast polarisation direction (ϕ) of $-10°$ and a lag time (δt) of 2 seconds.

allows for easier processing of the large dataset. Analysis windows are defined using cluster analysis (Teanby et al., 2004), where the optimum analysis window is sought for a predetermined search range. For preliminary analysis these search ranges are fixed relative to the expected arrival time, imposing a minimum and maximum length of 15 and 45 seconds respectively (Fig. 2.1).

Shear-wave splitting is measured for both phases independently using SHEBA. To ensure data quality all phases with a source polarisation and backazimuth discrepancy ≥ 10° are rejected, as such anomalies can manifest as shear-wave splitting discrepancies (Restivo and Helffrich, 2006). This results in a dataset of 4368 SKS-SKKS event station pairs (i.e., 4368 seismograms where both SKS and SKKS are recorded). An example of a clear splitting measurement, for an SKS phase recorded at COR, can be seen in figure **??**. Noisy data can also result in inaccurate splitting

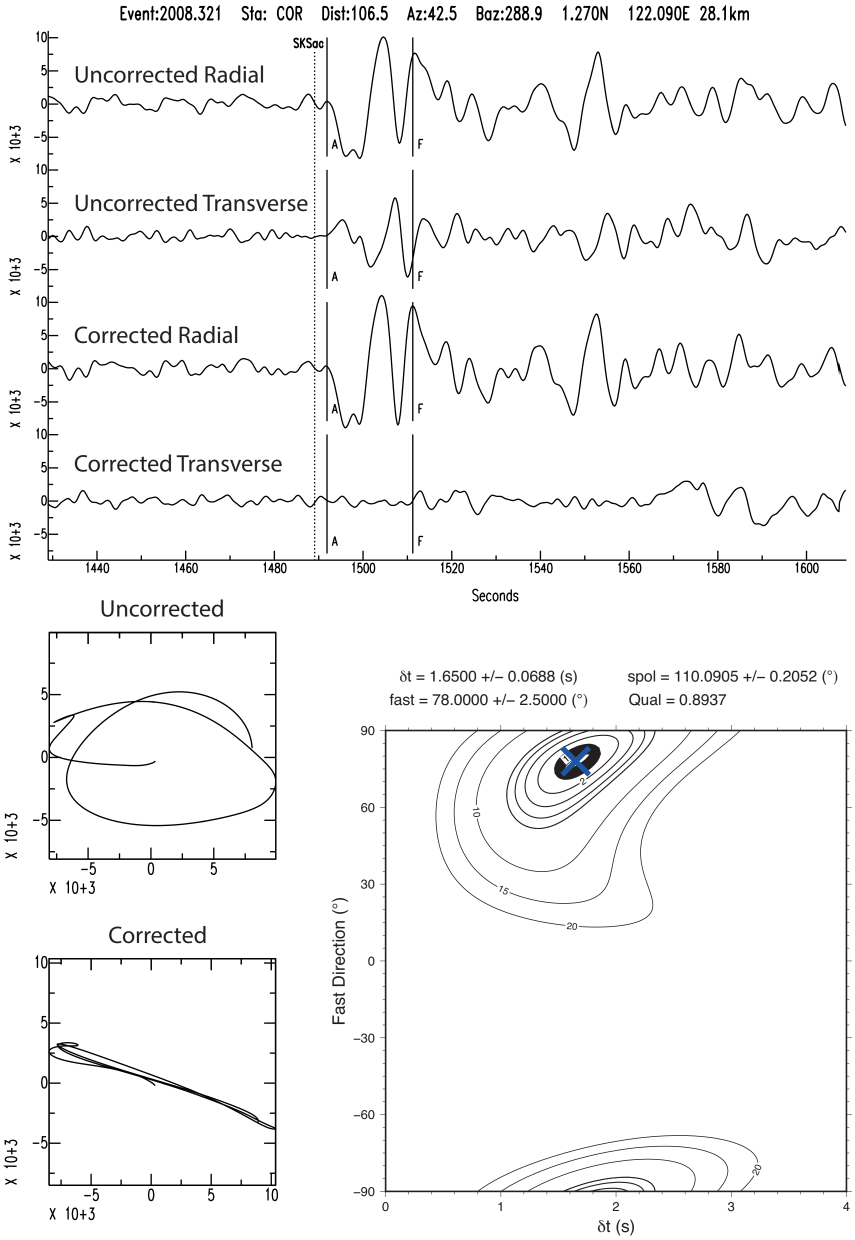

Figure 2.3: An example shear-wave splitting measurement made using the SHEBA shear-wave splitting analysis code. Shown here are the input (uncorrected) waveforms rotated to the radial-transverse co-ordinate system, the measurement corrected waveforms, hodograms (i.e., particle motion plots) of both sets of waveforms and the λ_2/ misfit surface. The blue cross on the misfit surface indicates the best fitting splitting parameters (ϕ,δt) and the bold line shows the F-test derived 95% confidence region.

measurements. Previous work by Restivo and Helffrich (1999) recommends shear-wave splitting can be confidently detected if the signal-to-noise ratio is greater than 8. This is in general a good rule of thumb, although ultimately choosing a higher signal-to-noise cutoff reduces the coverage that I can achieve. Using synthetic shear-waves the relationship between measured splitting parameters and the noise fraction can be probed. I generate a range of synthetic waveforms with splitting parameters of $\phi = -10°$ and $\delta t = 2.0$ seconds, adding random white noise so that the signal-to-noise ratio ranges between 1 and 20 (Fig. 2.2). From this simple test it is clear that the splitting parameter uncertainties, estimated using the corrections to the Silver and Chan (1991) method made by Walsh et al. (2013), decay exponentially as the signal-to-noise ratio increases. To maximise coverage I select to use all data with a signal-to-noise ration greater than 5, slightly less than the recommendations of Restivo and Helffrich (1999) but where the synthetic tests show that reasonable accuracy can be achieved. For the analysis I will do in Chapter 3 this accuracy is sufficient as I can use the quality factor Q to exclude poor measurements and the analysis that I undertake carefully treats the true uncertainty of each measurement. When events with a signal-to-noise ratio ≤ 5 and $-0.5 \leq Q \leq 0.5$ are rejected, this leaves a global dataset of 522 SKS-SKKS event station pairs (i.e., 522 seismograms with clear split or null measurements can be made for both SKS and SKKS with a signal-to-noise ratio greater than 5; Fig. 2.4). For the waveform inversions that I undertake in Chapter 4, using the highest quality data is more important. Therefore for this work I only use data with a signal-to-noise ratio greater than 10, as here the synthetic tests (Fig. 2.2) show highly accurate retrieval of the input splitting parameters.

2.3.2 ScS

I have also downloaded broadband seismic data mirroring a global dataset of ScS observations made by Walpole et al. (2017b). Upper mantle corrections are also required to use ScS phases to study D$''$, correcting for both source and receiver side seismic anisotropy. This requirement for high quality corrections restricts the size of the dataset to 170 ScS phases where high-quality source and receiver corrections are available, these are also taken from Walpole et al. (2017b) (Fig. 2.5). Shear-wave splitting is again measured using SHEBA and the published analysis windows. In this dataset there are 51 ScS phases with a signal-to-noise ratio greater than 10, these waveforms form the dataset used in Chapter 4.

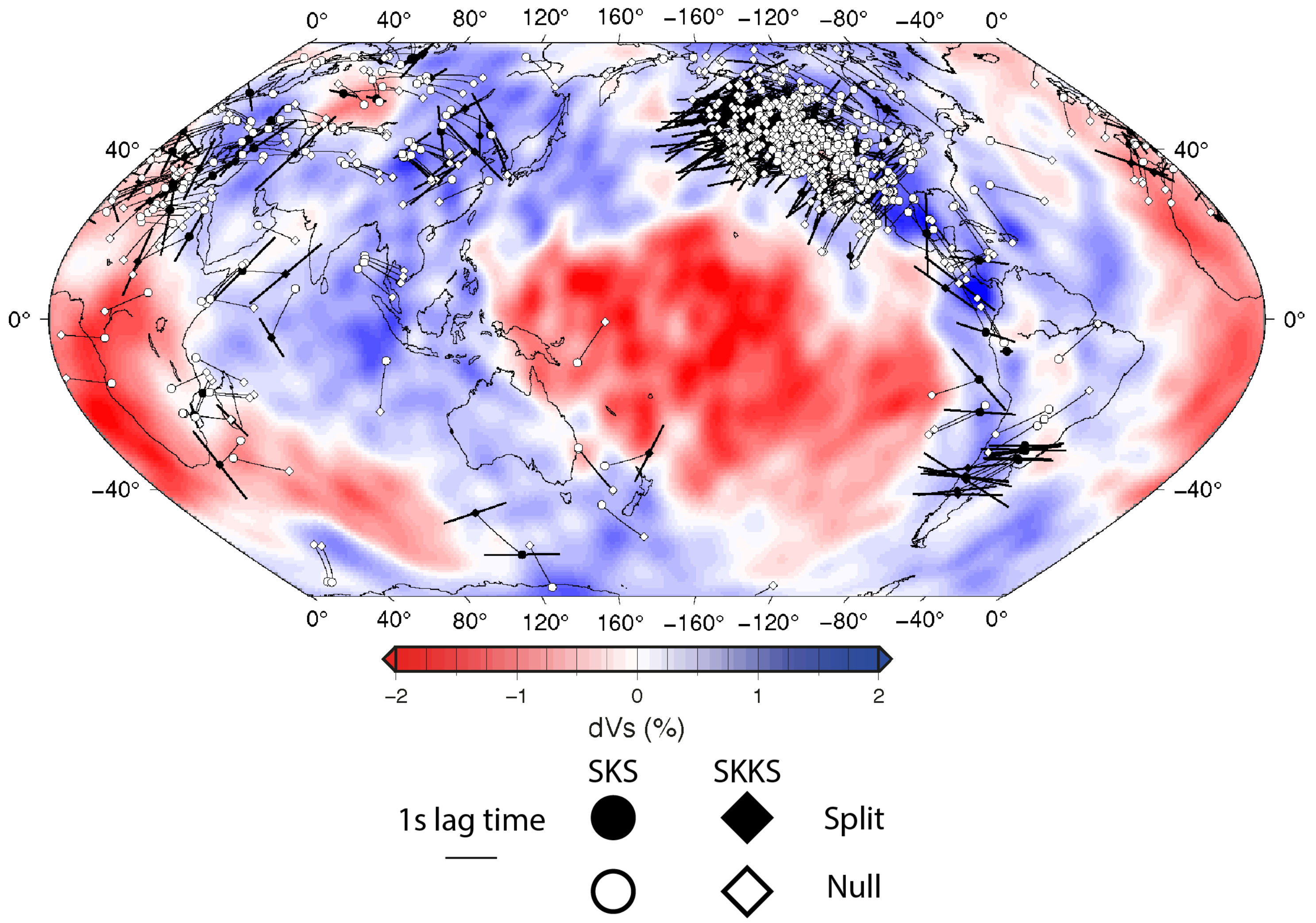

Figure 2.4: Map showing the final global dataset of 522 SKS-SKKS event-station pairs used in this chapter, plotted over the S40RTS tomography model (Ritsema et al., 2011). The SKS (circle) and SKKS (diamond) phases are drawn at the respective upgoing core-mantle boundary piercepoints and the phases that form event-station pairs are indicated by the connecting lines. Phases where shear-wave splitting was measured are coloured in black, whilst null measurements (i.e., phases that do not exhibit shear-wave splitting) are shown in in white. Subsets of this global dataset are analysed in greater detail in Chapter 3, where I develop a new robust method for discrepant shear-wave splitting analysis, and are used in inversions for seismic anisotropy in Chapter 4.

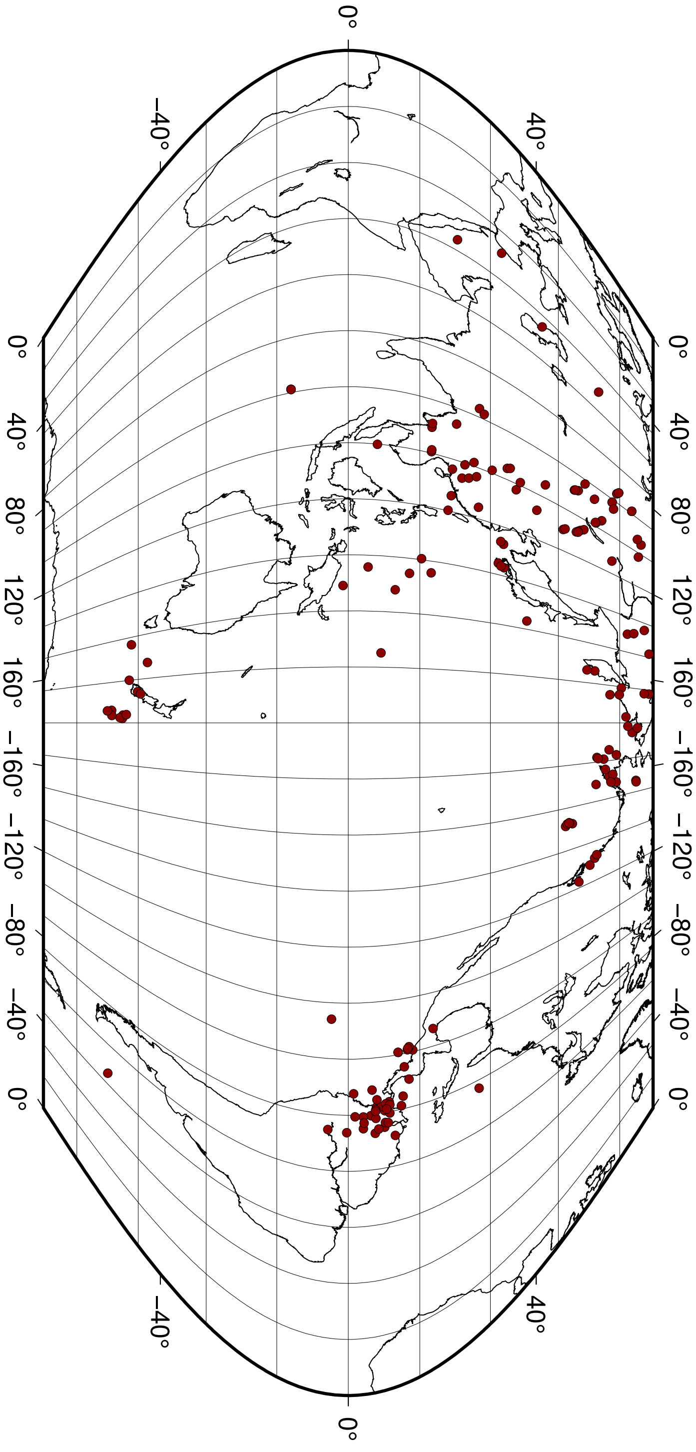

Figure 2.5: Map showing the ScS dataset (which is taken from Walpole et al., 2017b) which I reprocess for use in the inversions of Chapter 4. ScS phases are plotted at their core-mantle boundary bouncepoints. Here I show all 170 phases that I am able to retrieve from IRIS for which Walpole et al. (2017b) were able to derive high quality corrections for upper mantle shear-wave splitting at the source and receiver.

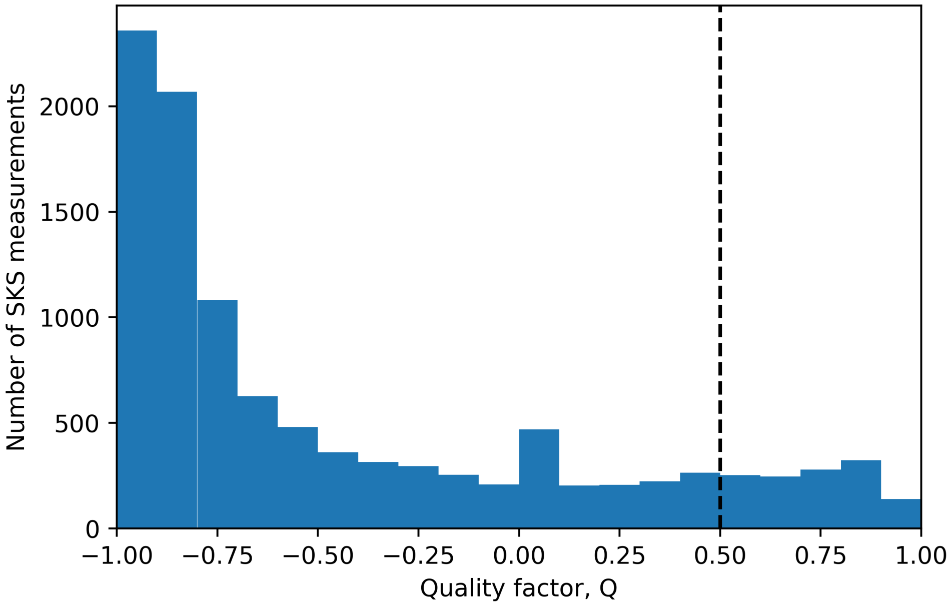

Figure 2.6: Histogram of the measurement quality factor, Q, (Wuestefeld et al., 2010) for all 10656 SKS phases classified as nulls by Walpole et al. (2014) after I have remeasured the shear-wave splitting using broadband data. Using a threshold of $Q \geq 0.5$ to define reasonable split measurements (dashed line) there are 1240 long-period nulls that show shear-wave splitting when remeasured using broadband data.

2.3.3 The impact of broadband data on previously null measurements

The frequency content of waveforms effectively imposes a minimum delay time, δt, for which shear-wave splitting that can be resolved. For the long period data of Walpole et al. (2014), where the upper corner frequency is 0.1Hz, the minimum resolvable δt is ca. 0.5 s. As we might expect, using higher frequency data allows for weaker anisotropy (which generates $\delta t < 0.5$s of shear-wave splitting) to be resolved. This is demonstrated by Walpole et al. (2014) for a select group of 'null stations', where $> 95\%$ of measurements are nulls, which when remeasured using a higher frequency content (with a high cut filter of 0.5Hz) all exhibited shear-wave splitting with $\delta \leq 0.2$s.

Naturally this effect is not limited to 'null stations'. This can be shown by comparing the long-period SKS shear-wave splitting measurements of Walpole et al. (2014) to my broadband measurements. Across the entire dataset there are 10656 SKS phases identified as null measurements by Walpole et al. (2014). When I measure shear-wave splitting for these phases using

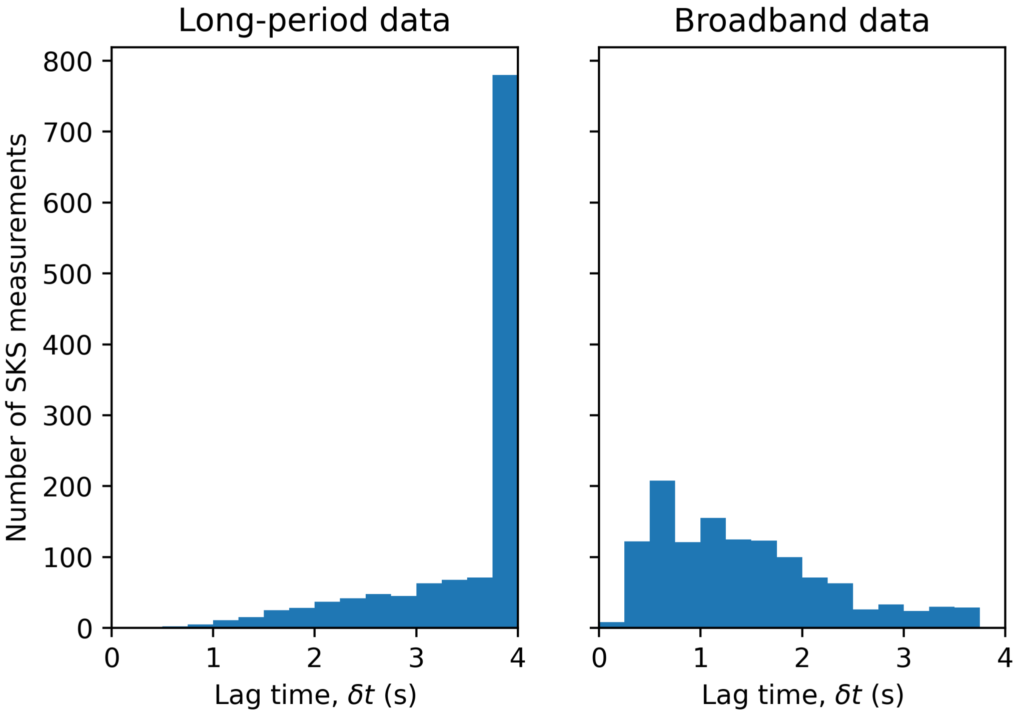

Figure 2.7: Histograms of the measured splitting lag (or delay) times (δt) for the 1240 SKS phases that were measured as nulls by Walpole et al. (2014) using long period data (left) which, when remeasured using broadband data (right), show shear-wave splitting. For null measurements the grid search algorithm used favours the maximum allowed lag time of 4s.

broadband data there are 1240 SKS phases (or ca. 11% of the dataset) where I measure clear shear-wave splitting, with all phases having a quality factor, $Q > 0.5$ (Fig. 2.6). This is also shown if we compare the delay (or lag) times, δt, measured by Walpole et al. (2014) and my remeasured values for this subset of 1240 SKS phases (Fig. 2.7). For the long-period data the trend is as we might expect for null measurements where δt can take any value provided the fast direction, ϕ, is correctly oriented. This gives null measurements a distinctive saddle shaped error surface (Fig. 2.8). In practice, particularly when shear-wave splitting is measured using a grid-search method, δt tends towards the maximum value allowed in the grid search. In contrast for the broadband data (Fig. 2.7) the distribution of the measured δt is more what we would expect for weak shear-wave splitting, with the majority of measurement in the range of 0.25 - 1.75s.

These results serve to highlight that null measurements are strongly controlled by the data used. A null measurement does not necessarily mean there is no seismic anisotropy, but merely that there is no resolvable shear-wave splitting in the input data. Nulls can also occur when the incoming polarisation of a shear-wave is parallel (or nearly parallel) to the fast polarisation direction of an anisotropic medium, or if it propagates through multiple anisotropic layers that are aligned such that the effective splitting cancel out (Silver and Savage, 1994).

2.4 Inspecting the global SKS-SKKS dataset

The final global SKS-SKKS shear-wave splitting dataset contains 522 SKS-SKKS event-station pairs, with most of the dataset (219 event-station pairs) of the data covering the Eastern Pacific region (Fig. 2.4). There are 53 SKS-SKKS event-station pairs where both phase are split ($Q > 0.5$), 382 event-station pairs where both phases are nulls ($Q < -0.5$), 28 event-station pairs have a split SKS and a null SKKS and 59 event-station pairs have a null SKS and a split SKKS.

One interesting observation is that my QA process rejects 134 of the 169 SKS-SKKS pairs studied by Deng et al. (2017). This occurs as only 35 SKS-SKKS pairs have a signal-to-noise ratio greater than 5 for both phases. This serves to highlight the potential pitfall of including higher frequency data as in this case the additional noise introduced causes most of the data to be excluded. However in regions where we have dense networks, such as the USArray for North America, including this higher frequency data could prove to be invaluable when we search for discrepant SKS-SKKS shear-wave splitting.

The size of the final dataset may appear small compared to the initial number of waveforms queried, with only ca. 3.6 % of the 14510 SKS waveforms resulting in a final SKS-SKKS pair. It is however approximately 5 times greater than the global dataset studied by Niu and Perez (2004). It is smaller than Restivo and Helffrich (2006)'s dataset of 1800 SKS and SKKS waveforms, although this comparison is difficult to make as I have excluded all SKS and SKKS phases that show significant source polarisation anomalies whilst Restivo and Helffrich (2006) were testing if polarisation anomalies (which were observed in ca. 5 % of their data) could explain discrepant SKS-SKKS shear-wave splitting. In both of these early global studies found that ca. 5 % of their data showed splitting discrepancies greater than the measurement errors, concluding that azimuthal (i.e., non-VTI) anisotropy is not widespread in D$''$ and exists only as small-scale local features.

Identifying discrepant shear-wave spitting by testing if the measured splitting parameters are within the measurement errors is the most intuitive approach. However it is easy to overlook that these measurement uncertainties, when following the Silver and Chan (1991) method, are

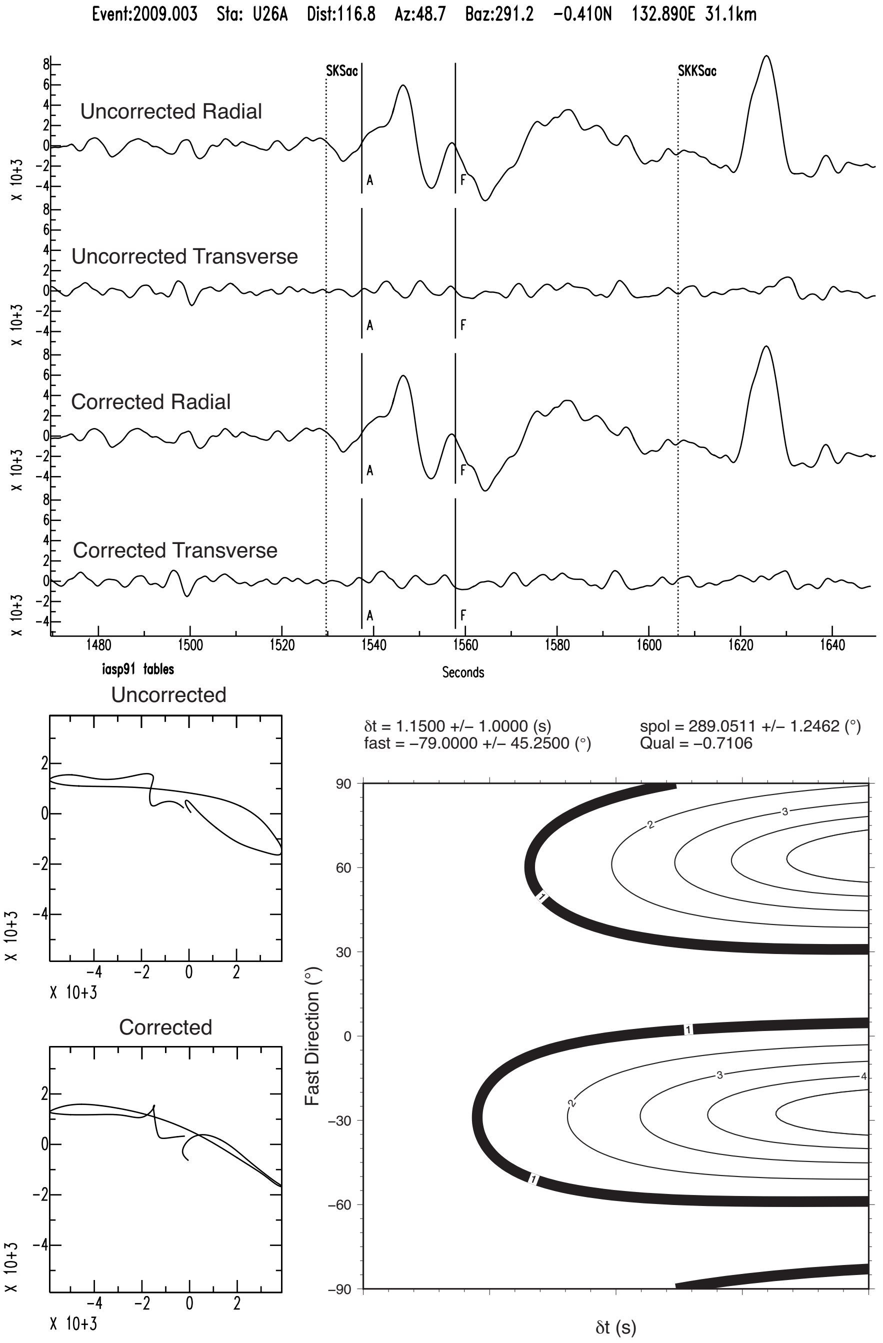

Figure 2.8: A null SKS phase at station U37A as measured by SHEBA. Here I show the uncorrected and corrected traces (top) and particle motions (below left), along with the eigenvalue surface (below right). Note how broad the set of (ϕ,δ) within the 95% confidence region (bold line) is. The linear (or near-linear) particle motion for the uncorrected traces, along with the saddle shaped λ_2/λ_1 misfit surface are characteristic features of a null measurement. In this example SHEBA has chosen $\delta t = 1.15 \pm 1\,\mathrm{s}$, but a common trend throughout the SKS and SKKS datasets is for $\delta t \rightarrow 4\,\mathrm{s}$, see figures 3.2, A.1 for further examples.

determined by approximating the length and width of an F-test derived 95 % confidence surface in the splitting parameters $\phi, \delta t$. There are issues with the approach as the approximation can break down for complex error surfaces (Walsh et al., 2013) and even in simple cases it does not always accurately reflect the true measurement uncertainty (Asplet et al., 2020). In Chapter 3 I shall explore this further and develop a new method to analyse discrepant shear-wave spitting, but for now I will assume that all 53 SKS-SKKS pairs in my dataset where both phases are split are not discrepant.

The 87 SKS-SKKS event-station pairs where one phase is null and the other is split are intriguing. The null measurements imply that there is no observable shear-wave splitting in the upper mantle for that event-station pair's backazimuth. There is no way to interpret these phases, disregarding possible finite frequency effects, that does not require some change in anisotropy in the lower mantle where the raypaths of the two phases diverge. Either the null phase is sampling no shear-wave splitting along its entire raypath, whilst the split phases encounters seismic anisotropy in D$''$, or the null phase encounters different seismic anisotropy to the split phase such that the effective splitting (combining the contributing of D$''$ and the upper mantle) results in a null measurement. Therefore it is clear that these pairs can be interpreted as exhibiting discrepant shear-wave splitting.

Even when assuming that all 53 SKS-SKKS pairs where both phases are split are not discrepant ca. 17 % of my global dataset shows discrepant shear-wave splitting. This is significantly higher that the previous global studies of Niu and Perez (2004) and Restivo and Helffrich (2006) and is more consistent with regional studies targeting a region of D$''$ that is expected to be anisotropic (e.g., Lynner and Long, 2014). It is worth noting, however, that data sampling the Eastern Pacific (219 pairs or ca. 42 % of the dataset), a region where discrepant SKS-SKKS shear-wave splitting has been observed before (Long, 2009), is likely biasing this global estimate. This regionality in the dataset limits what global conclusions can be drawn. These results, along with an increasing number of regional-scale shear-wave splitting studies (e.g., Ford et al., 2015; Deng et al., 2017; Grund and Ritter, 2018; Reiss et al., 2019, see Chapter 1 for a review), are challenging the view that azimuthal anisotropy is not widespread in D$''$. Reflecting this regional approach I will briefly overview the three main regions covered by my dataset, the Eastern Pacific, Northern Africa and East Asia.

Eastern Pacific

The majority of my dataset (219 SKS-SKKS pairs) samples the Eastern Pacific region (Fig. 2.9). The SKS-SKKS data primarily covers a fast shear-wave velocity anomaly and the backazimuthal coverage is restricted to ca. $260° - 290°$ (Fig. 2.9). As fast shear-wave velocity anomalies are typically associated with colder than average regions of D'' where we would expect post-perovskite to be stable and, therefore, to be able to observe D'' seismic anisotropy. A previous SKS-SKKS shear-wave splitting study did observe some discrepancies, which they attribute to lattice-preferred orientation (LPO) of post-perovskite (Long, 2009). There is some suggestion of this here, where there is a strong trend of 18 null-split pairs (i.e., SKS-SKKS pairs where one phase is split and the other is a null) occurring at longitudes of ca. $-130° - -120°$. For these pairs the nulls are predominately in the SKS phases with the SKKS phases sampling the fast shear-wave velocity to the East.

If we compare our shear-wave splitting results to a mantle flow model for D'', TX2008.V2 (Simmons et al., 2009), it is difficult to identify any clear trend. The measured fast directions do not align with the predicted horizontal velocity directions and there is no obvious difference in the data that samples upwelling or downwelling regions (Fig. 2.10). This can be explained, for SKS-SKKS pairs where both phases are split, by shear-wave splitting from the upper mantle which masks the signal from D''. This is a limitation of studying SKS-SKKS shear-wave splitting discrepancies as even where discrepancies can be identified, resolving the signal from D'' is challenging.

North Africa and Eurasia

This region is the second most densely covered, with 73 SKS-SKKS pairs stretching from Northern Africa to the 'Perm' anomaly in Central Eurasia (Fig. 2.11). North Africa has proved a popular region to study in recent years, with several studies taking advantage of temporary networks to probe the region in detail (Lynner and Long, 2014; Ford et al., 2015; Reiss et al., 2019, see Fig. 1.11). The Perm anomaly, which I only sample with 10 SKS-SKKS pairs, has also seen recent studies of SKS-SKKS shear-wave splitting where D'' anisotropy was inferred (Long and Lynner, 2015).

Owing to the limited size of the dataset in this region, a detailed comparison with previous work is unfeasible. When I focus in on Northern Africa, where the majority of the SKS-SKKS pairs

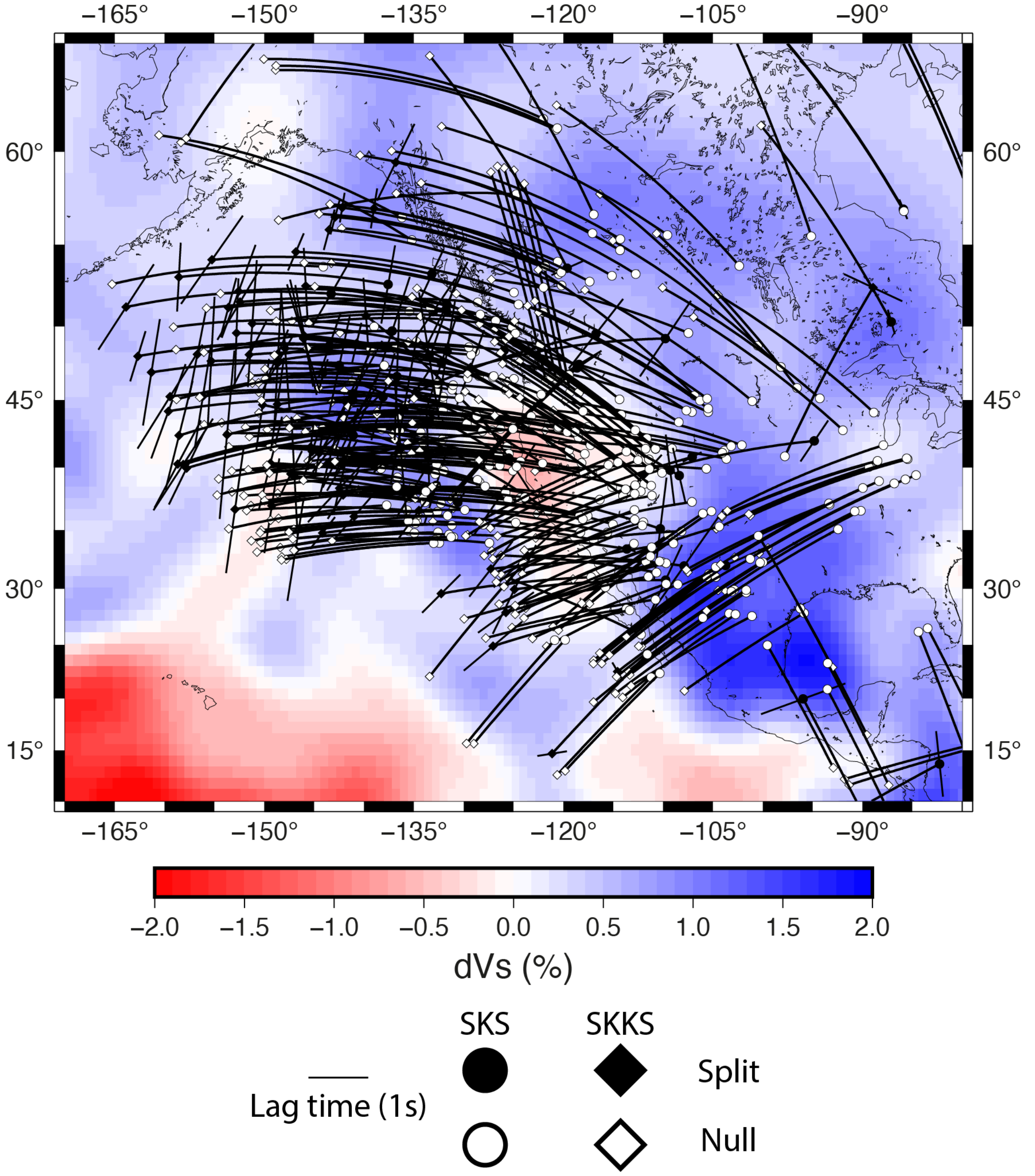

Figure 2.9: The 522 SKS-SKKS event-station pairs observed in the Eastern Pacific region. SKS (circle) and SKKS (diamond) are drawn at the upgoing core-mantle boundary piercepoint, calculated using TauP (Crotwell et al., 1999), with event-station pairs indicated by connecting great circle paths. Split phases are coloured in black, with the measured splitting parameters represented by the orientation (ϕ) and length (δt) of the black bars. Null measurements are coloured white. The data is plotted over the S40RTS tomography model at a depth of 2800km (Ritsema et al., 2011).

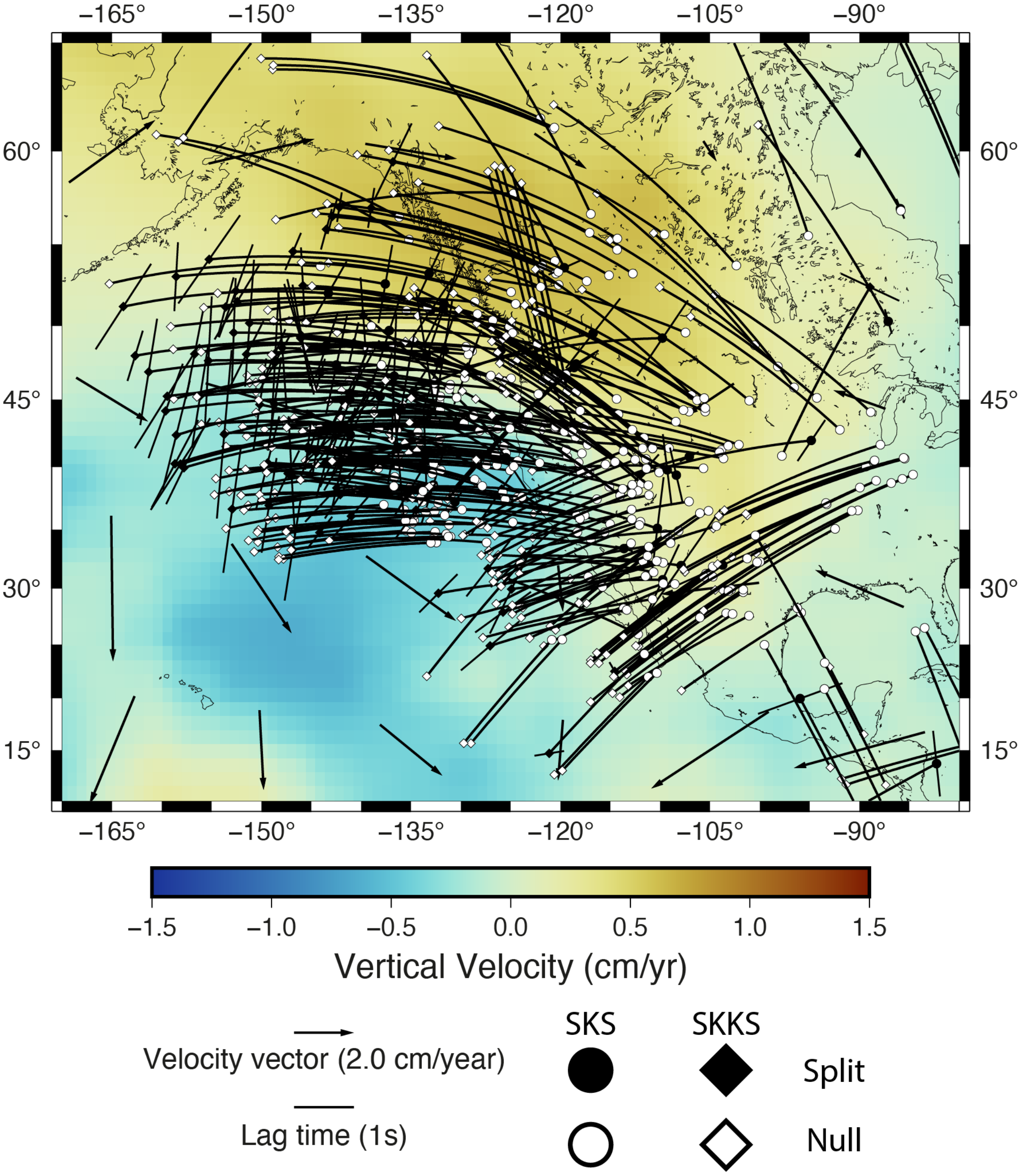

Figure 2.10: The 522 SKS-SKKS event stations pairs observed in the Eastern pacific, overlain on the TX2008.V2 mantle flow model (Simmons et al., 2009) at a depth of 2685 km. SKS and SKKS shear-wave splitting is plotted as in figure 2.9.

in the region is concentrated, there is some agreement with observations of Reiss et al. (2019) who observed significant SKS-SKKS splitting intensity discrepancies (which were primarily due to null-split pairs) only in data with backazimuths ranging from $225° - 270°$. I observe 5 null-split SKS-SKKS pairs beneath North Africa in that backazimuth range, but the majority of data is pairs of null measurements. Observations of azimuthal anisotropy is this region have been concentrated along the margin of the African LLSVP, with interpretations invoking LPO of post-perovskite in the colder portion of D$''$ outside of the LLSVP with weak or no anisotropy within the LLSVP (Lynner and Long, 2014; Reiss et al., 2019). I do not have enough data to strongly support or refute this hypothesis, but it is curious that of the 5 null-split pairs that I observe near the margin of the African LLSVP there are cases of pairs with a null SKS and split SKKS, where the SKKS phase is further from the LLSVP margin, the opposite of what Reiss et al. (2019) observed, where nearly all the null-split pairs had a split SKS and null SKKS. Comparing my observations to the mantle flow model TX2008.V2 (Fig. 2.12) again shows the difficulty in relating shear-wave splitting parameters to lowermost mantle flow. More detailed analysis, accounting for different potential mechanisms for D$''$ seismic anisotropy is required.

East Asia

This region is only covered by 38 SKS-SKKS event-station pairs (Fig. 2.13). There are limitations in both spatial and backazimuthal coverage, where nearly all pairs have a backazimuth in the range of $72° - 108°$. As this region sits between the Perm anomaly and Pacific LLSVP, if D$''$ seismic anisotropy is concentrated near the margins of low shear-wave velocity anomalies we would expect to observe D$''$ seismic anisotropy here. There is some suggestion of this in my data, with 5 null-split pairs observed beneath central China and Mongolia. It is not clear what is causing this discrepancy between SKS and SKKS in this region, comparing the data to S40RTS (Fig. 2.13) and TX2008.V2 (Fig. 2.14) does not show anything to explain these null-split pairs. In this case all 5 null-split pairs have a null SKS and split SKKS phase, so the difference in inclination in D$''$ (ca. 20°) could be causing the SKKS to sample anisotropy that SKS does not, but this is not a particularly satisfying explanation.

This region is promising for future studies of SKS-SKKS shear-wave splitting, particularly given the increasing instrumentation of mainland China. There are promising datasets of SKS and SKKS shear-wave splitting, although thus far authors have focused on studying upper mantle

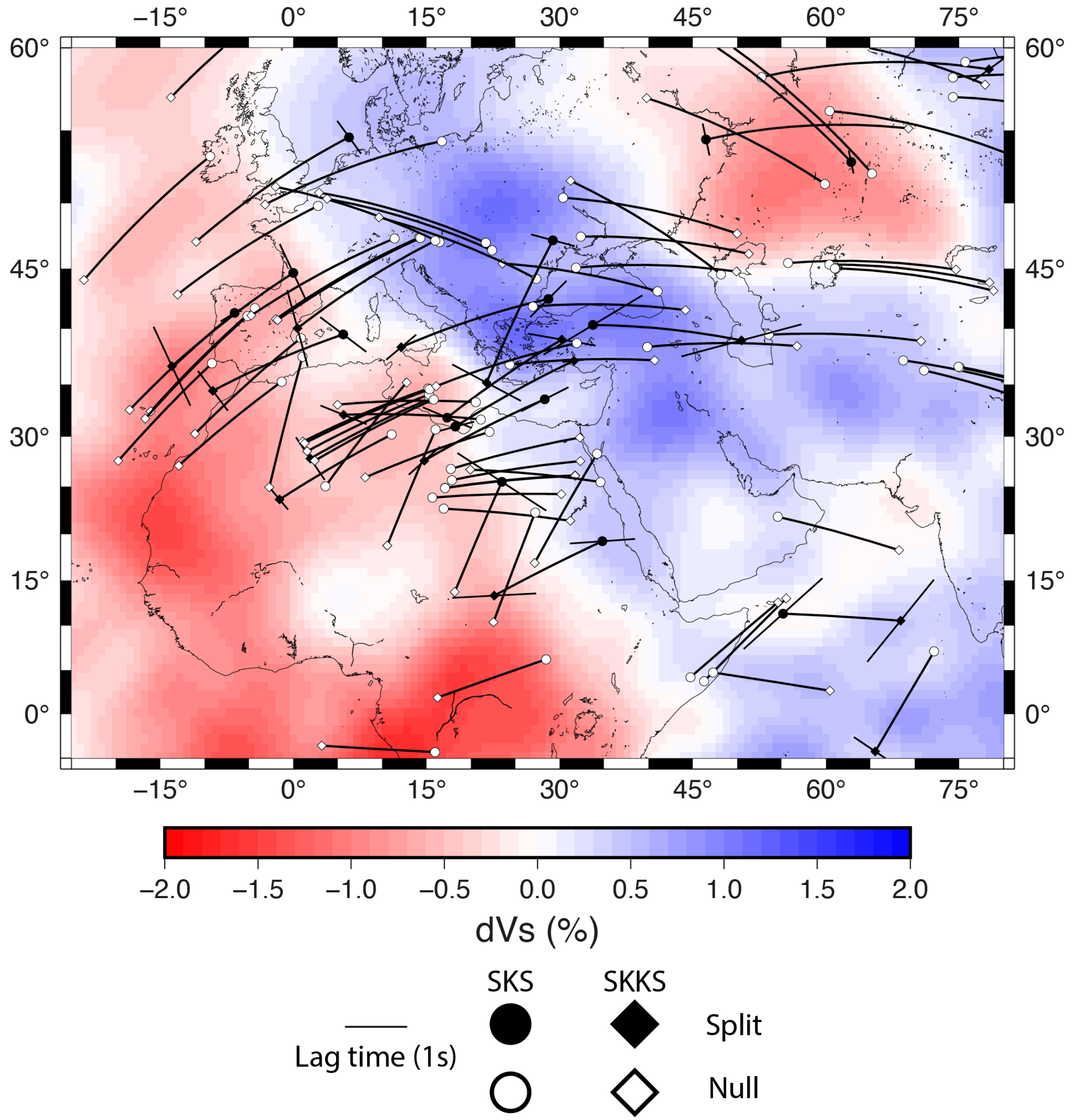

Figure 2.11: The 73 SKS-SKKS event stations pairs observed beneath Northern Africa and Eurasia, overlain on the S40RTS tomography model (Ritsema et al., 2011) at a depth of 2800 km. SKS and SKKS shear-wave splitting is plotted as in figure 2.9.

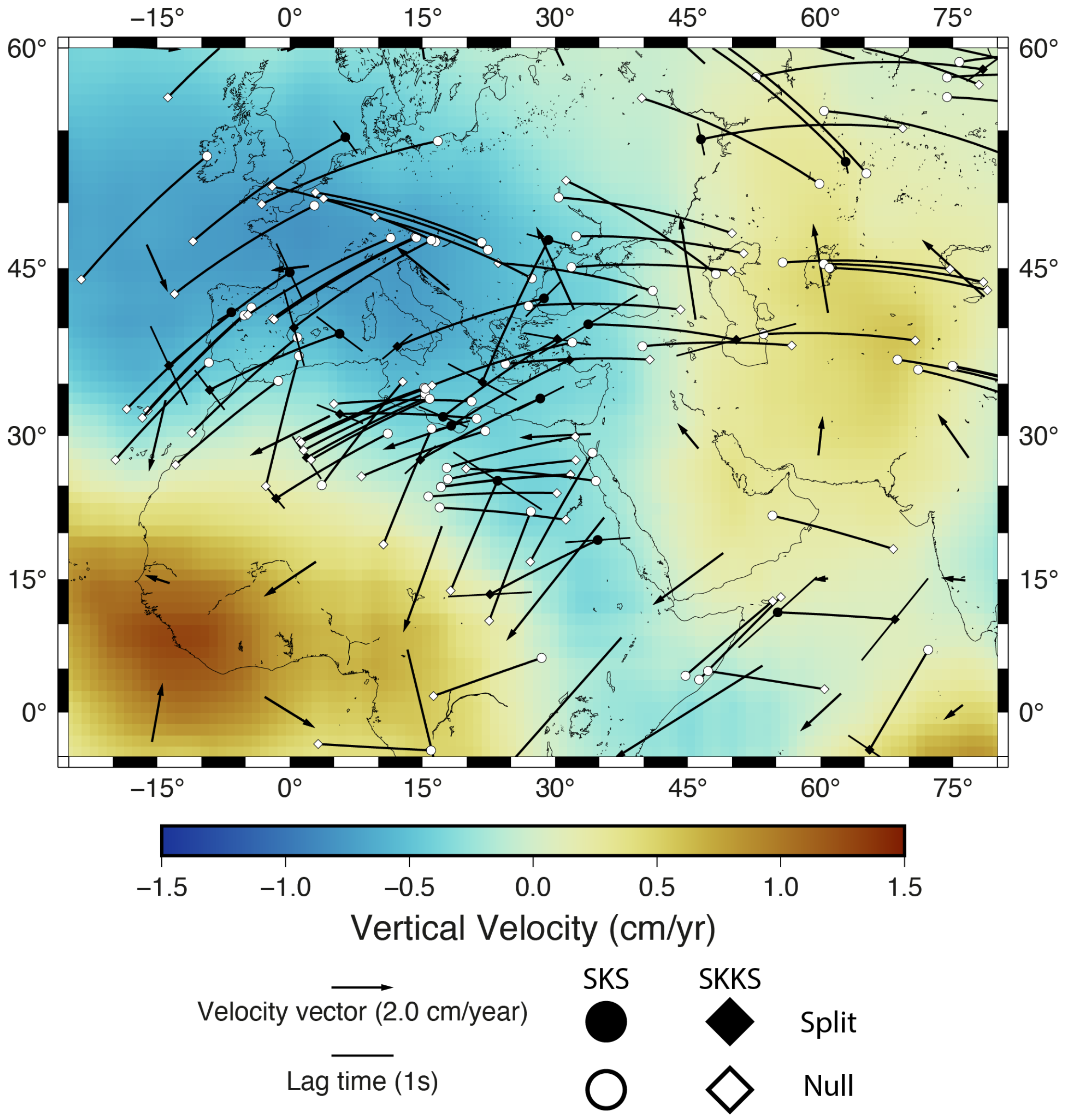

Figure 2.12: The 73 SKS-SKKS event stations pairs observed beneath Northern Africa and Eurasia, overlain on the TX2008.V2 mantle flow model (Simmons et al., 2009) at a depth of 2685 km. SKS and SKKS shear-wave splitting is plotted as in figure 2.9.

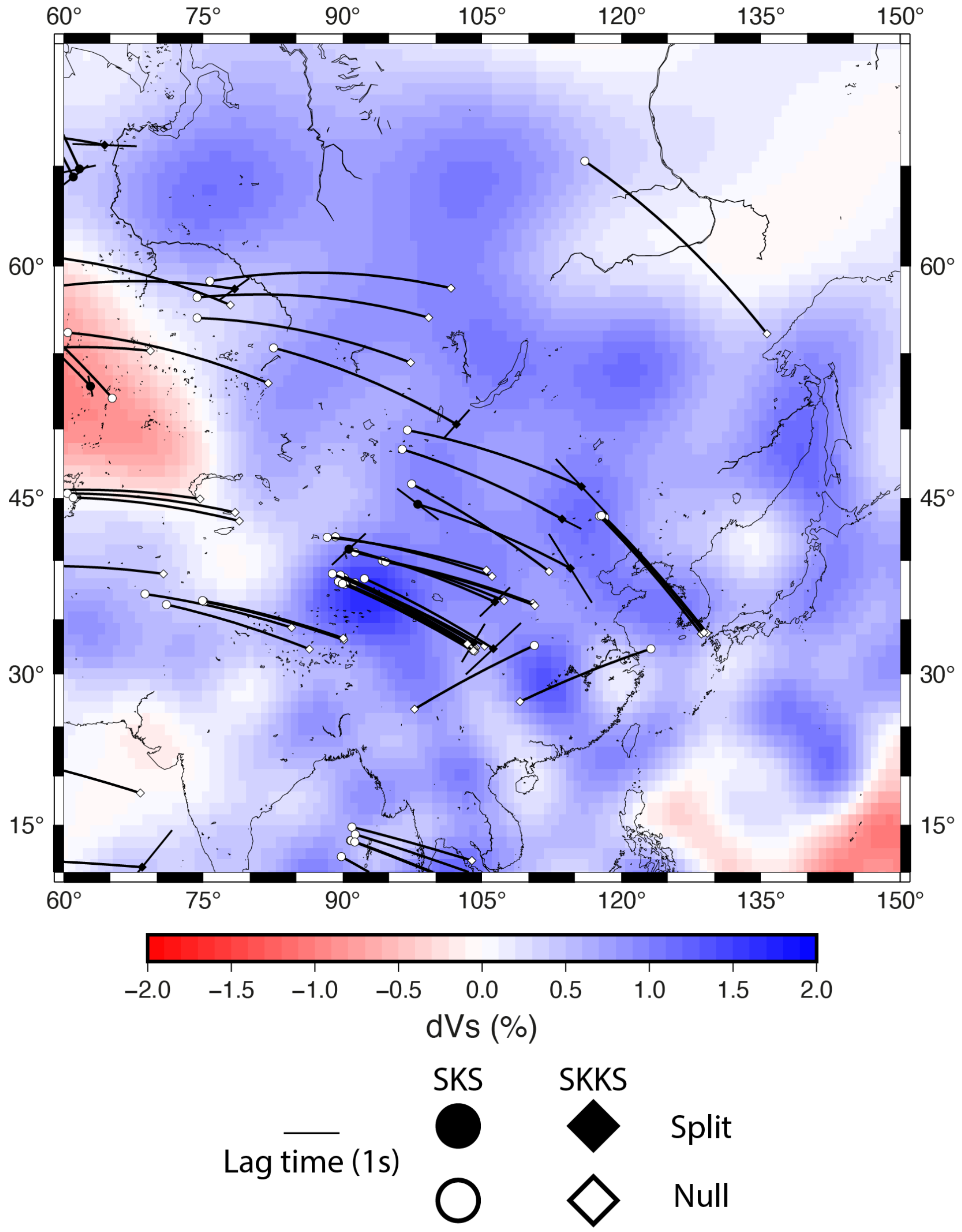

Figure 2.13: The 38 SKS-SKKS event stations pairs observed beneath East Asia, overlain on the S40RTS tomography model (Ritsema et al., 2011) at a depth of 2685 km. SKS and SKKS shear-wave splitting is plotted as in figure 2.9.

seismic anisotropy (e.g., Wu et al., 2015; Yang et al., 2019).

2.4.1 Data coverage constraints

As I have shown the coverage that I am able to achieve with my dataset of SKS-SKKS event-station pairs is reasonable, but only the Eastern Pacific region contains enough data for detailed

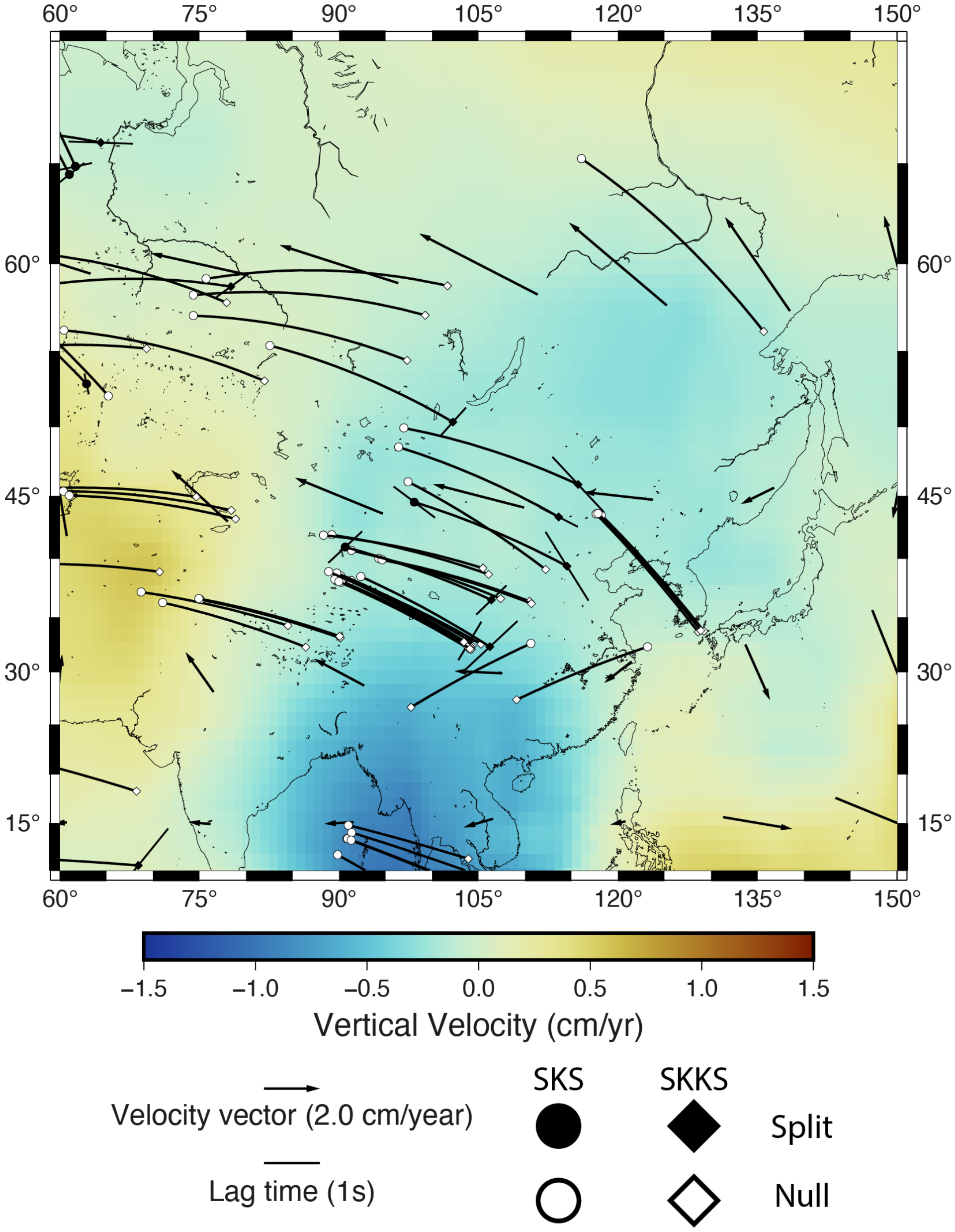

Figure 2.14: The 38 SKS-SKKS event stations pairs observed beneath East Asia, overlain on the TX2008.V2 mantle flow model (Simmons et al., 2009) at a depth of 2685 km. SKS and SKKS shear-wave splitting is plotted as in figure 2.9.

shear-wave splitting analysis. As discrepant splitting analysis benefits greatly from dense coverage and also because this region allows me to study a large continuous region of D$''$ that is adjacent to the Pacific LLSVP, this is where I will concentrate my studies in the following chapters. Previous work in the Eastern Pacific studying SKS-SKKS shear-wave splitting (Long, 2009) and in the Central Americas using S-ScS (Nowacki et al., 2010) have highlighted regions of azimuthal seismic anisotropy. This makes the Eastern Pacific an ideal region to develop and test new methods for probing D$''$ seismic anisotropy.

These coverage constraints also apply to my design for Chapter 4. The aim of this chapter is to jointly use ScS, SKS and SKKS data to better constrain D$''$ seismic anisotropy, therefore my study region needs to have all 3 phases overlapping. Additionally I want to only use the highest quality waveforms, which I define as having a signal-to-noise ratio greater than 10, to improve the stability of the inversion method that I develop. Losing the requirement to have SKS-SKKS pairs does greatly increase the number of SKS phases available, however the lack of widespread ScS coverage restricts potential study regions (Fig. 2.15). Ultimately I choose to continue studying D$''$ beneath the East Pacific as there is overlap between all three phases (Fig. 2.16) and using this region again allows me to test the results of Chapter 3.

2.5 Relating splitting parameters to splitting intensity

Using the global datasets I investigate the accuracy with which splitting intensity measurement can be related to splitting parameters. The motivation for this is to validate measurements made by SHEBA, which was initially approximating splitting intensity for each waveform using equation 2.14. One initial observation I made when measuring SKS-SKKS shear-wave splitting is that null measurements are poorly treated by the sinusoidal approximation (Asplet et al., 2020). This occurs as EV measurements of the splitting parameters for nulls effectively allow any δt provided the fast direction is correct, giving the distinctive saddle shape of grid search misfit surface for a null measurement. In the SHEBA grid searches it is quite common to see $\delta t \rightarrow 4.0$ for these nulls, which then results in incorrect estimates of large splitting intensities where null measurements should have a splitting intensity around 0. To investigate this behaviour and to test the accuracy of the approximation, routines for measuring splitting intensity by projection (2.13) were added to SHEBA and I re-processed my data using the same analysis windows. I also generate a set of 5658 synthetic shear-waves that are evenly spaced over the

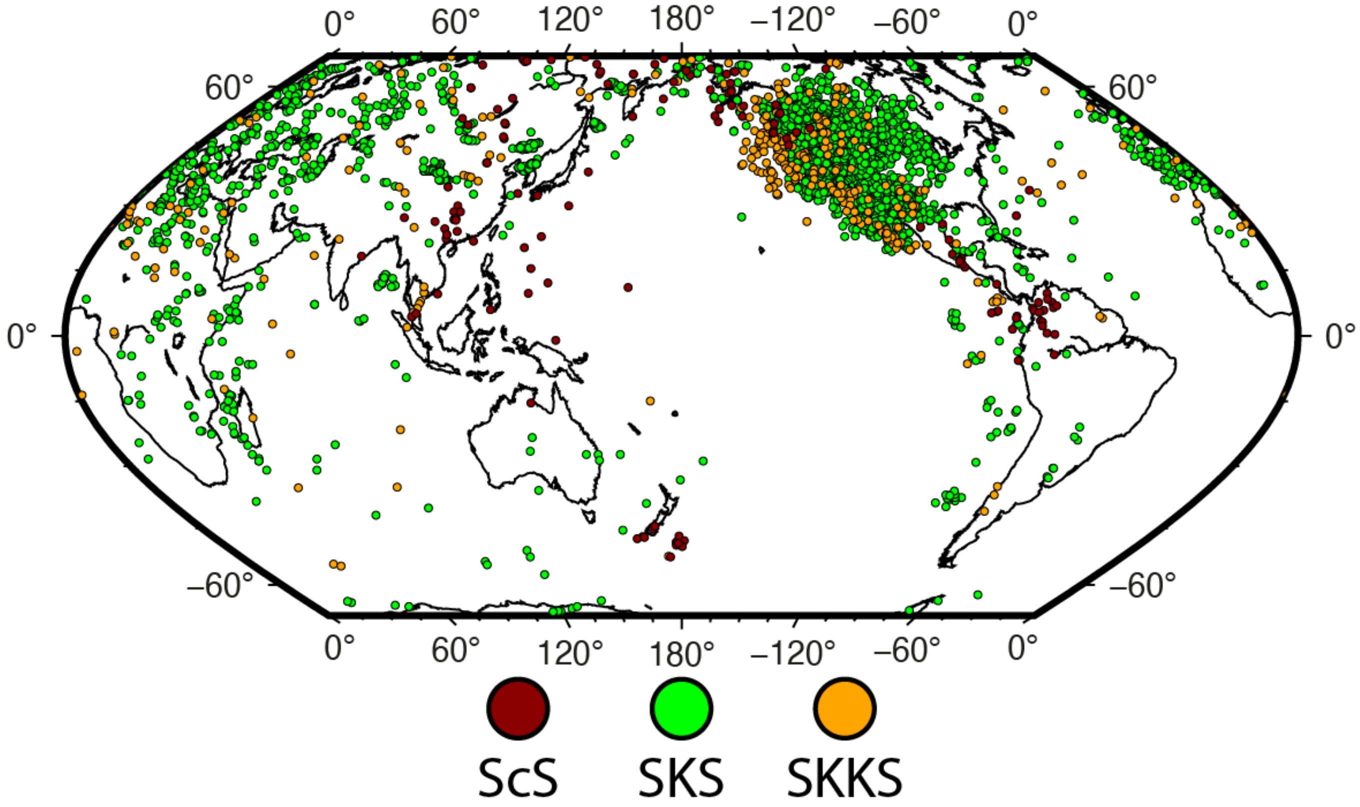

Figure 2.15: Global ScS (red), SKS (green) and SKKS (orange) data which has a signal-to-noise ratio greater than 10. ScS phases are plotted at their core-mantle boundary bouncepoint. SKS and SKKS phases are plotted at their up-going core-mantle boundary piercepoint. Bouncepoints and piercepoints are calculated using the TauP toolkit (Crotwell et al., 1999).

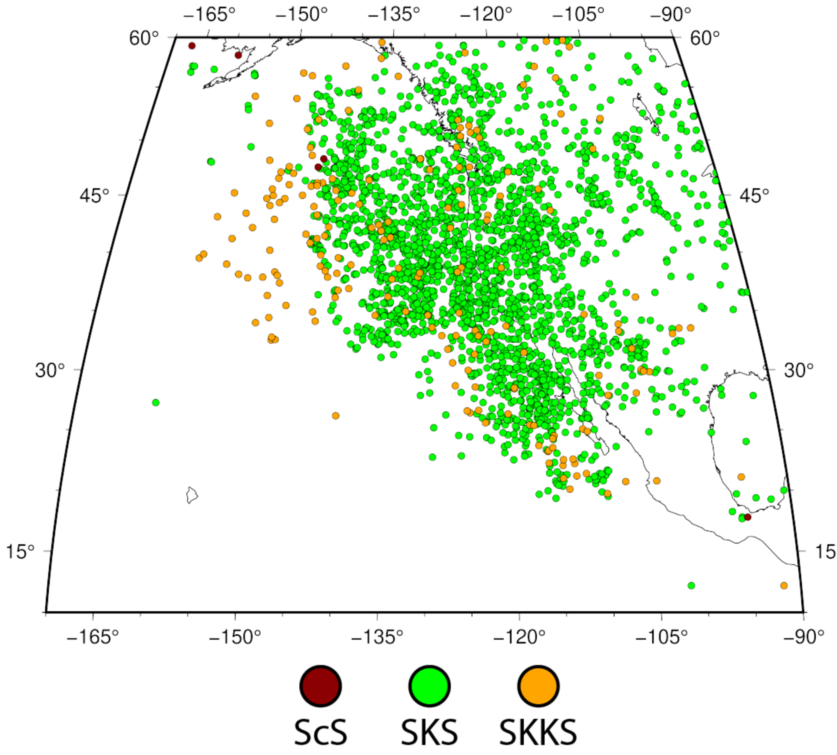

Figure 2.16: Shear-wave waveform data in the East Pacific region that has a signal-to-noise ratio greater than 10. ScS (red) phases are plotted at their core-mantle boundary bouncepoint. SKS (green) and SKKS (orange) phases are plotted at their up-going core-mantle boundary piercepoint. Bouncepoints and piercepoints are calculated using the TauP toolkit (Crotwell et al., 1999).

grid search range of $-90° \leq \phi \leq 90°$ and $0 \leq \delta t \leq 4$ and for source polarisation of 30°, 45° and 60°. These synthetics are simple wavelets calculated by taking the first-order derivative of a gaussian function and sampling at an appropriate rate to ensure a dominant frequency of 0.1 Hz. All synthetics used in this thesis are generate with this dominant frequency unless specified otherwise. If the approximation is accurate then I would expect both methods to return the same splitting intensity, particularly for split waveforms.

Comparing splitting intensities estimated from the splitting parameters (or measured ‘by approximation’) and measurements made by the projection method show some intriguing results (Fig. 2.17). For null measurements, the results are as I would expect. For SKS, SKKS, ScS and the synthetics null measurements (defined as measurements where $Q \leq -0.5$) made by projection are correctly returned with splitting intensities near 0, whilst measurements made by approximation are scattered over a large range of splitting intensities (Fig. 2.17). What is more curious is the pattern shown by split measurements (defined as measurements where $Q \geq 0.5$). This bowtie pattern is most clearly traced out by the synthetics, as they fully cover the range of splitting parameters, but it can also be clearly seen for the real SKS, SKKS and ScS measurements (Fig. 2.17).

We can further probe this by comparing the measured splitting intensity to measured splitting parameters ($\phi,\delta t$) for the synthetic data (Fig. 2.18). If splitting intensity can be described by the equation 3.10, then we would not expect the absolute value of the intensity to exceed the measure delay time. When measurements of splitting intensity made by projection are compared to measured delay time (Fig. 2.18) it appears that for delay times, $\delta t > 1.5 s$, the relationship starts to break down and over-estimate splitting intensity. This is perhaps not too surprising as for the synthetics a delay time of 1.5 s is not insignificant when compared to the dominant period of 10 s. For larger delay times, $\delta t > 2.75 s$, the projection method begins to substantially underestimate splitting intensity. As delay time as a fraction of the dominant period increases the radial component seismogram becomes increasingly distorted and we can no longer make the approximations in equations 2.10 and 2.11.

These observed discrepancies between approximated and projected splitting intensity also suggest that the approximation relation between splitting parameters and splitting intensity (equation 2.14) is not reliable for a single event. On the basis of these results I only use splitting intensity measurement made using the projection method, which is now fully implemented in SHEBA. The splitting intensity approximation should only be used for multichannel analysis at a single station, as in Chevrot (2000), it should not be used as a workaround to add splitting intensity measurements to existing codes that measure splitting parameters. This result also shows that it is unsafe to revisit catalogues of existing splitting parameters using the splitting intensity approximation. If we want to re-analyse past work using splitting intensity we would have to return to the waveform data. It is also clear that the dominant period of the data used is crucial, with current methods for measuring splitting intensity breaking down from approximately $\delta t/T > 0.15$. This may not be an issue when revisiting old long period record, but for teleseismic SKS and SKKS recorded by broadband seismometers splitting intensity measurements, where the measured delay time is greater than ca. 1.5 - 2 s, should be considered to be potentially unreliable. It may be possible to remedy this issue and to redefine splitting intensity where it is not limited by the assumption that $\delta t << T$. This, however, is a subject for future work.

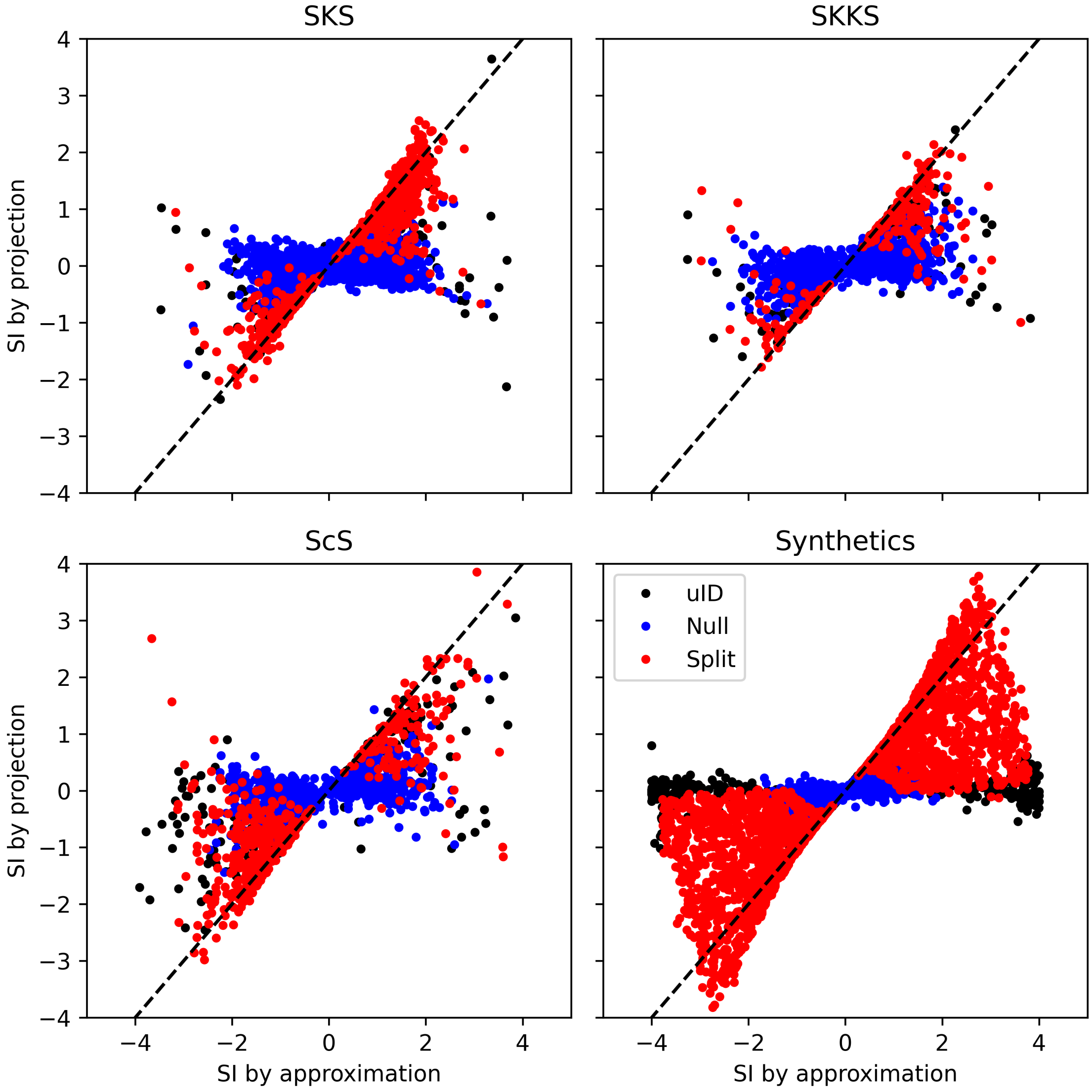

Figure 2.17: A comparison of two methods for measuring splitting intensity. The first is estimating splitting intensity from measured splitting parameters (or 'by approximation' using equation 2.14) and measuring splitting intensity by projection (using equation. 2.13). Measured splitting intensities are compared for globally collected datasets of SKS, SKKS and ScS phases and also for a set of simple synthetic shear-waves. Only waveforms with a signal-to-noise ratio greater than 5 are shown, corresponding to 8046 SKS, 1747 SKKS, 1502 ScS and 5658 synthetic shear-waves. Clearly split data (where $Q \geq 0.5$) is shown in red, null data (where $Q \leq -0.5$) in blue and unclassified data (where $-0.5 < Q < 0.5$) in black. If the approximation and projection methods for measuring splitting intensity agree we would expect the data to broadly lie on along the dashed line ($y = x$).

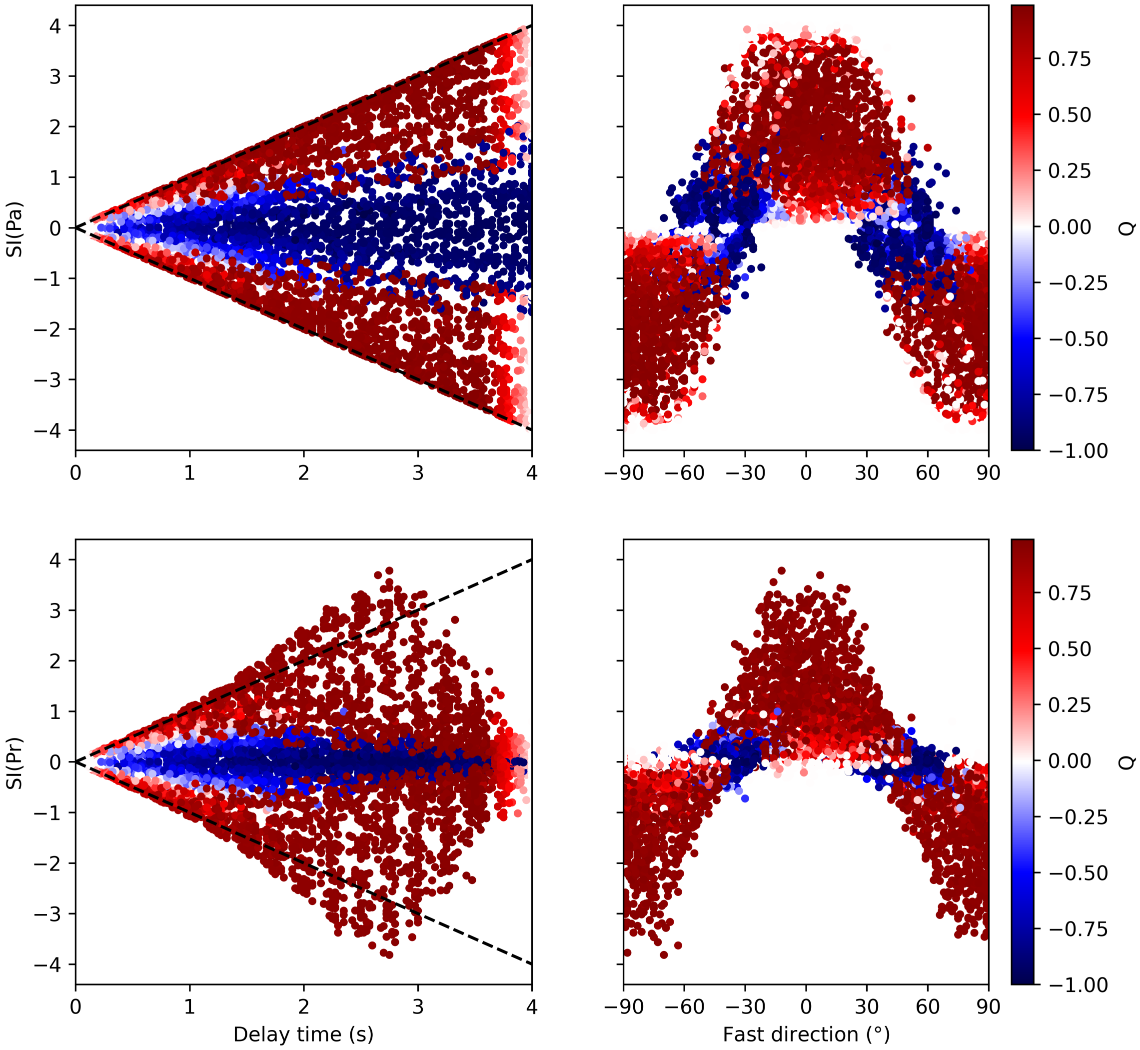

Figure 2.18: A comparison of splitting intensity and measured splitting parameters ($\phi, \delta t$) for synthetic shear-waves (which have a dominant frequency of 0.1 Hz). The top row shows splitting intensity measured 'by approximation' (using equation 2.14) and the bottom row shows splitting intensity measured by projection (using equation 2.13). Points are coloured by the splitting measurement quality factor Q.

2.6 Summary

In this chapter I have outlined the collection of a new broadband dataset of SKS-SKKS event-station pairs, derived from previous global dataset of SKS shear-wave splitting measurements. By using broadand data I was able to measure shear-wave splitting for 1240 SKS phases that were previously classified as null. The final dataset of 522 SKS-SKKS event-station pairs will form the backbone of the analysis done throughout this thesis.

In preliminary analysis of the data I find that at least 17 % of the SKS-SKKS event-station pairs show discrepant shear-wave splitting. This is a significant increase compared to previous analysis of global datasets, where ca. 5 % of the data was discrepant (Niu and Perez, 2004; Restivo and Helffrich, 2006). The majority of my data covers three regions: the Eastern Pacific (219 pairs), North Africa and Eurasia (73 pairs) and East Asia (38 pairs). Preliminary analysis of these regions is limited, highlighting potential seismic anisotropy near the margins of the Pacific and African LLSVPs. Comparing the shear-wave splitting result to the TX2008.V2 flow model (Simmons et al., 2009) demonstrates the need for a framework to relate our observations of shear-wave splitting to mantle flow models as we cannot straightforwardly compare fast directions to predicted flow.

Using my full global dataset I investigated observed discrepancies between estimates of splitting intensity from measured splitting parameters and direct measurements of splitting intensity. Systematic discrepancies between the two methods for measuring splitting intensity suggest that approximating splitting intensity from measured splitting parameters is not reliable and therefore SHEBA has been modified to measure splitting intensity by projection.

The coverage that I am able to achieve with my SKS-SKKS dataset informs the design of my research. As the dataset provides the densest coverage in D$''$ beneath the Eastern Pacific region, I chose to study this region in detail. In Chapter 3 I search for discrepant SKS-SKKS shear-wave splitting, using this new dataset to test and expand upon earlier work (Long, 2009). The limited overlap between the high quality measurements in my SKS-SKKS dataset and a previously collected ScS dataset (Walpole et al., 2017b) also strongly affects the design of the work I have undertaken in Chapter 4, where I will focus on a subregion in the Eastern Pacific.

Chapter 3

DISCREPANT SKS-SKKS SHEAR-WAVE SPLITTING IN THE EASTERN PACIFIC

This chapter was done in collaboration with my supervisors, James Wookey and Michael Kendall. The contents of this chapter is published as Asplet et al. (2020). Some material is repeated from sections 2.2 and 2.4.

3.1 Introduction

The lowermost $200\,km$ of the Earth's mantle, known as D$''$, is an important thermochemical boundary layer within the Earth, acting as a buffer between the liquid iron outer core and the solid silicate mantle. D$''$ is distinguished in some places from the lower mantle by a sharp vertical seismic discontinuity at the top of the layer (e.g., Lay and Helmberger, 1983; Sidorin et al., 1999). Seismology is our primary source of information on this region of the Earth and it reveals a heterogeneous, anisotropic layer full of complexities which we do not fully understand (for example see reviews by Garnero et al., 2016; Romanowicz and Wenk, 2017).

Among these complexities are the dynamics of the lower mantle, and how they relate to the upper mantle and surface. For example, we know from seismic tomography that D$''$ is dominated by two large antipodal regions, beneath Africa and the Pacific, with anomalously low shear-wave velocities (e.g., Ritsema et al., 2011; French and Romanowicz, 2014; Auer et al., 2014; Moulik and

Ekström, 2016). These large low shear-wave velocity provinces (LLSVPs) are widely considered to have crucial implications for the dynamics of the entire mantle. Despite advances in our understanding of LLSVP morphology (e.g., Cottaar and Lekic, 2016) the dynamics of LLSVPs and their relationship with deep mantle convection is still an open question (e.g., Davies et al., 2012a; Garnero et al., 2016).

Seismic anisotropy is an indicator of long-range order in materials and in the upper mantle, it is known to develop as a response to plastic flow (e.g., Tommasi et al., 2000). In D'', seismic anisotropy has been attributed to several mechanisms. Lattice preferred orientation (LPO) of post-perovskite (pPv), a high pressure polymorph of bridgmanite (Br) that is stable at D'' pressures (Murakami et al., 2004; Tateno et al., 2009), is an oft-invoked explanation (e.g., Wookey and Kendall, 2007). However there are outstanding questions surrounding the stability of pPv within D''. Due to the positive Clapeyron slope of the Br-pPv transition, pPv is most likely to be abundant in colder than average regions of D'' and non-existent in hot regions of D'' (Wookey et al., 2005b). There is also the possibility of the steep geotherm near the core-mantle boundary causing a second crossing of the Clapeyron slope, resulting in lenses of post-perovskite in D'' bounded by bridgmanite (Wookey et al., 2005b; Hernlund et al., 2005).

LPO of post-perovskite is not the sole candidate mechanism for D'' anisotropy. Other minerals, such as bridgmanite, periclase or ferropericlase, are also capable of producing LPO anisotropy (e.g., Cordier et al., 2004; Marquardt et al., 2018). Alternatively, there are suggestions that D'' anisotropy occurs due to some shape preferred orientation (SPO) of heterogenieties, such as partial melt inclusions smaller than the seismic wavelength (e.g., Kendall and Silver, 1998; Kendall, 2000). Consequentially, improving our observational constraints of D'' anisotropy allows us to improve our knowledge of D'' dynamics, composition and temperature conditions.

Shear-wave splitting (or seismic birefringence) is a phenomena that arises as a response to seismic anisotropy (Crampin, 1985). When a shear-wave enters an anisotropic medium, the energy of the incident shear-wave is split into two orthogonally polarised quasi shear-waves. One wave (the fast shear-wave) is polarised in the direction of the fastest shear velocity, causing the quasi shear-waves to be separated by a delay time which persists beyond the causative anisotropic region. Shear-wave splitting is typically characterised by this delay time, δt, and the polarisation of the fast wave, referred to as the fast direction, ϕ, measured in the geographic reference frame as an azimuth relative to North.

Shear-wave splitting from upper mantle anisotropy has been extensively studied (see, for example, reviews by Silver, 1996; Savage, 1999) and is known to be a clear signature of seismic anisotropy. This makes it our best tool for studying anisotropy in D$''$, provided that we can account for anisotropy in the upper mantle. One way of achieving this is by using event-station pairs of different shear-wave phases. By carefully choosing the phases we use, we can take advantage of where their ray paths overlap and diverge in the mantle to account for upper mantle anisotropy.

Studies of D$''$ typical use either near-horizontally propagating phases (S, ScS, Sdiff) (e.g., Lay and Young, 1991; Wookey et al., 2005a; Maupin et al., 2005; Thomas et al., 2007; Nowacki et al., 2010) or more steeply incident, on the order of $\sim 20°- \sim 60°$ depending on epicentral distance, phases (SKS, SKKS) (e.g., Niu and Perez, 2004; Restivo and Helffrich, 2006; Vanacore and Niu, 2011; Ford et al., 2015; Reiss et al., 2019) (Fig. 3.1). The limitations of using horizontally propagating phases is their long path length in D$''$, making it difficult to constrain the location of the observed anisotropy. Additionally, a lack of azimuthal coverage can restrict observations to vertical transverse isotropy (VTI), a geometry with a horizontal plane of isotropy with hexagonal symmetry. Given sufficient azimuthal coverage, this geometry can be generalised to allow for a tilted axis of symmetry (or tilted transverse isotropy, TTI) (e.g., Wookey and Kendall, 2008; Nowacki et al., 2010).

SKS and SKKS are radially polarised, as the core transiting P-wave only transmits a P and SV-wave into the mantle. This absence of SH-waves means that a VTI mantle will not produce shear-wave splitting in SKS and SKKS. Shear-wave splitting observed in these phases requires a more general form of anisotropy, such as azimithual anisotropy where there are azimuthal changes in velocity in the horizontal plane (Hall et al., 2004; Wookey and Kendall, 2007). This makes studying shear-wave splitting of SKS and SKKS ideal for constraining azimuthal anisotropy within D$''$. The ray paths of SKS and SKKS are almost coincident in the upper mantle and diverge by $\sim 800 km$ at the core-mantle boundary, for the epicentral distance range of $105° - 140°$ we consider here (Fig. 3.1). This significant deviation in D$''$ allows us to make the assumption that both SKS and SKKS sample different regions of D$''$. If we make the assumption that both SKS and SKKS sample the same upper mantle anisotropy, then any significant discrepancies in the shear-wave splitting measurements for these phases is best explained by a change in anisotropy between the two distinct domains of D$''$.

By comparing the shear-wave splitting measured for SKS and SKKS and testing if the

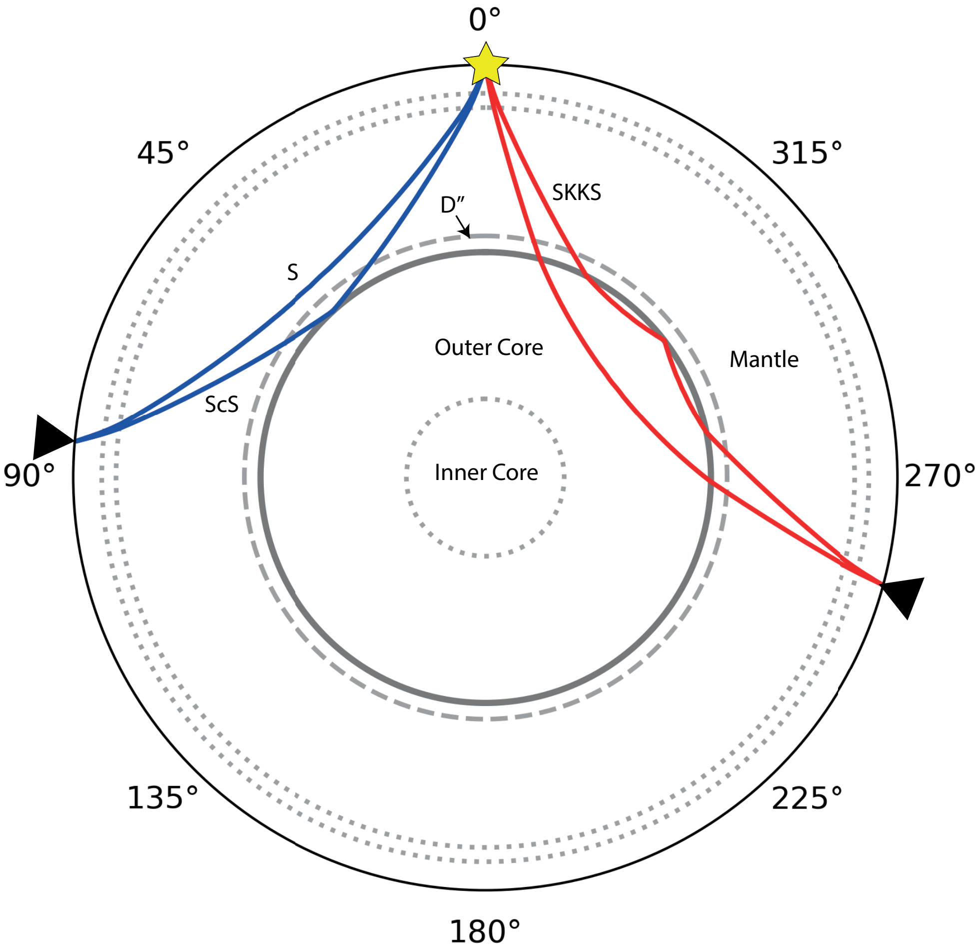

Figure 3.1: Raypaths of the phases (S, ScS, SKS and SKKS) typically used to study D″ anisotropy. Note the difference in the area of D″ sampled by ScS compared to that by SKS and SKKS. This allows for SKS and SKKS to sample D″ at a higher spatial resolution, although the shorter path length through D″ can result in a weaker shear-wave splitting signal. The divergence between SKS, SKKS raypaths through D″ is significant. At the shortest epicentral distances we consider ($\Delta = 105°$) SKS and SKKS exit the core approximately 700 km apart, this distance increases with Δ. This significant deviation leads to the assertion that discrepant splitting between these two phases is best explained by anisotropy in D″ (e.g., Niu and Perez, 2004; Long, 2009; Reiss et al., 2019). Adapted from Nowacki et al. (2011).

measurements disagree in a statistically significant manner we can constrain the shear-wave splitting attributable to D$''$ (Niu and Perez, 2004). Where this is the case, we call the SKS-SKKS event-station pair 'discrepant'. Observations of discrepant SKS-SKKS shear-wave splitting are uncommon, with only ~ 5% of cases showing discrepancy attributable to D$''$ anisotropy in global studies (Niu and Perez, 2004; Restivo and Helffrich, 2006). Discrepant SKS-SKKS shear-wave splitting has been observed near the margin of the African (Wang and Wen, 2007; Lynner and Long, 2014; Ford et al., 2015; Long and Lynner, 2015; Grund and Ritter, 2018; Reiss et al., 2019) and Pacific (Long, 2009; Deng et al., 2017) LLSVPs and at the margin of the so-called 'Perm' anomaly (Long and Lynner, 2015). Given the importance of these observations in constraining azimuthal anisotropy in D$''$ and therefore the dynamics of the lowermost mantle it is vital to ensure results are robust.

We review current methods for identifying discrepant shear-wave splitting, testing existing approaches based on comparing estimated 2σ measurement uncertainties (e.g., Lynner and Long, 2014) and splitting intensity (Deng et al., 2017; Grund and Ritter, 2018; Reiss et al., 2019). We identify and demonstrate clear improvements that can be made to these methods using a set of synthetic split shear-waves and develop a new, multiparameter, approach to identifying discrepant shear-wave splitting. Using our new methods, we search for discrepant SKS-SKKS shear-wave splitting in the Eastern Pacific.

3.2 Methods - Identifying discrepant shear-wave splitting

3.2.1 Shear-wave splitting analysis

Shear-wave splitting is characterised by the polarisation direction of the fast wave, ϕ, and the delay time between the fast and slow waves, δt. There are several methods for measuring these parameters, such as cross-correlation (XC) (Bowman and Ando, 1987) and eigenvalue minimisation (EV) (Silver and Chan, 1991; Walsh et al., 2013).

We use the EV method implemented in the shear-wave splitting analysis code SHEBA, which incorporates the cluster analysis codes of Wuestefeld et al. (2010) (based on the code of Teanby et al. (2004)) to find the optimum analysis window, based on manually defined start and end ranges. This is done to ensure sufficient degrees of freedom for the splitting analysis.

Due to the near-vertical incidence angle of SKS, SKKS at the surface, we use the horizontal seismogram components only. This also removes the need to correct for free-surface coupling effects (Walpole et al., 2014). We perform a grid search over $0s \leq \delta t \leq 4s$ and $-90° \leq \phi \leq 90°$ and calculate the corresponding smallest eigenvalue of the trace covariance matrix, normalised by the largest eigenvalue. A shear-wave that has not experienced shear-wave splitting has a covariance matrix of rank 1, corresponding to the shear-wave energy being resolved wholly onto the radial component seismogram (Silver and Chan, 1991; Walsh et al., 2013). We denote this normalised eigenvalue as λ_2. By searching for splitting parameters that minimise λ_2 we invert for the apparent splitting operator $\Gamma_a(\phi, \delta t)$ applied to waveform as it propagates through the Earth. Where Γ_a represents the contributions from anisotropy in the upper mantle, Γ_{UM}, and in D$''$, $\Gamma_{D''}$, and satisfies the relation

$$\Gamma_{UM} \cdot \Gamma_{D''} \cdot \hat{\mathbf{p}} = K\Gamma_a \cdot \hat{\mathbf{p}} \tag{3.1}$$

where K is some complex scalar and $\hat{\mathbf{p}}$ is the initial polarisation direction (Silver and Savage, 1994).

The identification of un-split (or null) waveforms is an important part of shear-wave splitting analysis. Nulls occur either where the medium is isotropic, or if the initial shear-wave polarisation is near-parallel (or perpendicular) to the fast direction. In both cases we know that any δt value measured is meaningless, and if the medium is anisotropic that ϕ may indicate the fast or slow direction. We use an automated approach to detect nulls, using the parameter Q (Wuestefeld et al., 2010). This quality factor takes advantage of the systematic failure of the XC method for measuring shear-wave splitting close to null directions (Wüstefeld and Bokelmann, 2007; Wuestefeld et al., 2010). By comparing shear-wave splitting measurements made by the EV and XC methods and calculating the ratio of delay time measurements:

$$\Delta = \frac{\delta t_{XC}}{\delta t_{EV}} \tag{3.2}$$

and normalised differences in the fast direction:

$$\Omega = \frac{(\phi_{EV} - \phi_{XC})}{45°} \tag{3.3}$$

An ideal 'good' measurement is defined by identical delay times and fast directions (i.e., $\Delta = 1, \Omega = 0$). For an ideal 'null' XC measurements show no delay time and the fast polarisation measurements differ by 45° (i.e., $\Delta = 0, \Omega = 1$). For an individual measurement, the quality factor, Q, is calculated from the distance to these ideal cases:

$$d_{null} = \sqrt{\Delta^2 + (\Omega - 1)^2}\sqrt{2} \tag{3.4}$$

$$d_{good} = \sqrt{(\Delta - 1)^2 + \Omega^2}\sqrt{2} \tag{3.5}$$

$$Q = \begin{cases} -(1 - d_{null}), \text{for } d_{null} \leq d_{good} \\ (1 - d_{good}), \text{for } d_{null} \geq d_{good} \end{cases} \tag{3.6}$$

Therefore Q ranges from -1 (a clear null), through 0 (poor), to +1 (a clear split). We use a cutoff of $Q > 0.7$ for split events or $Q < -0.7$ for nulls.

3.2.2 Splitting Intensity

Splitting intensity (SI), an alternate measure of shear-wave splitting, has become increasingly popular for differential splitting studies of D″ (e.g., Deng et al., 2017; Grund and Ritter, 2018). The principle advantage of splitting intensity is that it is a commutative (Chevrot, 2000), something that is not true of splitting operators (e.g., Silver and Savage, 1994; Silver and Long, 2011). Therefore the contribution from D″ can be recovered by taking the difference of the SI measured for SKS and SKKS. The limitation of splitting intensity is that we do not individually resolve the direction or strength of D″ anisotropy, but a combination of the two.

Splitting intensity is defined by the amplitude of the transverse component, **T**, relative to the time derivative of the radial component, $\dot{\mathbf{r}}$. If the signal-to-noise ratio is low, the optimal estimate of SI is obtained by projecting the transverse component onto the time derivative of the radial component (Chevrot, 2000) yielding:

$$SI = -2\frac{\mathbf{T}\dot{\mathbf{r}}}{||\dot{\mathbf{r}}^{\mathbf{2}}||} \tag{3.7}$$

where $||\dot{\mathbf{r}}^{\mathbf{2}}|| = \dot{\mathbf{r}}^{\mathbf{t}}\dot{\mathbf{r}}$ is the squared norm of $\dot{\mathbf{r}}$.

Assuming a simple case of a homogeneous anisotropic layer, SI can also be approximated as a re-parameterisation of $\phi, \delta t$ (Chevrot, 2000). If we assume that δt is small relative to the dominant period of the incoming wavelet $w(t)$, we can express $\dot{\mathbf{r}}$ and **T** as:

$$\dot{\mathbf{r}} \approx w'(t) \tag{3.8}$$

and

$$\mathbf{T} \approx -\frac{1}{2}(\delta t sin 2\beta) w'(t) \tag{3.9}$$

where β is the difference between the fast direction, ϕ, and the source polarisation of the wave. As SK(K)S phases are radially polarised when they exit the core, we assume that the source polarisation is equal to the backazimuth of the wave. From (3.8), (3.9) it is clear that:

$$SI \approx \delta t sin(2\beta) \tag{3.10}$$

This approximation for splitting intensity is used in recent splitting intensity studies of discrepant SKS-SKKS shear-wave splitting (e.g., Deng et al., 2017; Grund and Ritter, 2018; Reiss et al., 2019). In discrepant splitting studies, the absolute difference in splitting intensity,

$$\Delta SI = |SI_{SKS} - SI_{SKKS}| \tag{3.11}$$

is taken (Deng et al., 2017). The periodicity of the approximation (eqn. 3.10) introduces potential problems of non-uniqueness where a large range of $(\phi, \delta t)$ return the same ΔSI value. This effect is demonstrated when we model ΔSI using synthetic split shear-waves.

Another potential issue arises from the definition of a null, a shear-wave which is not split, in splitting intensity. A null is defined where $SI \approx 0$. When the splitting intensity approximation is made, this is not always the case. This arises from the grid search methods employed to measure $\phi, \delta t$. The approximation for SI assumes that in the case of a null $\delta t \approx 0s$. In the presence of noise δt can often be unconstrained, with $\delta t \rightarrow 4s$ in the grid search (Fig. 3.2). This issue is mitigated in recent studies (e.g., Deng et al., 2017; Reiss et al., 2019) through manual inspection of the SKS and SKKS waveforms, examining the linearity of the particle motion to visually confirm null measurements.

With the size of splitting datasets ever increasing, improving our measurements of splitting intensity to remove the requirement to visually inspect all null waveforms is preferable. Here we present an adjustment to the method for measuring SI, implementing the trace component projection as set out in equation 3.7. This removes the need to make the approximation and is computationally inexpensive and allows for easier automation of discrepant shear-wave splitting analysis. This also has the added advantage of making our splitting intensity measurements independent of our measured splitting parameters.

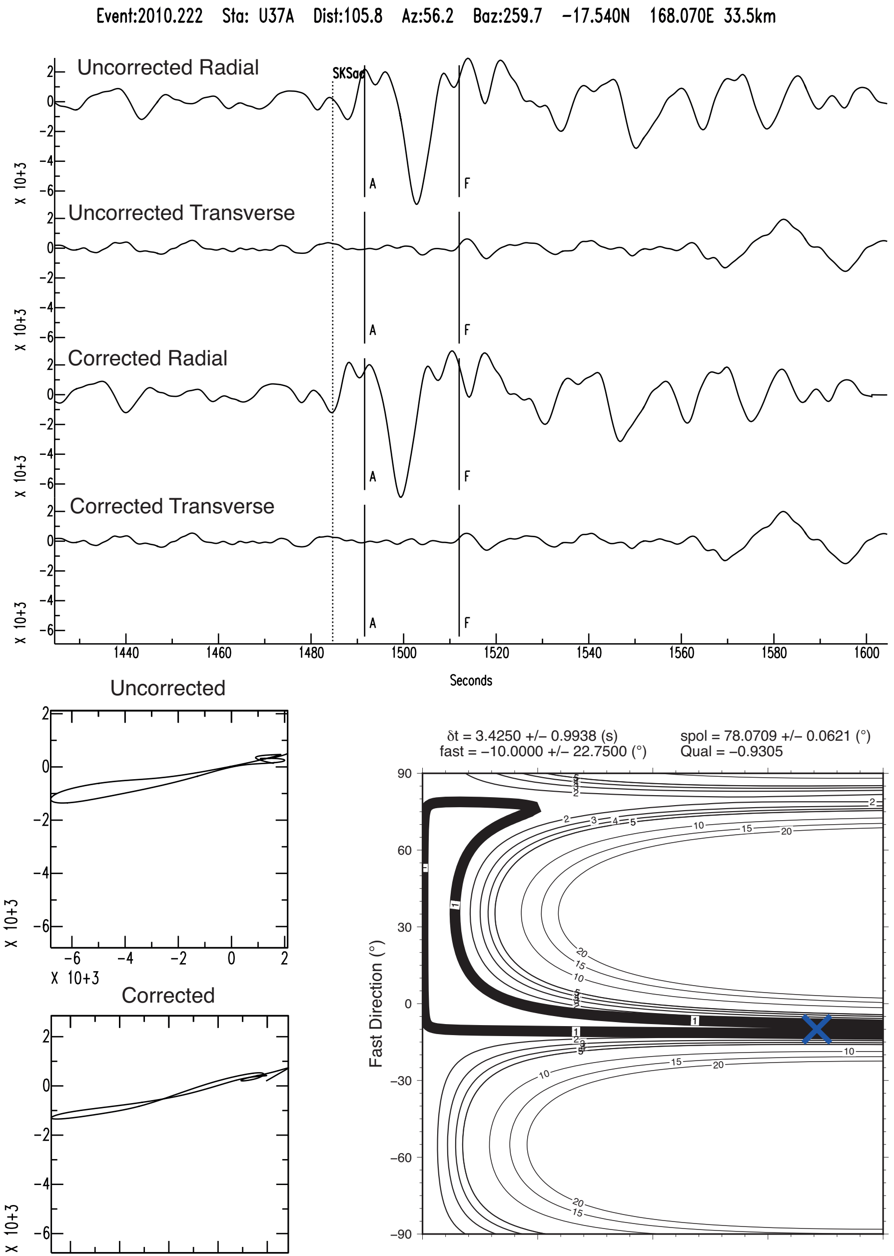

Figure 3.2: A null SKS phase at station U37A as measured by SHEBA (see supplementary figure S1 for an SKKS example). Here we show the uncorrected and corrected traces (top) and particle motions (below left), along with the eigenvalue surface (below right). Note how the grid search algorithm has moved across towards the maximum δt. This trend is seen throughout our dataset.

3.2.3 Robust identification of discrepant shear-wave splitting

The conventional approach for identifying discrepant shear-wave splitting is to compare $\phi, \delta t$ for each phase allowing for their estimated 2σ uncertainties (e.g., Lynner and Long, 2014). We use the estimated Gaussian uncertainties in $\phi, \delta t$ (Silver and Chan, 1991; Walsh et al., 2013) and test whether the two splitting measurements sit within these bounds. Whilst this approach is reasonable, it is limited by the approximation used to convert the F-test defined 95% confidence region of the λ_2 surface into the more useful individual parameter uncertainties $\sigma_{\phi}, \sigma_{\delta t}$ (Silver and Chan, 1991). Inspection of λ_2 measurement surfaces for a set of results quickly reveals that the 95% confidence region is seldom regular (Fig. 3.3)

This estimation of uncertainties has the potential to introduce regular error into the process of identifying discrepant shear-wave splitting. In particular there is a tendency for over-estimation of $\sigma_{\phi}, \sigma_{\delta t}$ (implying a lower confidence in the result). In turn, this can result in false identification of matching SKS-SKKS shear-wave splitting. In our new approach, we have developed an improved strategy to avoid these potential errors.

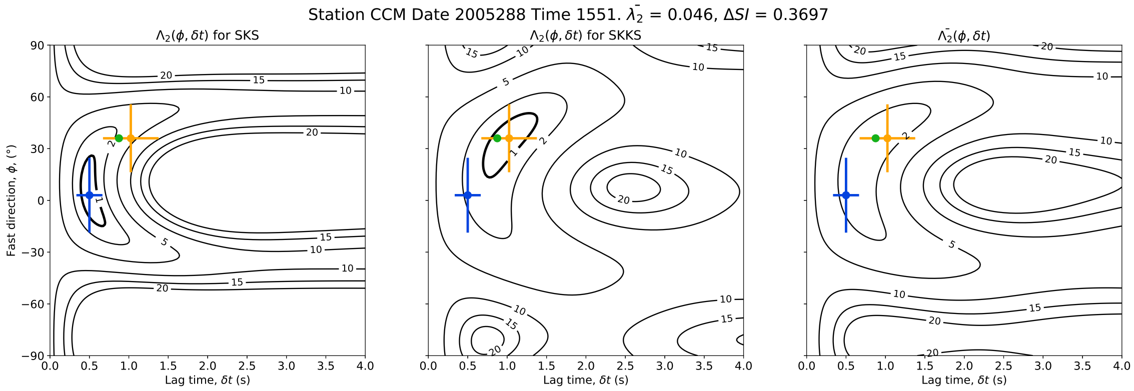

Figure 3.3: The Λ_2 surfaces output by SHEBA when measuring shear-wave splitting in SKS (left) and SKKS (center). The bold contour line bounds the 95% confidence region. The right panel shows that stacked surface $\bar{\Lambda_2}$. The minimum λ_2 for SKS (blue) and SKKS (orange) are plotted over all 3 surfaces along with the estimated 2σ uncertainties in $\phi, \delta t$. The minimum value of $\bar{\Lambda_2}$, $\bar{\lambda_2}$, is shown in green. In this example $\bar{\lambda_2}$ is less than the sum of the 95% confidence regions for SKS and SKKS (eqn. 3.12) and the measurements are classified as matching.

When measuring shear-wave splitting using eigenvalue minimisation, we apply our grid search over $\phi, \delta t$ and compute λ_2 at each node. This creates a surface, which we denote $\mathbf{\Lambda_2}(\phi, \delta t)$. In conventional shear-wave splitting analysis we are only concerned with the minimum value of this surface. However, $\mathbf{\Lambda_2}(\phi, \delta t)$ contains information which can help us test for discrepant splitting. Instead of characterising these misfit surfaces with Gaussian uncertainties $\sigma_{\phi},\sigma_{\delta t}$, we use all the information contained within them. This allows us to avoid errors made in the assumptions required to obtain $\sigma_{\phi},\sigma_{\delta t}$.

We achieve this by summing $\mathbf{\Lambda_2}_{SKS}(\phi,\delta t)$ and $\mathbf{\Lambda_2}_{SKKS}(\phi,\delta t)$, to produce a new surface $\bar{\mathbf{\Lambda}}_\mathbf{2}(\phi,\delta t)$ (Fig. 3.3). This new surface effectively describes how well each $\Gamma(\phi,\delta t)$ works as a solution for both phases. Therefore by taking the best fitting value of $\bar{\mathbf{\Lambda}}_\mathbf{2}$, which we denote $\bar{\lambda}_2$, we have a measure that can be used to determine whether the best fitting splitting solutions for each phase are discrepant.

To robustly identify discrepant shear-wave splitting, we need to account for uncertainty in our splitting measurements and define what we consider to be statistically significant differences between the solutions for SKS and SKKS. We calculate the λ_2 value that bounds the 95% confidence region in $\mathbf{\Lambda_2}(\phi,\delta t)$ for each phase, $\lambda_2^{95\%}$, using an F-test as set out in Silver and Chan (1991). We sum these two values, defining a threshold for $\bar{\lambda}_2$ that we can test against. By comparing $\bar{\lambda}_2$ to the sum of $\lambda_2^{95\%}$ for SKS and SKKS we can determine if the splitting measurements are discrepant. If:

$$\bar{\lambda}_2 > \lambda^{95\%}_{2_{SKS}} + \lambda^{95\%}_{2_{SKKS}} \tag{3.12}$$

then the shear-wave splitting measured for SKS and SKKS is classified as discrepant.

3.3 Synthetics

To test our approach, and to demonstrate some of the pitfalls in the various methodologies, we model $\bar{\lambda}_2$ and ΔSI in $\phi,\delta t$ space using synthetic shear-waves. We generate synthetics over a range of $0s \leq \delta t \leq 4s$ at intervals of $0.25s$ and $-90^\circ \leq \phi \leq 90^\circ$ at intervals of 5°, producing a evenly spaced grid of 629 synthetics (Fig. 3.4a). We generate synthetics for source polarisations of $30^\circ, 45^\circ$ & 60° and with a dominant frequency of 0.1 Hz. All synthetics are generated with a dominant frequency of 0.1 Hz. For clarity, we show results here from synthetics generated with a source polarisation of 45°. Random noise is added to the synthetics to mimic conditions for real data. For each source polarsiation we generate synthetics with a high signal-to-noise ratio (SNR), where $SNR \approx 37$, and with a low SNR, where $SNR \approx 10$. Shear-wave splitting is measured using SHEBA. The measured splitting parameters for the synthetics (Fig. 3.4b) and the

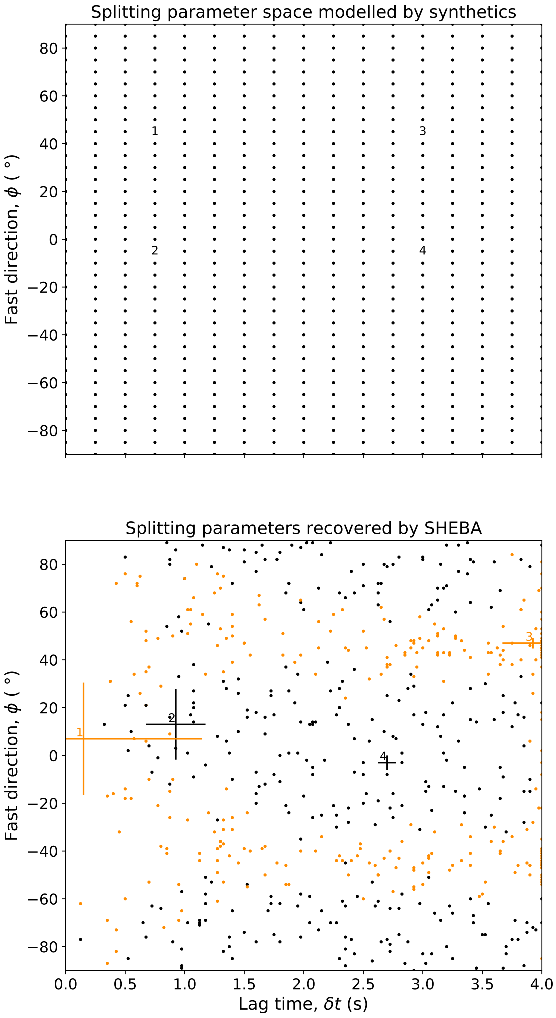

Figure 3.4: (Top) The initial grid of synthetic shear-waves, with a source polarisation of 45°. (bottom) Shear-wave splitting parameters measured by SHEBA for the set of synthetics shown above. Synthetics that are identified as nulls by the quality factor, Q (Wüstefeld and Bokelmann, 2007), are plotted in orange. Where $Q = -1$ this indicates a clear null and $Q = 1$ this indicates a clear split shear-wave. We use a threshold of $Q \leq -0.7$ to identify nulls. We highlight 4 example points (numbered) across both panels to track the migration of our synthetics from their input position to the measured splitting parameters. For null points this effect is significant, with most nulls with a low input δt being migrated along the source polarisation direction. Note source polarisation and fast direction do not need to directly align for a null to be recorded, even at a low signal-to-noise ratio. The majority of synthetics with a fast direction within 10° of the source polarisation axis are returned as nulls.

$\Lambda_2(\phi, \delta t)$ surfaces produced by SHEBA are used to test the performance of the different measures of discrepant shear-wave splitting.

To create synthetic event-station pairs, we select a single synthetic split shear-wave and denote it as 'SKS'. We then denote the whole grid of 629 synthetics as 'SKKS' and construct a set of 629 'SKS-SKKS' pairs. This allows us to visualise all possible sets of event-station pairs and the behaviour of different measures of discrepant shear-wave splitting (Fig. 3.5) across the parameter space. For these synthetic SKS-SKKS pairs we search for discrepant splitting using 2σ error bar matching (Fig. 3.5a), our new measure $\bar{\lambda_2}$ (Fig. 3.5b, 3.6b) and ΔSI using both the approximation for spitting intensity from measured splitting parameters (Fig. 3.5c, 3.6c) and the full projection approach (Fig. 3.5d, 3.6d).

Our synthetics demonstrate the error that can be introduced when using 2σ error bar matching (Fig. 3.5a, 3.6a). This is primarily restricted to nulls, where the shape of the error surface produces high estimates of $\sigma_{\phi}, \sigma_{\delta t}$ and thus spurious matches are found. This is expressed as false classification of matching splitting where $\delta t \approx 0 s$ and along the source polarisation axis ($45\,^{\circ}$) and its antipode ($-45\,^{\circ}$).

Our new measure, $\bar{\lambda_2}$, performs similarly to the 2σ method. This is to be expected given our method is a refinement of 2σ. However, unlike the 2σ method, our new measure clearly defines a single region of matching shear-wave splitting and does not show the same susceptibility to false classification of nulls. At a high signal-to-noise ratio the matching regions for $\bar{\lambda_2}$ and 2σ are both very tightly bound (Fig. 3.5b). As SNR decreases, this breaks down for both measures, as the noise expands the 95% confidence region in shear-wave splitting analysis. Synthetics generated at lower, more realistic, SNRs show this and that $\bar{\lambda_2}$ is more narrowly constrained (Fig. 3.6a,b). This occurs as at lower signal-noise ratios $\mathbf{\Lambda_2}(\phi, \delta t)$ tend to have 95% confidence regions which are not well fit by the rectangular approximation used to obtain $\sigma_{\phi}, \sigma_{\delta t}$.

Our synthetics results also highlight inherent non-uniqueness in ΔSI (Fig. 3.5c,d). Our results also clearly show the difference between measuring splitting intensity by approximation (Fig. 3.5c) and by projection (Fig. 3.5d). Both measures of splitting intensity define a broad region where $\Delta SI < 0.4$, although the region does not exhibit the same level of instability as 2σ and $\bar{\lambda_2}$ as SNR decreases (Fig. 3.6c,d).

These results clearly show that none of these measures alone are ideal for identifying discrepant shear-wave splitting. For example, splitting intensity difference even at high SNR does not define a regular matching region in $\phi,\delta t$ space when compared to $\bar{\lambda}_2$. At lower SNR ratios this difference is less pronounced, as increasing noise makes discrepant shear-wave splitting more difficult for all methods to resolve.

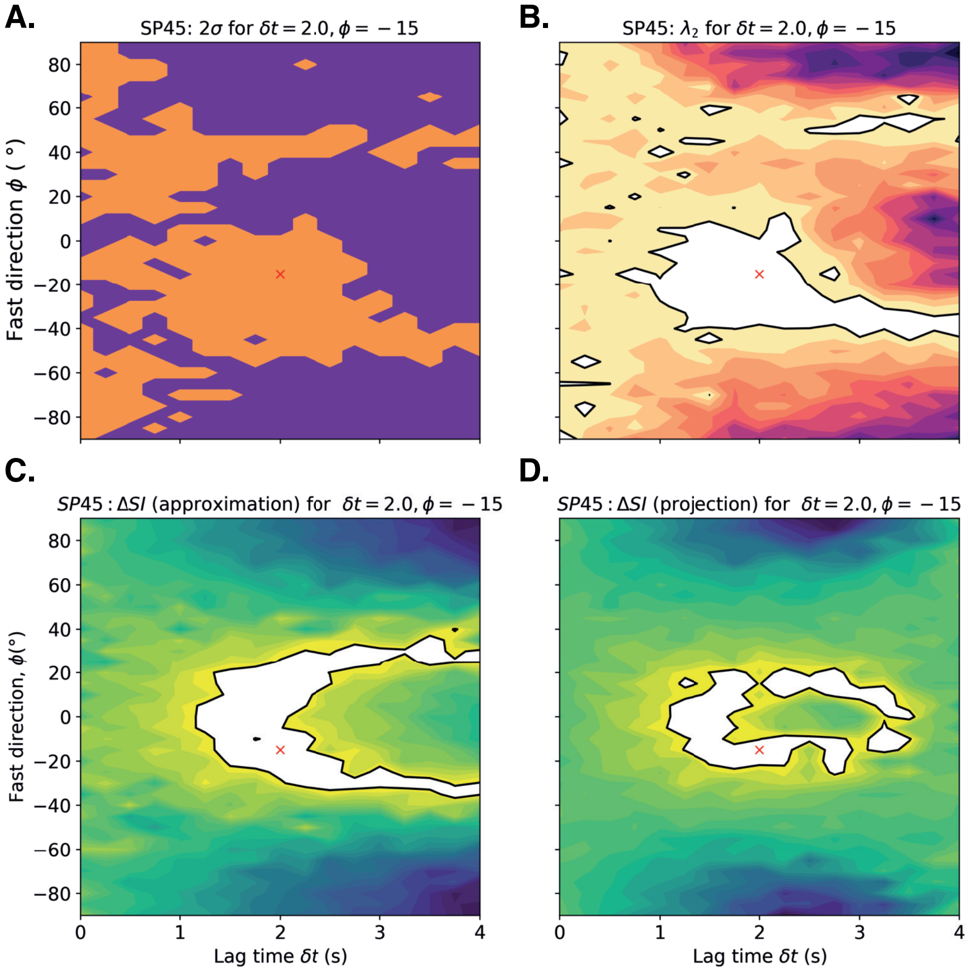

Figure 3.5: Synthetics grid with a source polarisation of 45°, synthetic pairs are constructed by “pairing" the result at grid position $\delta t = 2.0\,s, \phi = -15°$ (red cross) with all other points in the grid. Random white noise is added to the synthetics such that the mean SNR ≈ 10. Splitting measures for each synthetic pair are plotted at the position of the input $\phi,\delta t$ for the synthetic ‘SKKS’. A) Classification using 2σ where orange indicates matching pairs and purple discrepant pairs. B) $\bar{\lambda}_2$ contoured for all pair in the grid. The region in white, enclosed by the bold line, is where $\bar{\lambda}_2 \leq (\lambda^{95\%}_{2_{SKS}} + \lambda^{95\%}_{2_{SKKS}})$. C,D) ΔSI for splitting intensity measured by approximation (C.) and by projection (D.). The region in white indicates where $\Delta SI \leq 0.4$ the threshold suggested by Deng et al. (2017).

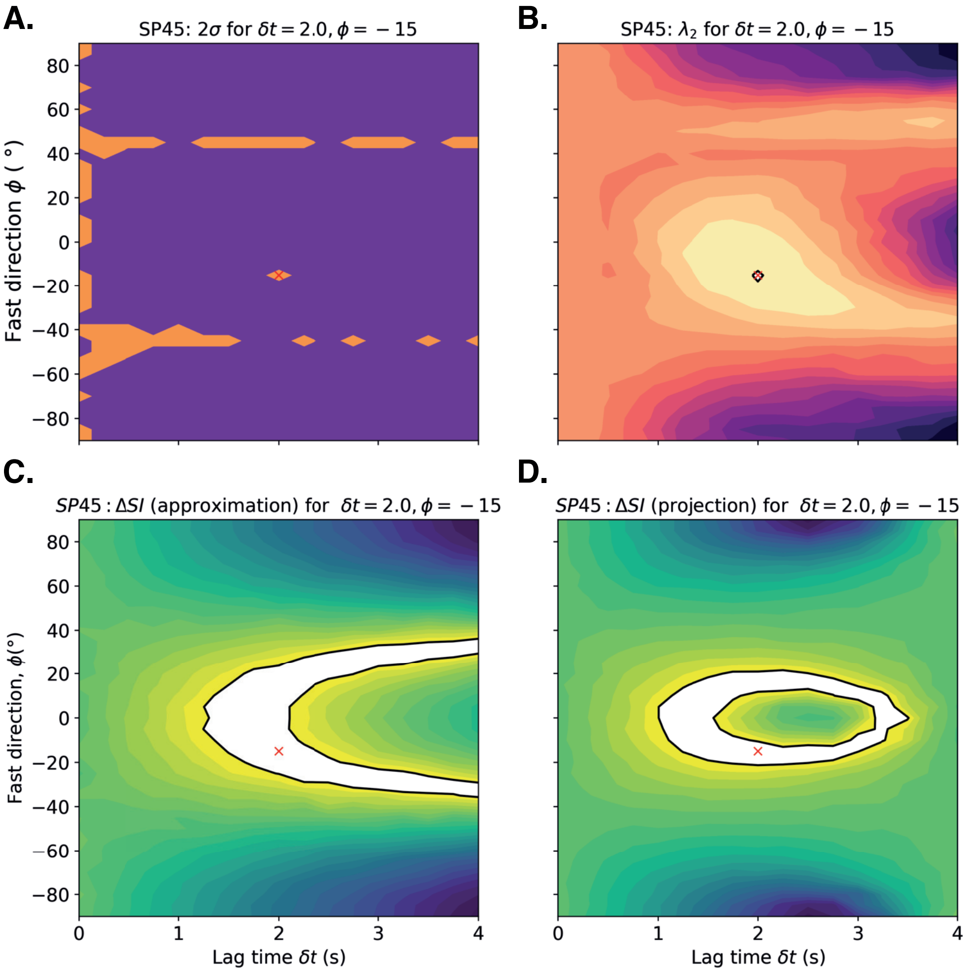

Figure 3.6: The same as Figure 3.5 with a random white noise added such that the mean SNR of the synthetics is now ≈ 37. Synthetic pairs are constructed by "pairing" the result at grid position $\delta t = 2.0\,s, \phi = -15^{\circ}$ (red cross) with all other points in the grid. Splitting measures for each synthetic pair are plotted at the position of the input $\phi, \delta t$ for the synthetic 'SKKS'. A) Classification using 2σ where orange indicates matching pairs and purple discrepant pairs. B) $\bar{\lambda}_2$ contoured for all pair in the grid. The region in white, enclosed by the bold line, is where $\bar{\lambda}_2 \leq (\lambda_{2_{SKS}}^{95\%} + \lambda_{2_{SKKS}}^{95\%})$. C,D) ΔSI for splitting intensity measure by approximation (C.) and by projection (D.). The region in white indicates where $\Delta SI \leq 0.4$ the threshold suggested by Deng et al. (2017).

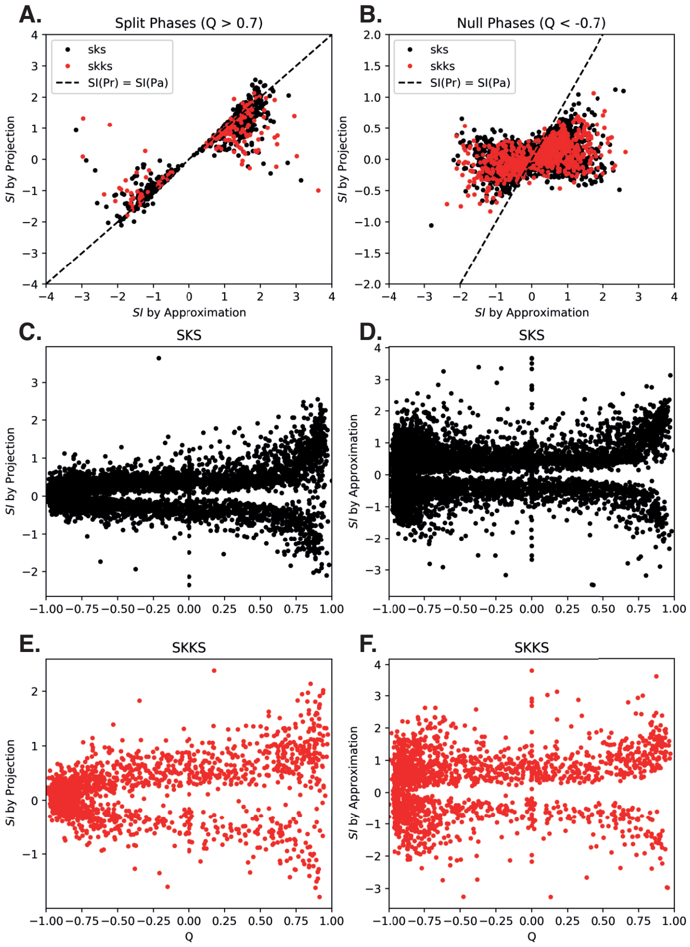

Figure 3.7: Splitting Intensity calculated using an approximation (Pa) (Chevrot, 2000; Deng et al., 2017) and the projection (Pr) (Chevrot, 2000). A) the projected and approximated SI for all the split phases in our dataset B) projected and approximated SI for all nulls. Note the contrast in spread of the two measures, where approximation ranges from -3 to 3 whilst projection most events are between -0.5 and 0.5. For a null, splitting intensity should be ≈ 0. C,E) Splitting intensity by projection against Q for SKS and SKKS respectively. D,F) Splitting intensity by approximation against Q for SKS and SKKS respectively. A Q of -1 indicates a clear null and a Q of 1 indicates a clear split shear-wave. This result can also be reproduced using our synthetics (Fig. 2.17, A.6)

3.3.1 Discussion

Our synthetics results demonstrate that there are problems with all measures of discrepant shear-wave splitting when used individually. Our new measure of discrepant shear-wave splitting does offers improvement, but comes with its own pitfalls. It is clear that measuring SI using the projection method offers improvement over approximating SI from the splitting parameters $\phi, \delta t$. The apparent non-uniqueness in ΔSI that we have identified (Fig. 3.5c,d) raises a potential issue in this approach that requires careful treatment in discrepant shear-wave splitting analysis.

When we compare methods for measuring splitting intensity for real data (Fig. 3.7) we confirm the issues suggested by the synthetic analyses, along with a broader disagreement between methods for split phases (Fig. 3.7a). This disagreement, particularly when we consider that the splitting intensity test for discrepancy relies on the difference between measurements, highlights that improvement can be made by using the full projection method.

Our new $\bar{\lambda}_2$ test does not have the same non-uniqueness issues as ΔSI, however it is strongly dependant on the signal-to-noise ratio of the data. When we explore its performance across $\phi, \delta t$ space with our synthetics, we see that $\bar{\lambda}_2$ defines a single, well-constrained region where we can classify the shear-wave splitting as matching. By summing the estimated 95% confidence λ_2 values (Silver and Chan, 1991) for SKS and SKKS we define a criteria for $\bar{\lambda}_2$ which scales with uncertainty in the individual measurements. A drawback is that these uncertainties increase with noise, which reduces the efficacy of $\bar{\lambda}_2$ when the signal-to-noise ratio is low. The matching region defined by $\bar{\lambda}_2$ broadens and in some cases can break down, reducing our ability to resolve discrepant shear-wave splitting. This is an important restriction as the signal-to-noise ratio is often relatively low (~ 8.0) for SKS and SKKS. Relying solely on either $\bar{\lambda}_2$ or ΔSI opens us to the risk of their pitfalls. These pitfalls can be somewhat mitigated where there is visual inspection of all waveforms (e.g., Deng et al., 2017; Reiss et al., 2019).

We know that SKS and SKKS are not sensitive to VTI anisotropy (Hall et al., 2004), which is a common approximation used when modelling anisotropy in D$''$ (e.g., Walker et al., 2011). We also know that discrepant splitting between these phases has to be explained by non-VTI anisotropy from D$''$, which requires us to invoke models of D$''$ anisotropy with lower symmetry. Therefore it is paramount that we have confidence that our observations of discrepant SKS-SKKS shear-wave splitting are accurate and robust.

In the low-SNR environment we are often forced to work in studying SKS-SKKS shear-wave splitting, the relative stability of ΔSI makes it a good complementary measure to $\bar{\lambda_2}$. The measures are complimentary to each other and combining them in a multiparameter approach helps to mitigate their drawbacks. Our $\bar{\lambda_2}$ test solves an issue of inherent non-uniqueness in the ΔSI method, and ΔSI resolves the issues with the broadening region of $\bar{\lambda_2} \leq (\lambda_{2_{SKS}}^{95\%} + \lambda_{2_{SKKS}}^{95\%})$ as signal-to-noise ratio decreases. Measuring splitting intensity using projection (Chevrot, 2000) decouples ΔSI from $\bar{\lambda_2}$. This gives us two independent measures to test for discrepant shear-wave splitting.

We suggest that applying both the ΔSI (where SI is measured using projection) and our $\bar{\lambda_2}$ test, gives us the most robust means for identifying discrepant SKS-SKKS shear-wave splitting. Using this multiparameter approach will allow for easier automation of discrepant shear-wave splitting analysis.

3.4 Multi-parameter discrepant splitting analysis, a case study.

3.4.1 The NE Pacific region

To test our new, multi-parameter, approach to identifying discrepant SKS-SKKS splitting, we construct a dataset of SKS-SKKS event station pairs. Whilst the full dataset has a global scope, we focus our analysis on a subset of SKS-SKKS pairs recorded at stations in the North Eastern Pacific (Fig. 3.8). This region contains several features in D′′ that we might expect to result in azimuthal anisotropy. This makes it an ideal region to search for discrepant SKS-SKKS shear-wave splitting.

The nearby strong lateral gradient in shear-wave velocity, associated with the margin of the Pacific LLSVP (Fig. 3.8) is one such feature. Recent studies have found that azimuthal anisotropy is concentrated at or near to the margins of the African LLSVP (Cottaar and Romanowicz, 2013; Lynner and Long, 2014; Ford et al., 2015), the Perm anomaly (Long and Lynner, 2015) and southern margins of the Pacific LLSVP (Deng et al., 2017; Creasy et al., 2017).

Previous studies of the Eastern Pacific using SKS-SKKS (Long, 2009) and S-ScS (Nowacki et al., 2010) have found evidence for azimuthal anisotropy in D′′. This anisotropy, particularly the TTI anisotropy modelled by (Nowacki et al., 2010), is attributed to deformation of D′′ surrounding subducted Farallon slab material. However the limited coverage of these studies leaves the full extent of this anisotropy unconstrained. By revisiting this region with a new SKS-SKKS dataset,

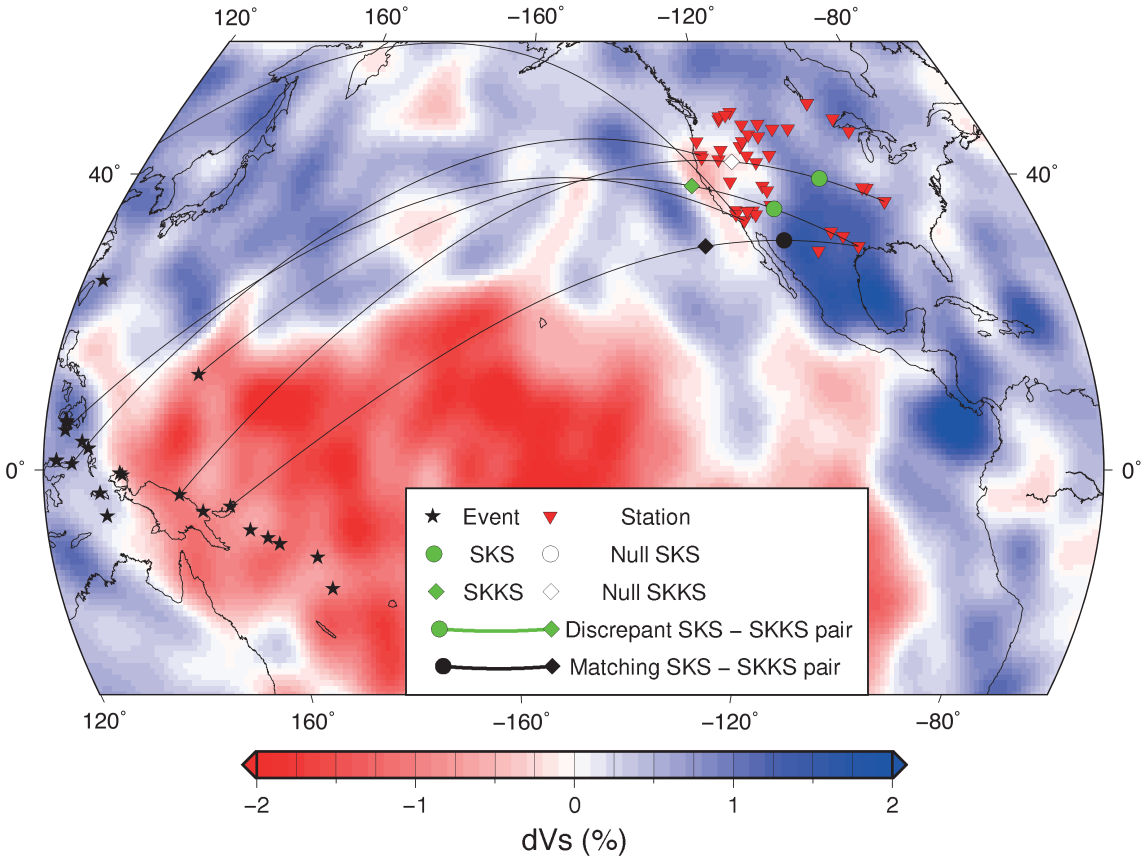

Figure 3.8: Event locations (stars) and stations (triangles) used to produce our Eastern Pacific dataset. Example raypaths taken by SKS, SKKS are drawn, with SKS and SKKS pierce points through the core-mantle boundary indicated by circles and diamonds respectively. This is plotted over the isotropic shear-wave velocity at the base of the mantle from the model S40RTS (Ritsema et al., 2011), show as a % deviation from the reference model.

we demonstrate the effectiveness of our new technique whilst also improving our constraints on D$''$ anisotropy.

3.4.2 Data

We construct our dataset from a previous dataset of SKS shear-wave splitting results by Walpole et al. (2014). We select a subset of these results that are clearly identified as being either split or null according to their quality factor, Q (Wuestefeld et al., 2010). We use a cutoff of $Q > 0.7$ for split events or $Q < -0.7$ for nulls. For the 954 events selected where we could also pick SKKS, we download broadband seismic data from the IRIS data management centre. All events are processed using SHEBA, where we measure $\phi, \delta t$, along with splitting intensity by both approximation and projection.

Shear-wave splitting in SKS and SKKS are measured independently. Prior to our analysis we detrend and demean the seismograms and check for data gaps or spikes. We filter all seismograms with a two-pass two-pole butterworth bandpass filter, with corner frequencies of 0.01 Hz and 0.5 Hz. We chose an upper corner frequency of 0.5 Hz in order to better resolve weakly split ($\delta t \approx 0.5$ s) phases. Excluding these higher frequencies can lead to weakly split phases being measured as nulls (Walpole et al., 2014). This is especially important as these weakly split results tend to occur at “null" stations where there is no apparent anisotropy in the upper mantle.

After performing shear-wave splitting analysis we remove events with a signal-to-noise ratio ≤ 5. Additionally we reject phases with a difference in backazimuth and source polarisation $\geq 10°$. For all SKKS phases, we then identify the SKS result for the same event and combine them to produce SKS-SKKS event-station pairs. This results in a dataset of 420 SKS-SKKS pairs with upwards core-mantle boundary pierce points in the Eastern Pacific. Additionally, we use our full dataset to test the performance of measuring splitting intensity by approximation and projection.

3.4.3 Results

Following our synthetic examples we test for discrepant SKS-SKKS splitting in our Eastern Pacific data using both $\bar{\lambda_2}$ and ΔSI. The 111 pairs where both phases are null and the 256 where one phase has a Q factor between -0.5 and 0.5, are discarded from our analysis.

After we apply our multiparameter discrepancy test ($\bar{\lambda_2}$ and ΔSI by projection) to the remaining 53 pairs, we find that 30 show discrepant SKS-SKKS splitting (Fig. 3.9). Of the

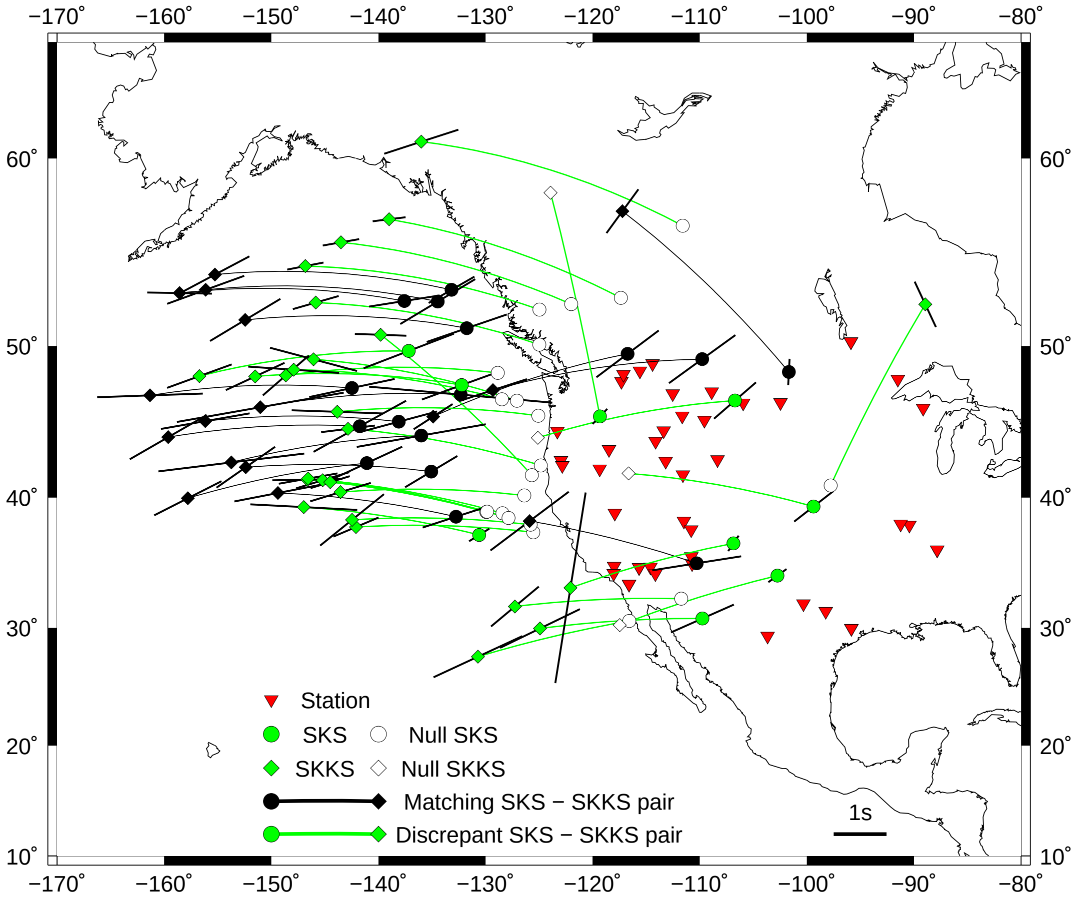

Figure 3.9: Matching and discrepant SKS-SKKS pairs where at least one phase has been split. SKS-SKKS event station pairs are classified as either matching (black) or discrepant (green) using our new measure $\bar{\lambda}_2$ and a modified ΔSI test (see text). SKS (circle) and SKKS (diamond) results are plotted at their up-going pierce points at the core-mantle boundary. These are calculated using TauP (Crotwell et al., 1999) assuming an IASP91 1-D velocity model (Kennett and Engdahl, 1991). For phases that are split, the associated parameters are drawn as bars oriented $\phi°$ from N with a length proportional to δt at the corresponding piercing point. For each event station pair SKS and SKKS piercing points are connected with a great circle arc. These connecting arcs are also coloured according to whether the pair is interpreted as matching (black) or discrepant (green). Null-split pairs are inferred as discrepant as in other studies (e.g., Grund and Ritter, 2018).

discrepant pairs, there are 5 cases where both SKS and SKKS are split. The remaining 25 discrepant pairs are cases where one phase (usually SKS) is null and the other is clearly split. The majority of the pairs follow a backazimuth of $260° - 290°$, with no clear correlation between backazimuth and discrepant splitting. We also see a few discrepant SKS-SKKS pairs at other backazimuths, but these events are too isolated to make any meaningful interpretation. We focus on the 48 SKS-SKKS pairs with pierce points between $\sim -160°$and $\sim -120°$ longitude and between $\sim 35°$and $\sim 60°$ latitude. We see that discrepancy is primarily correlated to longitude and that our splitting results are broadly consistent with latitude (Fig. 3.9). The most striking feature is the north-south line of 18 discrepant pairs with a null SKS and a split SKKS occurring at longitudes of $\sim -130°$ to $\sim -120°$. The measured splitting in SKKS for these event-station pairs has a mean δt of $1.15s \pm 0.02s$ and mean splitting intensity of 0.93 ± 0.05. There are 3 discrepant SKS-SKKS pairs in this sub-region where both phases are split. We also note that we only have two stations, FRD and ULM, where we see both null and split SKS.

Moving further West, we see a more complex transition to pairs which are discrepant, but with splitting in both SKS and SKKS, and then to where both phases return matching splitting. In contrast to the null-split pairs, the 12 matching event-station pairs here have a mean δt of $1.72s \pm 0.07$ and mean SI of 1.35 ± 0.11 for SKS and a mean δt of $1.80s \pm 0.03s$ and a mean SI of 1.24 ± 0.12 for SKKS. This increase in splitting is what we expect to observe as the null SKS phase in a null-split pair indicates that there is no contribution to shear-wave splitting from the upper mantle. Our observations of interspersed matching and discrepant SKS-SKKS pairs is broadly consistent with previous work in this region (Long, 2009), where anomalous SKS-SKKS splitting was observed along a similar backazimuth range further to the south (Fig. 3.9).

We also investigate the measured splitting intensity across our global dataset, to further explore the contrast between approximating SI and using the projection method. Our results (Fig. 3.7) again show the disagreement between the two methods. Separating split (Fig. 3.7a) and null (Fig. 3.7b) phases shows that the splitting intensity approximation is inaccurate in both cases, whilst we only expected it to perform poorly for nulls. Plotting the measured splitting intensities against the quality factor Q, an indicator of nulls, for SKS (Fig 3.7c,d) and SKKS (Fig 3.7e,f) also demonstrates the large range of splitting intensities returned for nulls by the approximation. It is also worth noting that these result can also be reproduced using synthetic shear-waves (Fig. 2.17, A.6). This systematic discrepancy between approximated and projected splitting intensity

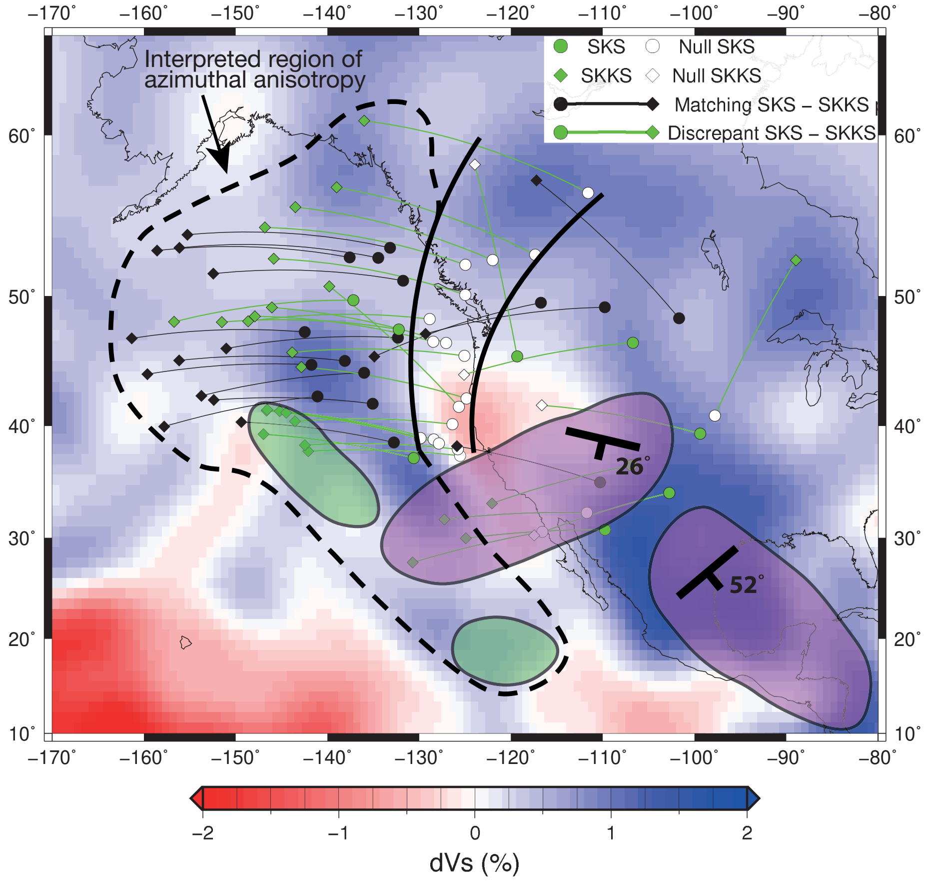

Figure 3.10: Matching and discrepant SKS-SKKS event-station pairs where at least one phase has been split, plotted over the S40RTS isotropic shear-wave velocity model at the core-mantle boundary (Ritsema et al., 2011). SKS (circle) and SKKS (diamond) results are plotted at their up-going pierce points at the core-mantle boundary. These are calculated using TauP (Crotwell et al., 1999) assuming an IASP91 1-D velocity model (Kennett and Engdahl, 1991). Our interpreted region of potential azimuthal anisotropy in D″ is shown by the dashed line. The solid lines denote where we see the change in anisotropy in D″ from our observation of null-split SKS-SKKS pairs. Previous studies of D″ anisotropy in this region are shown using SKS-SKKS (green bubbles) (Long, 2009) and S-ScS (purple) (Nowacki et al., 2010). The orientation and dip of the tilted transverse isotropy (TTI) modelling by Nowacki et al. (2010) is also shown.

suggests that approximated splitting intensity should be used with caution and where possible should be replaced with splitting intensity measured by projection.

3.5 Azimuthal Anisotropy in D$''$ beneath the Eastern Pacific

Our results in the Eastern Pacific show that, in line with other studies (e.g., Niu and Perez, 2004; Restivo and Helffrich, 2006), discrepant SKS-SKKS shear-wave splitting is uncommon, but resolvable. The clear observation of discrepant SKS-SKKS splitting near the edge of the Pacific LLSVP continues a global trend where discrepant SKS-SKKS shear-wave splitting has been observed at, or near, margins of the Pacific (Deng et al., 2017) and African (Lynner and Long, 2014; Reiss et al., 2019) LLSVPs and near the Perm anomaly (Long and Lynner, 2015). Our results corroborate and expand upon previous SKS-SKKS results in this region (Long, 2009), where a similar pattern of discrepant splitting was seen along a similar backazimuth range further South (Fig. 3.9). This is indicative of a province in D$''$ that exhibits azimuthal anisotropy. By including the observations of Long (2009), we can extend this interpretation further, covering a large province of D$''$ near the Eastern margin of the Pacific LLSVP across which we can interpret a change in seismic anisotropy (Fig. 3.9).

Our observations of null SKS phases, paired with split SKKS, demark where this change in anisotropy occurs. The clear north-south trend of SKS-SKKS null-split pairs over ~ 20° latitude is best explained by a change in D$''$ anisotropy. The weaker splitting parameters for the SKKS phases in these null-split pairs, compared to the nearby matching split SKS-SKKS pairs, suggests that these pairs do not sample any upper mantle anisotropy and instead SKKS is solely sampling azimuthal anisotropy in D$''$. This change in D$''$ anisotropy could be a simple rotation of the anisotropic medium between the regions sampled by SKS and SKKS, such that SKS is no longer sensitive to it due to alignment of the medium's fast direction and the polarisation of SKS. Alternatively there could be a change across this region, either to a different anisotropic mechanism or to isotropy.

We have no similar constraint on the westward extent of this region. Indeed, a plausible explanation for the transition from discrepant to matching SKS-SKKS shear-wave splitting is the province of azimuthal anisotropy is large enough that the more westerly pairs are both sampling the azimuthal anisotropy. This best explains why our result are so closely interspersed, with the SKKS pierce points of the null-split sampling the same region of D$''$ as many of our matching pairs. This province of azimuthal anisotropy must be broadly homogeneous, as we would expect any significant lateral variations within the region to also produce widespread discrepant SKS-SKKS shear-wave splitting whereas we only see 3 SKS-SKKS pairs in this region that are discrepant where both phases are split.

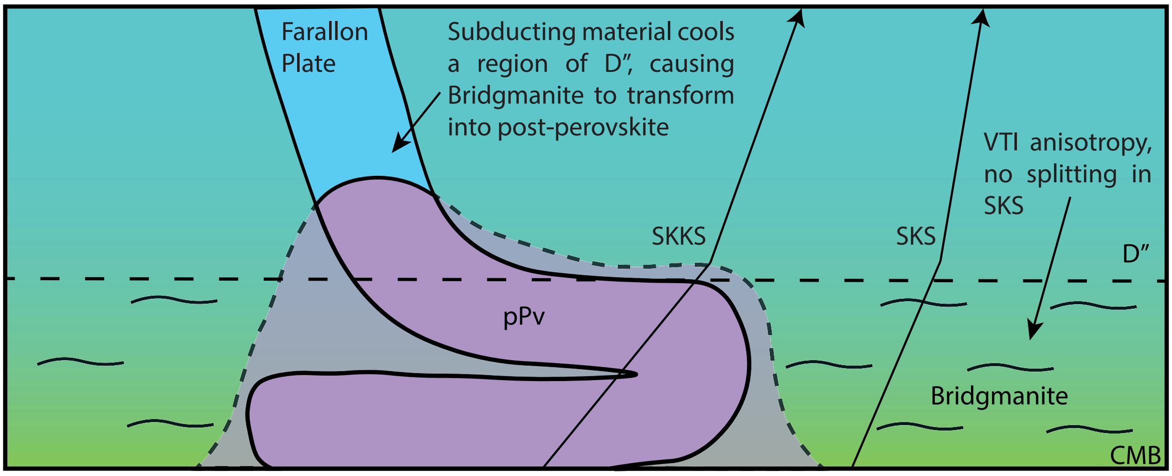

Figure 3.11: Summary cartoon of our interpretation of a post-perovskite ridge in D″. The cold Farallon slab collects along the core mantle boundary (following numeric models (e.g., McNamara et al., 2002)). In the pressure conditions of D″ and due to the positive claperyon slope (Murakami et al., 2004) this cold material crosses the phase transition to post-perovskite. The cooling effect of the collecting slab material may also sufficiently cool the surrounding native D″ material to extend the post-perovskite ridge. The surrounding D″ material must be isotropic or anisotropic with VTI in order to explain the consistent observations of null SKS phases.

A strong candidate for this azimuthal anisotropy is LPO of post-perovskite (pPv), extending away from the Pacific LLSVP (Fig. 3.10). Post-perovskite is known to be stable in the pressure and temperature conditions of the lowermost mantle (Murakami et al., 2004) and is often favoured by observational and modelling studies of D″ anisotropy (e.g., Walker et al., 2011; Ford et al., 2015; Creasy et al., 2017).

An interpretation of pPv requires a decrease in temperature to affect the phase transition from bridgmanite (Murakami et al., 2004). This is consistent with the body-wave tomography-derived shear-wave velocity (Fig 3.9), as faster velocities are attributed to colder regions in D″. These faster regions of the lowermost mantle are often inferred to be associated with subducted slab material. Plate motion models (Richards and Lithgow-Bertelloni, 1998) suggest the Farallon plate has reached the core-mantle boundary in this region and previous work invokes this as a probable cause of D″ anisotropy (Long, 2009). As the cold subducted material reaches the core-mantle boundary the pressure conditions become sufficient for bridgmanite to transition to post-perovskite. The cooling effect of the collecting slab material may also sufficiently cool the surrounding native D″ material to expand the post-perovskite province away from the slab.

As pPv has different elastic properties to bridgmanite, we do not require a change in lowermost mantle deformation across this region to explain our observations. However, we would expect for there to be deformation associated with the subducting Farallon slab. We may be detecting this with our 4 discrepant SKS-SKKS pairs where both phases are split, however they are too disparate to draw any meaningful interpretation.

Further data collection, especially an improvement in backazimuthal coverage, is needed to search for slab-associated deformation. Our observed trend of null-split pairs with a nulls SKS and split SKKS suggests a change in D$''$ anisotropy across the region. This could be explained by a change in deformation of D$''$ causing a rotation of the anisotropic medium, resulting in the SKS null. Alternatively we could be seeing an East-West transition from pPv to bridgmanite, where bridgmanite then does not produce anisotropy that SKS is sensitive to (Fig. 3.11).

Whilst LPO of post-perovskite is a strong candidate mechanism, other mechanisms cannot be ruled out. Bridgmanite and ferropericlase, the other two significant lowermost mantle minerals can generate significant anisotropy through LPO (e.g., Cordier et al., 2004; Marquardt et al., 2018). However both phases are ubiquitous throughout the lower mantle, which is generally considered to be isotropic away from D$''$ (Meade et al., 1995). This makes these phases less plausible explanations that post-perovskite. An SPO mechanism also cannot be ruled out. SPO models of layered disc-like or tubular melt inclusions have been shown to generate anisotropy very efficiently, requiring a very low volume-fraction (< 0.0001 of melt (Kendall and Silver, 1998)) to manifest a measurable signal.

Distinguishing between these candidate mechanism has thus far been a significant challenge to our understanding of D$''$. Indeed, SPO and LPO may yet prove to be complementary mechanisms, depending on the length scale of deformation within D$''$ with respect to the seismic wavelengths used. Recent forward modelling efforts (Ford et al., 2015; Creasy et al., 2017; Pisconti et al., 2019) have improved our constraints on D$''$ anisotropy, although most candidate mechanisms produce plausible results. Further expansion of these methods to remove the reliance on single-crystal elastic tensors, along with improving our observational constraints through the integration of ScS, SKS and SKKS shear-wave splitting data with reflected PdP and SdS polarities (Creasy et al., 2019) will allow us to greatly improve our understanding of D$''$ anisotropy.

3.6 Conclusions

We have shown using both synthetics and real data that if not carefully treated, current methods for identifying discrepant shear-wave splitting have limitations that may lead to both false positive and negative results. To ensure robust detection and analysis of discrepant shear-wave splitting we have developed a new measure derived from the eigenvalue minimisation method used to measure shear-wave splitting for each phase. Additionally, we propose some improvements to the measurement of spitting intensity and its application to discrepant splitting analysis. Combining these independent measures in a multi-parameter approach allows us to more rigorously test for discrepant shear-wave splitting and for easier automation of discrepant shear-wave splitting analysis. This allows us to use SKS-SKKS shear-wave splitting data to constrain D'' anisotropy with improved confidence.

Our SKS-SKKS results in the Eastern Pacific suggest a region of azimuthal anisotropy in D'', near the Eastern margin of the Pacific LLSVP. We also see a change in D'' anisotropy across this region, requiring a change in mechanism or in D'' deformation. Our observations are best explained by lattice preferred orientation of post-perovskite, where the change in anisotropy is potentially due to post-perovskite transitioning to bridgmanite. Our preferred model to achieve these conditions in D'' is the impingement of material from the Farallon slab near the core-mantle boundary. Future studies combining SKS-SKKS and S-ScS shear-wave splitting data using complementary backazimuth ranges, along with intensive forward modelling of predicted D'' anisotropy, should help to further improve our understanding of anisotropy of this part of D'', and its links to the dynamics of the Earth system.

3.7 Acknowledgements

We would like to thank Jack Walpole, Andy Nowacki for their comments and insight which has helped improve the quality of this manuscript. Suggestions provided by Xiaobo He and an anonymous reviewer have greatly improved the manuscript. JA is supported by a NERC GW4+ Doctoral Training Partnership studentship from the Natural Environment Research Council [NE/L002434/1] and by a postgraduate grant from the Government of Jersey. Maps were produced using GMT (Wessel and Smith, 1995). SHEBA is available at http://www.github.com/jwookey/sheba

.

CHAPTER 4

DIRECT INVERSION OF SHEAR-WAVE DATA FOR SEISMIC ANISOTROPY AND D$''$ DEFORMATION.

This chapter was done in collaboration with my supervisors, James Wookey and Michael Kendall. The contents of this chapter is in submission as Asplet et al., (2021).

4.1 Introduction

The D$''$ layer (Bullen, 1949) plays an essential role in mantle dynamics, forming a thermochemical boundary layer between the vigorously convecting liquid iron outer core and the overlying solid silicate mantle. D$''$ is a strongly heterogeneous layer, with large continent-sized anomalies (i.e., the Large Low Shear Velocity Provinces or LLSVPs) and smaller strongly heterogeneous ultra low velocity zones (Yu and Garnero, 2018; Thorne et al., 2021). Despite our improving picture of the structural features within D$''$ our understanding of deformation, or mantle flow, in this layer is limited. Geodynamic models of the lowermost mantle are restricted to relying on either plate motion reconstructions to drive mantle flow (e.g., Flament, 2019) or using constraints from global tomography (e.g., Forte et al., 2015), with limited consensus existing between models.

Seismic anisotropy, the variation in seismic wave speed with direction, is indicative of long-range order in materials and is commonly used to study deformation in the upper mantle (e.g., Tommasi et al., 2000; Becker and Lebedev, 2021). The lattice-preferred orientation (LPO) of olivine is widely described as the mechanism through which seismic anisotropy develops in response to upper mantle flow (e.g., Silver, 1996; Blackman and Kendall, 2002; Long and Becker, 2010). This is not the case for D$''$, where there are a broad range of mechanisms that can plausibly explain observations of seismic anisotropy. The LPO of post-perovskite, a high-pressure polymorph of bridgmanite (Murakami et al., 2004; Tateno et al., 2009), is commonly invoked as one of the more plausible mechanisms (e.g., Wookey et al., 2005a; Long, 2009; Nowacki et al., 2010; Ford et al., 2015; Creasy et al., 2017; Deng et al., 2017). However lattice-preferred orientation of the other primary constituents of D$''$, bridgmanite (Cordier et al., 2004; Couper et al., 2020) and ferropericlase (Marquardt et al., 2018), cannot be confidently ruled out. The preferred alignment of heterogeneities, such as partial melt inclusions, is another plausible candidate (Kendall and Silver, 1998; Kendall, 2000) particularly for hotter regions of D$''$ where we might expect to find melt (e.g., Hirose et al., 2015) and post-perovskite is unstable due to the positive Clapeyron slope of the bridgmanite to post-perovskite phase transition (Wookey et al., 2005b).

Shear-wave splitting, or seismic birefringence, is one of our best tools to constrain seismic anisotropy in D$''$. To constrain shear-wave splitting due to D$''$, however, we must also account for upper mantle anisotropy. This is typically done using pairs of shear-wave phases such as S-ScS (e.g., Wookey et al., 2005a; Thomas et al., 2007; Nowacki et al., 2010, etc.,) or SKS-SKKS (e.g., Niu and Perez, 2004; Restivo and Helffrich, 2006; Long, 2009; Reiss et al., 2019; Lutz et al., 2020, etc.,). A common criticism of shear-wave splitting studies is a lack of quantitative analysis of potential anisotropic mechanisms. Recent efforts have attempted to rectify this by forward modelling the orientations of candidate elastic tensors, attempting to reproduce measured shear-wave splitting parameters for ScS, SKS and SKKS data (e.g., Ford et al., 2015; Creasy et al., 2017; Wolf et al., 2019). The characterisations of the waveform data as splitting parameters limits the power of these methods and imports the inherent non-uniqueness of the shear-wave splitting problem into the model. Consequently, forward modelling has struggled to constrain unique orientations for all candidate mechanisms. This then limits the confidence we can place on either mineralogical or geodynamic interpretations of the data.

In this paper we revisit and revise the approach of Wookey (2012) to directly invert shear-wave waveform data for the orientation and strength of seismic anisotropy. Uniquely constraining the geometry of D$''$ anisotropy has been shown to require the use of multiple seismic phases (as these provide different propagation geometries) (Wookey and Kendall, 2008; Creasy et al., 2019). Our inversion framework allows for this, and we demonstrate it by jointly inverting ScS, SKS and

SKKS waveform data for the orientation and strength of seismic anisotropy of an anomalously fast (ca. 1.25% dVs) region of D$''$ beneath the Eastern Pacific (Fig. 4.1). Previous analysis of discrepant SKS-SKKS shear-wave splitting in the Eastern Pacific has shown this region of D$''$ to be anisotropic, with post-perovskite invoked as the most plausible mechanism (Long, 2009; Asplet et al., 2020). Global tomographic models of radial anisotropy show this region to broadly have $V_{SH} > V_{SV}$ which would imply predominantly horizontal flow in D$''$ (e.g. Panning et al., 2010; Moulik and Ekstrom, 2014; French and Romanowicz, 2014). To test these interpretations, we invert for a range of candidate mechanisms for seismic anisotropy in the lowermost mantle.

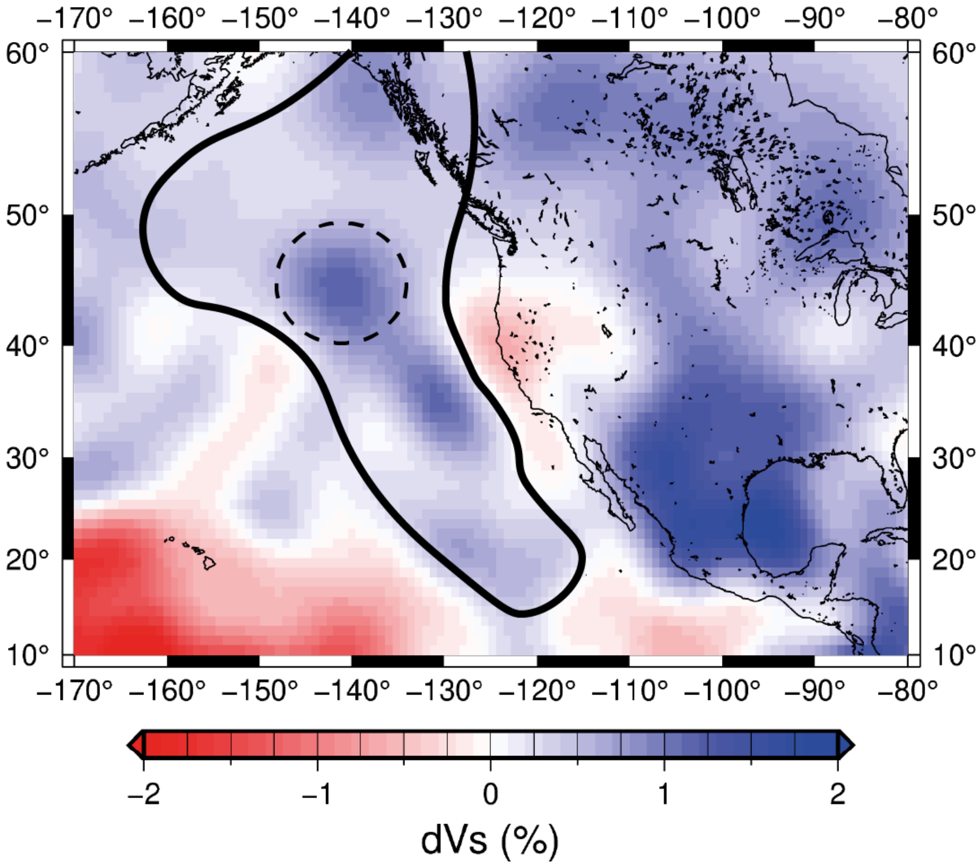

Figure 4.1: The extent of previous work identifying D$''$ seismic anisotropy from analysis of discrepant SKS-SKKS shear wave splitting (Long, 2009; Asplet et al., 2020) (bold line). Our target region, a fast anomaly in the S40RTS velocity model where the shear-wave velocity perturbation is ca. 1.25% above the global average, is indicated by the dashed line. We also show the S40RTS velocity model across the region (Ritsema et al., 2011).

4.2 Inversion Framework

4.2.1 Domain Parameterisation

We use a revised version of the inversion framework set out by Wookey (2012). In this method we directly invert shear-wave waveform data for the orientation and strength of seismic anisotropy of a region of interest. This region can be subdivided into a set of anisotropic domains. Each domain is assumed to be uniformly anisotropic, and is parameterised by:

- $\mathbf{C}$, a base elastic tensor
- α, β, γ, the orientation of $\mathbf{C}$ about the X1, X2 and X3 axes (Fig. 4.2)
- s, the dilution of $\mathbf{C}$ or the anisotropic strength

The most general form of $\mathbf{C}$ is a 4th rank tensor with 81 elastic constants ($3 \times 3 \times 3 \times 3$), however this can be reduced to a simpler 6×6 matrix with no loss of information using Voigt notation. Symmetry and thermodynamic arguments allow $\mathbf{C}$ to be reduced to 21 independent elastic constants (e.g., Mainprice, 2015). Inverting directly for arbitrary orientations of these elastic constants is not feasible. Instead we impose an initial candidate style of anisotropy, with the orientation parameters (α, β, γ) allowing the orientation of this initial model to be general. The strength parameter, s, controls the dilution of $\mathbf{C}$ by Voigt-Reuss-Hill averaging $\mathbf{C}$ with an isotropic equivalent tensor (Wookey, 2012).

In the inversion, we set out to find the model parameters that best explain any shear-wave splitting in the input waveforms. These model parameters can be a set of 1-3 of the angles α, β, γ (Fig. 4.2) and the strength parameter, s, for all domains in the inversion.

Each waveform is assumed to have a fixed ray path through the model and can interact with any number of anisotropic domains. These ray paths and the order in which each waveform interacts with the domains must be determined prior to the inversion, along with the ray's angle of incidence in each domain. We use the TauP toolkit (Crotwell et al., 1999) and the IASP91 1-D velocity model (Kennett and Engdahl, 1991) to perform the ray tracing and then calculate each waveforms' path length through each anisotropic domain it encounters. We neglect the effects of 3-D velocity structure. For ScS phases, we assume that the up- and down-going parts of the ray path sample the same seismic anisotropy in D$''$. This offers an improved treatment of the propagation of ScS phases in the lowermost mantle compared with the common simplifying

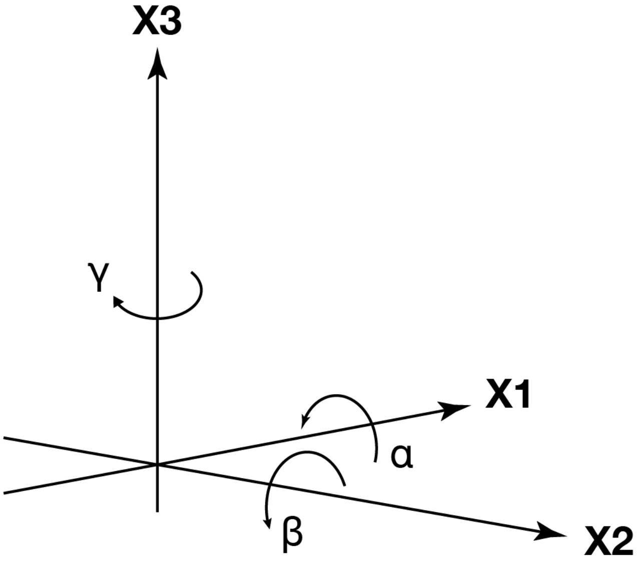

Figure 4.2: Definitions of the orientation parameters in our inversion. α is the clockwise (looking towards the origin) rotation about the X1 axis, β is the clockwise rotation about the X2 axis and γ is the clockwise rotation about the X3 axis.

assumption that the ScS propagates horizontally through D$''$ (e.g., Nowacki et al., 2010; Ford et al., 2015).

4.2.2 Sampling the model space

As each anisotropic domain can have up to 4 free model parameters (α, β, γ, s) for each assumed style of seismic anisotropy (e.g., Bridgmanite) this gives us a multi-dimensional model parameter space to explore. This is expensive to search using an exhaustive grid search method, which is commonly used for measuring shear-wave splitting (e.g., Silver and Chan, 1991). Following Wookey (2012) we treat the inversion problem as generally non-linear. We replace the previously used neighbourhood algorithm (Sambridge, 1999) with a Metropolis-Hastings (MH) Markov chain Monte Carlo (MCMC) sampler (Metropolis et al., 1953; Hastings, 1970), preferring the relative simplicity in probing the multi-dimensional model space. We note that other non-linear inversion algorithms (neighbourhood algorithm, simulated annealing, etc.,) could also be used for the inversion.

4.2.3 Model Evaluation

For each iteration our MCMC sampler chooses a uniformly random model parameter vector, m_i. This parameter vector is parsed for all domains configured with free parameters into the model rotations (α, β, γ) and tensor dilution (s) and are applied to the domains using Voigt-Ruess-Hill averaging. We then trace each ray path through our model, computing the predicted shear-wave splitting operator (Γ, which can be characterised as the pair of splitting parameters $\phi_i, \delta t_i$) for each anisotropic domain that is encountered. These splitting operators are estimated by solving the Christoffel equation:

$$(C_{ijkl}X_iX_j - \rho v^2 \delta_{kl})U_k = 0\,, \tag{4.1}$$

where X_i and X_j define the wavefront normal, ρ is the density, v is the phase velocity, U_k is the polarisation unit vector amplitude and δ is the Kronecker delta function. We then calculate the corresponding inverse shear-wave splitting operators for each model domain and correct each waveform for the shear-wave splitting predicted by the current set of model parameters. To remove the predicted shear-wave splitting we apply the inverse shear-wave splitting operators to the input waveform data in reverse propagation order, following their non-commutative nature (Silver and Savage, 1994).

If the sampled model parameters are reasonable we would expect to correctly predict and remove the shear-wave splitting for every input waveform. Alternatively, in the case of null data (i.e., waveforms where there is no shear-wave splitting) the model must not introduce any spurious residual shear-wave splitting. Therefore we can test our model by measuring the shear-wave splitting of the corrected waveform data. We characterise any residual shear-wave splitting using the normalised second eigenvalue, λ_2, of the trace covariance matrix of each corrected waveform. By summing λ_2 for each path in our model we achieve a measure of the model misfit for a candidate model, m_i,

$$f(m_i) = \sum_{j=1}^{n} \lambda_{2_j}\,. \tag{4.2}$$

This measure of misfit is analogous to stacking λ_2 misfit surfaces (e.g., Wolfe and Silver, 1998). In our Metropolis-Hasting sampler, we define the target probability distribution as the reciprocal of this model misfit:

$$P(m_i) \propto \frac{1}{f(m_i)}. \tag{4.3}$$

This is then used to calculate the acceptance ratio, a, for each candidate model compared to the previous accepted model:

$$a_{i+1} = \frac{f(m_{i+1})}{f(m_i)}. \tag{4.4}$$

From the ensemble of accepted models returned by our MH sampler, we can then either estimate the probability density function (following the MCMC approach), assuming our approximated target function is reasonable, or find the suite of models with the smallest misfits. Here we use the ensemble of model misfits, using our MCMC sampler to efficiently explore the parameter space and not to estimate the final probability density function. This allows us to more effectively quantitatively compare and evaluate inversions using different base elastic tensors.

4.3 Inverting for seismic anisotropy beneath the Eastern Pacific

4.3.1 Dataset used

We are able to identify 52 shear-wave phases that pass through our target region (Fig. 4.3) from recent work studying SKS and SKKS shear-wave splitting in the eastern Pacific (Asplet et al., 2020) and a global ScS dataset (Walpole et al., 2017b). Prior to analysis each waveform is filtered using a two-pass two-pole butterworth filter with corner frequencies of 0.01 Hz and 0.05 Hz. We preprocess the waveforms to establish data quality, performing shear-wave splitting analysis using SHEBA (Wuestefeld et al., 2010), which implements the eigenvalue minimisation method (Silver and Chan, 1991; Walsh et al., 2013). It is worth noting that whilst we do not require prior knowledge of the measured splitting parameters, our inversion does require analysis windows and statistical properties such as the signal to noise ratio and degrees of freedom to be computed in advance (Wookey, 2012). For each phase, the start and end analysis window ranges are manually selected and the waveforms are inspected to ensure data quality. The optimum analysis window from the picked range is determined using cluster analysis (Teanby et al., 2004; Wuestefeld et al., 2010).

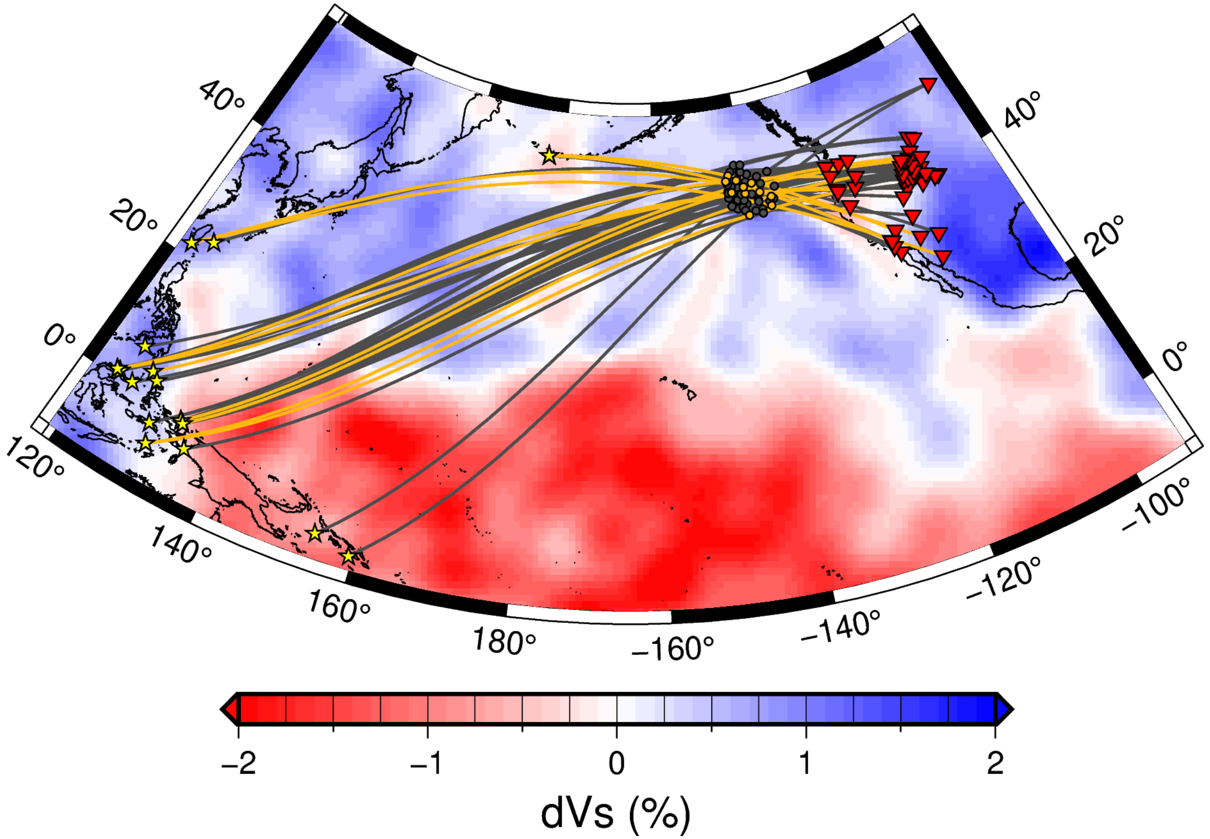

Figure 4.3: The 52 shear-wave phases (ScS, SKS and SKKS) considered for our inversions, plotted where each phases interacts with the core-mantle boundary (bounce points for ScS, pierce points for SKS and SKKS) along with the great circle path taken from source to receiver. Phases used in our inversion are coloured orange, with rejected data shown in grey. ScS bounce points and SKS/SKKS pierce points are calculated using the TauP toolkit (Crotwell et al., 1999) using the IASP-91 velocity model (Kennett and Engdahl, 1991).

Waveform data is only used in our inversion if the measured signal to noise ratio is greater than 10. Additionally, we test the quality of each splitting measurement using the quality factor, Q (Wüstefeld and Bokelmann, 2007) computed by SHEBA. We only include data where $Q \geq 0.7$ (i.e., a good split) or $Q \leq -0.9$ (a good null result).

This data curation leaves us with a final dataset of 11 shear-waves (2 ScS, 5 SKS and 4 SKKS phases) in our inversion (Fig. 4.4). Where each shear-wave phase being recorded at a separate station (Fig. 4.3, 4.5). Our backazimuthal coverage is restricted, with data having a backazimuth in the range of $270° - 290°$ or $310° - 315°$, which may introduce some directional bias into our inversions and make it challenging to distinguish between the different candidate elastic tensors. The coverage of the data used can be seen in figure 4.8, where I have drawn the sampling ray paths exiting each candidate elastic tensor. Prior to inversion, we measure the second eigenvalue of the trace covariance matrix for each (uncorrected) waveform. Summing these eigenvalues gives us a reference “misfit” for our input data of 1.743.

4.3.1.1 Upper Mantle Corrections

We define and apply pre-determined upper mantle corrections to our model. For our ScS data we use source and receiver side corrections derived from S and SKS shear-wave splitting (Walpole et al., 2017b). For SKS and SKKS phases, we take station averaged SKS results (Walpole et al., 2014) and assume that this adequately represents the shear-wave splitting each phase experiences in the upper mantle beneath the station. These corrections are incorporated in our inversion as fixed anisotropic domains that represent the upper mantle shear-wave splitting measurements.

4.3.2 Inversion configuration

As our targeted area of D$''$ is a small regional scale feature and our data are well grouped near its centre (fig. 4.5), we assume they sample a uniformly anisotropic region. This region can be represented by a single anisotropic domain in our inversion. We also assume that the domain is 250 km thick, with its base at the core-mantle boundary. Previous work in this region (Long, 2009; Asplet et al., 2020) has inferred azimuthal anisotropy, therefore we invert for the model parameters α, γ and s, keeping β fixed at 0°. For a transversely isotropic (TI) medium, α and

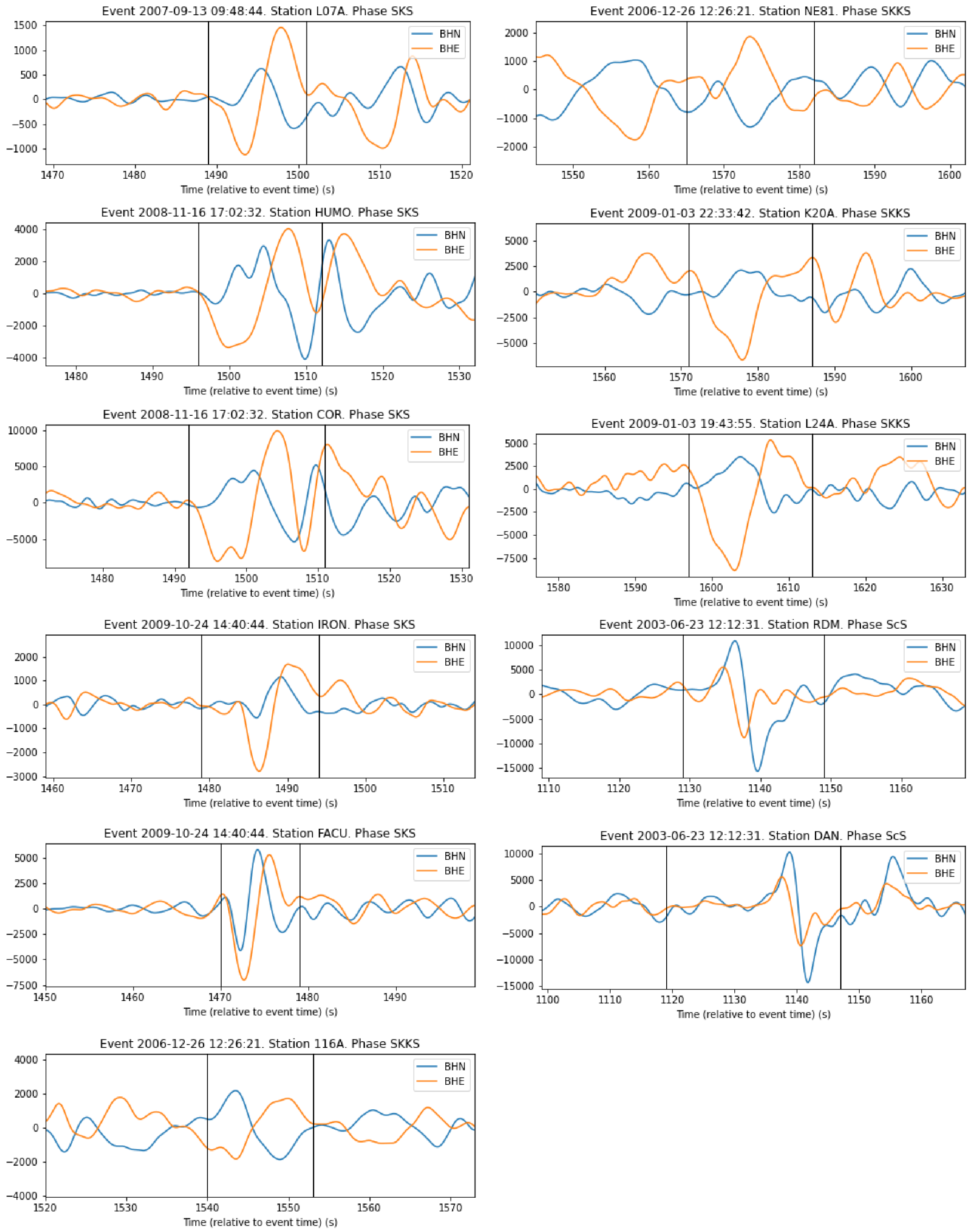

Event 2007-09-13 09:48:44. Station L07A. Phase SKS

Event 2006-12-26 12:26:21. Station NE81. Phase SKKS

Event 2008-11-16 17:02:32. Station HUMO. Phase SKS

Event 2009-01-03 22:33:42. Station K20A. Phase SKKS

Event 2008-11-16 17:02:32. Station COR. Phase SKS

Event 2009-01-03 19:43:55. Station L24A. Phase SKKS

Event 2009-10-24 14:40:44. Station IRON. Phase SKS

Event 2003-06-23 12:12:31. Station RDM. Phase ScS

Event 2009-10-24 14:40:44. Station FACU. Phase SKS

Event 2003-06-23 12:12:31. Station DAN. Phase ScS

Event 2006-12-26 12:26:21. Station 116A. Phase SKKS

Figure 4.4: Waveform data used in our inversions. The analysis windows, determined using the Wuestefeld et al. (2010) cluster analysis, are indicated by the black vertical lines. Particle motions in figure 4.7 are drawn only for data within the analysis windows.

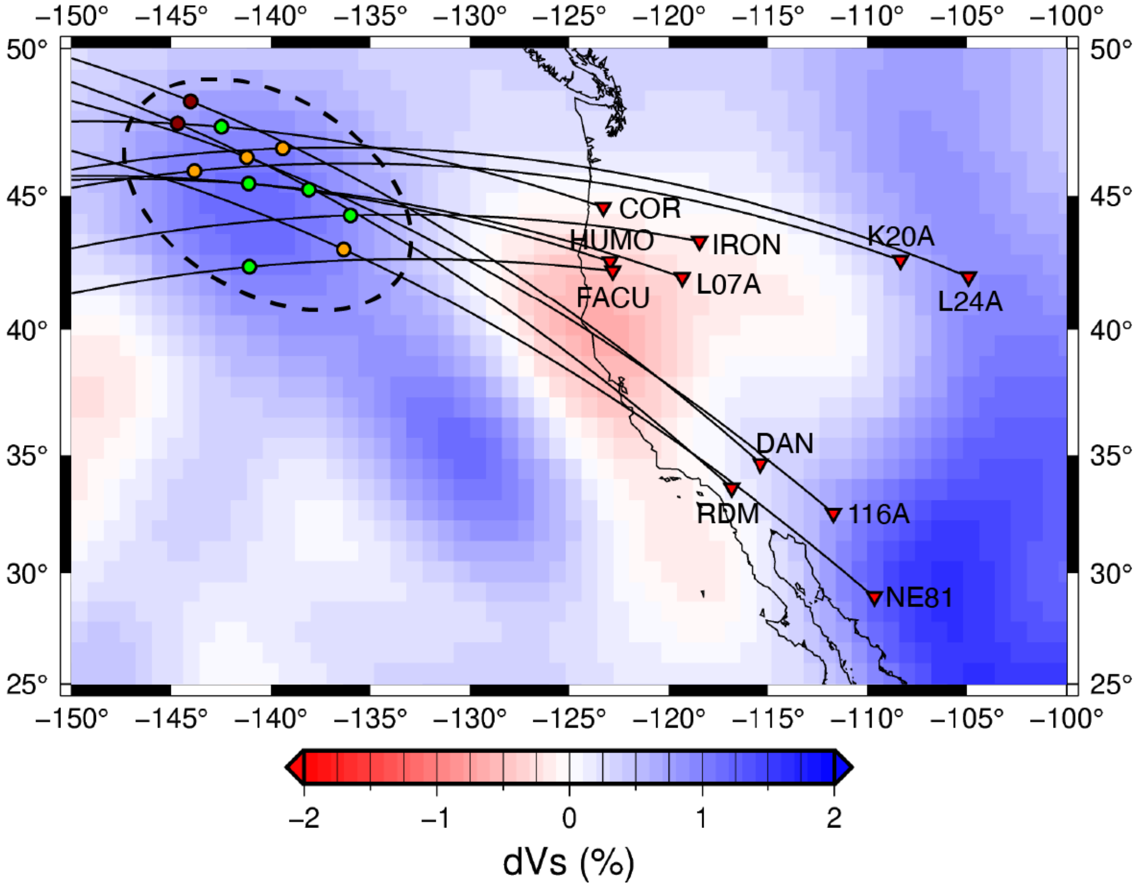

Figure 4.5: Great circle paths taken by each phase from source to seismic stations for the data used for our inversions. The 2 ScS phases (dark red) used are plotted at their core-mantle boundary bounce points. The 5 SKS (green) and 4 SKKS (orange) are plotted at their up-going core-mantle boundary pierce points. These locations are all calculated using the TauP toolkit (Crotwell et al., 1999) using the IASP-91 velocity model (Kennett and Engdahl, 1991). Our target region, which we assume to be uniformly anisotropic, is shown by the dashed ellipse. Also shown are shear-wave velocities (dVs) from the S40RTS tomographic model at a depth of 2800km (Ritsema et al., 2011).

γ correspond to the dip and strike of the symmetry plane, where $\alpha = 0°$ corresponds to vertical transverse isotropy (VTI) and $\alpha = 90°$ corresponds to horizontal transverse isotropy (HTI).

We perform inversions to evaluate a range of candidate elastic tensors, initially using a simple elliptical TI tensor. This model represents the effective anisotropy we might expect to see from, for example, SPO mechanisms such as the alignment of melt or heterogenous layers which have hexagonal symmetries (e.g. Backus, 1962; Karato, 1998b; Kendall and Silver, 1998) or LPO fabrics that have a dominant hexagonal component. Our choice of input tensor, with initial conditions VTI where $V_{SH} > V_{SV}$ (Fig. 4.6a), slightly restricts what we can model. As we do not allow the strength parameter s to be negative, this does not allow for TI anisotropy where $V_{SV} > V_{SH}$. We choose this starting tensor as global models of radial anisotropy generally prefer $V_{SH} > V_{SV}$ outside of the LLSVPs (Romanowicz and Wenk, 2017). We also invert for two commonly suggested candidates for D$''$ anisotropy, texture comprising the lattice-preferred orientation (LPO) of bridgmanite or post-perovskite (e.g., Tommasi et al., 2018; Creasy et al., 2020).

For bridgmanite, experimental results strongly suggest the dominant slip system in D$''$ conditions is [001](100) (Tsujino et al., 2016; Couper et al., 2020). To represent this in our model we rotate a single crystal bridgmanite elastic tensor (Wookey et al., 2005b) so that the [001] direction starts pointing along the X2 axis, with the (100) plane horizontal. In this configuration the model parameters α, γ correspond to the dip and strike of the (100) plane, with the [001] vector pointing down dip (Fig. 4.6b).

As there is no current consensus for a dominant slip system in post-perovskite under D$''$ conditions, we invert for both the [100](010) (Yamazaki et al., 2006; Miyagi et al., 2008) and [100](001) (Miyagi et al., 2010; Wu et al., 2017) slip systems. These candidate mechanisms have been shown to provide the most plausible fits to a range of seismic observations (e.g., Creasy et al., 2020). Again, we perform pre-inversion manipulation of a single crystal post-perovskite elastic tensor (Wookey et al., 2005b) to allow free rotation of each slip system where the slip plane is horizontal and [100] aligns with the X2 axis (fig. 4.6c,d).

In all our inversion we perform 2,000,000 iterations using our MH sampler with a 10,000 model burn-in period to stabilise the MCMC algorithm. It is worth noting that Wookey (2012) raises concerns over the potential computational expense of this inverse approach. Here, we are able to mitigate against this by parellelising the processing of each waveform for every sampled model. When using the optimal parallelisation of 1 thread per waveform in a high performance computing (HPC) environment, our inversions require only ca. 15 minutes of compute time. These inversion methods will inevitably become more expensive to run for larger models, where increased numbers of paths and domains increase the memory requirements. Small, well-designed, inversions offer a cheap method to probe D$''$ seismic anisotropy in a localised way.

4.4 Results

4.4.1 Elliptical transverse isotropy

The simple elliptical TI tensor performs well in our inversions, consistent with previous observations of D$''$ anisotropy in this region (Long, 2009; Asplet et al., 2020). Our inversion favours a tilted transverse isotropic (TTI) model which dips ~ 75° to the south-east (Fig. 4.6e, table 4.1). If we compare the best fitting model misfit of 0.254 to the representative misfit of 1.743 for the uncorrected input data, it is clear that the best model is accounting for the majority of the shear-wave splitting observed. When we correct the input waveforms using shear-wave splitting predicted by the best fitting model we can see that most phases are well linearised (fig. 4.7). For some phases, such as SKS recorded at HUMO and ScS recorded at DAN, are not perfectly linearised but do not show evidence of significant residual shear-wave splitting. This suggests that our assumption that all phases used in the inversion sample the same D$''$ is a reasonable one. Also, importantly, we are able to reproduce the null phases observed at stations NE81 and 116A.

Using this definition of the confidence region, it is clear that the best fitting model is exceedingly well constrained (Fig. 4.8a). There is a local minima when we slice through γ, s for the best fitting α parameter, but our sampler is able to disregard this and converge on the global minima. This gives us confidence that we are resolving seismic anisotropy from D$''$ and that we can strongly constrain the orientation and strength of a candidate model tensor.

4.4.2 Bridgmanite

The first mineralogical tensor we test is bridgmanite. Prior to the inversion, we rotate the base bridgmanite tensor (Wookey et al., 2005b) by 90° about the X2 axis and then by 90° about the X3

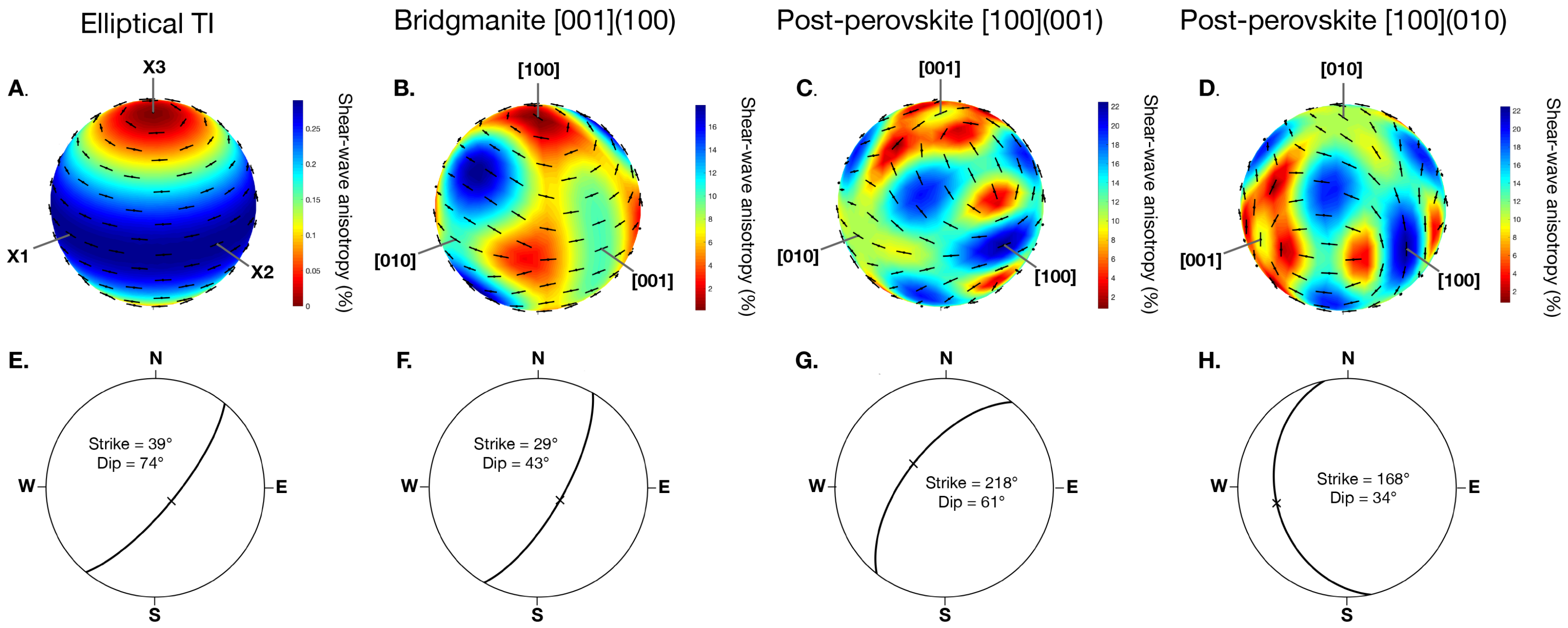

Figure 4.6: Initial model tensors (i.e., the model tensor when $\alpha = \gamma = 0°$), best fitting model tensor orientation and a stereonet plot showing the best fitting slip plane and direction for each of our candidate models: elliptical transverse isotropy (a,e), bridgmanite [001](100) (b,f), post-perovskite [100](001) (c,g) and post-perovskite [100](010) (d,h). Single crystal elastic tensors for bridgmanite and post-perovskite are taken from Wookey et al. (2005b).

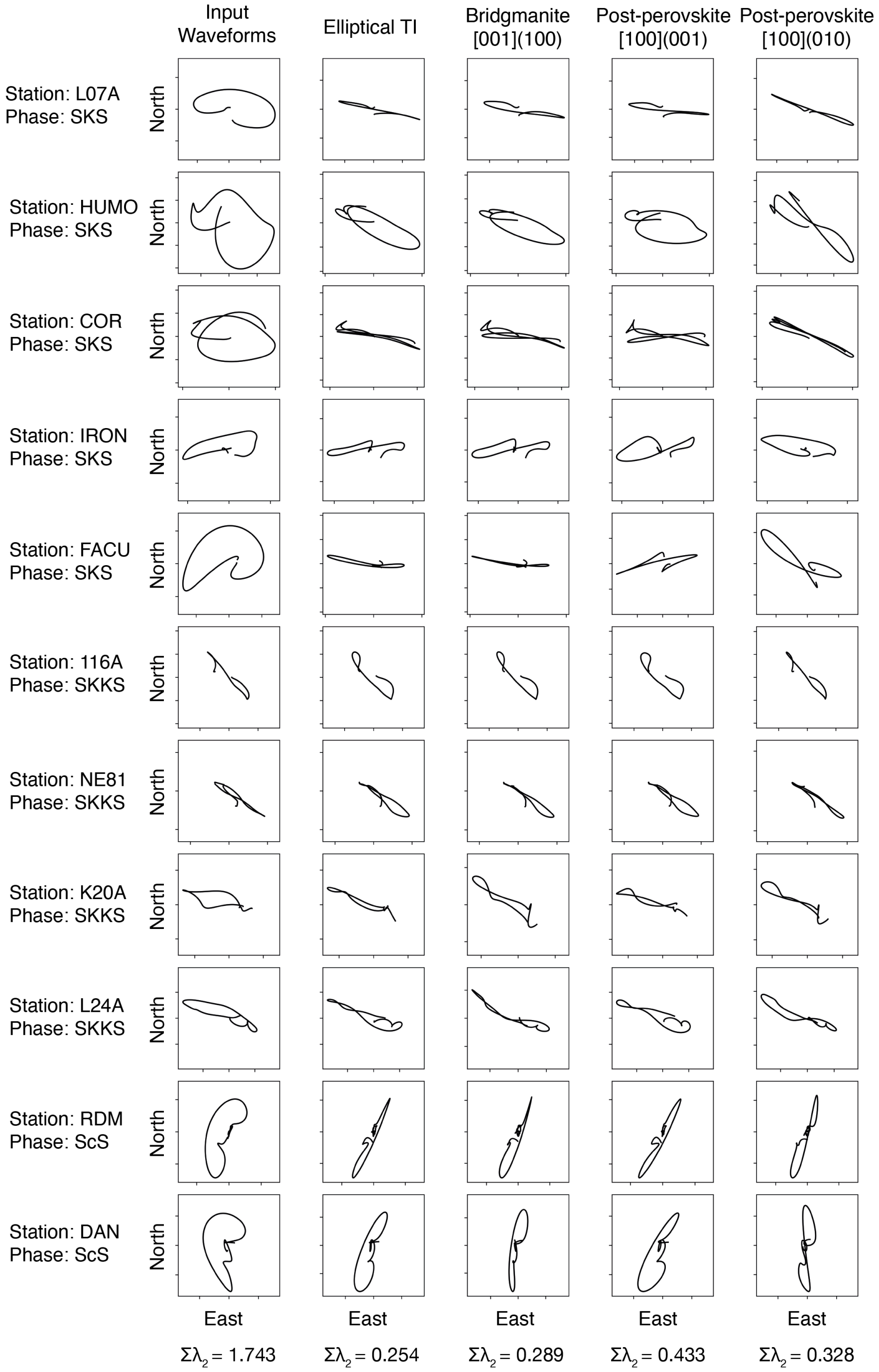

Figure 4.7: Particle motion plots for each phase used in our inversion. The first column shows the particle motions for our input data. The subsequent columns show particle motions for waveforms corrected by the best fitting model for each candidate mechanism that we test. From left to right these are elliptical transverse isotropy (TI), bridgmanite with [001](100) slip, and post-perovskite with [100](001) and [100](010) slip. At the base of each column the model misift (or representative misfit for the input waveforms), $\Sigma\lambda_2$ is shown.

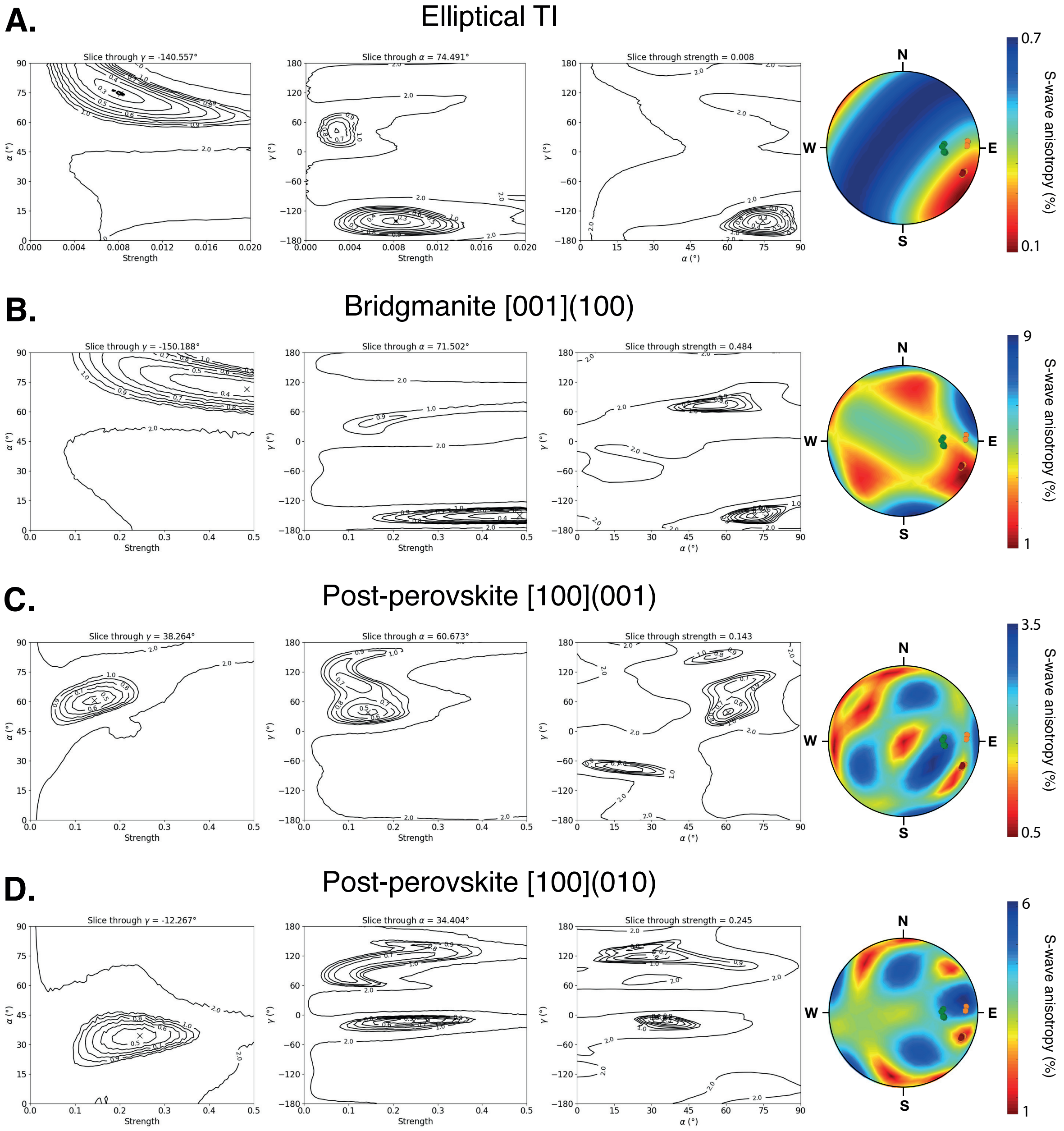

Figure 4.8: Summary of the inversion results for each of our candidate models. The contour plots show 2-D slices through our 3-D model space for each parameters intersecting at the best fitting model (blue cross). The right hand column shows upper hemisphere plot of the best fitting tensor orientation, with the black ticks indicating predicting fast shear-wave polarisation direction. Plotted on these best fitting tensors are paths taken by the data used in the inversions through the anisotropic domain, indicating what anisotropy each phase is sampling. The phases are drawn following the same scheme as figure 4.5, where the green circles representing the SKS data, the orange circles representing the SKKS data and the dark red circles representing the ScS data.

axis. This orients the elastic constants so that our inversion parameters α, γ correspond to the dip and strike of the (100) plane (Fig. 4.6b). This rotation represents the case where [001](100) is the dominant slip systems for bridgmanite (Tsujino et al., 2016; Couper et al., 2020).

We find the best fitting model gives a strike and dip of 029°/43° for the (100) plane (Fig. 4.6f). This model, with a misfit of 0.289, does not perform as well as the elliptical TI model. The difference in misfit is minor and we shall explore what constitutes a significant difference in misfit in a later section. Inspection of the corrected waveforms suggests that this difference is insignificant. The majority of waveform particle motions (Fig. 4.7) are as well corrected by the brigmanite model as elliptical TI. The main observable difference is the ScS phases recorded at DAN is better linearised, although this improvement is offset by minor shifts of the other phases. Our 2-D ensemble slices show that our inversion is convincingly converging to a unique solution for bridgmanite (Fig. 4.8b). The orientation parameters α, γ are exceedingly well constrained, whilst there is greater uncertainty in the strength parameter. Our inversion configuration does not allow us to fully capture the minima for the strength parameter (Fig. 4.8b) as we impose a maximum strength parameter of 0.5 for the single crystal inversions. This is to ensure inversion stability as strength parameters approaching 1 can cause the sampler to predict splitting operators with unphysically large delay times. Additionally for the single crystal tensors the strength parameter corresponds to the proportion of the domain that exhibits LPO. Having 50 % of D$''$ consist of perfectly aligned bridgmanite crystals is unfeasible so by imposing a maximum strength of 0.5 we are only excluding models which are physically unreasonable. For the bridgmanite model the best fitting strength parameter of 0.48 implies that 48 % of our model domain, approximately 121 km of D$''$, is crystal preferred oriented bridgmanite that has our best fitting orientation.

4.4.3 Post-perovskite

4.4.3.1 Inversion for a [100](001) dominant slip system

To correctly orient the [100](001) slip system, we rotate our single crystal post-perovskite tensor (Wookey et al., 2005b) by 90° about the X3 axis prior to the inversion. This rotates the elastic constants so that our model parameters α, γ correspond to the dip and strike of the (001) plane (Fig. 4.6c).

For this candidate slip system, our inversion favours a strike and dip of 218°/61° for the (001) plane (Fig. 4.6g) and strength parameter of 0.104 (table. 4.1). This result predicts lowermost mantle flow with an azimuth of 308° that has a substantial vertical component (Fig. 4.6g). The best fitting model has a misfit of 0.433 which is a worse fit than the previous TI and bridgmanite models, which have misfits of 0.254 and 0.289 respectively.

When we correct the input waveforms for the best fitting post-perovskite [100](001) model and compare it to our other candidate models we can see there are several phases which it cannot fully correct (Fig .4.7). Clear residual shear-wave splitting can be seen in the particle motion plots for SKS phases recorded at HUMO and IRON along with the ScS phase recorded at DAN. The post-perovskite [100](001) model is able to retrieve the null SKKS phases recorded at 116A and NE81 as well as our other models.

Examination of the model ensemble (Fig. 4.8c) shows that the best fitting model is well-constrained. In the slice through the best fitting strength parameter, $s = 0.14$, there are two local minima for α, γ, but our sampler is able to converge to a unique solution.

4.4.3.2 Inversion for a [100](010) dominant slip system

To correctly orient the [100](010) slip system, we rotate our base post-perovskite tensor (Wookey et al., 2005b) by 90° about the X3 axis and then by 90° about the X2 axis prior to the inversion. This rotates the elastic constants so that our model parameters α, γ correspond to the dip and strike of the (010) plane (Fig. 4.6d).

In this case, our best fitting model gives a strike and dip of 167.7°/34.4° for the (010) plane (Fig. 4.6h), with a strength parameter of 0.245 (table. 4.1). This corresponds to lowermost mantle flow with an azimuth of 257°. The [100](010) slip system offers an improved fit for post-perovskite, with a misfit of 0.328 compared to 0.433 for the [100](001) slip system. Although this is somewhat worse than misfit of the TI and bridgmanite models, it is unclear if the differences in model misfit are significant.

If we correct the input waveforms for our best fitting post-perovskite [100](010) model, the corrected particle motions (fig. 4.7) show that this slip system is able to correctly linearise the majority of paths in the model. Phases that were not well corrected by the (001)[100] model, such as the SKS recorded at HUMO and ScS recorded at DAN, are better treated by the (010)[100] best fitting model. This however trades off with residuals being introduced for SKS phases recorded at IRON and FACU, the latter being more concerning as it is well linearised by our other models. These trade-offs between models highlights the importance of utilising as broad a dataset as possible, in terms of backazimuth and inclination, in our inversions. Our 2D model ensemble slices also hint at the trade-offs between model parameters, in this case for the parameters γ and s. There is a pronounced secondary minima for these two parameters, when we slice through our best-fitting value for α (Fig. 4.8d), although the set of models it represents converge to a misfit of ca. 0.6 which is significantly larger that our final result. This again highlights the potential complexity in the model misfit surface and the importance in maximising the coverage achieved in the input data. Whilst the backazimuthal coverage of our dataset is somewhat limited, by using data from multiple phases we are sampling just a broad enough range of backazimuths and inclinations in our anisotropic domain to allow our inversions to strongly constrain a set of plausible orientations.

Model	α (°)	γ (°)	strength	misfit
Elliptical TI	75 ± 5	-141 ± 9	0.008 ± 0.002	0.254
Bridgmanite [001](100)	72 ± 5	-150 ± 32	0.48 ± 0.05	0.289
ppv [100](001)	61 ± 9	38 ± 35	0.14 ± 0.07	0.433
ppv [100](010)	34 ± 4	-12 ± 60	0.25 ± 0.05	0.328

Table 4.1: The best fitting models and the model misfit for each of the candidate mechanisms. For the elliptical transverse isotropic (TI) model α corresponds to the dip of the TI plane. For our bridgmanite and post-perovskite models α is the dip of the slip plane. The γ parameter is 180° offset from the strike of the TI or slip plane. For example our bridgmanite [001](100) model corresponds to the (100) plane with a strike/dip of 029°/72°. Uncertainties in our best fitting model parameters are derivied from bootstrap sampling (see supplementary figures B.1, B.2, B.3).

4.4.4 Testing inversion sensitivity and misfit significance

We investigate the sensitivity of our model parameters and our model misfits by bootstrapping our inversions. We randomly resample our input dataset and repeat the inversions for each candidate tensor. We take 500 random samples of our input data and repeat our inversions, extracting the best fitting model and its associated misfit. As model misfit is proportional to the number of paths used in the inversion, each of our samples randomly draws 11 paths, with replacement, from the original waveform data. For each of our candidate models we have already fully explored the parameter space in our previous inversions and know our sampler can converge to a unique solution. Therefore for our bootstrapped inversions we reduce the number of iterations of our

MH sample to 100,000. This is still a sufficient number of samples to achieve convergence for all inversions. This bootstrapping allows us to estimate uncertainties in both our model misfits and the model parameters α, γ, s (Figs. 4.9, B.1, B.2, B.3). This allows for robust estimation of uncertainty in all our model parameters except for γ where the periodicity of this model parameters results in a bimodal distribution (Fig. B.2).

The bootstrapping results show that the differences in misfit for our candidate models are not significant. For each of our candidate models, the best fitting model is within $1\,\sigma$ of the sample mean (Fig. 4.9). When we compare the misfit distributions for the different candidates, we can see the same trends that were observed when we compare the best fitting models. The elliptical transverse isotropic model has the lowest sample mean misfit of 0.222, followed by bridgmanite (0.267), post-perovskite [100](010) (0.286) and post-perovskite [100](001) (0.348). However the sample means of all the candidate mechanisms are within 1σ of each other and therefore we cannot formally distinguish between our models using misfit alone.

4.5 Discussion

By directly inverting shear-wave data we are able to uniquely constrain the best fitting orientation and strength for each of the candidate mechanisms for seismic anisotropy in our targeted region of D″. This offers some improvement over forward modelling techniques, which have struggled to identify unique orientations in some cases (Ford et al., 2015; Creasy et al., 2017). However this improvement in performance could stem from our inversions using more data than these previous studies, albeit with fewer unique azimuths, which has been shown to be crucial for constraining the orientation of seismic anisotropy in D″ (Wookey and Kendall, 2008; Creasy et al., 2019). Although we cannot confidently identify a single best fitting model, our results are instructive for future studies of D″ seismic anisotropy.

For our inversion method, as with forward modelling approaches, the challenge remains in quantitatively identifying a single mechanism to explain the seismic anisotropy in our targeted region of D″. The elliptical transverse isotropic model performs the best out of all the candidate mechanism we evaluate here, a result we might consider vexing given that forward modelling of LPO development in D″ argues strongly for an orthorhombic symmetry (e.g., Tommasi et al., 2018). The shape preferred orientation (SPO) of heterogeneities in D″ could reasonably give us a TI symmetry. As the initial conditions of our TI tensor is VTI with $V_{SH} > V_{SV}$ this restricts

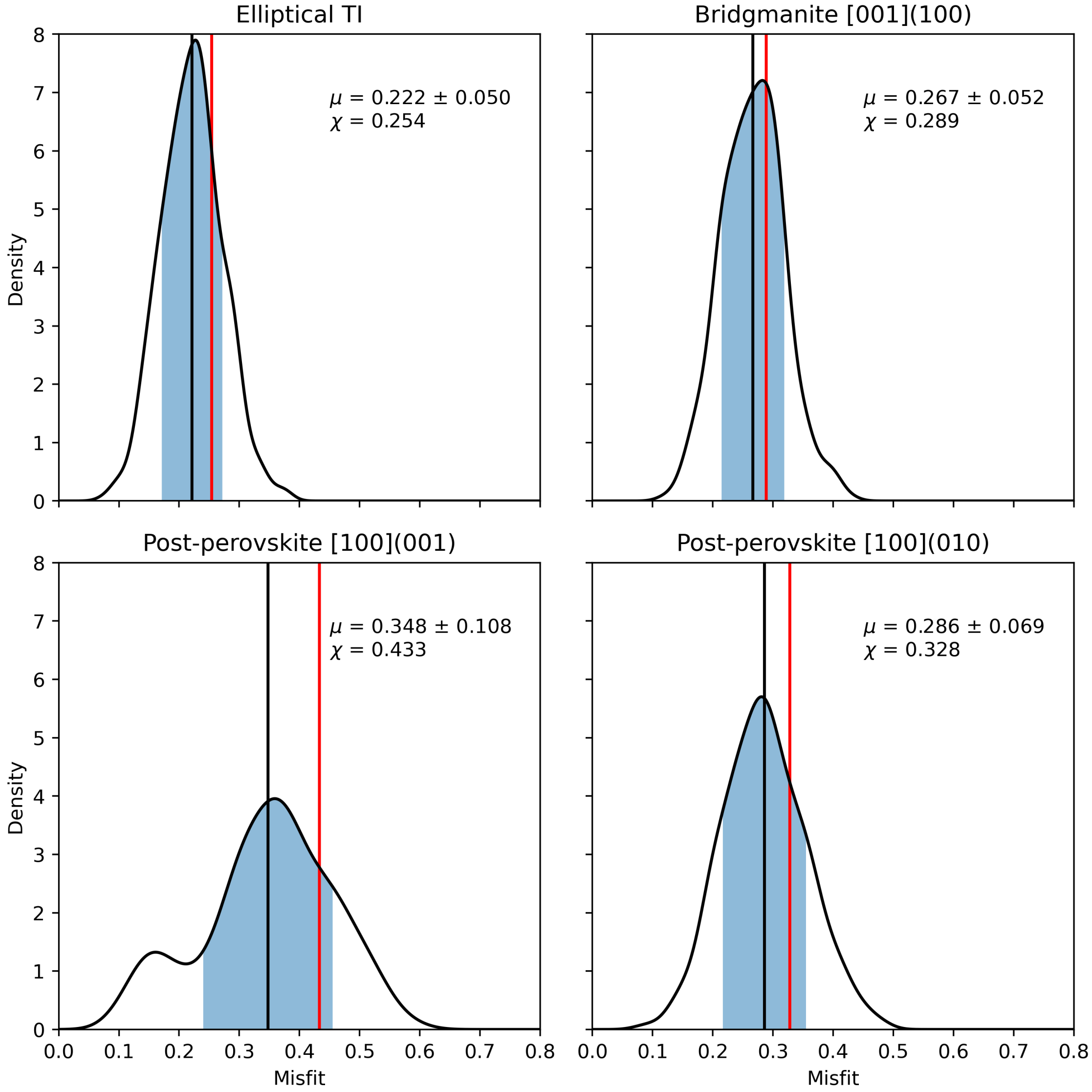

Figure 4.9: Results of our bootstrapped inversions summarised as probability density functions for model misfit. We use the same set of 500 samples for each candidate mechanism. The red vertical line indicates the model misfit from our main inversions (χ), where all 11 paths are used. The black vertical line indicates the mean of the bootstrapped model misfits (μ). The region within 1 standard deviation of the mean bootstrapped misfit is shaded blue.

the plausible SPO mechanisms. For example our results cannot be explained by near-vertical melt tubules as that mechanism would require a negative strength parameter. Plausible SPO mechanism include sheets of heterogeneous material, possibly remnant subducted slab material or thin lenses of post-perovskite, or melt layers, with a melt fraction $< 1\%$ (Kendall and Silver, 1996). However, it is worth noting that recent geodynanmic modelling suggests that it is is difficult to preserve melt a the core-mantle boundary (Dannberg et al., 2021). Alternatively this result can be interpreted as highlighting the poor performance of our single crystal mechanisms, with the effective anisotropy produced by LPO textures of post-perovskite or bridgmanite being more similar to TI than the orthorhombic single crystal symmetry. Similar results have been seen in recent visco-plastic self-consistent (VPSC) modelling of D″ anisotropy where most polycrystalline D″ textures, with the exception of post-perovskite [100](001) and ferropericlase, show anisotropy similar to a TI pattern (Creasy et al., 2020).

Of our single crystal mechanisms, bridgmanite gives the best misfit and returns orientation parameters ($\alpha = 72° \pm 5, \gamma = -150° \pm 32$) that are within the bootstrapped estimates of uncertainty of our best fitting TI model ($\alpha = 74° \pm 5, \gamma = -141° \pm 9$). However, purely examining model misfit does not necessarily ensure that the model is plausible, we must also consider the physical implications for D″ of each of our single crystal mechanisms. For our target region, the best fitting bridgmanite model has a strength parameter of 0.484, which implies that ca. 50% of D″ is perfectly aligned bridgmanite crystals. As D″ is expected to be ca. 70% (Mg, Fe)SiO_3 (Hirose et al., 2015) this could only be plausible if the deformation of bridgmanite can generate a very strong lattice preferred orientation texture. At D″ conditions, models of bridgmanite dislocation dynamics predict deformation by pure climb creep (Boioli et al., 2017), a mechanism that produces little to no lattice preferred orientation. Therefore it seems improbable that we are seeing such strong alignment of bridgmanite in our target region. With our target region sitting on a positive shear-wave velocity anomaly, which are generally inferred to be colder than average regions of D″, we would expect post-perovskite to be the more stable phase (e.g., Murakami et al., 2004; Tateno et al., 2009), an interpretation favoured by previous SKS-SKKS shear-wave splitting studies of this region (Long, 2009; Asplet et al., 2020). For these reasons we discount bridgmanite as a plausible mechanism for D″ anisotropy in this region.

An intriguing result is the contrast between the best fitting models for the two post-perovskite slip systems, [100](001) and [100](010), that we consider. Whilst we would expect the different slip systems to favour contrasting orientations, we would expect both results to return similar strength parameters instead of results of 0.14 ± 0.07 and 0.25 ± 0.05. Whilst the [100](010) slip system offers the better model misfit, it achieves this by requiring almost double the proportion of D$''$ that consists of preferentially aligned post-perovskite. For [100](010) our results require 25 % of D$''$ to consist of perfectly aligned post-perovskite crystals, compared to 14 % alignment for the [100](001) slip system. What this discrepancy in strength parameters tells us is that the backazimuthal coverage used is insufficient. If we compare the regions of the best fitting elastic tensors that are strength of anisotropy sampled by each group of phases is similar across all three single-crystal models. For these orthorhombic tensors, our sampler is able to find an orientation which when appropriately scaled by the strength parameter can reasonably explain our input data. This is not an inherent issue with the inversion technique and indeed issues with backazimuthal coverage affect forward modelling methods as well (e.g., Creasy et al., 2019), but it is an issue that needs to be considered when designing future inversions. For this reason, as in previous work, we struggle to prefer a single post-perovskite slip system (e.g., Ford et al., 2015; Creasy et al., 2017, 2020). This discrepancy in preferred strength parameter between the two slip systems offers a potential future avenue for comparison, if we can determine what is a plausible proportion of LPO post-perovskite in D$''$.

4.5.1 Implications for the lowermost mantle

For each candidate mechanisms, we are able to infer an expected mantle flow direction in our target region D$''$ from the best fitting orientation parameters. We assume that deformation is due to simple shear along the symmetry plane for our TI model and along the dominant slip planes for our single crystal models. This gives us predicted flow directions that correspond to the slip direction along the best fitting orientation of the slip plane from our inversions (Fig. 4.6). For example, our results for post-perovskite with [100](001) as the dominant slip system predicts Northwesterly flow which is downwelling, as the best fitting model has the [100] axis dipping 60° with an azimuth of 308°.

We compare these predicted flow directions to two recent mantle flow models (Fig. 4.10). The first model, TX2008.V2, is determined by the joint inversion of global S-wave travel times, the global gravity field, dynamic surface topography, tectonic plate motions and the excess ellipticity of the core-mantle boundary (Simmons et al., 2009). The second flow model is based on global mantle

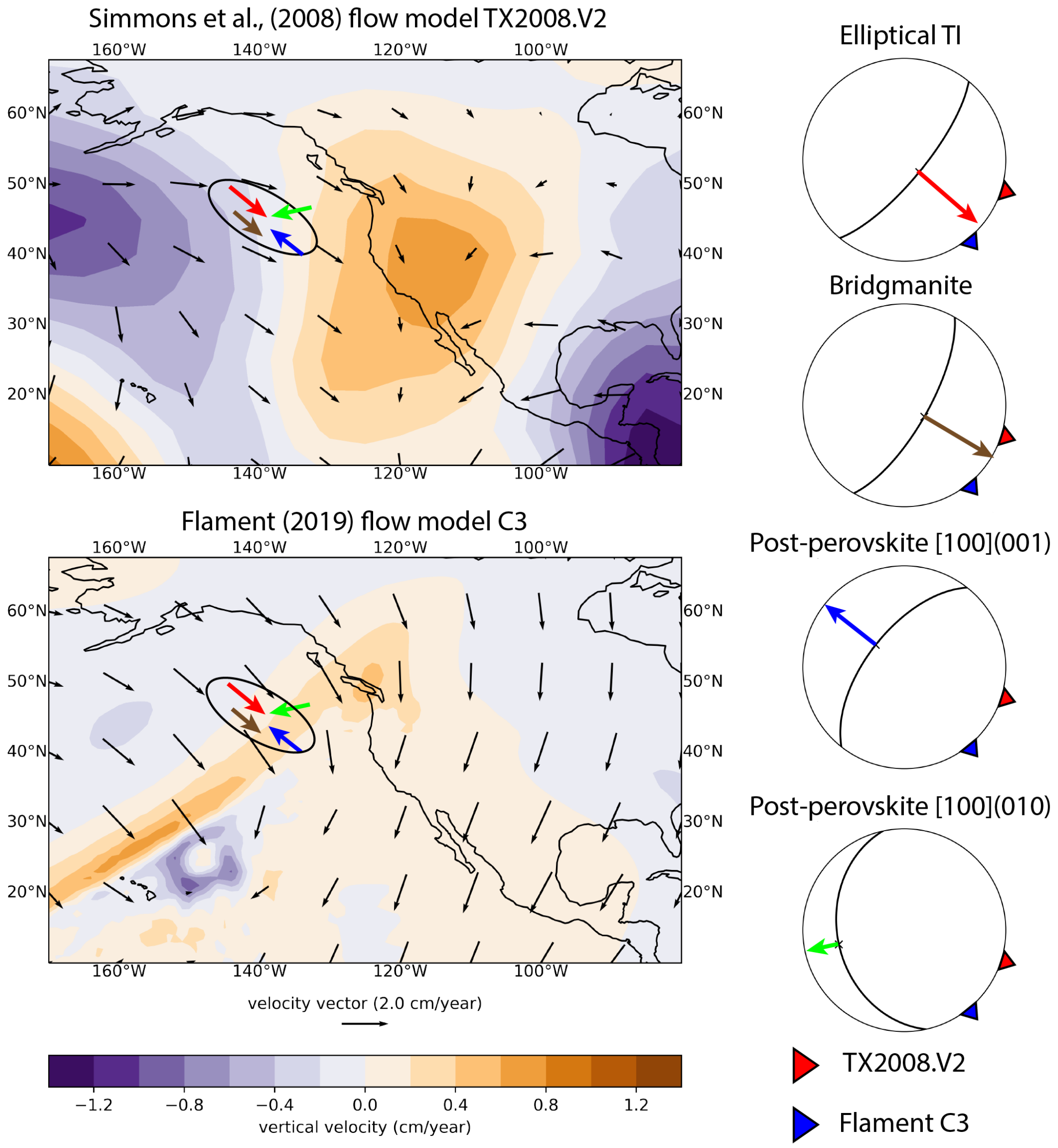

Figure 4.10: Map comparing the flow directions implied for our target region (circled) by our inversion results and the lowermost mantle flow models of Simmons et al. (2009) and Flament (2019). Also shown are stereonets showing the best fitting slip plane indicated by our results, plotted as in figure 4.6. The coloured arrows annotated on the stereonets and flow models indicate the horizontal flow implied our model results for elliptical TI (red), bridgmanite (brown), post-perovskite [100](001) (blue) and post-perovskite [100](010) (green). The coloured triangles on the stereonets indicate the horizontal flow direction predicted by the Simmons et al. (2009) model (red) and the Flament (2019) model (blue).

convection simulations driven by tectonic reconstructions including subducting slab and LLSVP locations, dynamic topography data and global tomography models (Flament, 2019, Case 3). There is limited agreement between the models across the Eastern Pacific region in general, but for our study area both models predict approximately Southeasterly flow that is predominantly horizontal (Fig. 4.10). A simple comparison of velocity vectors to our predicted flow directions demonstrates the potential insights that can be gained from comparing seismic anisotropy results to global convection models. Future work will require a more detailed framework for comparing results, with the ultimate aim of incorporating seismic anisotropy results into global geodynamic models to constrain flow orientations in D″.

Our TI model shows good first order agreement with TX2008.V2 and the Flament model for horizontal flow if we assume that flow is downwelling (i.e., flow is going down the dipping TI plane). In the TI case we have no constraint on shear directions as either upwelling or downwelling flow could cause the alignment of layers. In either case given that our TI model is steeply dipping, with a dip of 74°, we would expect stronger radial flow than TX2008.V2 predicts. The bridgmanite model also shows good agreement for horizontal flow direction, but the orientation of the [001] axis predicts downwelling flow which disagrees with both flow models. The post-perovskite models however do not show good agreement with either flow model. The post-perovskite [100](001) model does agree with the predicted orientation of horizontal flow, although the orientation of the [100] axis implies flow in the opposite, northeast, direction compared to the southeasterly flow predicted by both models (Fig. 4.10). This can be reconciled if flow is upwelling (i.e., flow up the dip of the (001) plane in the [-100] direction) as the symmetry of the single crystal tensor allows for either solution. This interpretation is consistent with the (Flament, 2019) flow model which predicts modest upwelling in our study region. Post-perovskite [100](010) does not agree with either flow model. However this does not necessarily mean that this mechanism can be discounted. In future work, if we can confidently discriminate between candidate mechanisms, these results could be used to test mantle flow models.

Previous studies of our target region of D″ have invoked the impingement of downgoing Farallon slab material to explain the seismic anisotropy observed (Long, 2009; Asplet et al., 2020). The downwelling of material in our study region is not supported by either mantle flow model. However our anisotropy results, particularly the TI model, do suggest stronger vertical deformation than the mantle flow models. There is strong evidence for Farallon slab material having reached the core-boundary beneath North America from plate motion models (Richards and Lithgow-Bertelloni, 1998), global tomography (e.g., Ritsema et al., 2011) and shear-wave splitting (Nowacki et al., 2010). A potential explanation for our results is that our target region is comprised of orphaned Farallon slab material, where the tip of the slab has broken off below 660 km depth leaving the 'parent' slab to travel laterally in the mid-mantle before later descending to the core-mantle boundary (Grima et al., 2020). This orphaned slab material has accumulated at the core-mantle boundary and has been subsequently deformed by the prevailing, predominantly horizontal, flow regime. Alternatively our target region could be comprised of remnant material from some other paleoslab that has accumulated at the core-mantle boundary.

4.5.2 Future development of shear-wave inversion

Despite the success of our inversion technique in constraining the orientations of potential mechanisms for D″ seismic anisotropy, there are some important limitations to consider and overcome if we are to expand our inversions for broader swaths of the lowermost mantle. To constrain anisotropy in D″ we need crossing ray paths and, ideally, ScS, SKS and SKKS shear-wave data. There are large regions of the lowermost mantle where we currently do not have sufficient data to constrain D″ anisotropy (Creasy et al., 2019). This is further constrained by the requirement that we only use data recorded at stations where we have a good knowledge of upper mantle anisotropy so we can correct for it. One potential avenue to explore is the incorporation of SdS and PdP reflected phases as the reflection polarities can help constrain D″ seismic anisotropy (Pisconti et al., 2019).

Another limitation is the assumption that each inversion domain is uniformly anisotropic. We assume that all the waveforms input into our inversions are sampling the same seismic anisotropy in D″. The persistent residual splitting we observed at IRON suggests that these assumptions can be flawed, although for our work it does not have any significant effect on the results. Improved treatment of the data, particularly of ScS phases which we assume sample the same anisotropy on both sides of the core-mantle boundary bouncepoint, in future work is desirable and would further improve the accuracy of results.

Finally, there is the question of the applicability of using single crystal tensors in future studies of D″ seismic anisotropy. As we seek to constrain both the composition and dynamics of D″ it is imperative that we use candidate mechanisms that best reflect potential anisotropic textures in D″. That our single crystal models where outperformed by a simple TI model is perhaps indicative that the effective anisotropy that we can observed is not best represented by single crystal tensors, especially with VPSC modelling showing that some strained D″ fabrics show a strong hexagonal symmetry component instead of the starting orthorhombic crystal symmetry (Creasy et al., 2020). Future work, using our inversion method to exhaustively test libraries of VPSC models for D″ seismic anisotropy calculated for a wide range of plausible assumptions for deformation geometry, slip system, mineralogy and strain (Creasy et al., 2020) is needed to confidently interpret mantle flow.

4.6 Conclusions

We have outlined a framework for the direct inversion of shear-wave waveform data for the orientation and strength of seismic anisotropy in D″. By jointly inverting SKS, SKKS and ScS data which image a fast shear-wave velocity anomaly beneath the Eastern Pacific, we have demonstrated that our method can uniquely constrain the orientation of different candidate elastic tensors and allows for quantitative evaluation of these candidates. All four of our candidate mechanisms can plausibly explain our input data when assessed purely in terms of model misfit, with a simple transverse isotropic tensor proving the best fit. Interrogation of the best fitting model parameters, particularly the anisotropic strength parameter suggests that post-perovskite is the most plausible single crystal mechanism, although we are unable to uniquely identify a dominant slip system. Our method for direct inversion of shear-wave data gives us a powerful new tool to accurately constrain lowermost mantle anisotropy. This complements recent advances in modelling expected D″ textures for different candidate minerals and slip systems (Creasy et al., 2020). Together these advances offer the potential to give us great insights into seismic anisotropy in D″ and begin to constrain flow at the base of the mantle.

4.7 Acknowledgements

We would like to thank Andrew Walker and Nicolas Flament for providing the mantle flow models used in this work. JA is supported by a NERC GW4+ Doctoral Training Partnership studentship from the Natural Environment Research Council [NE/L002434/1] and by a postgraduate grant from the Government of Jersey. The facilities of IRIS Data Services, and specifically the IRIS

Data Management Center, were used for access to waveforms, related metadata, and/or derived products used in this study. IRIS Data Services are funded through the Seismological Facilities for the Advancement of Geoscience (SAGE) Award of the National Science Foundation under Cooperative Support Agreement EAR-1851048. Figures were drawn using Matplotlib (Hunter, 2007), Cartopy (Met Office, 2010 - 2015) and GMT (Wessel and Smith, 1995).

CHAPTER 5

CONCLUSIONS

Advances in global seismic tomography, geodynamics and mineral physics have given us a increasingly detailed picture of D$''$ as a thermochemical boundary layer full of structural, and potentially compositional, heterogeneities. Despite these advances, significant outstanding questions remain. What are the current dynamics of D$''$? Are LLSVPs remnants of primordial mantle, slowly growing accumulations of subducted material or clusters of thermal plumes? How variable are the temperature conditions, which control the prevalence of post-perovskite, in D$''$ and are critical for convection in the outer core? Are there significant amounts of melt near the core-mantle boundary? These are all questions that can be potentially answered if we can perform detailed studies of seismic anisotropy in D$''$.

Our understanding of seismic anisotropy in D$''$ is at something of a crossroads. Increased instrumentation has given us ever-growing seismic datasets that have enabled detailed regional scale shear-wave splitting studies of D$''$, particularly studies of SKS and SKKS phases in recent years (e.g., Long, 2009; Deng et al., 2017; Creasy et al., 2017; Grund and Ritter, 2018; Reiss et al., 2019; Lutz et al., 2020). It has, however, proved challenging to discriminate between the range of candidate mechanisms for seismic anisotropy in D$''$. Lattice preferred orientation of post-perovskite, bridgmanite and ferropericlase, along with shape preferred orientation models can plausibly explain most shear-wave splitting observations (e.g., Ford et al., 2015; Creasy et al., 2017). We have lacked the frameworks to robustly identify discrepant SKS-SKKS shear-wave splitting and to use shear-wave splitting observations to strongly constrain the orientation of candidate mechanisms for seismic anisotropy in D″. This motivates the work done in my thesis, to develop methods that will allows us to better constrain and understand D″ seismic anisotropy.

New methodologies, however, require a high quality dataset to test them. In Chapter 2 I built a new global dataset of SKS-SKKS shear-wave splitting, with the final dataset containing 522 high-quality SKS-SKKS event-station pairs. By using broadband data, I am able to resolve SKS shear-wave splitting that was previously classified as nulls (Walpole et al., 2014). I find that ca. 17 % of my dataset shows discrepant shear-wave splitting, which is over three times greater than previous studies (Niu and Perez, 2004; Restivo and Helffrich, 2006). These results suggest that azimuthal anisotropy may be more widespread in D″ than previously believed. Additional analysis of splitting intensity measurements using my global dataset highlight systematic discrepancies between measuring splitting intensity by projection (Chevrot, 2000) and approximating splitting intensity from measured splitting parameters. This result shows that it is unsafe to revisit catalogs of existing splitting parameters using the splitting intensity approximation to perform new analysis.

As the majority of my SKS-SKKS dataset (219 pairs) covers the Eastern Pacific region I focus on this region to develop new techniques to probe D″ seismic anisotropy. In Chapter 3 (published in Asplet et al., 2020) I explore discrepant SKS-SKKS shear-wave splitting using data from the Eastern Pacific and synthetics. Using these I show that current methods for identifying discrepant shear-wave splitting have limitations that may lead to both false positive and negative results. To address this I have developed a new multi-parameter method for studying discrepant shear-wave splitting, combining a new measure derived from the eigenvalue minimisation method used to measure shear-wave splitting and splitting intensity discrepancies. This new technique allows for robust analysis of discrepant shear-wave splitting and for easier automation.

When I apply this new technique to my Eastern Pacific SKS-SKKS shear-wave splitting data, the results highlight a significant region of azimuthal anisotropy in D″, near the Eastern margin of the Pacific LLSVP. The longitudinal transition from matching to discrepant shear-wave splitting points to a change in D″ seismic anisotropy across the Eastern Pacific. These results are best explained by lattice preferred orientation of post-perovskite, where the change in anisotropy is potentially due to post-perovskite transitioning to bridgmanite. A potential model to achieve these conditions in D″ is the impingement of material from the Farallon slab near the core-mantle boundary.

In Chapter 4 (submitted as Asplet et al., 2021) I set out to test my interpretation of post-perovskite in the Eastern Pacific. To achieve this I develop a technique to directly invert multiple phases of shear-wave waveform data for the orientation and strength of seismic anisotropy in D''. This method allows us to quantify how well candidate models explain observed shear-wave splitting and allows us to combine observations from multiple shear-wave phases. I demonstrate this by jointly inverting SKS, SKKS and ScS data which image a fast shear-wave velocity anomaly beneath the Eastern Pacific. The inversion results strongly constrain the orientation of the different candidate elastic tensors and allows for quantitative evaluation of these candidates. In this case, all four candidate mechanisms can plausibly explain the input data when assessed purely in terms of model misfit. A simple transverse isotropic tensor, such as might result from the shape preferred orientation of melt (e.g., Kendall and Silver, 1996) or potentially a strained lattice preferred orientation (LPO) post-peroskite fabric (Creasy et al., 2020), provides the best fit. Interrogation of the best fitting model parameters, particularly the anisotropic strength parameter suggests that post-perovskite (with either [100](001) or [100](010) as the dominant slip system) is the most plausible of the mechanisms that I have evaluated. The predicted horizontal flow directions for the elliptical TI and post-perovskite [100](001) show good agreement with recent mantle circulation models (Simmons et al., 2009; Flament, 2019), whilst post-perovskite [100](010) does not. However, post-perovskite [100](010) cannot be discounted as a candidate mechanism at this stage. If post-perovskite is responsible for seismic anisotropy then the most reasonable explanation is the accumulation of subducted slab material at the core-mantle boundary. This subducted slab could consist of 'orphaned' material from the Farallon slab (Grima et al., 2020) or remnant material from a previous paleoslab that has accumulated in this region.

5.1 Future Work

The techniques that I have developed here will allow us to further probe lowermost mantle seismic anisotropy. The main issue that has plagued its study is our inability to uniquely identify a candidate mechanism and constrain its orientation, limiting our ability to interpret lowermost mantle seismic anisotropy in terms of mantle flow. Until we can achieve this, the prospect of mapping flow across the lowermost mantle is a distant prospect. Whilst my inversion technique can strongly constrain the orientation of mechanisms, it is still challenging to distinguish between different mechanisms using seismic observations alone. Future tests using full-waveform synthetics could be used to determine what conditions are required to confidently discriminate between mechanisms. Recent work has demonstrated that the new global wavefield simulation code AXISEM3D (Leng et al., 2019) can efficiently simulate the global wavefield for various anisotropic models at the base of the mantle (e.g., Tesoniero et al., 2020; Wolf et al., 2021). From these simulations it is clear that SKS and SKKS are sensitive to lowermost mantle anisotropy, although finite frequency effects can cause some small discrepancies in the upper mantle (Tesoniero et al., 2020). Tests of synthetic SKS, SKKS and ScS sensitivity to heterogeneous anisotropy suggest that these phases are only sensitive to layers of anisotropy that are more than 80 km thick (Wolf et al., 2021). These experiments also suggest that the ray theory assumptions that I have made are generally reliable for SKS and SKKS, but for complex anisotropic scenarios the full-wave effects can become significant (Wolf et al., 2021) and these effects will require more careful consideration in the future. The recent advances in full-waveform synthetics are exciting and offer a new avenue to explore how well we can constrain D'' anisotropy with our current techniques and to develop new methods to exploit all the information held in the full seismic wavefield.

Currently we are reliant on external constraints from mineral physics, although there is the potential to leverage geodynamic modelling to reduce the search space for the orientation parameters. In Chapter 4 I am only able to discount bridgmanite as a mechanism using mineral physics constraints from Boioli et al. (2017), as it appears to be too strong to produce the ca. 50% alignment required. Distinguishing between the two candidate slip-system for post-perovskite will likely require further advances in mineral physics, either from advanced atomistic computations or from further experiments on $MgSiO_3$ post-perovskite and its low-pressure analogues. When we are able to confidently identify a single mechanism, the comparisons of anisotropy to mantle flow models will become an invaluable constraint for geodynamic models.

There are also further improvements that can be made to my inversion method and to other observational methods. The treatment of ScS phases can be improved to better reflect the true ray geometry. More critical is the need to expand our coverage both spatially and azimuthally, as multiple crossing raypaths are required to accurately constrain the orientation of seismic anisotropy (Creasy et al., 2019). There are large swaths of the lowermost mantle that have not been studied. As the locations of good source events are fixed, the only way we can improve our coverage in through increased instrumentation. As I show in Chapter 2 Eastern Asia is a potentially interesting region, near the Eastern margins of the Pacific LLSVP that we should be able to study in great detail using data from Chinese arrays. Searching for discrepant SKS-SKKS shear-wave splitting, which my global dataset shows some evidence for in Eastern Asia, is a useful technique that allows us to search for azmiuthal anisotropy in D$''$ before committing to the more data intensive inversions.

The most exciting future avenue is ocean bottom seismometers, which will allows us to probe new regions of D$''$, such as beneath the Central Pacific, Southern Atlantic and Southern India ocean. Regions that cannot be sampled using land based stations. Building a truly global dataset of ScS, SKS, SKKS and potentially Sdiff shear-wave splitting is the first step towards being able to constrain seismic anisotropy throughout the lowermost mantle. With my current inversion method global scale inversion seems unfeasible as each anisotropic domain adds an extra 3-dimensions to the model parameter space. As we slowly move towards whole mantle inversions the method will undoubtedly require revisions, or our inversion strategy will have to be carefully designed to reduce the parameter space.

The accuracy of the input elastic tensors is crucial for any modelling of D$''$ seismic anisotropy. My inversion results have shown that mechanisms, such as bridgmanite, can reasonably explain the input data, but physical implications of the models (the required alignment in this case) are unrealistic. Using single-crystal tensors is also undesirable, as these tensors do not necessarily represent the anisotropic fabric that would develop in lowermost mantle conditions. Recent visco-plastic self-consistent modelling has given us a library of candidate tensors (Creasy et al., 2020). Incorporating these into future inversions is an exciting proposition, albeit one that could computationally expensive if we fully explore the library of 336 elastic tensors. Constraints could also be improved by including other seismic observations, such as PdP, SdS reflection polarities (Pisconti et al., 2019) and Stoneley modes (Koelemeijer et al., 2017). Probing attenuation anisotropy in D$''$ is one exciting future avenue to identify potential melt SPO in D$''$ and add further constrains to seismic anisotropy. Combining these different observations would be intriguing to explore and may allow us to uniquely constrain D$''$ seismic anisotropy and move toward mapping flow in the lowermost mantle.

The techniques that I have developed are not restricted to studies of D$''$ alone. My discrepant shear-wave splitting method could be adapted to search for discrepancies between any set of comparable shear-waves. For example, it could be used to search for changes in anisotropy before and after hydraulic fracture stimulation using observations of shear-wave splitting in microseismic data (e.g., Verdon and Kendall, 2011). Equally my inversion technique can be applied to any setting where retrieving the orientation and strength of seismic anisotropy from shear-wave data is desirable. Indeed, upper mantle and near-surface applications may be more favourable as the backazimuthal coverage tends to be more complete. Studying subduction zone anisotropy (e.g., Abt and Fischer, 2008) would be an interesting prospect to invert for multiple layers of anisotropy, as would studying ice fabrics within glaciers (e.g., Smith et al., 2017).

APPENDIX A

APPENDIX A - SUPPLEMENTARY FIGURES FOR CHAPTER 3

This appendix contains the supplementary figures from Asplet et al. (2020), which constitutes chapter 3 of this thesis.

A.1 Supplementary Figures

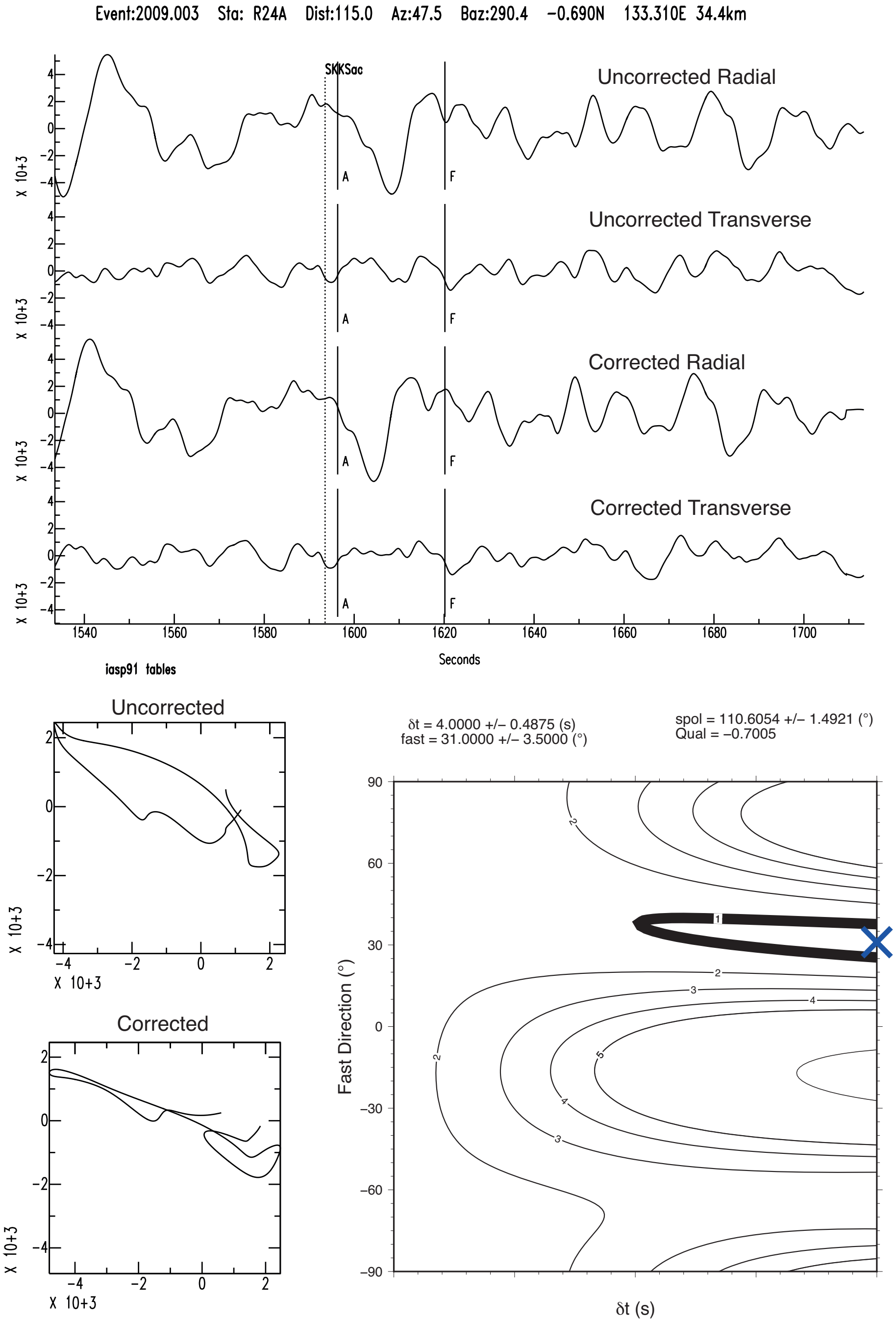

Figure A.1: A null SKKS phase at station R24A as measured by SHEBA (see figure 3.2 for an SKS example). Here we show the uncorrected and corrected traces (top) and particle motions (below left), along with the eigenvalue surface (below right). This example has the highest Q value of all identified nulls used in our study, a classification that is easily confirmed when inspected the particle motion and eigenvalue surface. Note how the grid search algorithm has moved across towards the maximum δt. This trend is seen throughout our dataset.

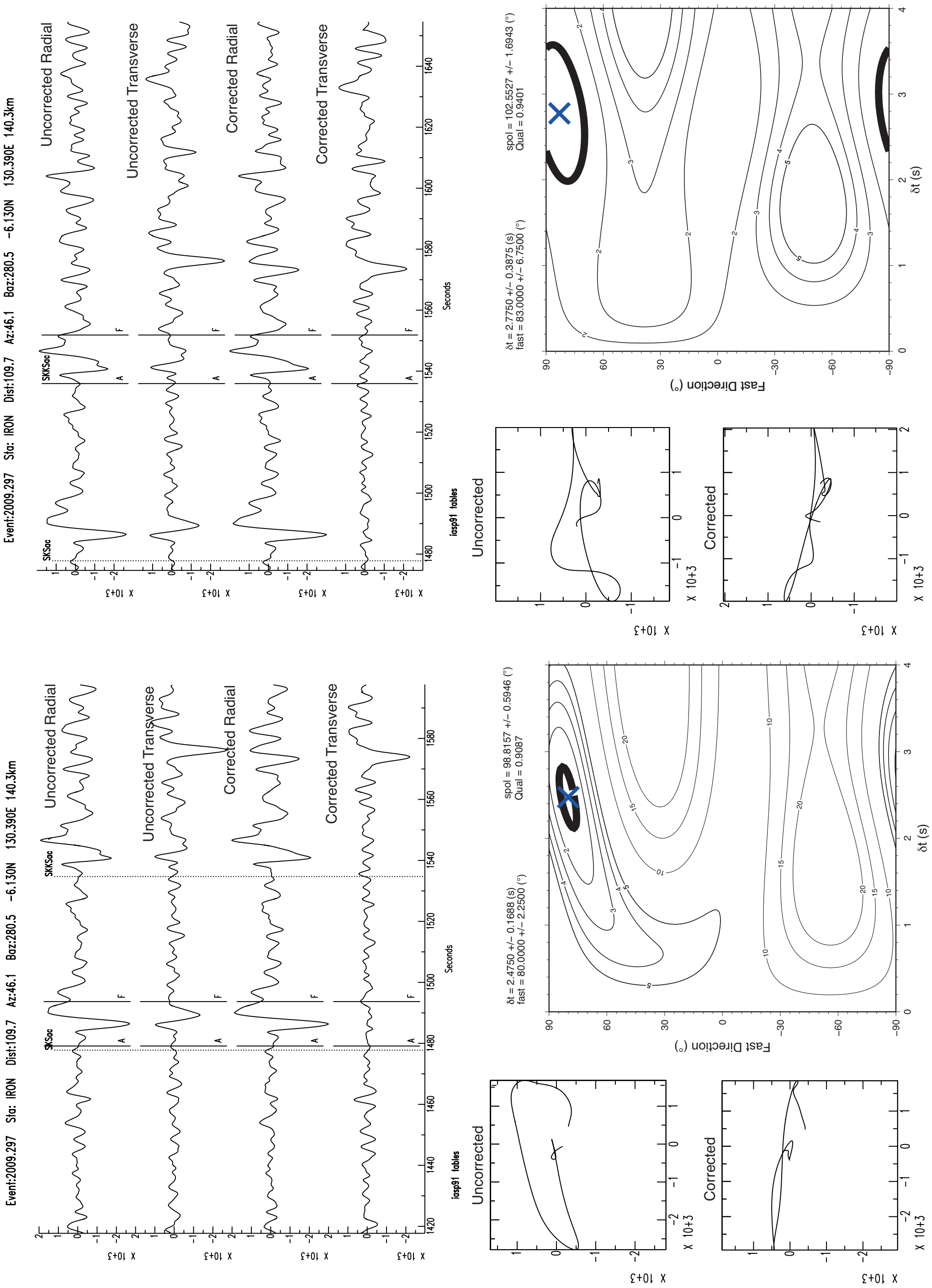

Figure A.2: A matching SKS-SKKS event-station pair recorded at station IRON. This case shows an example where $\Delta SI = 0.59$, which would classify this pair as discrepant. By including our $\bar{\lambda_2}$ test we instead classify this pair as matching, which is evident from the agreement of the splitting parameters.

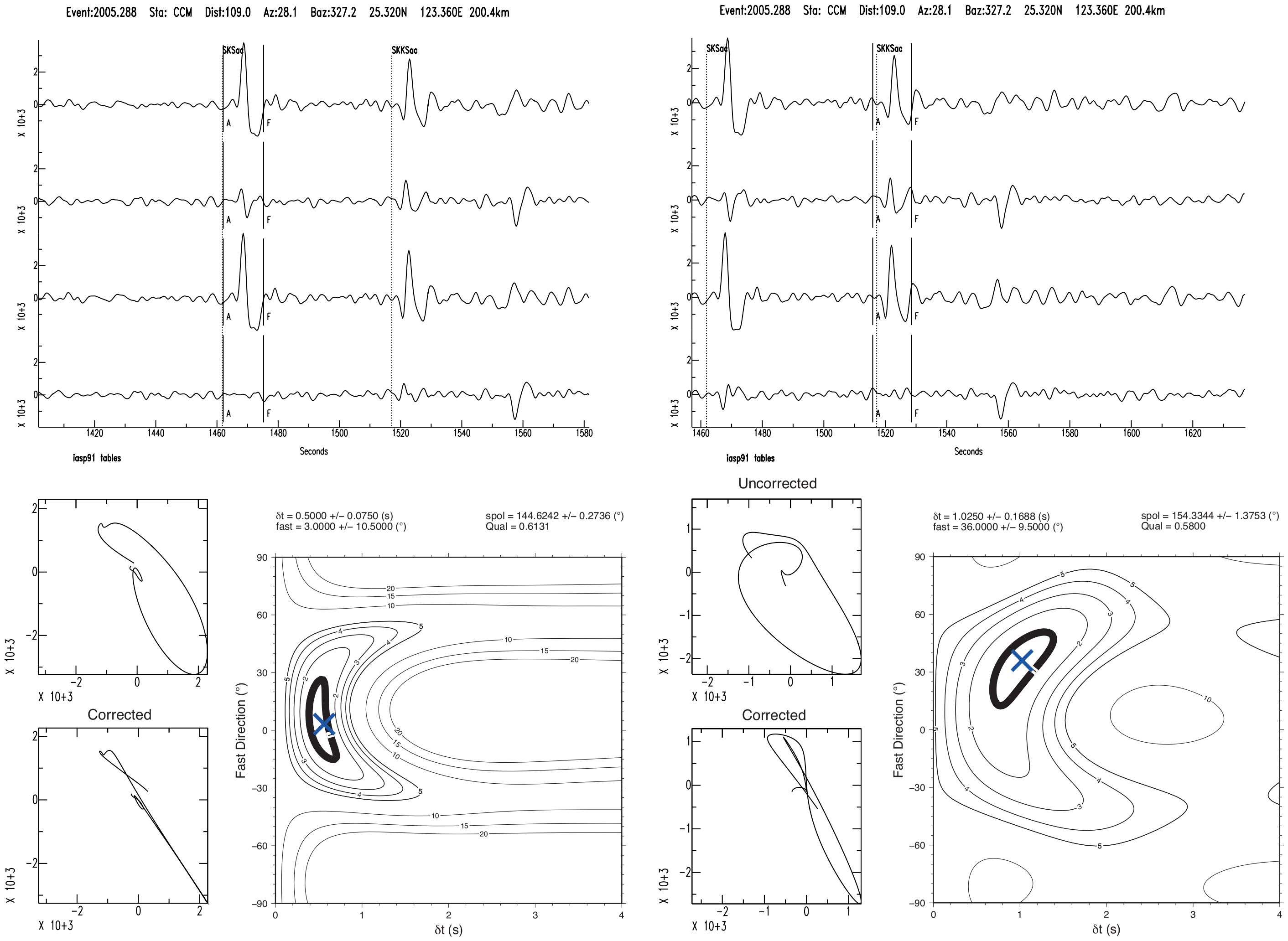

Figure A.3: A matching SKS-SKKS event-station pair recorded at station CCM. In this case $\bar{\lambda}_2 = 0.046$ and is greater than sum of the two 95% confidence levels, $\lambda_2^{95\%} = 0.042$. This suggests that the pair is discrepant. However for this example $\Delta SI = 0.29$, resulting in the pair being classified as matching. In this case there is a source polarisation discrepancy of $\approx 10°$ and the SNR of SKKS (8.3) is much less than that of SKS (17.9). With this we are not confident that this example can be classified as discrepant and is an example of where ΔSI is complimentary to $\bar{\lambda}_2$.

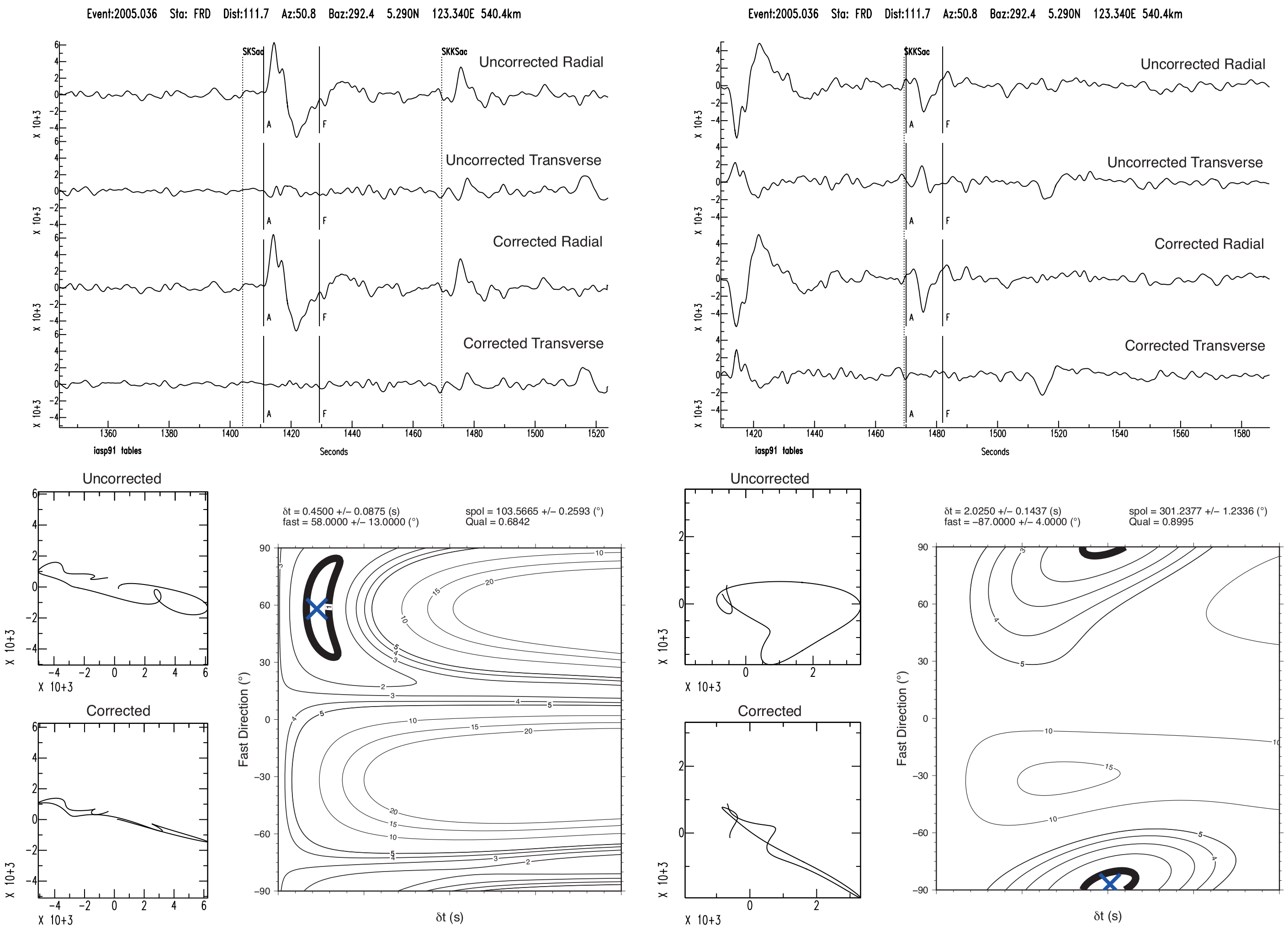

Figure A.4: A discrepant SKS-SKKS event-station pair recorded at station FRD. Here we show the uncorrected and corrected traces and particle motions, along with the eigenvalue surface for SKS (left) and SKKS (right). This is the most extreme example of discrepant shear-wave splitting recorded in our dataset. In this example $\Delta SI = 0.78$ and $\bar{\lambda_2} = 0.035$ which is greater than the sum of the two 95% confidence levels, $\lambda_2^{95\%} = 0.033$.

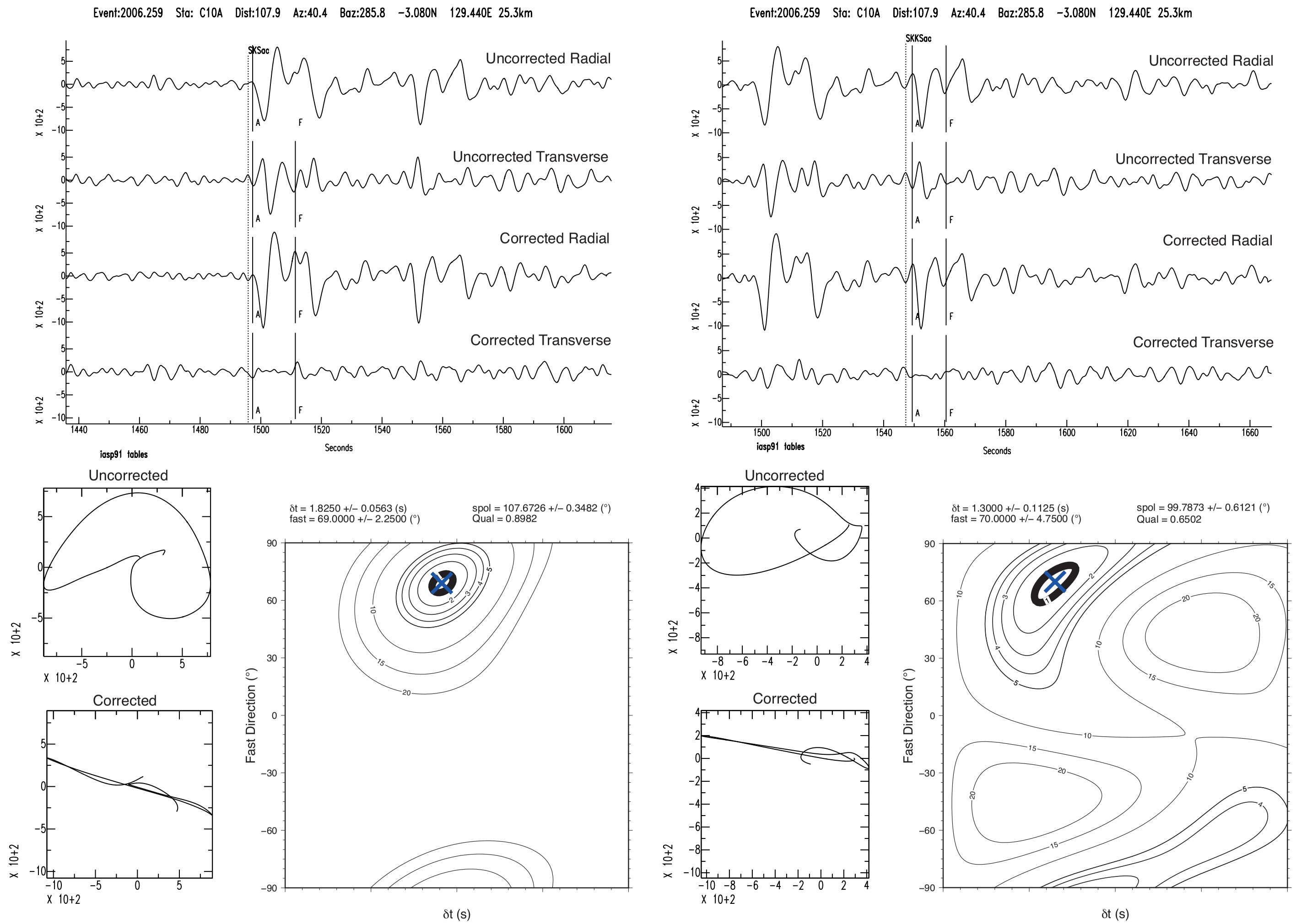

Figure A.5: A discrepant SKS-SKKS event-station pair recorder at station C10A. Here we show the uncorrected and corrected traces and particle motions, along with the eigenvalue surface for SKS (left) and SKKS (right). The discrepancy in this example is significantly smaller compared to SFA.4 and more typical of the other discrepant split pairs we observe. Whilst the discrepancy appears small it is clearly identified by both measures, with a $\Delta SI = 0.89$ and $\bar{\lambda_2} = 0.037$ which is much greater than the sum of the two 95% confidence levels, $\lambda_2^{95\%} = 0.022$ the result is interesting as we would typically expect SKS (left) to have a smaller delay time than SKKS (right) as SKKS has a longer path in D$''$.

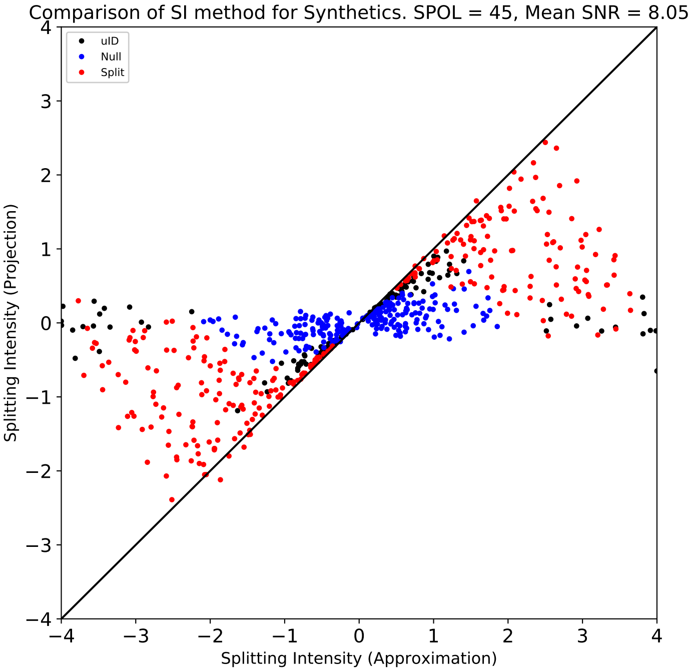

Figure A.6: A reproduction of Figure 3.7A, comparing Splitting Intensity calculated using an approximation (Pa) (Chevrot, 2000; Deng et al., 2017) and the projection (Pr) (Chevrot, 2000), using synthetics. The synthetics used here are the same as those used to test our discrepancy measures and are generated on a evenly spaced grid of 629 synthetic split shear-waves over a range of $0 \leq \delta t \leq 4s$ and $-90 \leq \phi \leq 90°$, with a mean SNR of ≈ 8. Synthetics are coloured base on their classification by Q (Wuestefeld et al., 2010) (see text). Splits synthetics (Q > 0.5) are shown in red, null synthetics (Q < -0.5) are shown in blue and synthetics where $0.5 \leq Q \leq 0.5$ are shown in black. The solid line shows $SI(Pr) = SI(Pa)$, which we would expect most of the results to sit near if the approximation is accurate.

APPENDIX B

APPENDIX A - SUPPLEMENTARY FIGURES FOR CHAPTER 4

This appendix contains the supplementary figures from Asplet et al., 2021, which constitutes chapter 4 of this thesis.

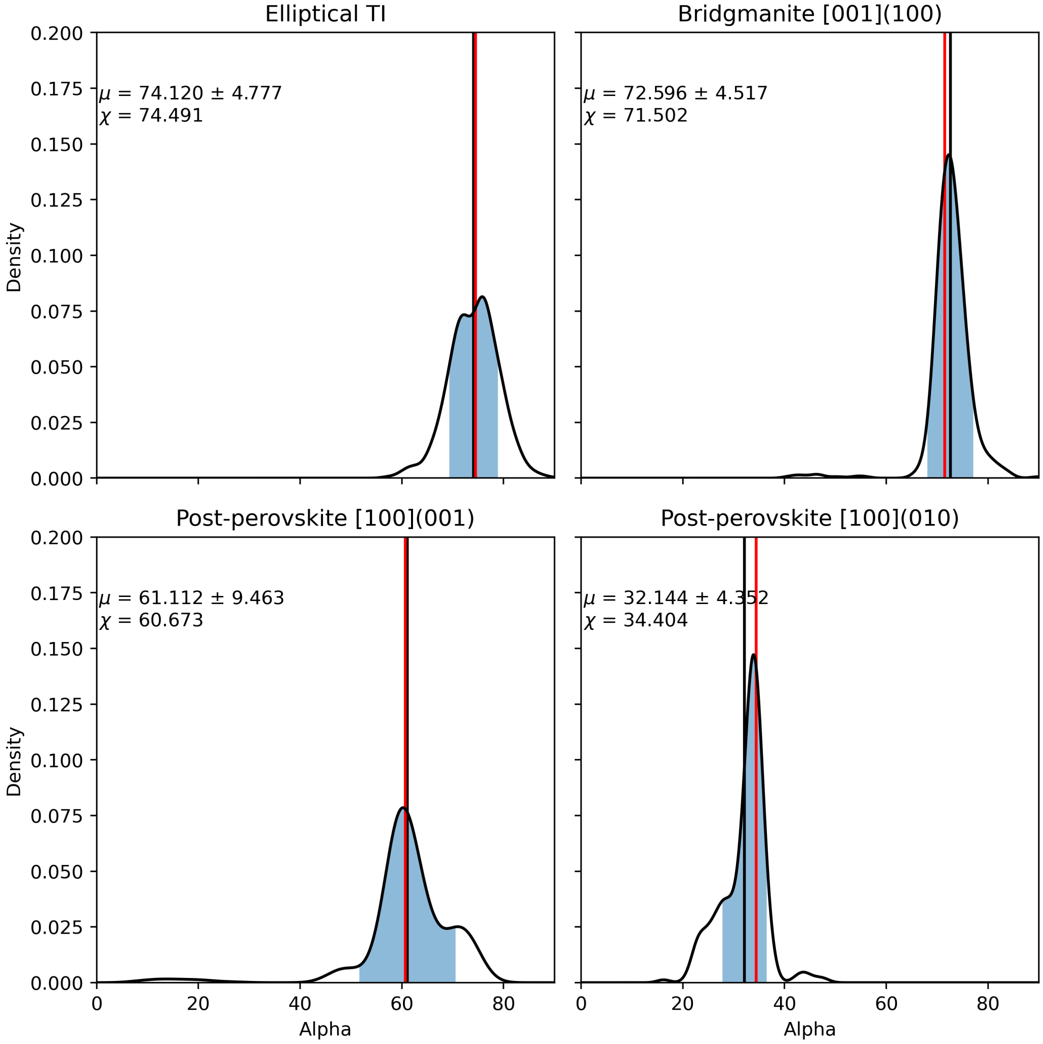

Figure B.1: Results of our bootstrapped inversions summarised as probability density functions for the orientation parameter α. We use the same set of 500 samples for each candidate mechanism. The red vertical line indicates the best fitting value of α from our main inversions (χ), where all 11 paths are used. The black vertical line indicates the mean α parameter of the bootstrap samples (μ). The region within 1 standard deviation of the mean is shaded blue.

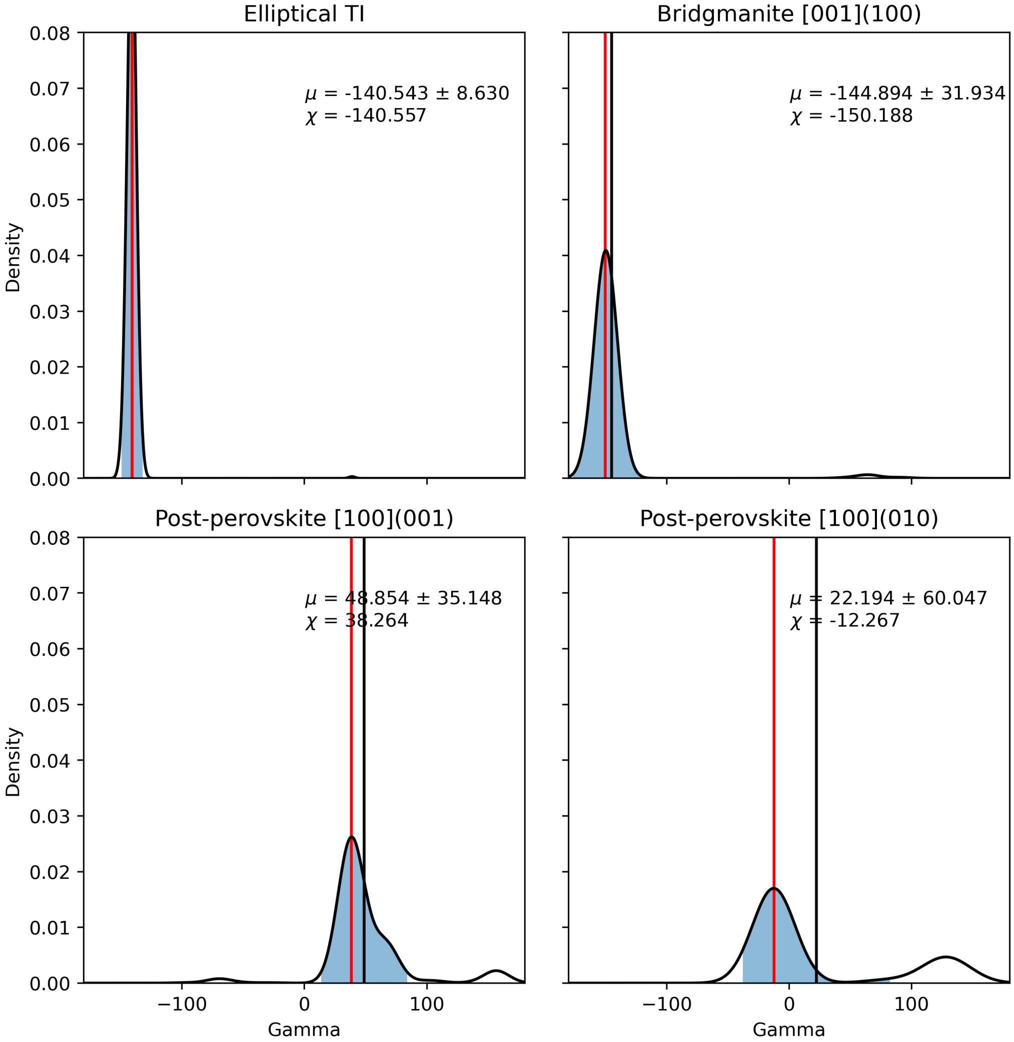

Figure B.2: Results of our bootstrapped inversions summarised as probability density functions for the orientation parameter γ. We use the same set of 500 samples for each candidate mechanism. The red vertical line indicates the best fitting value of γ from our main inversions (χ), where all 11 paths are used. The black vertical line indicates the mean γ parameter of the bootstrap samples (μ). The region within 1 standard deviation of the mean is shaded blue.

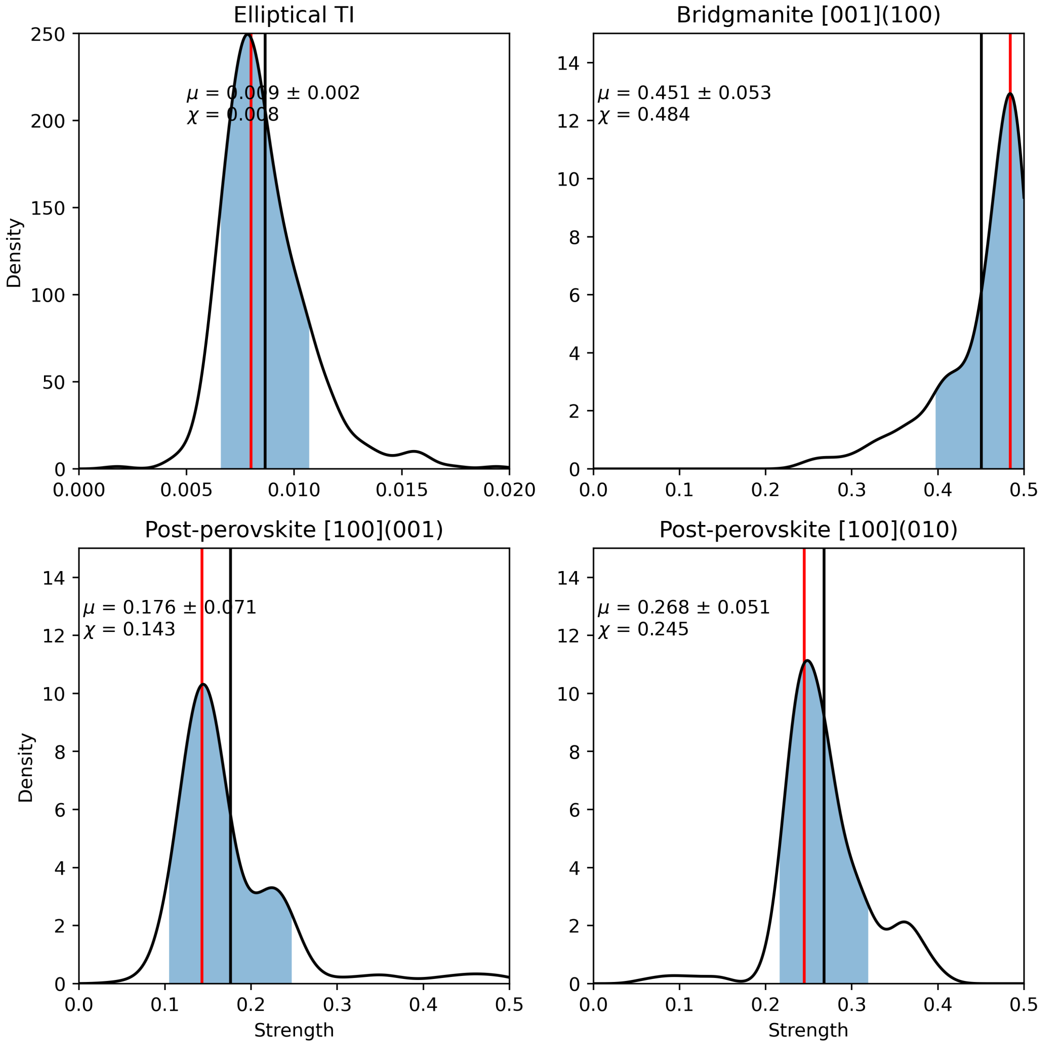

Figure B.3: Results of our bootstrapped inversions summarised as probability density functions for the strength parameter, s. We use the same set of 500 samples for each candidate mechanism. The red vertical line indicates the best fitting value of s from our main inversions (χ), where all 11 paths are used. The black vertical line indicates the mean strength parameter of the bootstrap samples (μ). The region within 1 standard deviation of the mean is shaded blue.

BIBLIOGRAPHY

Abt, D.L., Fischer, K.M., 2008.
Resolving three-dimensional anisotropic structure with shear wave splitting tomography.
Geophysical Journal International 173, 859–886.
doi:`10.1111/j.1365-246X.2008.03757.x`.

Adam, J.C., Romanowicz, B., 2015.
Global scale observations of scattered energy near the inner-core boundary: Seismic constraints on the base of the outer-core.
Physics of the Earth and Planetary Interiors 245, 103–116.
doi:`10.1016/j.pepi.2015.06.005`.

Allègre, C.J., Poirier, J.P., Humler, E., Hofmann, A.W., 1995.
The chemical composition of the Earth.
Earth and Planetary Science Letters 134, 515–526.
doi:`10.1016/0012-821X(95)00123-T`.

Ammann, M.W., Brodholt, J.P., Wookey, J., Dobson, D.P., 2010.
First-principles constraints on diffusion in lower-mantle minerals and a weak D$''$ layer.
Nature 465, 462–465.
doi:`10.1038/nature09052`.

Anders, E., 1977.
Chemical compositions of the moon, earth, and eucrite parent body.
Philosophical Transactions of the Royal Society of London. Series A, Mathematical and Physical Sciences 285, 23–40.

Andrault, D., Pesce, G., Bouhifd, M.A., Bolfan-Casanova, N., Heńot, J.M., Mezouar, M., 2014.
Melting of subducted basalt at the core-mantle boundary.

Science 344, 892–895.
doi:`10.1126/science.1250466`.

Asplet, J., Wookey, J., Kendall, M., 2020.
A potential post-perovskite province in D$''$ beneath the Eastern Pacific: evidence from new analysis of discrepant SKS–SKKS shear-wave splitting.
Geophysical Journal International 221, 2075–2090.
doi:`10.1093/gji/ggaa114`.

Auer, L., Boschi, L., Becker, T.W., Giardini, D., 2014.
Savani : A variable resolution whole-mantle model of anisotropic shear velocity variations based.
Journal of Geophysical Research: Solid Earth , 3006–3034doi:`10.1002/2013JB010773. Received`.

Backus, G.E., 1962.
Long-wave elastic anisotropy produced by horizontal layering.
Journal of Geophysical Research 67, 4427–4440.

Badro, J., Côté, A.S., Brodholt, J.P., 2014.
A seismologically consistent compositional model of Earth's core.
Proceedings of the National Academy of Sciences of the United States of America 111, 7542–7545.
doi:`10.1073/pnas.1316708111`.

Ballmer, M.D., Houser, C., Hernlund, J.W., Wentzcovitch, R.M., Hirose, K., 2017.
Persistence of strong silica-enriched domains in the Earth's lower mantle.
Nature Geoscience 10, 236–240.
doi:`10.1038/ngeo2898`.

Baron, M.A., Lord, O.T., Myhill, R., Thomson, A.R., Wang, W., Trønnes, R.G., Walter, M.J., 2017.
Experimental constraints on melting temperatures in the MgO–SiO2 system at lower mantle pressures.
Earth and Planetary Science Letters 472, 186–196.
doi:`10.1016/j.epsl.2017.05.020`.

Becker, T.W., Lebedev, S., 2021.

Dynamics of the upper mantle in light of seismic anisotropy, in: Marquardt, H., Ballmer, M., Cottaar, S., Jasper, K. (Eds.), Mantle Convection and Surface Expressions. American Geophysical Union (AGU). Geophysical Monograph. chapter 10, pp. 257–282.

doi:`https://doi.org/10.1002/9781119528609.ch10`.

Birch, A.F., 1940.

The alpha-gamma transformation of iron at high pressures, and the problem of the Earth's magnetism.

American Journal of Science 238, 192–211.

doi:`10.2475/ajs.238.3.192`.

Birch, F., 1952.

Elasticity and constitution of the Earth's interior.

Journal of Geophysical Research 57, 227–286.

doi:`10.1029/jz057i002p00227`.

Blackman, D.K., Kendall, J.M., 2002.

Seismic anisotropy in the upper mantle 2. predictions for current plate boundary flow models.

Geochemistry, Geophysics, Geosystems 3, 1–26.

doi:`10.1029/2001GC000247`.

Boioli, F., Carrez, P., Cordier, P., Devincre, B., Gouriet, K., Hirel, P., Kraych, A., Ritterbex, S., 2017.

Pure climb creep mechanism drives flow in Earth's lower mantle.

Science Advances 3.

doi:`10.1126/sciadv.1601958`.

Bono, R.K., Tarduno, J.A., Nimmo, F., Cottrell, R.D., 2019.

Young inner core inferred from Ediacaran ultra-low geomagnetic field intensity.

Nature Geoscience 12, 143–147.

doi:`10.1038/s41561-018-0288-0`.

Bowman, J.R., Ando, M., 1987.

Shear-wave splitting in the upper-mantle wedge above the Tonga subduction zone J.

Geophysical Journal of the Royal Astronomical Society 88, 25–41.

Buffett, B.A., Garnero, E.J., Jeanloz, R., 2000.
Sediments at the top of earth's core.
Science 290, 1338–1342.
doi:`10.1126/science.290.5495.1338`.

Bull, A.L., McNamara, A.K., Ritsema, J., 2009.
Synthetic tomography of plume clusters and thermochemical piles.
Earth and Planetary Science Letters 278, 152–162.
doi:`10.1016/j.epsl.2008.11.018`.

Bullen, K.E., 1946.
A Hypothesis on Compressibility at Pressures of the Order of a Million Atmospheres.
Nature 157, 405.
doi:`10.1038/157405a0`.

Bullen, K.E., 1949.
Compressibility-pressure hypothesis and the Earth's interior.
Month. Not. R. Astr. Soc., Geophys. Suppl. 5, 355–368.

Cammarano, F., Goes, S., Deuss, A., Giardini, D., 2005.
Is a pyrolitic adiabatic mantle compatible with seismic data?
Earth and Planetary Science Letters 232, 227–243.
doi:`10.1016/j.epsl.2005.01.031`.

Catalli, K., Shim, S.H., Prakapenka, V., 2009.
Thickness and Clapeyron slope of the post-perovskite boundary.
Nature 462, 782–785.
doi:`10.1038/nature08598`.

Chandler, B.C., Chen, L.W., Li, M., Romanowicz, B., Wenk, H.R., 2021.
Seismic anisotropy, dominant slip systems and phase transitions in the lowermost mantle.
Geophysical Journal International 227, 1665–1681.
doi:`10.1093/gji/ggab278`.

Chang, S.J., Ferreira, A.M.G., Ritsema, J., van Heijst, H.J., Woodhouse, J.H., 2015.
Joint inversion for global isotropic and radially anisotropic mantle structure including crustal thickness perturbations.
Journal of Geophysical Research: Solid Earth 120, 4278–4300.
doi:`10.1002/2014JB011824`.

Chevrot, S., 2000.
Multichannel analysis of shear wave splitting.
Journal of Geophysical Research: Solid Earth 105, 21579–21590.
doi:`10.1029/2000JB900199`.

Chevrot, S., Monteiller, V., 2009.
Principles of vectorial tomography - The effects of model parametrization and regularization in tomographic imaging of seismic anisotropy.
Geophysical Journal International 179, 1726–1736.
doi:`10.1111/j.1365-246X.2009.04370.x`.

Christensen, U.R., Hofmann, A.W., 1994.
Segregation of subducted oceanic crust in the convecting mantle.
Journal of Geophysical Research: Solid Earth 99, 19867–19884.
doi:`10.1029/93JB03403`.

Cleary, J.R., 1974.
The D'' region.
Phys. Earth Planet. Inter. 30, 13–27.

Cobden, L., Thomas, C., 2013.
The origin of D” reflections: a systematic study of seismic array data sets.
Geophysical Journal International 194, 1091–1118.
doi:`10.1093/gji/ggt152`.

Cordier, P., Ungar, T., Zsoldos, L., Tichy, G., 2004.
Dislocation creep in MgSiO3 perovskite at conditions of Earth’s uppermost lower mantle.
Nature 428, 837 – 840.
doi:`10.1029/2003pa000939`.

Cottaar, S., Heister, T., Rose, I., Unterborn, C., 2014a.
BurnMan: A lower mantle mineral physics toolkit.
Geochemistry, Geophysics, Geosystems 15, 1164–1179.
doi:`10.1002/2013GC005122`.

Cottaar, S., Lekic, V., 2016.
Morphology of seismically slow lower-mantle structures.
Geophysical Journal International 207, 1122–1136.
doi:`10.1093/gji/ggw324`.

Cottaar, S., Li, M., McNamara, A.K., Romanowicz, B., Wenk, H.R., 2014b.
Synthetic seismic anisotropy models within a slab impinging on the core–mantle boundary.
Geophysical Journal International 199, 164–177.
doi:`10.1093/gji/ggu244`.

Cottaar, S., Li, Z., 2019.
A large ultra-low velocity zone at the potential base of the galapagos plume, in: AGU Fall Meeting Abstracts, pp. DI33A–04.

Cottaar, S., Romanowicz, B., 2012.
An unsually large ULVZ at the base of the mantle near Hawaii.
Earth and Planetary Science Letters 355-356, 213–222.
doi:`10.1016/j.epsl.2012.09.005`.

Cottaar, S., Romanowicz, B., 2013.
Observations of changing anisotropy across the southern margin of the African LLSVP.
Geophysical Journal International 195, 1184–1195.
doi:`10.1093/gji/ggt285`.

Couper, S., Speziale, S., Marquardt, H., Liermann, H.P., Miyagi, L., 2020.
Does Heterogeneous Strain Act as a Control on Seismic Anisotropy in Earth's Lower Mantle?
Frontiers in Earth Science 8, 1–20.
doi:`10.3389/feart.2020.540449`.

Crampin, S., 1985.

Evaluation of anisotropy by shear-wave splitting.
GEOPHYSICS 50, 142–152.
doi:`10.1190/1.1441824`.

Crampin, S., Gao, Y., 2006.
A review of techniques for measuring shear-wave splitting above small earthquakes.
Physics of the earth and planetary interiors 159, 1–14.
doi:`10.1016/j.pepi.2006.06.002`.

Creasy, N., Long, M.D., Ford, H.A., 2017.
Deformation in the lowermost mantle beneath Australia from observations and models of seismic anisotropy.
Journal of Geophysical Research: Solid Earth 122, 5243–5267.
doi:`10.1002/2016JB013901`.

Creasy, N., Miyagi, L., Long, M.D., 2020.
A Library of Elastic Tensors for Lowermost Mantle Seismic Anisotropy Studies and Comparison With Seismic Observations.
Geochemistry, Geophysics, Geosystems 21, 1–20.
doi:`10.1029/2019GC008883`.

Creasy, N., Pisconti, A., Long, M.D., Thomas, C., Wookey, J., 2019.
Constraining lowermost mantle anisotropy with body waves: A synthetic modeling study.
Geophysical Journal International , 766–783doi:`10.1093/gji/ggz049`.

Crotwell, H.P., Owens, T.J., Ritsema, J., 1999.
The taup toolkit : Flexible seismic travel-time and ray-path utilities.
Seismological Research Letters 70, 154–160.

Dannberg, J., Myhill, R., Gassmöller, R., Cottaar, S., 2021.
The morphology, evolution and seismic visibility of partial melt at the core-mantle boundary: Implications for ULVZs.
Geophysical Journal International doi:`10.1093/gji/ggab242`.

Davies, D.R., Goes, S., Davies, J., Schuberth, B., Bunge, H.P., Ritsema, J., 2012a.

Reconciling dynamic and seismic models of Earth's lower mantle: The dominant role of thermal heterogeneity.
Earth and Planetary Science Letters 353-354, 253–269.
doi:`10.1016/J.EPSL.2012.08.016`.

Davies, D.R., Goes, S., Davies, J.H., Schuberth, B.S., Bunge, H.P., Ritsema, J., 2012b.
Reconciling dynamic and seismic models of Earth's lower mantle: The dominant role of thermal heterogeneity.
Earth and Planetary Science Letters 353-354, 253–269.
doi:`10.1016/j.epsl.2012.08.016`.

De Wijs, G.A., Kresse, G., Vočadlo, L., Dobson, D., Alfè, D., Gillan, M.J., Price, G.D., 1998.
The viscosity of liquid iron at the physical conditions of the Earth's core.
Nature 392, 805–807.
doi:`10.1038/33905`.

Deng, J., Long, M.D., Creasy, N., Wagner, L., Beck, S., Zandt, G., Tavera, H., Minaya, E., 2017.
Lowermost mantle anisotropy near the eastern edge of the pacific llsvp : constraints from sks – skks splitting intensity measurements.
Geophysical Journal International 210, 774–786.
doi:`10.1093/gji/ggx190`.

Dobson, D.P., Brodholt, J.P., 2005.
Subducted banded iron formations as a source of ultralow-velocity zones at the core-mantle boundary.
Nature 434, 371–374.
doi:`10.1038/nature03430`.

Dorfman, S.M., Shieh, S.R., Meng, Y., Prakapenka, V.B., Duffy, T.S., 2012.
Synthesis and equation of state of perovskites in the (Mg, Fe)3Al2Si3O12 system to 177GPa.
Earth and Planetary Science Letters 357-358, 194–202.
doi:`10.1016/j.epsl.2012.09.024`.

Dziewonski, A.M., Anderson, D.L., 1981.
Preliminary reference Earth model.

Physics of the Earth and Planetary Interiors 25, 297–356.
doi:10.1016/0031-9201(81)90046-7.

Dziewonski, A.M., Gilbert, F., 1971.
Solidity of the Inner Core of the Earth inferred from Normal Mode Observations.
Nature 234, 465–466.
doi:10.1038/234465a0.

Dziewonski, A.M., Lekic, V., Romanowicz, B.A., 2010.
Mantle Anchor Structure: An argument for bottom up tectonics.
Earth and Planetary Science Letters 299, 69–79.
doi:10.1016/j.epsl.2010.08.013.

Eakin, C.M., Wirth, E.A., Wallace, A., Ulberg, C.W., Creager, K.C., Abers, G.A., 2019.
SKS Splitting Beneath Mount St. Helens: Constraints on Subslab Mantle Entrainment.
Geochemistry, Geophysics, Geosystems 20, 4202–4217.
doi:10.1029/2019GC008433.

Faccenna, C., Becker, T.W., Auer, L., Billi, A., Boschi, L., Brun, J.P., Capitanio, F.A., Funiciello, F., Horvàth, F., Jolivet, L., Piromallo, C., Royden, L., Rossetti, F., Serpelloni, E., 2014.
Mantle dynamics in the mediterranean.
Reviews of Geophysics 52, 283–332.
doi:https://doi.org/10.1002/2013RG000444.

Fei, H., Katsura, T., 2020.
High water solubility of ringwoodite at mantle transition zone temperature.
Earth and Planetary Science Letters 531, 115987.
doi:10.1016/j.epsl.2019.115987.

Fei, H., Yamazaki, D., Sakurai, M., Miyajima, N., Ohfuji, H., Katsura, T., Yamamoto, T., 2017.
A nearly water-saturated mantle transition zone inferred from mineral viscosity.
Science advances 3, e1603024.
doi:10.1126/sciadv.1603024.

Ferreira, A.M., Faccenda, M., Sturgeon, W., Chang, S.J., Schardong, L., 2019.

Ubiquitous lower-mantle anisotropy beneath subduction zones.
Nature Geoscience 12, 301–306.
doi:10.1038/s41561-019-0325-7.

Ferreira, A.M., Woodhouse, J.H., Visser, K., Trampert, J., 2010.
On the robustness of global radially anisotropic surface wave tomography.
Journal of Geophysical Research: Solid Earth 115.
doi:10.1029/2009JB006716.

Flament, N., 2019.
Present-day dynamic topography and lower-mantle structure from palaeogeographically constrained mantle flow models.
Geophysical Journal International 216, 2158–2182.
doi:10.1093/gji/ggy526.

Flanagan, M.P., Shearer, P.M., 1999.
A map of topography on the 410-km discontinuity from pp precursors.
Geophysical research letters 26, 549–552.
doi:10.1029/1999GL900036.

Ford, H.A., Long, M.D., He, X., Lynner, C., 2015.
Lowermost mantle flow at the eastern edge of the african large low shear velocity province.
Earth and Planetary Science Letters 420, 12 – 22.
doi:10.1016/j.epsl.2015.03.029.

Forte, A.M., Simmons, N.A., Grand, S.P., 2015.
Constraints on 3-d seismic models from global geodynamic obervables: Implications for the global mantle convective flow, in: Romanowicz, B.A., Dziewonski, A.M. (Eds.), Treatise of Geophysics. 2nd ed.. Elsevier, Amsterdam, Netherlands. volume 1, pp. 853–907.

French, S.W., Romanowicz, B., 2015.
Broad plumes rooted at the base of the Earth's mantle beneath major hotspots.
Nature 525, 95–99.
doi:10.1038/nature14876.

French, S.W., Romanowicz, B.A., 2014.
Whole-mantle radially anisotropic shear velocity structure from spectral-element waveform tomography.
Geophysical Journal International 199.
doi:`10.1093/gji/ggu334`.

Frost, D.A., Rost, S., 2014.
The P-wave boundary of the Large-Low Shear Velocity Province beneath the Pacific.
Earth and Planetary Science Letters 403, 380–392.
doi:`10.1016/j.epsl.2014.06.046`.

Frost, D.A., Rost, S., Selby, N.D., Stuart, G.W., 2013.
Detection of a tall ridge at the core–mantle boundary from scattered pkp energy.
Geophysical Journal International 195, 558–574.
doi:`10.1093/gji/ggt242`.

Fukao, Y., 1984.
Evidence from core-reflected shear waves for anisotropy in the Earth's mantle.
Nature 309, 695–698.
doi:`10.1038/309695a0`.

Fukao, Y., Obayashi, M., 2013.
Subducted slabs stagnant above, penetrating through, and trapped below the 660 km discontinuity.
Journal of Geophysical Research: Solid Earth 118, 5920–5938.
doi:`10.1002/2013JB010466`.

Fukao, Y., Obayashi, M., Inoue, H., Nenbai, M., 1992.
Subducting slabs stagnant in the mantle transition zone.
Journal of Geophysical Research 97, 4809–4822.
doi:`10.1029/91JB02749`.

Fukao, Y., Obayashi, M., Nakakuki, T., Utada, H., Suetsugu, D., Irifune, T., Ohtani, E., Yoshioka, S., Shiobara, H., Kanazawa, T., Hirose, K., 2009.
Stagnant slab: A review.

Annual Review of Earth and Planetary Sciences 37, 19–46.
doi:`10.1146/annurev.earth.36.031207.124224`.

Gaherty, J.B., Lay, T., 1992.
Investigation of laterally heterogeneous shear velocity structure in d$''$ beneath eurasia.
Journal of Geophysical Research: Solid Earth 97, 417–435.
doi:`10.1029/91JB02347`.

Garnero, E., Helmberger, D., Engen, G., 1988.
Lateral variations near the core-mantle boundary.
Geophysical Research Letters 15, 609–612.
doi:`10.1029/GL015i006p00609`.

Garnero, E., Helmberger, D., Grand, S., 1993.
Preliminary evidence for a lower mantle shear wave velocity discontinuity beneath the central pacific.
Physics of the earth and planetary interiors 79, 335–347.
doi:`10.1016/0031-9201(93)90113-N`.

Garnero, E.J., Maupin, V., Lay, T., Fouch, M.J., 2004.
Variable azimuthal anisotropy in earth's lowermost mantle.
Science 306, 259–261.
doi:`10.1126/science.1103411`.

Garnero, E.J., McNamara, A.K., Shim, S.H., 2016.
Continent-sized anomalous zones with low seismic velocity at the base of Earth's mantle.
Nature Geoscience 9, 481–489.
doi:`10.1038/ngeo2733`.

Garnero, E.J., Revenaugh, J., Williams, Q., Lay, T., Kellogg, L.H., 1998.
Ultralow velocity zone at the core-mantle boundary, in: Gurnis, M., Wysession, M.E., Knittle, E., Buffet, B.A. (Eds.), The Core-Mantle Boundary Region. American Geophysical Union, Washington, D.C., USA. Geodynamics, pp. 319–334.
doi:`https://doi.org/10.1029/GD028p0319`.

Goryaeva, A.M., Carrez, P., Cordier, P., 2015.
Modeling defects and plasticity in MgSiO3 post-perovskite: Part 2—screw and edge [100] dislocations.
Physics and Chemistry of Minerals 42, 793–803.
doi:`10.1007/s00269-015-0763-8`.

Goryaeva, A.M., Carrez, P., Cordier, P., 2016.
Low viscosity and high attenuation in MgSiO3 post-perovskite inferred from atomic-scale calculations.
Scientific Reports 6, 34771.
doi:`10.1038/srep34771`.

Goryaeva, A.M., Carrez, P., Cordier, P., 2017.
Modeling defects and plasticity in MgSiO3 post-perovskite: Part 3—Screw and edge [001] dislocations.
Physics and Chemistry of Minerals 44, 521–533.
doi:`10.1007/s00269-017-0879-0`.

Grima, A.G., Lithgow-Bertelloni, C., Crameri, F., 2020.
Orphaning regimes: The missing link between flattened and penetrating slab morphologies.
Frontiers in Earth Science 8.
doi:`10.3389/feart.2020.00374`.

Grocholski, B., Catalli, K., Shim, S.H., Prakapenka, V., 2012.
Mineralogical effects on the detectability of the postperovskite boundary.
Proceedings of the National Academy of Sciences 109, 2275–2279.
doi:`10.1073/pnas.1109204109`.

Grund, M., Ritter, J.R.R., 2018.
Widespread seismic anisotropy in Earth's lowermost mantle beneath the Atlantic and Siberia.
Geology 47, 123–126.
doi:`10.1130/G45514.1`.

Gutenberg, B., 1914.

über erdbebenwellen viia. beobachtungen an registrierungen von fernbeben in göttingen und folgerungen über die konstitution des erdkörpers.
Nachrichten der Gesellschaft der Wissenschaften zu Göttingen MathematischphysikaIische Klass , 125 – 177.

Hall, S.A., Kendall, J.M., van der Baan, M., 2004.
Some comments on the effects of lower-mantle anisotropy on SKS and SKKS phases.
Physics of the Earth and Planetary Interiors 146, 469–481.
doi:`10.1016/j.pepi.2004.05.002`.

Hastings, W.K., 1970.
Monte carlo sampling methods using Markov chains and their applications.
Biometrika 57, 97–109.
doi:`10.1093/biomet/57.1.97`.

Helffrich, G., Kaneshima, S., 2010.
Outer-core compositional stratification from observed core wave speed profiles.
Nature 468, 807–810.
doi:`10.1038/nature09636`.

Helffrich, G.R., Wood, B.J., 2001.
The Earth's mantle.
Nature 412, 501–507.
doi:`10.1038/35087500`.

Hernlund, J.W., Houser, C., 2008.
On the statistical distribution of seismic velocities in Earth's deep mantle.
Earth and Planetary Science Letters 265, 423–437.
doi:`10.1016/j.epsl.2007.10.042`.

Hernlund, J.W., McNamara, A.K., 2015.
The core-mantle boundary region, in: Schubert, G. (Ed.), Treatise of Geophysics. 2nd ed.. Elsevier, Oxford. volume 7, pp. 461–519.
doi:`10.1016/B978-0-444-53802-4.00136-6`.

Hernlund, J.W., Thomas, C., Tackley, P.J., 2005.

A doubling of the post-perovskite phase boundary and structure of the Earth's lowermost mantle.

Nature 434, 882–886.

doi:`10.1038/nature03472`.

Van der Hilst, R., De Hoop, M., Wang, P., Shim, S.H., Ma, P., Tenorio, L., 2007.

Seismostratigraphy and thermal structure of earth's core-mantle boundary region.

science 315, 1813–1817.

doi:`10.1126/science.1137867`.

Van der Hilst, R.D., Widiyantoro, S., Engdahl, E., 1997.

Evidence for deep mantle circulation from global tomography.

Nature 386, 578–584.

doi:`10.1038/386578a0`.

Hirose, K., Nagaya, Y., Merkel, S., Ohishi, Y., 2010.

Deformation of MnGeO3 post-perovskite at lower mantle pressure and temperature.

Geophysical Research Letters 37.

doi:`doi.org/10.1029/2010GL044977`.

Hirose, K., Sinmyo, R., Hernlund, J., 2017.

Perovskite in Earth's deep interior.

Science 358, 734–738.

doi:`10.1126/science.aam8561`.

Hirose, K., Wentzcovitch, R., Yuen, D., Lay, T., 2015.

Mineralogy of the deep mantle — the post-perovskite phase and its geophysical significance, in: Schubert, G. (Ed.), Treatise on Geophysics. 2nd ed.. Elevier, Oxford. volume 2, pp. 85–115.

doi:`10.1016/B978-0-444-53802-4.00054-3`.

Hofmann, A.W., 1997.

Mantle geochemistry: the message from oceanic volcanism.

Nature 385, 219–229.

doi:`10.1038/385219a0`.

Hofmann, A.W., White, W.M., 1982.
Mantle plumes from ancient oceanic crust.
Earth and Planetary Science Letters 57, 421–436.
doi:`10.1016/0012-821X(82)90161-3`.

Horan, M., Carlson, R., Walker, R., Jackson, M., Garçon, M., Norman, M., 2018.
Tracking Hadean processes in modern basalts with 142-Neodymium.
Earth and Planetary Science Letters 484, 184–191.
doi:`10.1016/j.epsl.2017.12.017`.

Houser, C., 2016.
Global seismic data reveal little water in the mantle transition zone.
Earth and Planetary Science Letters 448, 94–101.
doi:`10.1016/j.epsl.2016.04.018`.

Hudson, J.A., 1980.
The excitation and propagation of elastic waves.
Cambridge University Press.

Hunt, S.A., Weidner, D.J., Li, L., Wang, L., Walte, N.P., Brodholt, J.P., Dobson, D.P., 2009.
Weakening of calcium iridate during its transformation from perovskite to post-perovskite.
Nature Geoscience 2, 794–797.
doi:`10.1038/ngeo663`.

Hunter, J.D., 2007.
Matplotlib: A 2d graphics environment.
Computing in Science & Engineering 9, 90–95.
doi:`10.1109/MCSE.2007.55`.

Immoor, J., Marquardt, H., Miyagi, L., Lin, F., Speziale, S., Merkel, S., Buchen, J., Kurnosov, A., Liermann, H.P., 2018.
Evidence for {100}<011> slip in ferropericlase in Earth's lower mantle from high-pressure/high-temperature experiments.
Earth and Planetary Science Letters 489, 251–257.
doi:`10.1016/j.epsl.2018.02.045`.

Irving, J.C., Cottaar, S., Lekic, V., 2018.

Seismically determined elastic parameters for Earth's outer core.

Science Advances 4.

doi:10.1126/sciadv.aar2538.

Jacobs, J.A., 1953.

The Earth's Inner Core.

Nature 172, 297–298.

doi:10.1038/172297a0.

Jeffreys, H., 1939.

The times of P,S, and SKS and the velocities of P and S.

Mon. Not. R. Astron. Soc. 4, 498–533.

Jellinek, A.M., Gonnermann, H.M., Richards, M.A., 2003.

Plume capture by divergent plate motions: Implications for the distribution of hotspots, geochemistry of mid-ocean ridge basalts, and estimates of the heat flux at the core-mantle boundary.

Earth and Planetary Science Letters 205, 361–378.

doi:10.1016/S0012-821X(02)01070-1.

Jenkins, J., Mousavi, S., Li, Z., Cottaar, S., 2021.

A high-resolution map of Hawaiian ULVZ morphology from ScS phases.

Earth and Planetary Science Letters 563, 116885.

doi:10.1016/j.epsl.2021.116885.

Jones, C.A., 2011.

Planetary Magnetic Fields and Fluid Dynamos.

Annual Review of Fluid Mechanics 43, 583–614.

doi:10.1146/annurev-fluid-122109-160727.

Karato, S.i., 1998a.

Seismic Anisotropy in the Deep Mantle, Boundary Layers and the Geometry of Mantle Convection, in: Plomerová, J., Liebermann, R.C., Babuška, V. (Eds.), Geodynamics of Lithosphere & Earth's Mantle, Birkhäuser Basel, Basel. pp. 565–587.

doi:`10.1007/978-3-0348-8777-9_19`.

Karato, S.i., 1998b.
Some remarks on the origin of seismic anisotropy in the D″ layer.
Earth, Planets and Space 50, 1019–1028.
doi:`10.1186/BF03352196`.

Karato, S.I., Jung, H., Katayama, I., Skemer, P., 2008.
Geodynamic significance of seismic anisotropy of the upper mantle: New insights from laboratory studies.
Annual Review of Earth and Planetary Sciences 36, 59–95.
doi:`10.1146/annurev.earth.36.031207.124120`.

Karki, B.B., Wentzcovitch, R.M., de Gironcoli, S., Baroni, S., 1999.
First-principles determination of elastic anisotropy and wave velocities of MgO at lower mantle conditions.
Science 286, 1705–1707.
doi:`10.1126/science.286.5445.1705`.

Karki, B.B., Wentzcovitch, R.M., de Gironcoli, S., Baroni, S., 2000.
High-pressure lattice dynamics and thermoelasticity of mgo.
Phys. Rev. B 61, 8793–8800.
doi:`10.1103/PhysRevB.61.8793`.

Kellogg, L.H., Hager, B.H., Van Der Hilst, R.D., 1999.
Compositional stratification in the deep mantle.
Science 283, 1881–1884.
doi:`10.1126/science.283.5409.1881`.

Kendall, J.M., 2000.
Seismic anisotropy in the boundary layers of the mantle, in: Karato, S., Forte, A., Liebermann, R., Masters, G., Stixtrude, L. (Eds.), Earth's Deep Interior: Mineral physics and Tomography From the Atomic to the Global Scale. American Geophysical Union. volume 117 of *Geophysical Monographs*, pp. 133–159.
doi:`10.1029/GM117p0133`.

Kendall, J.M., Shearer, P.M., 1994.

Lateral variations in D” thickness from long-period shear wave data.

Journal of Geophysical Research 99, 11575–11590.

doi:`10.1029/94jb00236`.

Kendall, J.M., Silver, P.G., 1996.

Constraints from seismic anisotropy on the nature of the lowermost mantle.

Nature 381, 409–412.

doi:`10.1038/381409a0`.

Kendall, J.M., Silver, P.G., 1998.

Investigating causes of d” anisotropy, in: Gurnis, M., Wysession, M., Knittle, E., Buffet, B.A. (Eds.), The Core-Mantle Boundary Region. American Geophysical Union. volume 28 of *Geodynamics*, pp. 97–118.

doi:`10.1029/GD028`.

Kennett, B.L.N., Engdahl, E.R., 1991.

Traveltimes for global earthquake location and phase identification.

Geophysical Journal International 105, 429–465.

doi:`10.1111/j.1365-246X.1991.tb06724.x`.

Kim, D., Lekić, V., Ménard, B., Baron, D., Taghizadeh-Popp, M., 2020.

Sequencing seismograms: A panoptic view of scattering in the core-mantle boundary region.

Science 368, 1223–1228.

doi:`10.1126/science.aba8972`.

King, S.D., Frost, D.J., Rubie, D.C., 2015.

Why cold slabs stagnate in the transition zone.

Geology 43, 231–234.

doi:`10.1130/G36320.1`.

Koelemeijer, P., Deuss, A., Ritsema, J., 2017.

Density structure of Earth’s lowermost mantle from Stoneley mode splitting observations.

Nature Communications 8, 15241.

doi:`10.1038/ncomms15241`.

Koelemeijer, P., Ritsema, J., Deuss, A., van Heijst, H.J., 2016.
SP12RTS: a degree-12 model of shear- and compressional-wave velocity for Earth's mantle.
Geophysical Journal International 204, 1024–1039.
doi:`10.1093/gji/ggv481`.

Labrosse, S., Hernlund, J.W., Coltice, N., 2007.
A crystallizing dense magma ocean at the base of the Earth's mantle.
Nature 450, 866–869.
doi:`10.1038/nature06355`.

Lay, T., Helmberger, D.V., 1983.
A lower mantle S-wave triplication and the shear velocity structure of D".
Geophysical Journal of the Royal Astronomical Society 75, 799–837.
doi:`10.1111/j.1365-246X.1983.tb05010.x`.

Lay, T., Young, C.J., 1991.
Analysis of seismic sv waves in the core's penumbra.
Geophysical Research Letters 18, 1373–1376.
doi:`10.1029/91GL01691`.

Lehmann, I., 1936.
P'.
Bureau Central Séismologique International Strasbourg. Publications du Bureau Central Scientifiques A 14, 87–115.

Lekic, V., Cottaar, S., Dziewonski, A., Romanowicz, B., 2012.
Cluster analysis of global lower mantle tomography: A new class of structure and implications for chemical heterogeneity.
Earth and Planetary Science Letters 357-358, 68–77.
doi:`10.1016/j.epsl.2012.09.014`.

Leng, K., Nissen-Meyer, T., Van Driel, M., Hosseini, K., Al-Attar, D., 2019.
Axisem3d: broad-band seismic wavefields in 3-d global earth models with undulating discontinuities.
Geophysical Journal International 217, 2125–2146.

doi:doi.org/10.1093/gji/ggz092.

Li, J., Wang, X., Wang, X., Yuen, D.A., 2013.
P and sh velocity structure in the upper mantle beneath northeast china: Evidence for a stagnant slab in hydrous mantle transition zone.
Earth and Planetary Science Letters 367, 71–81.
doi:10.1016/j.epsl.2013.02.026.

Li, M., McNamara, A.K., 2013.
The difficulty for subducted oceanic crust to accumulate at the Earth's core-mantle boundary.
Journal of Geophysical Research: Solid Earth 118, 1807–1816.
doi:10.1002/jgrb.50156.

Li, M., McNamara, A.K., Garnero, E.J., 2014.
Chemical complexity of hotspots caused by cycling oceanic crust through mantle reservoirs.
Nature Geoscience 7, 366–370.
doi:10.1038/ngeo2120.

Lin, Y.P., Zhao, L., Hung, S.H., 2014.
Full-wave effects on shear wave splitting.
Geophysical Research Letters 41, 799–804.
doi:10.1002/2013GL058742.

Lister, J.R., Buffett, B.A., 1995.
The strength and efficiency of thermal and compositional convection in the geodynamo.
Physics of the Earth and Planetary Interiors 91, 17–30.
doi:10.1016/0031-9201(95)03042-U.

Liu, J., Li, J., Hrubiak, R., Smith, J.S., 2016.
Origins of ultralow velocity zones through slab-derived metallic melt.
Proceedings of the National Academy of Sciences of the United States of America 113, 5547–5551.
doi:10.1073/pnas.1519540113.

Long, M.D., 2009.

Complex anisotropy in D” beneath the eastern Pacific from SKS – SKKS splitting discrepancies.
Earth and Planetary Science Letters 283, 181–189.
doi:10.1016/j.epsl.2009.04.019.

Long, M.D., Becker, T.W., 2010.
Mantle dynamics and seismic anisotropy.
Earth and Planetary Science Letters 297, 341–354.
doi:10.1016/j.epsl.2010.06.036.

Long, M.D., Benoit, M.H., Chapman, M.C., King, S.D., 2010.
Upper mantle anisotropy and transition zone thickness beneath southeastern North America and implications for mantle dynamics.
Geochemistry, Geophysics, Geosystems 11.
doi:https://doi.org/10.1029/2010GC003247.

Long, M.D., Lynner, C., 2015.
Seismic anisotropy in the lowermost mantle near the Perm Anomaly.
Geophysical Research Letters 42, 7073–7080.
doi:10.1002/2015GL065506.

Lutz, K.A., Long, M.D., Creasy, N., Deng, J., 2020.
Seismic anisotropy in the lowermost mantle beneath North America from SKS-SKKS splitting intensity discrepancies.
Physics of the Earth and Planetary Interiors 305, 106504.
doi:10.1016/j.pepi.2020.106504.

Lynner, C., Long, M.D., 2014.
Lowermost mantle anisotropy and deformation along the boundary of the african llsvp.
Geophysical Research Letters 41, 3447–3454.
doi:10.1002/2014GL059875.

Mainprice, D., 2015.
Seismic anisotropy of the deep earth from a mineral and rock physics perspective. treatise of geophysics, 2, in: Schubert, G. (Ed.), Treatise of Geophysics. 1st ed.. Elsevier. volume 2, pp. 437–491.

doi:`10.1016/B978-044452748-6.00045-6`.

Mao, W.L., Shen, G., Prakapenka, V.B., Meng, Y., Campbell, A.J., Heinz, D.L., Shu, J., Hemley, R.J., Mao, H.K., 2004.
Ferromagnesian postperovskite silicates in the D” layer of the Earth.
Proceedings of the National Academy of Sciences of the United States of America 101, 15867–15869.
doi:`10.1073/pnas.0407135101`.

Marquardt, H., Buchen, J., Mendez, A.S., Kurnosov, A., Wendt, M., Rothkirch, A., Pennicard, D., Liermann, H.P., 2018.
Elastic Softening of (Mg 0.8 Fe 0.2)O Ferropericlase Across the Iron Spin Crossover Measured at Seismic Frequencies.
Geophysical Research Letters 45, 6862–6868.
doi:`10.1029/2018GL077982`.

Marquardt, H., Speziale, S., Reichmann, H.J., Frost, D.J., Schilling, F.R., Garnero, E.J., 2009.
Elastic shear anisotropy of ferropericlase in earth’s lower mantle.
Science 324, 224–226.
doi:`10.1126/science.1169365`.

Maupin, V., Garnero, E.J., Lay, T., Fouch, M.J., 2005.
Azimuthal anisotropy in the d” layer beneath the caribbean.
Journal of Geophysical Research: Solid Earth 110, B08301.
doi:`10.1029/2004JB003506`.

McNamara, A.K., 2019.
A review of large low shear velocity provinces and ultra low velocity zones.
Tectonophysics 760, 199–220.
doi:`10.1016/j.tecto.2018.04.015`.

McNamara, A.K., Van Keken, P.E., Karato, S.I., 2002.
Development of anisotropic structure in the earth’s lower mantle by solid-state convection.
Nature 416, 310–314.
doi:`10.1038/416310a`.

Meade, C., Silver, P.G., Kaneshima, S., 1995.
Laboratory and seismological observations of lower mantle isotropy.
Geophysical Research Letters 22, 1293–1296.

Megnin, C., Romanowicz, B., 2000.
The three-dimensional shear velocity structure of the mantle from the inversion of body, surface and higher-mode waveforms.
Geophysical Journal International 143, 709–728.
doi:`10.1046/j.1365-246X.2000.00298.x`.

Met Office, 2010 - 2015.
Cartopy: a cartographic python library with a matplotlib interface.
Exeter, Devon.
URL: `http://scitools.org.uk/cartopy`.

Metropolis, N., Rosenbluth, A.W., Rosenbluth, M.N., Teller, A.H., Teller, E., 1953.
Equation of State Calculations by Fast Computing Machines.
The journal of chemical physics 21, 1087—-1092.

Mitrovica, J.X., Forte, A.M., 2004.
A new inference of mantle viscosity based upon joint inversion of convection and glacial isostatic adjustment data.
Earth and Planetary Science Letters 225, 177–189.
doi:`10.1016/j.epsl.2004.06.005`.

Miyagi, L., Kanitpanyacharoen, W., Kaercher, P., Lee, K.K., Wenk, H.R., 2010.
Slip systems in MgSiO3 post-perovskite: Implications for D” anisotropy.
Science 329, 1639–1641.
doi:`10.1126/science.1192465`.

Miyagi, L., Kanitpanyacharoen, W., Stackhouse, S., Militzer, B., Wenk, H.R., 2011.
The enigma of post-perovskite anisotropy: deformation versus transformation textures.
Physics and Chemistry of Minerals 38, 665–678.
doi:`10.1007/s00269-011-0439-y`.

Miyagi, L., Nishiyama, N., Wang, Y., Kubo, A., West, D.V., Cava, R.J., Duffy, T.S., Wenk, H.R., 2008.
Deformation and texture development in CaIrO3 post-perovskite phase up to 6GPa and 1300K.
Earth and Planetary Science Letters 268, 515–525.
doi:`10.1016/j.epsl.2008.02.005`.

Montagner, J.P., Kennett, B.L., 1996.
How to reconcile body-wave and normal-mode reference earth models.
Geophysical Journal International 125, 229–248.
doi:`10.1111/j.1365-246X.1996.tb06548.x`.

Moulik, P., Ekstrom, G., 2014.
An anisotropic shear velocity model of the Earth's mantle using normal modes, body waves, surface waves and long-period waveforms.
Geophysical Journal International 199, 1713–1738.
doi:`10.1093/gji/ggu356`.

Moulik, P., Ekström, G., 2016.
The relationships between large-scale variations in shear velocity, density, and compressional velocity in the Earth's mantle.
Journal of Geophysical Research: Solid Earth 121, 2737–2771.
doi:`10.1002/2015JB012679`.

Mound, J., Davies, C., Rost, S., Aurnou, J., 2019.
Regional stratification at the top of Earth's core due to core–mantle boundary heat flux variations.
Nature Geoscience 12, 575–580.
doi:`10.1038/s41561-019-0381-z`.

Murakami, M., Hirose, K., Kawamura, K., Sata, N., Ohishi, Y., 2004.
Post-Perovskite Phase Transition in MgSiO3.
Science 304, 855–858.
doi:`10.1126/science.1095932`.

Murakami, M., Hirose, K., Sata, N., Ohishi, Y., 2005.

Post-perovskite phase transition and mineral chemistry in the pyrolitic lowermost mantle.
Geophysical Research Letters 32, 1–4.
doi:`10.1029/2004GL021956`.

Murakami, M., Ohishi, Y., Hirao, N., Hirose, K., 2012.
A perovskitic lower mantle inferred from high-pressure, high-temperature sound velocity data.
Nature 485, 90–94.
doi:`10.1038/nature11004`.

Musgrave, M., 1970.
Crystal acoustics.
1 ed., Holden-Day, San Francisco, USA.

Nakagawa, T., Tackley, P.J., 2011.
Effects of low-viscosity post-perovskite on thermo-chemical mantle convection in a 3-D spherical shell.
Geophysical Research Letters 38.
doi:`10.1029/2010GL046494`.

Ni, S., Tan, E., Gurnis, M., Helmberger, D., 2002.
Sharp sides to the African superplume.
Science 296, 1850–1852.
doi:`10.1126/science.1070698`.

Nimmo, F., 2015.
Energetics of the Core, in: Schubert, G. (Ed.), Treatise on Geophysics. 2nd ed.. Elsevier. volume 8, pp. 27–55.
doi:`10.1016/B978-0-444-53802-4.00139-1`.

Niu, F., Perez, A.M., 2004.
Seismic anisotropy in the lower mantle: A comparison of waveform splitting of SKS and SKKS.
Geophysical Research Letters 31, 1–4.
doi:`10.1029/2004GL021196`.

Nomura, R., Ozawa, H., Tateno, S., Hirose, K., Hernlund, J., Muto, S., Ishii, H., Hiraoka, N., 2011.

Spin crossover and iron-rich silicate melt in the Earth's deep mantle.
Nature 473, 199–202.
doi:`10.1038/nature09940`.

Nowacki, A., Cottaar, S., 2021.
Towards imaging flow at the base of the mantle with seismic, mineral physics and geodynamic constraints, in: Marquardt, H., Ballmer, M., Cottaar, S., Jasper, K. (Eds.), Mantle Convection and Surface Expressions. American Geophysical Union. Geophysical Monograph, pp. 329–352.
doi:`10.1002/9781119528609.ch13`.

Nowacki, A., Walker, A.M., Wookey, J., Kendall, J.M., 2013.
Evaluating post-perovskite as a cause of D'' anisotropy in regions of palaeosubduction.
Geophysical Journal International 192, 1085–1090.
doi:`10.1093/gji/ggs068`.

Nowacki, A., Wookey, J., Kendall, J.M., 2010.
Deformation of the lowermost mantle from seismic anisotropy.
Nature 467, 1091–1094.
doi:`10.1038/nature09507`.

Nowacki, A., Wookey, J., Kendall, J.M., 2011.
New advances in using seismic anisotropy, mineral physics and geodynamics to understand deformation in the lowermost mantle.
Journal of Geodynamics 52, 205–228.
doi:`10.1016/J.JOG.2011.04.003`.

Oganov, A.R., Ono, S., 2004.
Theoretical and experimental evidence for a post-perovskite phase of MgSiO3 in Earth's D" layer.
Nature 430, 445–448.
doi:`10.1038/nature02701`.

Otsuka, K., Karato, S.I., 2012.
Deep penetration of molten iron into the mantle caused by a morphological instability.
Nature 492, 243–246.

doi:`10.1038/nature11663`.

Panning, M., Romanowicz, B., 2006.
A three-dimensional radially anisotropic model of shear velocity in the whole mantle.
Geophysical Journal International 167, 361–379.
doi:`10.1111/j.1365-246X.2006.03100.x`.

Panning, M.P., Lekić, V., Romanowicz, B.A., 2010.
Importance of crustal corrections in the development of a new global model of radial anisotropy.
Journal of Geophysical Research 115.
doi:`10.1029/2010JB007520`.

Pearson, D., Brenker, F., Nestola, F., McNeill, J., Nasdala, L., Hutchison, M., Matveev, S., Mather, K., Silversmit, G., Schmitz, S., et al., 2014.
Hydrous mantle transition zone indicated by ringwoodite included within diamond.
Nature 507, 221–224.
doi:`10.1038/nature13080`.

Peters, B.J., Carlson, R.W., Day, J.M.D., Horan, M.F., 2018.
Hadean silicate differentiation preserved by anomalous 142Nd/144Nd ratios in the Réunion hotspot source.
Nature 555, 89–93.
doi:`10.1038/nature25754`.

Peters, B.J., Mundl-Petermeier, A., Carlson, R.W., Walker, R.J., Day, J.M.D., 2021.
Combined Lithophile-Siderophile Isotopic Constraints on Hadean Processes Preserved in Ocean Island Basalt Sources.
Geochemistry, Geophysics, Geosystems 22.
doi:`10.1029/2020gc009479`.

Pisconti, A., Thomas, C., Wookey, J., 2019.
Discriminating Between Causes of D” Anisotropy Using Reflections and Splitting Measurements for a Single Path.
Journal of Geophysical Research: Solid Earth , 4811–4830doi:`10.1029/2018JB016993`.

Pradhan, G.K., Fiquet, G., Siebert, J., Auzende, A.L., Morard, G., Antonangeli, D., Garbarino, G., 2015.
Melting of MORB at core-mantle boundary.
Earth and Planetary Science Letters 431, 247–255.
doi:`10.1016/j.epsl.2015.09.034`.

Reiss, M.C., Long, M.D., Creasy, N., 2019.
Lowermost Mantle Anisotropy Beneath Africa From Differential SKS - SKKS Shear-Wave Splitting.
Journal of Geophysical Research: Solid Earth , 8540–8564doi:`10.1029/2018jb017160`.

Restivo, A., Helffrich, G., 1999.
Teleseismic shear wave splitting measurements in noisyenvironments.
Geophysical Journal International 137, 821–830.
doi:`10.1046/j.1365-246x.1999.00845.x`.

Restivo, A., Helffrich, G., 2006.
Core—mantle boundary structure investigated using sks and skks polarization anomalies.
Geophysical Journal International 165, 288–302.
doi:`10.1111/j.1365-246X.2006.02901.x`.

Richards, M.A., Lithgow-Bertelloni, C., 1998.
The Dynamics of Cenozoic and Mesozoic Plate Motions.
Reviews of Geophysics 36, 27–78.
doi:`10.1029/97RG02282`.

Ringwood, A., 1977.
Composition of the core and implications for origin of the earth.
Geochemical Journal 11, 111–135.

Ringwood, A., Major, A., 1966.
High-pressure transformations in pyroxenes.
Earth and Planetary Science Letters 1, 351–357.

Ringwood, A.E., 1991.

Phase transformations and their bearing on the constitution and dynamics of the mantle.
Geochimica et Cosmochimica Acta 55, 2083–2110.
doi:`10.1016/0016-7037(91)90090-R`.

Ringwood, A.E., Major, A., 1970.
The system mg2sio4 fe2sio4 at high pressures and temperatures.
Physics of the Earth and Planetary Interiors 3, 89–108.

Ritsema, J., Deuss, A., Heijst, H.J.V., Woodhouse, J.H., 2011.
S40RTS: a degree-40 shear-velocity model for the mantle from new Rayleigh wave dispersion, teleseismic traveltime and normal-mode splitting function measurements.
Geophysical Journal Internationalo 184, 1223–1236.
doi:`10.1111/j.1365-246X.2010.04884.x`.

Ritsema, J., Ni, S., Helmberger, D.V., Crotwell, H.P., 1998.
Evidence for strong shear velocity reductions and velocity gradients in the lower mantle beneath Africa.
Geophysical Research Letters 25, 4245–4248.
doi:`10.1029/1998GL900127`.

Rodríguez, E.E., Portner, D.E., Beck, S.L., Rocha, M.P., Bianchi, M.B., Assumpção, M., Ruiz, M., Alvarado, P., Condori, C., Lynner, C., 2021.
Mantle dynamics of the Andean Subduction Zone from continent-scale teleseismic S-wave tomography.
Geophysical Journal International 224, 1553–1571.
doi:`10.1093/gji/ggaa536`.

Rokosky, J.M., Lay, T., Garnero, E.J., 2006.
Small-scale lateral variations in azimuthally anisotropic D” structure beneath the Cocos Plate.
Earth and Planetary Science Letters 248, 411–425.
doi:`10.1016/j.epsl.2006.06.005`.

Romanowicz, B., Wenk, H.R., 2017.
Anisotropy in the deep earth.
Physics of the Earth and Planetary Interiors 269, 58–90.

doi:10.1016/j.pepi.2017.05.005.

Rost, S., Garnero, E.J., Williams, Q., Manga, M., 2005.
Seismological constraints on a possible plume root at the core-mantle boundary.
Nature 435, 666–669.
doi:10.1038/nature03620.

Rudolph, M.L., Lekić, V., Lithgow-Bertelloni, C., 2015.
Viscosity jump in Earth's mid-mantle.
Science 350, 1349–1352.
doi:10.1126/science.aad1929.

Sambridge, M., 1999.
Geophysical inversion with a neighbourhood algorithm—i. searching a parameter space.
Geophysical Journal International 138, 479–494.
doi:10.1046/j.1365-246X.1999.00876.x.

Sandvol, E., Hearn, T., 1994.
Bootstrapping shear-wave splitting errors.
Bulletin of the Seismological Society of America 84, 1971–1977.

Savage, M., 1999.
Seismic anisotropy and mantle deformation: What have we learned from shear wave splitting?
Reviews of Geophysics 37, 65–106.
doi:10.1029/98RG02075.

Schaeffer, A.J., Lebedev, S., Becker, T.W., 2016.
Azimuthal seismic anisotropy in the Earth's upper mantle and the thickness of tectonic plates.
Geophysical Journal International 207, 901–933.
doi:10.1093/gji/ggw309.

Schlaphorst, D., Kendall, J.M., Baptie, B., Latchman, J.L., Tait, S., 2017.
Gaps, tears and seismic anisotropy around the subducting slabs of the Antilles.
Tectonophysics 698, 65–78.
doi:10.1016/j.tecto.2017.01.002.

Schubert, G., Masters, G., Olson, P., Tackley, P., 2004.
Superplumes or plume clusters?
Physics of the Earth and Planetary Interiors 146, 147–162.
doi:10.1016/j.pepi.2003.09.025.

Shearer, P.M., 2019.
Introduction to Seismology.
Cambridge University Press.
doi:10.1017/9781316877111.

Shearer, P.M., Masters, T.G., 1992.
Global mapping of topography on the 660-km discontinuity.
Nature 355, 791–796.
doi:10.1038/355791a0.

Shih, X.R., Meyer, R.P., Schneider, J.F., 1989.
An automated, analytical method to determine shear-wave splitting.
Tectonophysics 165, 271–278.
doi:10.1016/0040-1951(89)90052-8.

Sidorin, I., Gurnis, M., Helmberger, D.V., 1999.
Evidence for a Ubiquitous Seismic Discontinuity at the Base of the Mantle Evidence Seismic Base for of the a Ubiquitous at Mantle the.
Science 286, 1326–1331.
doi:10.1126/science.286.5443.1326.

Silver, P.G., 1996.
Seismic Anisotropy beneath the continents: Probing the Depths of Geology.
Annual Review of Earth and Planetary Sciences 24, 385–432.
doi:10.1146/annurev.earth.24.1.385.

Silver, P.G., Chan, W.W., 1988.
Implications for continental strucutre and evolution from seismic anisotropy.
Nature 331, 450.
doi:10.1038/335034a0.

Silver, P.G., Chan, W.W., 1991.

Shear wave splitting and subcontinental mantle deformation.

Journal of Geophysical Research 96, 16429–16454.

doi:`10.1029/91JB00899`.

Silver, P.G., Long, M.D., 2011.

The non-commutivity of shear wave splitting operators at low frequencies and implications for anisotropy tomography.

Geophysical Journal International 184, 1415–1427.

doi:`10.1111/j.1365-246X.2010.04927.x`.

Silver, P.G., Savage, M.K., 1994.

The Interpretation of shear-wave splitting parameters in the presence of two anisotropic layers.

Geophysical Journal International 5, 689–691.

doi:`10.1111/j.1365-246X.1994.tb04027.x`.

Simmons, N.A., Forte, A.M., Grand, S.P., 2009.

Joint seismic, geodynamic and mineral physical constraints on three-dimensional mantle heterogeneity: Implications for the relative importance of thermal versus compositional heterogeneity.

Geophysical Journal International 177, 1284–1304.

doi:`10.1111/j.1365-246X.2009.04133.x`.

Smith, E.C., Baird, A.F., Kendall, J.M., Martín, C., White, R.S., Brisbourne, A.M., Smith, A.M., 2017.

Ice fabric in an antarctic ice stream interpreted from seismic anisotropy.

Geophysical Research Letters 44, 3710–3718.

doi:`10.1002/2016GL072093`.

Song, X., Helmberger, D.V., 1992.

Velocity structure near the inner core boundary from waveform modeling.

Journal of Geophysical Research: Solid Earth 97, 6573–6586.

doi:`10.1029/92JB00330`.

Souriau, A., Poupinet, G., 1991.

The velocity profile at the base of the liquid core from pkp (bc+ cdiff) data: an argument in favour of radial inhomogeneity.
Geophysical Research Letters 18, 2023–2026.
doi:`10.1029/91GL02417`.

Stackhouse, S., Brodholt, J.P., Wookey, J., Kendall, J.M., Price, G.D., 2005.
The effect of temperature on the seismic anisotropy of the perovskite and post-perovskite polymorphs of MgSiO3.
Earth and Planetary Science Letters 230, 1–10.
doi:`10.1016/j.epsl.2004.11.021`.

Stephenson, J., Tkalčić, H., Sambridge, M., 2021.
Evidence for the Innermost Inner Core: Robust Parameter Search for Radially Varying Anisotropy Using the Neighborhood Algorithm.
Journal of Geophysical Research: Solid Earth 126.
doi:`10.1029/2020JB020545`.

Su, W.J., Dziewonski, A.M., 1997.
Simultaneous inversion for 3-D variations in shear and bulk velocity in the mantle.
Physics of the Earth and Planetary Interiors 100, 135–156.
doi:`10.1016/S0031-9201(96)03236-0`.

Sun, D., Helmberger, D., Miller, M.S., Jackson, J.M., 2016.
Major disruption of d ”beneath alaska.
Journal of Geophysical Research: Solid Earth 121, 3534–3556.

Sun, N., Wei, W., Han, S., Song, J., Li, X., Duan, Y., Prakapenka, V.B., Mao, Z., 2018a.
Phase transition and thermal equations of state of (Fe,Al)-bridgmanite and post-perovskite: Implication for the chemical heterogeneity at the lowermost mantle.
Earth and Planetary Science Letters 490, 161–169.
doi:`10.1016/j.epsl.2018.03.004`.

Sun, W., Yoshino, T., Sakamoto, N., Yurimoto, H., 2018b.
Supercritical fluid in the mantle transition zone deduced from h–d interdiffusion of wadsleyite.
Earth and Planetary Science Letters 484, 309–317.

doi:`10.1016/j.epsl.2017.12.032`.

Szwillus, W., Afonso, J.C., Ebbing, J., Mooney, W.D., 2019.
Global Crustal Thickness and Velocity Structure From Geostatistical Analysis of Seismic Data.
Journal of Geophysical Research: Solid Earth 124, 1626–1652.
doi:`https://doi.org/10.1029/2018JB016593`.

Tackley, P.J., 2000.
Mantle convection and plate tectonics: Toward an integrated physical and chemical theory.
Science 288, 2002–2007.
doi:`10.1126/science.288.5473.2002`.

Tackley, P.J., 2012.
Dynamics and evolution of the deep mantle resulting from thermal, chemical, phase and melting effects.
Earth-Science Reviews 110, 1–25.
doi:`10.1016/j.earscirev.2011.10.001`.

Tandon, G.P., Weng, G.J., 1984.
The effect of aspect ratio of inclusions on the elastic properties of unidirectionally aligned composites.
Polymer Composites 5, 327–333.
doi:`10.1002/pc.750050413`.

Tateno, S., Hirose, K., Ohishi, Y., 2014.
Melting experiments on peridotite to lowermost mantle conditions.
Journal of Geophysical Research: Solid Earth 119, 4684–4694.
doi:`10.1002/2013JB010616`.

Tateno, S., Hirose, K., Sata, N., Ohishi, Y., 2005.
Phase relations in Mg3Al2Si3 O12 to 180 GPa: Effect of Al on post-perovskite phase transition.
Geophysical Research Letters 32.
doi:`10.1029/2005GL023309`.

Tateno, S., Hirose, K., Sata, N., Ohishi, Y., 2007.

Solubility of FeO in (Mg,Fe)SiO3 perovskite and the post-perovskite phase transition.
Physics of the Earth and Planetary Interiors 160, 319–325.
doi:`10.1016/j.pepi.2006.11.010`.

Tateno, S., Hirose, K., Sata, N., Ohishi, Y., 2009.
Determination of post-perovskite phase transition boundary up to 4400K and implications for thermal structure in D” layer.
Earth and Planetary Science Letters 277, 130–136.
doi:`10.1016/J.EPSL.2008.10.004`.

Teanby, N.A., Kendall, J., Baan, M.V.D., 2004.
Automation of Shear-Wave Splitting Measurements using Cluster Analysis.
Bulletin of the Seismologial Society of America 94, 453–463.
doi:`10.1785/0120030123`.

Tesoniero, A., Leng, K., D. Long, M., Nissen-Meyer, T., 2020.
Full wave sensitivity of SK(K)S phases to arbitrary anisotropy in the upper and lower mantle.
Geophysical Journal International 222, 412–435.
doi:`10.1093/gji/ggaa171`.

Thomas, C., Garnero, E.J., Lay, T., 2004.
High-resolution imaging of lowermost mantle structure under the Cocos plate.
Journal of Geophysical Research: Solid Earth 109.
doi:`10.1029/2004JB003013`.

Thomas, C., Wookey, J., Simpson, M., 2007.
D” anisotropy beneath southeast asia.
Geophysical Research Letters 34, L04301.
doi:`10.1029/2006GL028965`.

Thorne, M.S., Garnero, E.J., Jahnke, G., Igel, H., McNamara, A.K., 2013.
Mega ultra low velocity zone and mantle flow.
Earth and Planetary Science Letters 364, 59–67.
doi:`10.1016/j.epsl.2012.12.034`.

Thorne, M.S., Leng, K., Pachhai, S., Rost, S., Wicks, J., Nissen-Meyer, T., 2021.
The Most Parsimonious Ultralow-Velocity Zone Distribution From Highly Anomalous SPdKS Waveforms.
Geochemistry, Geophysics, Geosystems 22, e2020GC009467.
doi:`10.1029/2020GC009467`.

Tommasi, A., Goryaeva, A., Carrez, P., Cordier, P., Mainprice, D., 2018.
Deformation, crystal preferred orientations, and seismic anisotropy in the Earth's D" layer.
Earth and Planetary Science Letters 492, 35–46.
doi:`10.1016/j.epsl.2018.03.032`.

Tommasi, A., Mainprice, D., Canova, G., Chastel, Y., 2000.
Viscoplastic self-consistent and equilibrium-based modeling of olivine lattice preferred orientations: Implications for the upper mantle seismic anisotropy.
Journal of Geophysical Research: Solid Earth 105, 7893–7908.
doi:`10.1029/1999JB900411`.

Torsvik, T.H., Van Der Voo, R., Doubrovine, P.V., Burke, K., Steinberger, B., Ashwal, L.D., Trønnes, R.G., Webb, S.J., Bull, A.L., 2014.
Deep mantle structure as a reference frame for movements in and on the Earth.
Proceedings of the National Academy of Sciences of the United States of America 111, 8735–8740.
doi:`10.1073/pnas.1318135111`.

Trønnes, R.G., 2010.
Structure, mineralogy and dynamics of the lowermost mantle.
Mineralogy and Petrology 99, 243–261.
doi:`10.1007/s00710-009-0068-z`.

Tsuchiya, J., Tsuchiya, T., Wentzcovitch, R.M., 2005.
Vibrational and thermodynamic properties of MgSiO3 postperovskite.
Journal of Geophysical Research: Solid Earth 110, 1–6.
doi:`10.1029/2004JB003409`.

Tsujino, N., Nishihara, Y., Yamazaki, D., Seto, Y., Higo, Y., Takahashi, E., 2016.

Mantle dynamics inferred from the crystallographic preferred orientation of bridgmanite.
Nature 539, 81–84.
doi:`10.1038/nature19777`.

Vanacore, E., Niu, F., 2011.
Characterization of the d″ beneath the galapagos islands using skks and sks waveform.
Earthquake Science 24, 87–99.
doi:`10.1007/s11589-011-0772-8`.

Verdon, J.P., Kendall, J.M., 2011.
Detection of multiple fracture sets using observations of shear-wave splitting in microseismic data.
Geophysical Prospecting 59, 593–608.
doi:`10.1111/j.1365-2478.2010.00943.x`.

Vinnik, L., Romanowicz, B., Le Stunff, Y., Makeyeva, L., 1995.
Seismic anisotropy in the D" layer.
Geophysical Research Letters 22, 1657–1660.
doi:`10.1029/95GL01327`.

Walker, A.M., Forte, A.M., Wookey, J., Nowacki, A., Kendall, J.M., 2011.
Elastic anisotropy of D " predicted from global models of mantle flow.
Geochemistry, Geophysics, Geosystems 12, 1–22.
doi:`10.1029/2011GC003732`.

Walpole, J., Wookey, J., Kendall, J.M., Masters, T.G., 2017a.
Seismic anisotropy and mantle flow below subducting slabs.
Earth and Planetary Science Letters 465, 155–167.
doi:`10.1016/j.epsl.2017.02.023`.

Walpole, J., Wookey, J., Masters, G., Kendall, J.M., 2014.
A uniformly processed data set of SKS shear wave splitting measurements: A global investigation of upper mantle anisotropy beneath seismic stations.
Geochemistry, Geophysics, Geosystems 15, 1991–2010.
doi:`10.1002/2014GC005278`.

Walpole, J., Wookey, J.M., Nowacki, A., Walker, A., Kendall, J.M., Masters, G., Forte, A.M., 2017b. Structure in the lowermost mantle from seismic anisotropy, in: AGU Fall Meeting Abstracts, pp. DI43C–02.

Walsh, E., Arnold, R., Savage, M.K., 2013.
Silver and Chan revisited.
Journal of Geophysical Research: Solid Earth 118, 5500–5515.
doi:`10.1002/jgrb.50386`.

Walte, N.P., Heidelbach, F., Miyajima, N., Frost, D.J., Rubie, D.C., Dobson, D.P., 2009.
Transformation textures in post-perovskite: Understanding mantle flow in the D" layer of the earth.
Geophysical Research Letters 36.
doi:`10.1029/2008GL036840`.

Wang, X., Tsuchiya, T., Hase, A., 2015.
Computational support for a pyrolitic lower mantle containing ferric iron.
Nature Geoscience 8, 556–559.
doi:`10.1038/ngeo2458`.

Wang, Y., Wen, L., 2007.
Complex seismic anisotropy at the border of a very low velocity province at the base of the Earth's mantle.
Journal of Geophysical Research 112, B09305.
doi:`10.1029/2006JB004719`.

Wänke, H., 1981.
Constitution of terrestrial planets.
Philosophical Transactions of the Royal Society of London. Series A, Mathematical and Physical Sciences 303, 287–302.

Ward, J., Nowacki, A., Rost, S., 2020.
Lateral Velocity Gradients in the African Lower Mantle Inferred From Slowness Space Observations of Multipathing.
Geochemistry, Geophysics, Geosystems 21, e2020GC009025.

doi:`10.1029/2020GC009025`.

Weber, M., Davis, J., 1990.
Evidence of a laterally variable lower mantle structure from p-and s-waves.
Geophysical Journal International 102, 231–255.
doi:`10.1111/j.1365-246X.1990.tb00544.x`.

Wentzcovitch, R.M., Tsuchiya, T., Tsuchiya, J., 2006.
MgSiO3 postperovskite at D” conditions.
Proceedings of the National Academy of Sciences of the United States of America 103, 543–546.
doi:`10.1073/pnas.0506879103`.

Wessel, P., Smith, W.H.F., 1995.
New version of the generic mapping tools.
Eos, Transactions American Geophysical Union 76, 329–329.
doi:`10.1029/95EO00198`.

de Wit, R.W., Trampert, J., 2015.
Robust constraints on average radial lower mantle anisotropy and consequences for composition and texture.
Earth and Planetary Science Letters 429, 101–109.
doi:`10.1016/j.epsl.2015.07.057`.

Witte, H., 1932.
Beiträge zur Berechnung der Geschwindigkeit der Raumwellen im Erdinnern.
Nachrichten der Gesellschaft der Wissenschaften zu Göttingen Heft 2, 199–241.

Wolf, J., Creasy, N., Pisconti, A., Long, M.D., Thomas, C., 2019.
An investigation of seismic anisotropy in the lowermost mantle beneath Iceland.
Geophysical Journal International 219, S152–S166.
doi:`10.1093/gji/ggz312`.

Wolf, J., Long, M.D., Leng, K., Nissen-Meyer, T., 2021.
Sensitivity of SK(K)S and ScS phases to heterogeneous anisotropy in the lowermost mantle from global wavefield simulations.

Geophysical Journal International 228, 366–386.
doi:`10.1093/gji/ggab347`.

Wolfe, C.J., Silver, P.G., 1998.
Seismic anisotropy of oceanic upper mantle: Shear wave splitting methodologies and observations.
Journal of Geophysical Research: Solid Earth 103, 749–771.
doi:`10.1029/97JB02023`.

Wookey, J., 2012.
Direct probabilistic inversion of shear wave data for seismic anisotropy.
Geophysical Journal International 189, 1025–1037.
doi:`10.1111/j.1365-246X.2012.05405.x`.

Wookey, J., Kendall, J.M., 2007.
Seismic anisotropy of post-perovskite and the lowermost mantle, in: Hirose, K., Brodholt, J., Lay, T., Yuen, D. (Eds.), Post-Perovskite: The Last Mantle Phase Transition. American Geophysical Union. volume 174 of *Geophysical Monograph*, pp. 171–189.
doi:`10.1029/174GM13`.

Wookey, J., Kendall, J.M., 2008.
Constraints on lowermost mantle mineralogy and fabric beneath siberia from seismic anisotropy.
Earth and Planetary Science Letters 275, 32–42.
doi:`10.1016/J.EPSL.2008.07.049`.

Wookey, J., Kendall, J.M., Barruol, G., 2002.
Mid-mantle deformation inferred from seismic anisotropy.
Nature 415, 777–780.
doi:`10.1038/415777a`.

Wookey, J., Kendall, J.M., Rümpker, G., 2005a.
Lowermost mantle anisotropy beneath the north pacific from differential s—scs splitting.
Geophysical Journal International 161, 829–838.
doi:`10.1111/j.1365-246X.2005.02623.x`.

Wookey, J., Stackhouse, S., Kendall, J.m., Brodholt, J., Price, G.D., 2005b.
Efficacy of the post-perovskite phase as an explanation for lowermost-mantle seismic properties.
Nature 438, 1004–7.
doi:`10.1038/nature04345`.

Wu, J., Zhang, Z., Kong, F., Yang, B.B., Yu, Y., Liu, K.H., Gao, S.S., 2015.
Complex seismic anisotropy beneath western Tibet and its geodynamic implications.
Earth and Planetary Science Letters 413, 167–175.
doi:`10.1016/j.epsl.2015.01.002`.

Wu, X., Lin, J.F., Kaercher, P., Mao, Z., Liu, J., Wenk, H.R., Prakapenka, V.B., 2017.
Seismic anisotropy of the D” layer induced by (001) deformation of post-perovskite.
Nature Communications 8, 8–13.
doi:`10.1038/ncomms14669`.

Wuestefeld, A., Al-Harrasi, O., Verdon, J.P., Wookey, J., Kendall, J.M., 2010.
A strategy for automated analysis of passive microseismic data to image seismic anisotropy and fracture characteristics.
Geophysical Prospecting 58, 755–773.
doi:`10.1111/j.1365-2478.2010.00891.x`.

Wüstefeld, A., Bokelmann, G., 2007.
Null detection in shear-wave splitting measurements.
Bulletin of the Seismological Society of America 97, 1204–1211.
doi:`10.1785/0120060190`.

Wysession, M., T., L., Revenaugh, J., Williams, Q., Garnero, E., Jeanloz, R. Kellogg, L.H., 1998.
The d” discontinuity and its implications, in: Gurnis, M., Wysession, M., Knittle, E., Buffet, B.A. (Eds.), The core-mantle boundary region. American Geophysical Union. volume 28 of *Geodynamics*, pp. 273–297.
doi:`10.1029/GD028`.

Wysession, M.E., Okal, E.A., Bina, C.R., 1992.
The structure of the core-mantle boundary from diffracted waves.

Journal of Geophysical Research 97, 8749.
doi:`10.1029/92JB00511`.

Xie, L., Yoneda, A., Yamazaki, D., Manthilake, G., Higo, Y., Tange, Y., Guignot, N., King, A., Scheel, M., Andrault, D., 2020.
Formation of bridgmanite-enriched layer at the top lower-mantle during magma ocean solidification.
Nature Communications 11, 1–10.
doi:`10.1038/s41467-019-14071-8`.

Yamazaki, D., Karato, S.i., 2001.
Some mineral physics constraints on the rheology and geothermal structure of earth's lower mantle.
American Mineralogist 86, 385–391.
doi:`10.2138/am-2001-0401`.

Yamazaki, D., Yoshino, T., Ohfuji, H., ichi Ando, J., Yoneda, A., 2006.
Origin of seismic anisotropy in the D" layer inferred from shear deformation experiments on post-perovskite phase.
Earth and Planetary Science Letters 252, 372–378.
doi:`10.1016/j.epsl.2006.10.004`.

Yang, J., Faccenda, M., 2020.
Intraplate volcanism originating from upwelling hydrous mantle transition zone.
Nature 579, 88–91.
doi:`10.1038/s41586-020-2045-y`.

Yang, X., Li, H., Li, Y., Lü, Q., Zhang, G., Jiang, G., Li, X., 2019.
Seismic anisotropy beneath eastern China from shear wave splitting.
Geophys. J. Int 218, 1642–1651.
doi:`10.1093/gji/ggz242`.

Young, C.J., Lay, T., 1987.
Evidence for a shear velocity discontinuity in the lower mantle beneath india and the indian ocean.

Physics of the earth and planetary interiors 49, 37–53.
doi:`10.1016/0031-9201(87)90131-2`.

Young, C.J., Lay, T., 1990.
Multiple phase analysis of the shear velocity structure in the d" region beneath alaska.
Journal of Geophysical Research: Solid Earth 95, 17385–17402.
doi:`10.1029/JB095iB11p17385`.

Yu, S., Garnero, E.J., 2018.
Ultralow Velocity Zone Locations: A Global Assessment.
Geochemistry, Geophysics, Geosystems 19.
doi:`10.1002/2017GC007281`.

Yuan, K., Romanowicz, B., 2017.
Seismic evidence for partial melting at the root of major hot spot plumes.
Science 357, 393–397.
doi:`10.1126/science.aan0760`.

Zhang, S., Cottaar, S., Liu, T., Stackhouse, S., Militzer, B., 2016.
High-pressure, temperature elasticity of Fe- and Al-bearing MgSiO3: Implications for the Earth's lower mantle.
Earth and Planetary Science Letters 434, 264–273.
doi:`10.1016/j.epsl.2015.11.030`.

Zhang, Z., Stixrude, L., Brodholt, J., 2013.
Elastic properties of MgSiO3-perovskite under lower mantle conditions and the composition of the deep Earth.
Earth and Planetary Science Letters 379, 1–12.
doi:`10.1016/j.epsl.2013.07.034`.